

Investigations and numerical modeling of mechanical properties of tempered martensitic steel Eurofer97 at various loading rates, temperatures and after spallation irradiation

THÈSE N° 8535 (2018)

PRÉSENTÉE LE 4 MAI 2018

À LA FACULTÉ DES SCIENCES DE BASE

LABORATOIRE DE PHYSIQUE DES RÉACTEURS ET DE COMPORTEMENT DES SYSTÈMES

PROGRAMME DOCTORAL EN PHYSIQUE

ÉCOLE POLYTECHNIQUE FÉDÉRALE DE LAUSANNE

POUR L'OBTENTION DU GRADE DE DOCTEUR ÈS SCIENCES

PAR

Serafin KNITEL

acceptée sur proposition du jury:

Prof. R. Houdré, président du jury

Dr Ph. Spätig, directeur de thèse

Dr P. Mueller, rapporteur

Dr I. Kubena, rapporteur

Prof. N. Baluc, rapporteuse



ÉCOLE POLYTECHNIQUE
FÉDÉRALE DE LAUSANNE

Suisse
2018

Acknowledgements

Per definition the acknowledgment is a statement that is printed at the beginning of a book/thesis where the author expresses gratitude to others. Finally, being at this part of the doctoral program it turns out that it is maybe the most difficult one, even it is well defined. The possibility to forget someone who had an important contribution to this thesis is high and possibly there are too few lines there as well. Nevertheless, I will give a try not to forget anyone.

First and foremost, I want to thank my supervisor Dr. Philippe Spätig who made this project possible including the funding from the Swiss National Foundation (Grant No 200020-159932). During the four years, he had always time for discussion no matter if related to work or not. It was mostly him who provided me with scientific knowledge needed to further advance in work as well as to fulfill the desired approach to solve efficiently problems. Despite many deadlines, a few issues and my “Habsburger” English, which he will miss eventually, he always found a solution and got me back on track. I really appreciated to work with such an open minded, humorous and unruffled person. Thanks a lot.

Besides my supervisor it was Dr. Elisabeth Müller who improved my skills in electron microscopy. Additionally, I want to thank Dr. Müller for the fruitful discussions, Dr. Sigita Trabesinger who helped me a lot with the ion polish device. Furthermore, I am thankful for all the support which I got from Beat Baumgartner, Roger Schwenold, Roger Brun, Hans Kottmann, Stefan Stutz and Andrej Bullmer who helped me with experimental issues, technical sketches and the sample preparation, Zaiqing Que who spent much time with me performing the EBSD analysis and other SEM techniques (thanks also to An Zhang at that point) and Milan Heczko for his support in electron microscopy and crystallography.

An important person during my time at PSI was Dr. Ignasi Villacampa who was from the very beginning always there to help me by sharing his knowledge/skills in discussions, by enjoying EPFL courses with me and he encouraged me many times. Moreover, I was also supported from many others including Loic Favre for sharing his knowledge related to work as well as Switzerland and Dr. Mesiam Sistaninia who introduced me to FEM simulations. Among them, I would also thank: Dr. Freytag Koen and Dr. Vicente I & II for their FEM support.

Generally, I would like to thank my group for spending time together at lunch and/or at the coffee break and my boss Hans-Peter Seifert who was always interested in scientific, political and geographical discussions. Of course there are many others at PSI who made my stay as nice as possible including people in the sport club and from other groups.

Last but not least, I want to thank my family including Astrid who helped me to overcome difficult times. I also want to point out that the order of appearance is not indicating a value. It is simply the superposition of all people I met which made this work possible.

Abstract

The reduced activation tempered martensitic steel Eurofer97 is a reference steel for structural applications in fusion reactors. The first-wall and blanket materials will be subjected to high thermal and neutron fluxes and will experience very complex, time-dependent mechanical loading. Owing to impinging neutrons in materials, point defects and gaseous impurities (hydrogen and helium) are created and accumulated in the form of small defect clusters in the microstructure altering the mechanical properties. Notably, fracture toughness decreases as strength increases. Eurofer97, being a body centered cubic alloy, presents a ductile-to-brittle transition temperature T_0 that shifts to higher temperatures after irradiation.

The main objective was to study the loading rate and irradiation effects on plastic flow and fracture properties of Eurofer97. Tensile and fracture tests were performed at temperatures in the transition region, at low and high loading rates on unirradiated material. Tensile properties of irradiated material were assessed after irradiation in the Swiss neutron spallation source SINQ to a dose of about 11 dpa and helium content of 500 appm at about 250 °C. The information gathered from the mechanical tests was used either as input in finite element models of fracture specimens, or as benchmark data to calibrate and verify the predictions of the models. Fractographic observations were also conducted.

The tensile tests on unirradiated Eurofer97 showed a strong temperature dependence and strain rate sensitivity of the stress at low temperature, consistent with a mechanism of nucleation and propagation of double kink on screw dislocation. At high loading rate, the strain rate hardening was partially compensated by thermal softening due to quasi-adiabatic heating. The tensile properties after irradiation showed strong irradiation hardening (increase of the yield stress) accompanied by a drastic decrease of uniform elongation. The constitutive behavior at large strains, representative of those at crack tip, was obtained with an inverse method, based on finite element (FE) models of tensile specimens, developed to derive the true stress-strain curves from the load-displacement ones. These curves were used as input for the FE models of fracture specimens. Comparative fractographic observations on unirradiated and irradiated specimens did not reveal any strong effect of irradiation or helium on fracture mechanism, which remains transgranular cleavage. This observation indicates that higher helium concentration than 500 appm is necessary to initiate intergranular cleavage by helium bubble precipitation on grain boundaries.

Dynamic fracture tests were performed on unirradiated Eurofer97. A shift of about 10 °C of T_0 by one order of magnitude in loading rate was determined, which was in good agreement with results obtained on different ferritic steels. Static fracture toughness tests were also performed on disk compact tension specimens that can be accommodated in irradiation tubes of SINQ.

Different FE models of fracture specimens were developed to include strain-rate sensitivity of flow stress, heating resulting from the plastic work in the fracture process zone and loading rate. The structure of the stress field at the crack tip was studied and the temperature dependence of a lower bound to toughness data in the transition was reconstructed using a calibrated criterion of local approach to brittle fracture.

Keywords: tempered martensitic steel, thermo-nuclear fusion reactor, ductile to brittle transition, static and dynamic fracture toughness, irradiation embrittlement, inverse method, finite element modeling, local approach of brittle fracture

Résumé

L'acier martensitique revenu Eurofer97 à faible activation est le matériau structural de référence pour les réacteurs à fusion. La première paroi et la couverture seront soumises à des flux thermiques et neutroniques importants et subiront de complexes charges en fonction du temps. En raison du flux neutronique dans les matériaux, des défauts ponctuels et des impuretés gazeuses (hydrogène et hélium) sont créés et s'accumulent sous la forme d'amas de défauts dans la microstructure et altèrent les propriétés mécaniques. La ténacité en fracture décroît notablement alors la résistance en déformation croît. L'Eurofer97, ayant une structure cubique centrée, présente une température de transition ductile-fragile T_0 qui augmente après irradiation.

L'objectif principal a été l'étude des effets de vitesse de chargement et d'irradiation sur l'écoulement plastique et les propriétés en fracture de l'Eurofer97. Des essais de traction et de fractures ont été conduits à des températures dans la région de transition, à faible et haute vitesse de charge sur du matériau non-irradié. Les propriétés en traction du matériau irradié ont été évaluées après irradiation à 250 °C dans la source de spallation SINQ à une dose de 11 dpa et un contenu en hélium de 500 appm. L'information obtenue des essais de mécanique a été utilisée soit comme input pour les modèles par éléments finis, soit comme données de référence pour calibrer et vérifier les prévisions des modèles. Des observations fractographiques ont également été conduites.

Les essais de tractions sur l'Eurofer97 non-irradié ont montré une forte dépendance et sensibilité de la contrainte d'écoulement à la vitesse de déformation à basse température, cohérent avec un mécanisme de nucléation et propagation de double kink sur les dislocations vis. À haute vitesse de charge, le durcissement de vitesse de déformation était partiellement compensé par un adoucissement thermique résultant de chauffage adiabatique. Les propriétés en traction après irradiation ont montré un fort durcissement d'irradiation (augmentation de la limite d'élasticité) accompagné d'une diminution drastique de l'élongation uniforme. Le comportement constitutif à haute déformation, représentatives de celles en pointe de fissure, a été obtenu avec une méthode inverse, basée sur la modélisation par éléments finis des échantillons de traction, développée pour dériver les courbes de contrainte-déformation vraies des courbes de force-déplacement. Des observations fractographiques comparatives entre des échantillons non-irradiés et irradiés n'ont pas révélé d'effet marqué de l'irradiation ou de l'hélium sur les mécanismes de fracture, qui restent du clivage transgranulaire. Cette observation indique qu'une concentration d'hélium supérieure à 500 appm est nécessaire pour initier du clivage intergranulaire par précipitation de bulles d'hélium aux joints de grains.

Des essais de fracture dynamique ont été réalisés sur l'Eurofer97 non-irradié. Une augmentation de 10 °C de la température T_0 par ordre de grandeur de vitesse de charge a été déterminée, ce qui est en bon accord avec des résultats obtenus sur différents aciers ferritiques. Des essais de fracture statique ont aussi été conduits sur des échantillons traction compacts ronds qui peuvent être accommodés dans des tubes d'irradiation de SINQ.

Différents modèles par éléments finis ont été développés pour inclure la sensibilité de la contrainte d'écoulement à la vitesse de déformation, le chauffage dû au travail plastique dans la zone de fracture et la vitesse de charge. La structure du champ de contrainte en tête de fissure a été étudiée et la dépendance en température de la limite inférieure de donnée de ténacité en fracture dans la transition a été reconstruite avec un critère calibré d'approche locale de la fracture fragile.

Mots-clés: aciers martensitiques revenus, réacteurs à fusion thermonucléaire, transition fragile-ductile, ténacité en fracture statique et dynamique, fragilisation d'irradiation, méthode inverse, modélisation par éléments finis, approche locale de la fracture fragile

Content

ACKNOWLEDGEMENTS.....	I
ABSTRACT.....	III
RÉSUMÉ.....	V
LIST OF FIGURES	X
LIST OF TABLES	XV
LIST OF ABBREVIATIONS	XVI
CHAPTER 1 INTRODUCTION	1
1.1 OBJECTIVES OF THE THESIS	3
CHAPTER 2 LITERATURE REVIEW.....	5
2.1 FUSION	5
2.1.1 Tokamak.....	5
2.1.1.1 Test Blanket Modules	6
2.1.1.2 Fusion challenges.....	7
2.2 DEVELOPMENT OF REDUCED ACTIVATION FERRITIC/MARTENSITIC STEELS	9
2.3 IRRADIATION DAMAGE.....	10
2.3.1 Irradiation effects on ferritic/martensitic steels.....	12
2.3.1.1 Irradiation hardening.....	13
2.3.1.2 Irradiation Creep.....	14
2.3.1.3 Irradiation embrittlement.....	15
2.3.1.4 He effect	17
2.4 IRRADIATION TECHNIQUES.....	20
2.4.1 Ion accelerators	21
2.4.2 Fission reactors.....	21
2.4.3 Spallation neutron irradiation	22
2.4.3.1 Swiss spallation Neutron Source SINQ.....	23
2.4.4 International fusion materials irradiation facility.....	24
2.5 LOCAL APPROACH TO FRACTURE	25
2.5.1 Cleavage fracture mechanism	26
2.5.2 Local fracture models.....	27
CHAPTER 3 EXPERIMENTAL PROCEDURES.....	31
3.1 MATERIALS	31
3.2 SCANNING ELECTRON MICROSCOPY	32
3.3 SAMPLE PREPARATION.....	33
3.4 IRRADIATION CONDITIONS	34
3.5 TENSILE TESTS, SPECIMENS AND TESTING CONDITIONS	36
3.5.1 Standard round shaped specimen	36
3.5.2 Non-standard disk tensile specimen	36
3.6 FRACTURE TOUGHNESS TESTS	38
3.7 FINITE ELEMENT MODELLING	42

3.7.1	Standard round shaped tensile FEM.....	42
3.7.2	Non-standard disk tensile specimen FEM.....	43
3.7.3	Inverse approach.....	44
3.7.4	Fracture FEM.....	50
3.7.4.1	3D Compact Tension FE Model.....	50
3.7.4.2	2D Compact Tension FE Model.....	51
3.7.4.3	Modified boundary layer model.....	52
3.7.4.4	Disk Compact Tension FE Model.....	54
CHAPTER 4	RESULTS.....	57
4.1	MICROSTRUCTURE OF EUROFER97-(14).....	57
4.1.1	Grain size determination.....	57
4.1.2	PAG, lath and sub-grain analysis.....	58
4.1.3	Precipitates analysis.....	59
4.2	TENSILE PROPERTIES OF EUROFER97-(25).....	63
4.2.1	Ø 5 mm tensile specimen tests.....	63
4.2.2	Ø 3 mm tensile specimen tests.....	64
4.3	TENSILE PROPERTIES OF EUROFER97-(14).....	67
4.3.1	DTS tensile tests results.....	67
4.3.2	Optical microscopy and fractography.....	69
4.3.2.1	Optical microscopy.....	69
4.3.2.2	SEM analysis.....	70
4.4	FRACTURE TOUGHNESS MEASUREMENTS.....	76
4.4.1	Quasi static fracture tests on Eurofer97-(14).....	76
4.4.2	Dynamic fracture tests on Eurofer97-(25).....	77
4.4.3	Fractographic observations on 0.18T CT specimen, Eurofer97-(25).....	78
4.5	FINITE ELEMENT MODELING RESULTS.....	82
4.5.1	Post-necking analysis of Ø 5 mm standard tensile specimen, Eurofer-(25).....	82
4.5.2	Strain rate effect including thermal effects on tensile tests of Eurofer97-(25).....	85
4.5.3	Flow properties determination of disk tensile specimens, Eurofer97-(14).....	87
4.5.4	Local Approach to Fracture.....	89
4.5.4.1	3D and 2D CT model, Eurofer97-(25).....	89
4.5.4.2	Modified boundary layer model with T-stress consideration.....	93
4.5.4.3	2D CT model with loading rate and thermal effects consideration.....	97
4.5.4.4	Quasi-static loading model with strain rate effects included.....	97
4.5.4.5	Dynamic Loading.....	99
4.5.4.6	2D Disk CT model, Eurofer97-(14).....	102
CHAPTER 5	DISCUSSION.....	105
5.1	TENSILE PROPERTIES OF EUROFER97.....	105
5.1.1	Temperature and strain rate dependence of the yield stress.....	105
5.1.2	Irradiation-hardening.....	107
5.1.3	Strain-hardening.....	108
5.2	LOCAL APPROACH TO BRITTLE FRACTURE.....	109
5.2.1	Specimen size dependent calibration.....	109
5.2.2	Impact of flow properties, strain rate and thermal effects.....	112
5.2.3	Prediction of dynamic toughness of Eurofer97-(25).....	114
5.2.4	Prediction of the Eurofer97-(14) toughness after irradiation.....	115
5.2.5	Impact of different FE models on the local approach.....	116
5.2.6	DTS stress field analysis at fracture.....	118
CHAPTER 6	CONCLUSIONS.....	121
REFERENCE	125
CURRICULUM VITAE	142

List of Figures

Figure 1: Sketch of the design window of fusion reactor structural steels including the arising limitations (adapted from [1]).	1
Figure 2: Left: Illustration of the fracture modes for a BCC steel at different temperature. Right: Ductile to brittle transition temperature defined by the master curve. Additional shifts due to irradiation ΔT_{ih} and He embrittlement ΔT_{He} are indicated as example.	2
Figure 3: ITER design and cross section of the reactor. Reactor cut-away shows in-vessel components.	6
Figure 4: European Test blanket modules. a) General set-up. b) HCCL concept. c) HCPB concept. (from [10])	7
Figure 5: Calculated variation in dpa and He production in Eurofer97 per full power year in DEMO depending on the position in the first wall (from [12]).	8
Figure 6: Possible occurring strain rates at a plasma disruption in relation to other phenomena's (from [20]).	9
Figure 7: Calculated γ -surface dose rate. Left: Fe and some important alloying elements (from [26]). Right: RAFM steels and Fe after being irradiated to a 12.5 MW/m ² spectrum (from [27]).	10
Figure 8: Left: Schematic representation of displacement damage. Right: Kinchin-Pease model indicating the number of displaced atoms N versus the energy of the PKA.	11
Figure 9: Left: Calculated total PKA spectra for pure Fe in the first wall of a DEMO (impact of the different TBMs is indicated). Right: Frenkel pair production in Fe under DEMO conditions (both from [32]).	11
Figure 10: Left: Stress/strain diagram of Eurofer97 (from [41]). Right: Evolution uniform elongation with irradiation dose (from [42]). Dashed lines are guidance for the eyes.	13
Figure 11: Left: Yield stress evolution with irradiation temperature. Right: Yield stress increase with irradiation dose at $T < 350$ °C (both from [42]). Dashed lines are guidance for the eyes.	13
Figure 12: Left: Upper temperature limit for different steels based on a 10 ⁴ h creep rupture time (from [51]). Right: Diametral strain of various 9Cr steels in dependence of irradiation dose at hoop-stresses between 150 - 220 MPa at 325 °C (from [52]).	14
Figure 13: Modified master-curve of unirradiated Eurofer97 steel, $T_0 = 78$ °C (from [59]).	16
Figure 14: Fracture toughness results and corresponding master-curves in the unirradiated and irradiated conditions (from [67]).	16
Figure 15: Left: DBTT measured by Charpy tests shift in relation to Cr content for different irradiation doses (from [24]). Right: DBTT measured by Charpy tests shift in FM steels at different irradiation temperatures (from [42]).	17
Figure 16: Left: Cross section for (n, α) reaction for neutrons with different energy (from [74]). Right: Cross sections for 14 MeV neutrons producing He in various elements. Dashed lines indicate the trends of the indicated reactions (from [75]).	18
Figure 17: Left: Observed swelling with increasing dpa for austenitic and FM steels (from [34]). Right: Effect of He on swelling and void density at different He concentration for Eurofer97 irradiated to 16.3 dpa (from [77]).	18
Figure 18: Left: Hardening induced by spallation irradiation (data points) and neutron irradiation (lines). Right: DBTT shift for FM steels irradiated by spallation in comparison with neutron irradiated (both from [34]).	19
Figure 19: Sketch of the DBTT shift caused by irradiation hardening and He induced grain boundary weakening (from [34]).	20
Figure 20: Left: Dpa and He profile obtained in Fe via dual ion beam irradiation at JANNUS using 2MeV Fe ²⁺ and 2MeV He ²⁺ (from [96]). Right: Surviving defect fraction as function of the PKA energy calculated from molecular dynamics [30]. Range of displacement cascade energies associated with a 1 MeV ion beam (from [80]).	21
Figure 21: Neutron spectra of a fission (averaged spectra of pressurized water reactor) and fusion reactor. Left: Full energy range. Right: Spectra above 1 MeV as indicated by the blue arrow (both from [102]).	22

Figure 22: Neutron spectra from spallation sources (ESS, XADS) in comparison with spectra fission (HFR, BOR60) and fusion (DEMO). The international fusion materials irradiation facility (IFMIF) spectrum is given as well (from [114]).	23
Figure 23: Neutron irradiation facility at Paul Scherrer Institute. Proton beam is indicated in red. 1) Cock-croft-Walton column, 2) 4-sector injector cyclotron, 3) 8-sector mainring cyclotron and 4) SINQ target (from [116]).	23
Figure 24: Sketch of the SINQ target indicating the specimen position. Dimension of a specimen rod is given (from [112]).	24
Figure 25: Left: Schematic of IFMIF facility including the two accelerators, the target and test cell (from [121]). Right: Illustration of the IFMIF target.	25
Figure 26: Left: Schematic representation of the cleavage fracture mechanism in ferritic steels. Right: Normal stress σ_n at a crack tip illustrating the critical distance λ^* at which the critical stress for failure σ_f is reached. Carbide cracking near the peak stress is indicated.	26
Figure 27: Left: Illustration of the local approach indicating the stressed area $\sigma_n \geq \sigma^*$ which includes several carbides. Right: Predicted K_{Jc} by the local approach in comparison to the master curve for a $T_0 = -45^\circ\text{C}$ (from [72]).	27
Figure 28: Left: Yield stress shift of 200 MPa and corresponding $K_{Jc}(T)$ curve considering σ^* is not a function of temperature. Right: Comparison of the predicted $K_{Jc}(T)$ by the local approach (dashed lines) and the master curve for different shifts in yield stress with the assumption that σ^* is a function of temperature (red curve) (from [72]).	28
Figure 29: Left: Rod positions within the target array. Right: Sample layout within rod 12. Lower: X-ray image of rod 12 after irradiation (DTS positions are indicated).	34
Figure 30: Beam properties: Deposited energy D, calculated irradiation damage and He accumulation for rod 12. Gray areas indicate the DTS position.	35
Figure 31: Beam current and temperature history of SINQ STIP-V during 2007-2008 (adopted from Dai. Y. unpublished).	35
Figure 32: Standard round shaped tensile specimens (Dimensions in millimeters).	36
Figure 33: Non-standard disk tensile specimen geometry and dimensions as well as the designed DTS clamping system (dimensions in millimeters).	37
Figure 34: Engineering stress/strain curves of tested DTS specimens at room temperature and corresponding image of tested specimens.	37
Figure 35: Fracture compact tension specimens; Left: 0.18T CT and Right: 0.14T DCT specimen as well as the developed gripping system is shown (dimensions in millimeters).	38
Figure 36: Left: Compact tension specimen sketch Right: Plastic area A_p determination.	39
Figure 37: Schematic master curve shape for the lower and upper bound as well as the median. The transition temperature definition is indicated.	41
Figure 38: Axisymmetric FE model of the standard round shaped tensile specimen. Boundary conditions are indicated.	42
Figure 39: Illustrative comparison of plastic strain distribution within a standard round and a non-standard DT specimen at low loading level.	43
Figure 40: Left: 3D FE model of the non-standard DTS. Boundary conditions are indicated. Right: Refined mesh at gage section.	44
Figure 41: Left: Engineering stress/strain curve with the three regions indicated. Right: Piece-wise reconstruction of the material properties as (true stress, plastic strain) pairs.	45
Figure 42: Schematic explanation of the inverse approach in the elastic and plastic region.	46
Figure 43: Plastic strain distribution within the extended gage length including an illustration of the confined deformation beyond onset of necking.	47
Figure 44: Left: Disk tensile specimen test in comparison with a standard $\varnothing 5$ mm round shaped tensile specimen. Right: Reconstructed experimental DTS curve.	49
Figure 45: Flow property curves in terms of true stress/true plastic strain obtained by the inverse approach in comparison with the experimental data from a standard tensile test.	49
Figure 46: 3D FE CT mesh with details of the initial crack root.	50

Figure 47: 2D FE CT mesh indicating the J-integral path and refined mesh at the crack tip.	52
Figure 48: 2D FE SSY mesh indicating the nodes where boundary conditions were applied and details of the initial crack tip root.	53
Figure 49: a) 2D CT model and b) Modified boundary layer model including coordinate system.	54
Figure 50: 2D FE DCT mesh indicating the J-integral path and refined mesh at the crack tip.	54
Figure 51: Optical microscope images from etched Eurofer97-(14).	57
Figure 52: EBSD results of Eurofer97-(14). Left: Overview image of the martensitic structure. Right: Image at higher magnification showing the grain and sub-grain structure.	58
Figure 53: Microstructural investigation of Eurofer97-(14) using SEM. All images were taken using the QBSD. In the right upper image some PAG and packet boundaries are indicated.	59
Figure 54: Analytical investigation of precipitates in Eurofer97-(14) using SEM. Left upper image was taken with an In-lens detector and others with the QBSD.	60
Figure 55: Various precipitations investigated in Eurofer97-(14) using SEM. All images show the inverted recorded contrast.	60
Figure 56: SEM EDX analysis of precipitations. Left: EDX-mapping of two Cr rich particles. Right: EDX-mapping of a tantalum rich particle.	61
Figure 57: EDX point spectrum of a Ta rich particle. Vanadium peak is magnified in the lower right spectrum.	62
Figure 58: EDX point spectrum of a Cr rich particle. Vanadium peak is magnified in the lower right spectrum.	62
Figure 59: Tensile curves of Eurofer97-(25) at different temperatures and displacement rates conducted with the standard \varnothing 5 mm round shaped specimens.	64
Figure 60: Tensile curves of Eurofer97-(25) at -196 and -150 °C. Deformation at almost constant stress is indicated. ...	64
Figure 61: Tensile curves of Eurofer97-(25) at different temperatures and displacement rates performed with the standard \varnothing 3 mm round shaped specimen.	65
Figure 62: Strain rate analysis of Eurofer97-(25). Left: Tensile curves at different temperatures and displacement rates. Right: Determined shift in stress caused by an increase in strain rate by factor 10 at different temperatures.	66
Figure 63: Non-standard DTS tensile curves of the Eurofer97-(14) at different temperature. Left: Unirradiated Right: Irradiated.	67
Figure 64: Yields stress at 0.2 % and 1 % of plastic strain for the irradiated and unirradiated Eurofer97-(14).	68
Figure 65: Yield stress difference between unirradiated and irradiated at 0.2 and 1 % of plastic strain.	68
Figure 66: Engineering failure strain and stress for the irradiated and unirradiated Eurofer97-(14) DTS.	69
Figure 67: Comparison of the gage section of the tested irradiated as well as unirradiated DTS at various temperatures.	70
Figure 68: Fracture surface of the unirradiated DTS of Eurofer97-(14) at 200 °C using SEM. Lower right image was taken with the In-lens detector and others with ET detector.	72
Figure 69: Fracture surface of the irradiated DTS of Eurofer97-(14) at 200 °C using SEM. Lower right image was taken with the In-lens detector and others with ET detector.	73
Figure 70: Fracture surface of the unirradiated DTS of Eurofer97-(14) at -100 °C using SEM. Lower right image was taken with the In-lens detector and others with ET detector.	74
Figure 71: Fracture surface of the irradiated DTS of Eurofer97-(14) at -100 °C using SEM. All images were taken with the ET detector.	75
Figure 72: Left: Fracture toughness results for the quasi-static 0.14T DCT tests of Eurofer97-(14) adjusted to 1T. Transition temperature is indicated. Right: Determined transition temperature at increasing M value.	76
Figure 73: Left: Fracture toughness results for the dynamic 0.18T CT tests of Eurofer97-(25) adjusted to 1T. Transition temperature is indicated. Right: Determined transition temperature at increasing M value.	77
Figure 74: Loading rate in terms of dK_{Ic}/dt for the dynamic 0.18T CT tests of Eurofer97-(25) at different temperatures. Average value is indicated.	78
Figure 75: Fracture surface of the quasi-static tested 0.18T CT specimen of Eurofer97-(25) at -120 °C. SEM images were taken with the ET detector.	80
Figure 76: Fracture surface of the dynamic tested 0.18T CT specimen of Eurofer97-(25) at -120 °C. SEM images were taken with the ET detector.	81

Figure 77: Experimental engineering curves and corresponding FEM results of the \varnothing 5 mm round shaped standard tensile specimen of Eurofer97-(25).	82
Figure 78: Determined flow properties of Eurofer97-(25) at -196, -150 and -100 °C using the standard tensile \varnothing 5 mm round shaped tensile test results. Values beyond UTS were obtained by an inverse method.	83
Figure 79: Determined flow properties of Eurofer97-(25) at -50, 20 and 200 °C using the standard tensile \varnothing 5 mm round shaped tensile test results. Values beyond UTS were obtained by an inverse method.	84
Figure 80: Eurofer97-(25) obtained results and FEM approach. Left: Experimental tensile curves. Right: Flow curves used as input for FEM.	85
Figure 81: Tensile and flow curve of Eurofer97-(25) in comparison to the FEM results. Non-thermal FEM considers only strain rate; thermal FEM includes strain rate and thermal effects.	86
Figure 82: Calculated FE distributions of the standard tensile model which included strain rate and thermal effects at 10 % engineering strain. From left: Maximum principal stress in MPa, plastic equivalent strain, temperature in K and logarithmic strain rate in s^{-1}	87
Figure 83: Experimental engineering curves of the DTS tests and corresponding FEM reconstruction results. Left: Unirradiated. Right: Irradiated Eurofer97-(14).	88
Figure 84: Inverse determined flow properties in terms of true stress and true plastic strain for Eurofer97-(14). Left: Unirradiated. Right: Irradiated Eurofer97-(14).	88
Figure 85: Inverse determined flow properties of the unirradiated and irradiated DTS of Eurofer97-(14).	89
Figure 86: Left: Fracture toughness data with corresponding lower bound of the 3D 0.18T CT specimen. The stars indicate the FEM results. Right: Maximum principal stress σ_1 and plastic equivalent strain $\epsilon_{p,eq}$ at the crack tip.	90
Figure 87: Stressed volume encompassed by the maximum principal stress at different temperatures for the 0.18T and 0.88T model loaded to $K_{Jc(0.01)}$ (see Table 9 and Table 10).	91
Figure 88: Results of the 2D 0.18T FE model loaded to $K_{Jc(0.01)}$ (see Table 12). Left: Maximum principal stress σ_1 and plastic equivalent strain $\epsilon_{p,eq}$ at the crack tip. Right: Stressed volume encompassed by the maximum principal stress at different temperatures.	92
Figure 89: Stressed volume encompassed by the maximum principal stress at different temperatures for both 3D and 2D model loaded to $K_{Jc(0.01)}$ (see Table 9 and Table 12). Cross over range is indicated.	93
Figure 90: Maximum principal stress at the crack tip at different temperatures of the 2D 0.18T CT model, the MBL model without T-stress (SSY) and the MBL model considering T-stress (SSY+T).	94
Figure 91: Left: Determined T-stress at different temperatures to fit the stress field of a 0.18T CT specimen at the lower bound. Right: Biaxiality ratio for different specimen including 0.18T CT result. Literature values adapted from [184] for homogeneous material.	95
Figure 92: Stressed volume encompassed by the maximum principal stress at different temperatures. Left: MBL model without T-stress consideration Right: MBL model with T-stress consideration loaded to $K_{Jc(0.01)}$ (see Table 12).	96
Figure 93: Stressed volume encompassed by the maximum principal stress at different temperatures for 3D and 2D model in comparison with the MBL model which considers the T-stress loaded to $K_{Jc(0.01)}$ (see Table 12). Cross over range is indicated.	96
Figure 94: Stressed volume encompassed by the maximum principal stress at different temperatures loaded to $K_{Jc(0.01)}$ (see Table 17). Comparison of “no-strain rate”, “strain rate” and “thermal” FEM analysis. Left: Only strain rate is considered Right: Strain rate and thermal effects are considered.	97
Figure 95: Comparison of static and quasi-static FEM analysis of the 2D 0.18T CT FE model at different temperatures loaded to $K_{Jc(0.01)}$ (see Table 17). Left: Maximum principal stress at the crack tip. Right: Mechanical strain rate at the tip.	98
Figure 96: Comparison of the dynamic loaded 2D 0.18T CT models with “Quasi+SR”, “strain rate”, “adiabatic” and “thermal” analysis at -150 °C loaded to $K_{Jc(0.01)}$ (see Table 18). Left: Maximum principal stress at the crack tip. Right: Stressed volume encompassed by the maximum principal stress.	99
Figure 97: Comparison of the dynamic loaded 2D 0.18T CT models with “adiabatic” and “thermal” analysis at -150 °C. Left: Temperature and plastic strain at the crack tip in Kelvin. Right: Temperature field from the “thermal” analysis.	100

Figure 98: Left: Mechanical strain rate at the crack tip for the different models loaded to $K_{Jc(0.01)}$ (see Table 17). Right: Stressed volume encompassed by the maximum principal stress at different temperatures. Comparison of the “Quas+SR” and “strain rate” FEM analysis.	101
Figure 99: Left: Stressed volume encompassed by the maximum principal stress at different temperatures for the 2D DCT 0.14T model. Right: 1% Lower bound for the 0.14T CT indicating the data extraction from simulation.....	102
Figure 100: Left: Stressed volume encompassed by the maximum principal stress at different temperatures for the 2D DCT 0.14T model using the modified result loaded to $K_{Jc(0.01)}$ (see Table 23). Right: Maximum principal stress σ_I and plastic equivalent strain $\varepsilon_{p,eq}$ at the crack tip.	103
Figure 101: Eurofer97-(25) and Eurofer97-(14) yield stress versus temperature T and strain rate compensated temperature T'. Data from this study and from NRG [187]......	106
Figure 102: Activation volume in dependence of the shear yield stress for Eurofer97-(25) and F82H (from [186]).	107
Figure 103: Yield stress increase due to irradiation compared with literature values. Left: At room temperature [34]. Right: At 200 °C [2].	108
Figure 104: Stressed volume encompassed by the max principal stress at different temperatures for Eurofer97-(25) obtained from a 3D 0.88T FE model loaded to $K_{Jc(0.01)}$ (see Table 24). Left: Size was adjusted according to ASTM, equation (33). Right: Size was adjusted by local approach, equation (34)......	110
Figure 105: Adjustment factor $c=K_1/K_2$ in dependence of K_1 for the master-curve, local approach and the proposed method. K_{min} is indicated; K_1 correspond to 0.18T CT and K_2 to 0.88T CT.	112
Figure 106: Left: Determined flow properties at -150 °C with different elastic/plastic transition used as an input for Abaqus. Right: Impact of the different input on the stressed volume.	112
Figure 107: Left: Flow properties at -150 °C for two strain rates. Right: Stressed volume caused from the quasi-static loading FEM considering strain rate effects in comparison to FEM results obtained from a single strain rate.....	113
Figure 108: Maximum principal stress at the crack tip. Left: Quasi-static loading FEM considering strain rate effects in comparison to FEM with a single strain rate. Right: Impact of dynamic loading and thermal effects.	114
Figure 109: Left: Predicted T_0 using the local approach to fracture in comparison with the experimental result. K_{Jc} values obtained at different σ^* at $V^*=1.68 \cdot 10^6 \mu m^3$ are indicated. Right: Transition temperature shift ΔT_0 due to increased loading rate obtained from Eurofer97 in comparison with literature data (from [197, 198, 199])......	115
Figure 110: Left: Determined K_{Jc} values for the irradiated FEM including the 1 % lower bound for $T_0=132$ and 267 °C for 0.14T CT. Right: Corresponding stress/strain fields at K_{Jc}	116
Figure 111: Determined critical parameter ranges from different 0.18T FE model approaches. Left: Critical stress. Right: Critical volume.	117
Figure 112: Stress field at the crack tip. Left: 2D 0.18T CT and MBL model under SSY condition at -100 °C. Right: 2D 0.18T CT models whereas no strain rate and strain rate effect were considered at -150 °C.	118
Figure 113: Maximum principal stress distribution overlaid with the experimental fracture surface for the irradiated and unirradiated DTS tests at 200 °C. Units are in MPa.	119
Figure 114: Calculated maximum principal stress on the fracture at -100 °C of unirradiated and irradiated specimens. Units are in MPa.	120

List of Tables

Table 1: Chemical composition of the two Böhler Eurofer97 batches used in this work.	32
Table 2: Determined range of irradiation damages in Fe calculated by the energy deposition of the beam.	35
Table 3: Material properties of Eurofer97 which were used as an input for Abaqus.	43
Table 4: Measure and amount of elements being used for the FEM model for 0.18T and 0.88T CT.	51
Table 5: Determined grain size number G and corresponding grain diameter d both according to ASTM 112-13.	58
Table 6: Applied displacement rates and corresponding engineering strain rates.	63
Table 7: Applied displacement rates and corresponding engineering strain rates.	65
Table 8: Determined shift in stress due to a change in strain rate of factor 10 for Eurofer97-(25).	66
Table 9: K_{Jc} lower bound values at different temperatures for the 0.18T sized specimen and the corresponding K_{Jc} values where the stress/strain fields were calculated from the 3D CT model. D is the difference between those in percent.	90
Table 10: K_{Jc} lower bound values at different temperatures for the 0.88T sized specimen and the corresponding K_{Jc} values where the stress/strain fields were calculated from the 3D CT model. D is the difference between those in percent.	90
Table 11: Determined critical parameter σ^* - V^* range for the 3D 0.18T and 0.88T model.	91
Table 12: K_{Jc} lower bound values at different temperature for the 0.18T sized specimen and the K_{Jc} values where stress/strain fields where calculated from the 2D CT model. D is the difference between those in percent. $K_{Jc-FEM1(0.01)}$ was calculated by the J integral and $K_{Jc-FEM2(0.01)}$ by the load/displacement curve.	92
Table 13: Determined critical parameter σ^* - V^* range for the 2D 0.18T model.	92
Table 14: Calculated biaxility ratio for the 0.18T CT specimen at different temperature.	95
Table 15: Determined critical parameter σ^* - V^* range for the SSY model with and without T-stress consideration.	96
Table 16: Determined critical parameters σ^* - V^* for the quasi-static 0.18T CT FEM analysis. Difference between the “strain rate” and “thermal” model to the “no-strain rate” model is given.	98
Table 17: K_{Jc} lower bound values at different temperature for the 0.18T sized specimen and the K_{Jc} values where stress/strain fields where calculated from the 2D CT “strain rate” and “thermal” model. D gives the maximum difference between those in percent.	98
Table 18: K_{Jc} lower bound values at -150 °C for the 0.18T sized CT specimen and the K_{Jc} values where stress/strain fields where calculated from various the 2D CT models. D is the difference between those in percent. $K_{Jc-FEM(0.01)}$ was calculated by the J integral.	99
Table 19: Maximum principal stress at the peak and position for the four FEM analyses at -150 °C. d_p is the peak position and σ_{Ip} the peak stress.	100
Table 20: Determined critical parameters σ^* - V^* for the dynamic test using the “strain rate” 2D 0.18T CT FEM analysis. Difference D between the dynamic and quasi-static results is given in %.	102
Table 21: Determined critical parameter range σ^* - V^* for the 2D 0.14D CT FEM analysis.	103
Table 22: Determined critical parameter range σ^* - V^* for the 2D 0.14D CT FEM analysis using the modified cross over.	103
Table 23: K_{Jc} lower bound values at different temperatures for the 0.14T sized specimen and the corresponding K_{Jc} values where the stress/strain fields were calculated from the 2D CT model. D is the difference between those in percent. The K_{Jc} at -100 °C is the modified one.	104
Table 24: K_{Jc} lower bound values for different CT sizes. The 0.88T sizes were adjusted from the 0.18T model by the master-curve (MC) equation (33) and by the local approach (LC) equation (34).	110
Table 25: Determined critical parameter range σ^* - V^* for the 3D 0.88T and 3D 0.18T CT FEM analysis.	110

List of Abbreviations

appm	Atomic Parts Per Million
ASTM	American Standard of Testing Materials
BCA	Binary Collision Approximation
BCC	Body Centered Cubic
BLM	Boundary Layer Model
CQ	Current Quench
CT	Compact Tension
DBTT	Ductile to Brittle Transition Temperature
DCT	Disk Compact Tension
DEMO	Demonstration Power Plant
dpa	Displacements Per Atom
DTS	Disk Tensile Specimen
EBS	Electron Back Scatter Diffraction
EDX	Energy-Dispersive X-Ray
ER	Logarithmic Strain Rate
ET	Everhart-Thornley
FCC	Face Centered Cubic
FEM	Finite Element Model
FM	Ferritic Martensitic
FP	Frenkel Pair
fpv	Full Power Year
HCLL	Helium Cooled Lithium Lead
HCPB	Helium Cooled Pebble Bed
IFMIF	International Fusion Materials Irradiation Facility
LIPAC	Linear IFMIF Prototype Accelerator
MBL	Modified Boundary Layer
PAG	Prior Austenite Grain
PDs	Plasma Disruptions
PEEQ	Plastic Equivalent Strain
PKA	Primary Knock on Atom
PSI	Paul Scherrer Institute
QBSD	Quadrant Back Scattering Detector
RAFM	Reduced Activation Ferritic/Martensitic
RPV	Reactor Pressure Vessel
SE	Secondary Electron
SEM	Scanning Electron Microscope
SINQ	Swiss Spallation Neutron Source
SSY	Small Scale Yielding
STIM	Stopping of Ions in Matter
TBMs	Test Blanket Modules
TEM	Transmission Electron Microscopy
TQ	Thermal Quench

UCSB	University of California, Santa Barbara
UTS	Ultimate Tensile Strength
WD	Working Distance
Z	Atomic Number

Chapter 1 Introduction

Due to the high energy demand on the planet, new energy technologies have to be developed. Thermonuclear fusion energy is a promising option as it is clean and fuel is abundant. Many scientific and technical hurdles have already been overcome but still some big issues remain unsolved. One particular problem concerns the material degradation due to the intense flux of high-energy fusion neutron. Material feasibility studies for fusion reactors are motivated by the long term view for commercial power plants. However, the demanding fusion conditions to the plasma facing components remain beyond the capability of current commercial materials. In particular, it is a challenge to determine and improve the design temperature limits controlled by neutron irradiation (see Figure 1).

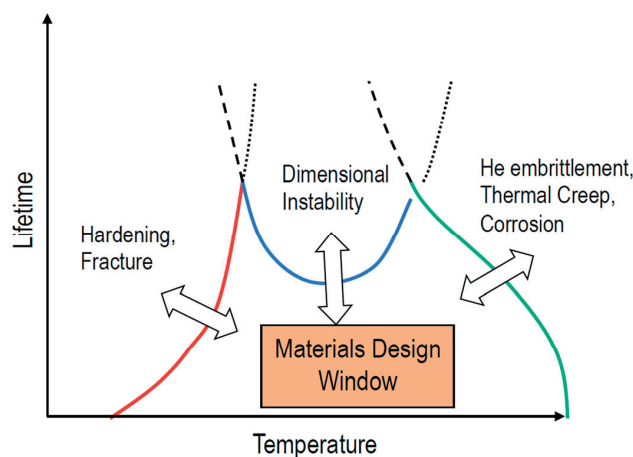


Figure 1: Sketch of the design window of fusion reactor structural steels including the arising limitations (adapted from [1]).

The lower temperature limit is determined by embrittlement of the material due to irradiation hardening. At higher temperature, the limit is controlled by several factors including thermal and irradiation-induced creep, and helium embrittlement. At moderate temperature, dimensional instabilities may come into play. Besides the material issues, the reactor blanket has to be designed to fulfil functional tasks, such as tritium breeding and removing the heat produced by the impinging neutrons. To maximize the net power outcome of the power plant, materials with good high-temperature properties must be considered. Therefore, fusion reactor materials research has to be addressed on a fundamental scientific basis to develop structural and functional materials capable of withstanding the harsh environment of a fusion reactor.

Tremendous progress has been made in structural material for the first wall and blanket of future fusion reactor, where ferritic/martensitic and oxide dispersion strengthened steels are leading candidates. In the International Thermonuclear Experimental Reactor (ITER) under construction in Cadarache, six different TBMs will be tested. Two TBMs currently developed in Europe will be made of Eurofer97 steel as structural material. Eurofer97 is an advanced reduced activation ferritic/martensitic steel that possesses good ther-

mo-mechanical properties before and after irradiation and dimensional stability under irradiation. The conjunction of high resistance against irradiation of the reduced activation ferritic/martensitic steels, good balance of the overall mechanical properties, and low swelling arises from the body centered cubic (BCC) structure of these steels. However, the main drawback of the ferritic/martensitic steel resides in their fracture behavior that exhibits a so-called ductile to brittle transition with decreasing temperature. This behavior is illustrated in Figure 2 left, where the temperature dependence of fracture toughness is illustrated and where we can distinguish three regions: lower shelf, transition and upper shelf. Basically, the fracture mode is brittle on the lower shelf and in the transition while it is ductile in the upper shelf. Neutron irradiation at the operating temperature of the reactor causes a substantial increase in yield stress, which in turn shifts the ductile to brittle transition region to higher temperatures. This phenomenon is called embrittlement that requires assessment methods to safely manage the operation limits in terms of temperature and loading. The embrittlement can be quantified with a reference temperature T_0 at a toughness of $100 \text{ MPa}\sqrt{\text{m}}$ in the transition. The embrittlement is then characterized by a shift of T_0 (ΔT_{ih}) (Figure 2 right).

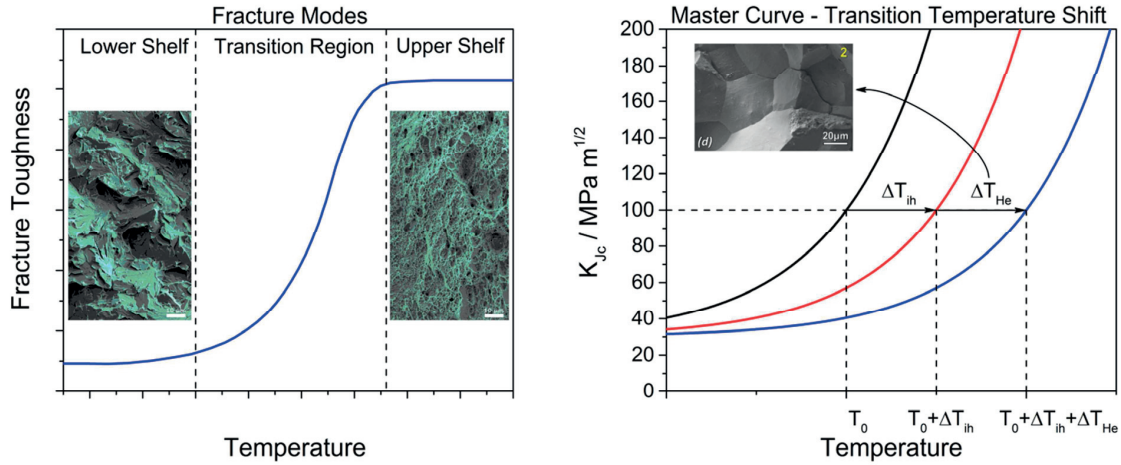


Figure 2: Left: Illustration of the fracture modes for a BCC steel at different temperature. Right: Ductile to brittle transition temperature defined by the master curve. Additional shifts due to irradiation ΔT_{ih} and He embrittlement ΔT_{He} are indicated as example.

Furthermore, neutron flux induces transmutation products like hydrogen and helium which may cause an additional shift of the DBTT, where He plays the major role. Helium is suspected to induce an additional embrittlement at relative large concentration (> 500 atom part per million) by a non-hardening effect that would manifested in an increasing fraction of intergranular fracture in comparison to cleavage fracture [2]. Other upward or downward shifts of T_0 can occur due to loading rate, crack configuration (shallow versus deep crack), dimension of the cracked structure with regard to the crack length. Loading-temperature history adds complexity in dealing with embrittlement.

Another challenge, which the structural materials have to face, are plasma disruptions, where the magnetic confinement is lost, exposing the first wall to massive thermal and electromagnetic loads in only a few ms. High heat loads are dissipated during a disruption causing erosion of the material and induce thermal stresses due to the large temperature gradient. In addition, electromagnetic forces can lead to very high forces which act on the structure within a short time. The thin walled structure of the first wall makes it necessary to develop fracture toughness analysis method to address the combined effect of neutron irradiation, high loading rates and constraint levels on embrittlement.

1.1 Objectives of the thesis

The main goal of this PhD work is to gain insight in a number of key issues that mediate the ductile to brittle transition temperature T_0 of the reference reduced activation tempered martensitic steel Eurofer97.

First, the role of the loading rate on fracture toughness on unirradiated Eurofer97 has to be investigated as it has been very little documented and investigated. In order to do so, mechanical tests have to be performed to assess the tensile properties and fracture properties over a range of temperatures in the transition region, at low and high loading rates. The tensile properties will serve as input for finite element models of loaded cracks results, while the static and dynamic fracture tests will constitute the database to calibrate and verify local approach models of brittle fracture.

Second, the effect of irradiation on the tensile properties of irradiated specimens will be determined after spallation neutron/proton irradiation at about 250 °C in SINQ target at Paul Scherrer Institute. The objective is to evaluate the evolution of the tensile properties and fracture behavior after high dose with a significant amount of helium (about 11 dpa and 500 appm He). Since small and non-standard tensile specimens have to be used, the determination of the tensile properties requires the development of an indirect analysis method, which *per se* constitutes one objective of this work. Tensile tests and finite element modeling are the tools foreseen to attain this objective.

The third objective is to link not only the tensile properties to the fracture behavior in the transition region but also their respective evolution after irradiation. Local approach of brittle fracture models appear as a very powerful method to deal with this problem. For reliable prediction of embrittlement, sensitivity analysis of the parameters of the model considered has to be carried out on the various models envisaged. Actually, 3D and simplified 2D models of fracture specimens will be used, their advantages and limitations discussed, and their predictions compared with the experimental results.

Chapter 2 Literature Review

In this chapter, first a short overview of the current fusion reactor concepts is given, followed by a brief summary of the development of tempered ferritic/martensitic steels for thermonuclear fusion reactor applications. Fundamental mechanisms of irradiation on material are covered and their impact on the material and fracture properties presented. The available irradiation techniques with their respective advantages and drawbacks are discussed. Finally, local approaches to brittle fracture, which are finite element guided methods to address cleavage fracture, are introduced.

2.1 Fusion

Francis William Aston made in 1920 precise measurements of many different atoms, among them hydrogen and helium. He found that four hydrogen nuclei were heavier than a helium nucleus [3]. Consequently, Sir Arthur Eddington speculated that the source of stellar energy was the conversion of hydrogen to helium [4]. Nuclear fusion was discovered. It was also Eddington which gave the following remark at that time:

“If, indeed, the subatomic energy in the stars is being freely used to maintain their great furnaces, it seems to bring a little nearer to fulfillment our dream of controlling this latent power for the well-being of the human race — or for its suicide”.

Since this statement was made, much time has passed and we still do not have any operating controlled fusion reactor with a positive energy output. On contrary to the sun, fusion reactors will need a different fuel for nuclear fusion reactions to take place. Deuterium and tritium is envisaged for the first generation of fusion reactors to create helium-4. This fusion reaction is the easiest to trigger due to its large cross section [5]:



Temperature of about 100 millions of degree Celsius has to be reached in the plasma for this reaction to occur. Magnetic and inertial confinements for fusion have been investigated, whereas emphasis has been put on the magnetic one. Currently the two most advanced systems, which confine plasma with magnetic fields, are the tokamak and the stellarator [6]. The difference among them is how they achieve the plasma equilibrium. While tokamaks are axisymmetric, stellarators consist of a complicated twisted coil design. Due to the symmetry and simpler concept, the tokamak design appears more promising than the stellarator one. Thus, in the following emphasis is given to the tokamak design and issues.

2.1.1 Tokamak

First developed by Soviet research, the tokamak concept was selected for the International Thermonuclear Experimental Reactor (ITER). ITER is being built to demonstrate the feasibility of producing a net energy gain and to breed tritium within the blanket. In Figure 3, the design of ITER is shown with a cross view of the reactor. The vacuum vessel, the divertor and the blanket modules are highlighted. The vacuum vessel

supports the blanket as well as the divertor modules and acts as the first safety barrier. At the bottom of the vacuum vessel, the divertor can be found. Its function is to remove helium and impurities from the reactor. Furthermore, it is the part that has to withstand the highest heat loads.

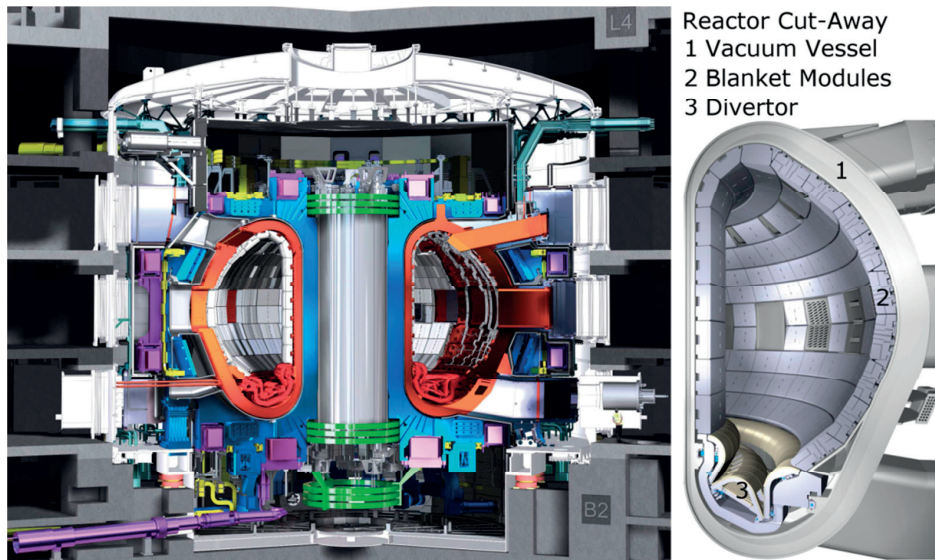


Figure 3: ITER design and cross section of the reactor. Reactor cut-away shows in-vessel components.

One of the most challenging components in ITER is the blanket. It has to extract the majority of the plasma heat, it is the main contributor in providing neutron shielding for the magnets and vessel structure, and it provides limiting surfaces that define the plasma boundary during start-up and ramp down [7] [8].

Due to the manifold tasks and the exposed irradiation, the blanket modules design and concept for future fusion reactors is not yet chosen. Therefore, up to 6 test blanket modules (TBMs) from six different teams will be tested in ITER simultaneously [9].

2.1.1.1 Test Blanket Modules

Several different TBMs concepts will be tested in ITER located in the equatorial ports of the fusion reactor. Emphasis will be put on the two developed reference breeding blanket concepts from Europe, which are based on the demonstration fusion power plant reactor (DEMO) specifications. In both concepts, pressurized helium acts as a coolant [10]:

1. The Helium Cooled Lithium Lead (HCLL) concept: A eutectic Pb-16Li, which is enriched in ^6Li is used as a tritium breeder as well as a neutron multiplier.
2. The Helium Cooled Pebble Bed (HCPB) concept: Lithiated ceramic, which is enriched in ^6Li , acts as a tritium breeder and beryllium pebbles as a neutron multiplier.

Both are designed for optimized heat extraction in the range of 300 to 500 °C. In Figure 4, the basic set-up as well as the two different designs are shown.

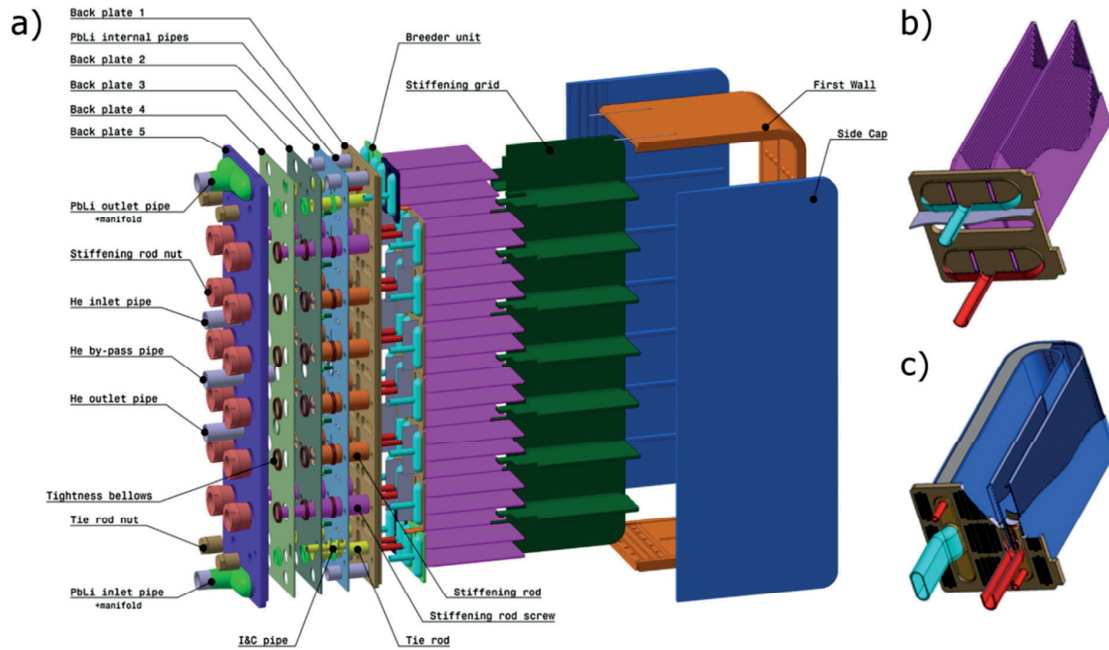


Figure 4: European Test blanket modules. a) General set-up. b) HCCL concept. c) HCPB concept. (from [10])

The first wall, the side cap and the stiffening grid separate the entire box volume into several cuboids, which contain the breeder/multiplier as well as the heat extraction plates. In other words, the TBMs basic set-up is the same for both concepts. They simply differ by the inserts which will be put into the described cuboids. The cooling distribution unit which provides the pressurized helium is attached at the back of the TBM structure. From the design it can be seen that the structure consists of plates with various thickness. This clearly contrasts with the massive walls of a reactor pressure vessel of a fission reactor.

2.1.1.2 Fusion challenges

The ITER goal is to test the feasibility of fusion and should provide valuable experience of the behavior of the reactor as well as the design. Nevertheless, there are still huge gaps between ITER and a commercial fusion power plant. In particular, for DEMO reactor the requirements to the structural material will increase due to the longer pulse of the plasma (>2h) or even steady state and the overall higher power of the power plant. As a consequence, the irradiation dose on the first wall, blanket and divertor in DEMO will be much higher than in ITER.

2.1.1.2.1 Irradiation damage

The neutron fluence on the first wall of ITER is estimated to be around $0.3\text{--}0.5\text{ MWa/m}^2$, whereas in DEMO the neutron fluence increases up to 10 MWa/m^2 [11]. Therefore, the irradiation induced damage in the structural material increases significantly. In material science, the radiation damage in solids is usually measured in displacements per atom (dpa) instead of neutron fluence. The dpa represents the average number of times any atom in the material has been knocked out of its lattice position. Federic et al. calculated the expected damage for DEMO in the first wall made of steel in terms of dpa and He production (see Figure 5). Depending on the position in the fusion reactor first wall (FW), the material suffers from severe radiation damage per full power year (fpy). However, with increasing distance from the first wall, the radia-

tion damage reduces significantly. Depending on the TBMs concept, the dose on the vacuum vessel can be less than 0.01 dpa/fpy [12].

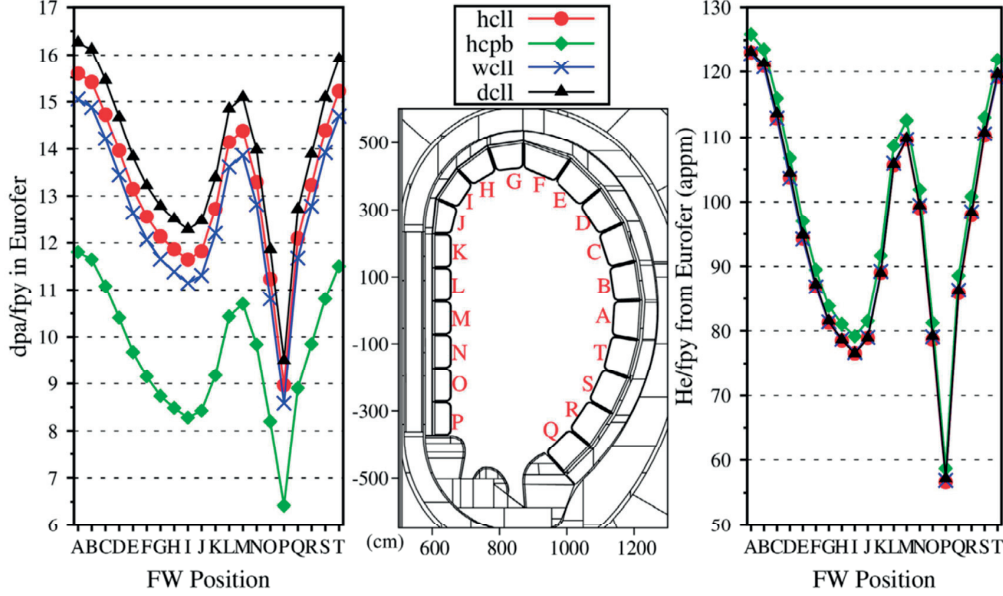


Figure 5: Calculated variation in dpa and He production in Eurofer97 per full power year in DEMO depending on the position in the first wall (from [12]).

ITER will provide results on plasma physics and tritium breeding but the high dpa and transmutation production rate in materials for DEMO are beyond any experience. Initially, the requirements for the first wall materials in DEMO have been set to withstand neutron damage up to 20 dpa [12] but will have to be increased even further. In order to achieve this goal, characterization of materials exposed to a fusion neutron spectrum at such high doses has to be performed, especially to assess the role of helium on the degradation of the mechanical properties.

2.1.1.2.2 Plasma disruptions

In tokamaks the plasma can become unstable if the plasma current or pressure increases too much causing a sudden termination of the plasma confinement. Such events are called plasma disruptions (PDs) and are known since that confinement concept was proposed in the 1960s [13]. PDs are rapid events and cause the entire loss of thermal and magnetic energy stored in the plasma. The short time scale and the amount of energy dissipated during a PD increases the requirement of resistance of the first wall material. A disruption can be basically split into two phases [14]:

1. Thermal quench (TQ): Thermal energy is lost and dissipated to the first wall.
2. Current quench (CQ): The magnetic energy is dissipated and the plasma current rapidly reduces.

Therefore, high heat loads is dissipated during the TQ and possibly also at the CQ through ohmic heating [14]. However, most serious thermal load occurs at the TQ and causes local melting and vaporization. Beside the erosion due to vaporization and spallation, the temperature increase leads to large gradients within the bulk and causes thermal stresses [15]. The heat load increases temperature at the surface and sub-surface significantly. However, the occurrence of thermal stresses may exceed the material yield strength and cause plastic deformation [16].

Furthermore, the rapid changes in magnetic field during a disruption induce eddy currents in the conductive first wall. Additionally, so called halo currents flow through the structure when the disrupting plasma makes contact with the first wall [17]. In combination with present magnetic field, severe electromagnetic forces will be induced. The resulting forces on the structure are significant and have to be considered [18] [17]. As already mentioned, the PD events are rapid and occur within a timescale of \sim ms. Therefore the electromagnetic forces will be applied to the first wall within short time and may cause severe damage. Kasada et al. estimated from the calculations of [19] and an approximately blanket structure of a few millimeter that a strain rate of 0.1 s^{-1} can be reached during a PD [20] (see Figure 6).

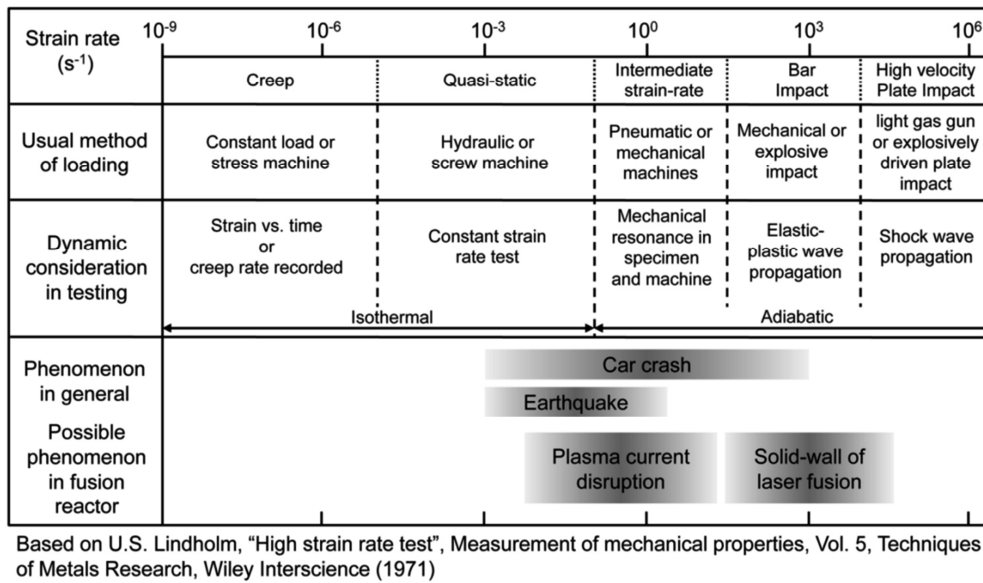


Figure 6: Possible occurring strain rates at a plasma disruption in relation to other phenomena's (from [20]).

To avoid such plasma disruptions, control systems monitor the current plasma conditions. However, such control system can only minimize the probability of disruptions but cannot avoid them. Therefore, safety consideration for future fusion power plants should include dynamic deformation behavior of the structural material as well.

2.2 Development of reduced activation ferritic/martensitic steels

In contrary to the vacuum vessel made of austenitic stainless steel 304 containing boron for effective neutron shielding performance [21], new alloys had to be developed for the first wall and the blanket, which have to have a good balance of properties under irradiation, i.e., good strength and ductility, high fracture toughness, reasonable fatigue and creep resistance as well as limited swelling. Austenitic steels undergo high swelling rate at higher neutron doses which produces unacceptable volumetric swelling in structural components [22] [23]. Ferritic/martensitic (FM) steels do show a better swelling resistance also at higher neutron doses and were therefore preferred. FM steels with a Cr content of 8–12 wt% have been investigated due to their good irradiation resistance. In addition, the microstructure of FM steels can be controlled by applying heat treatments that results in the desired mechanical properties [24].

Besides the above mentioned material properties, emphasis was given on the development of so called low or reduced activation materials. The idea is to reduce the long term activation behavior to achieve a low level waste within a few hundred years compared to several 100 000 years for a conventional steel. There-

fore, the chemical composition of conventional 9% Cr steels had to be modified by replacing Mo, Nb, and Ni by W, V and Ta in order to obtain low residual activation [25] (see Figure 7). The resulting alloys are called reduced activation ferritic/martensitic (RAFM) steels.

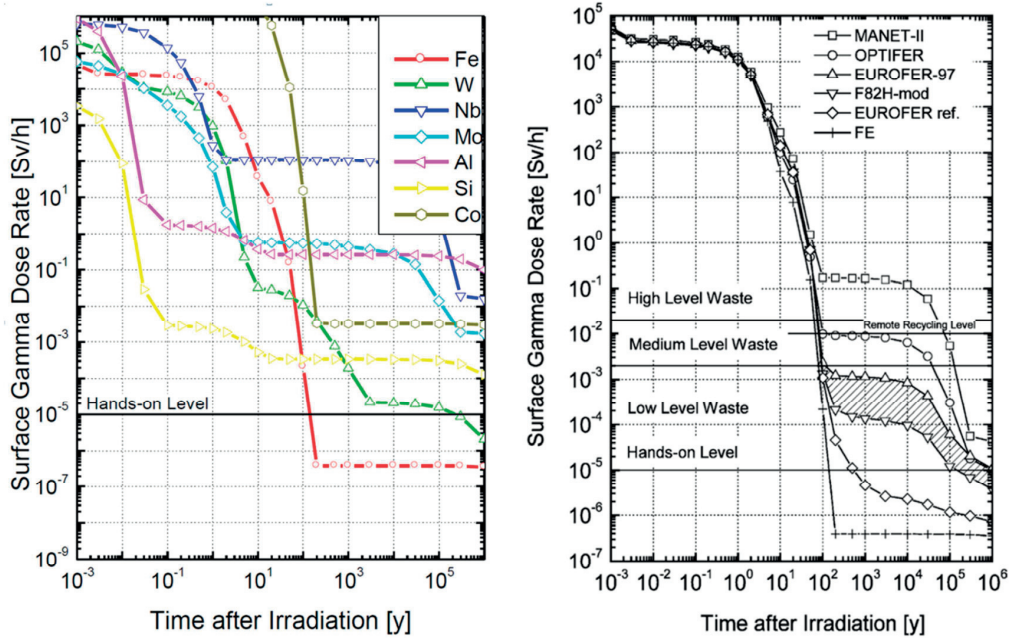


Figure 7: Calculated γ -surface dose rate. Left: Fe and some important alloying elements (from [26]). Right: RAFM steels and Fe after being irradiated to a 12.5 MW/m^2 spectrum (from [27]).

Two RAFM steels namely Eurofer97 and F82H are currently the most promising RAFM steels in terms of material properties as well as fabrication and already have a large database. Therefore, both TBM concepts developed by Europe will use Eurofer97 as a structural material [10].

2.3 Irradiation damage

Radiation on solids usually results in degradation of their material properties. To develop irradiation resistant materials, it is crucial to understand the basic process of damage production and accumulation. The initial production of defects follows the interaction of an incident energetic particle with a lattice atom, which results in a certain recoil energy (transferred kinetic energy). As a consequence, the lattice atom is knocked out of its lattice position if the transferred energy is higher than a threshold energy E_d , which is of the order of few tens eV in metals and depends on the material and the lattice orientation (see Figure 8). The created displaced atom is called primary knock on atom (PKA, see Figure 8) and can create additional displaced atoms while moving through the lattice if it has enough kinetic energy. A displacement cascade is formed. In order to displace an atom, a certain threshold energy E_d is needed. If the energy of the displaced atom falls below E_d , the cascade is terminated. The creation of a vacancy and interstitial atom is called a Frenkel pair (FP) or Frenkel defect.

The accumulated damage in solids is commonly indexed by displacements per atom (dpa). A major advantage of using dpa to measure the irradiation damage is the fact that it allows to compare results obtained between different irradiation sources [28]. However, dpa cannot be used as a measure to compare irradiation behavior in different materials [29]. Also it has to be pointed out that a given dpa value cannot

be directly related to the accumulated damage as only a minority of displaced atoms survives as a defect, namely 30 % of the primary defects survive the short time cascade recombination [30].

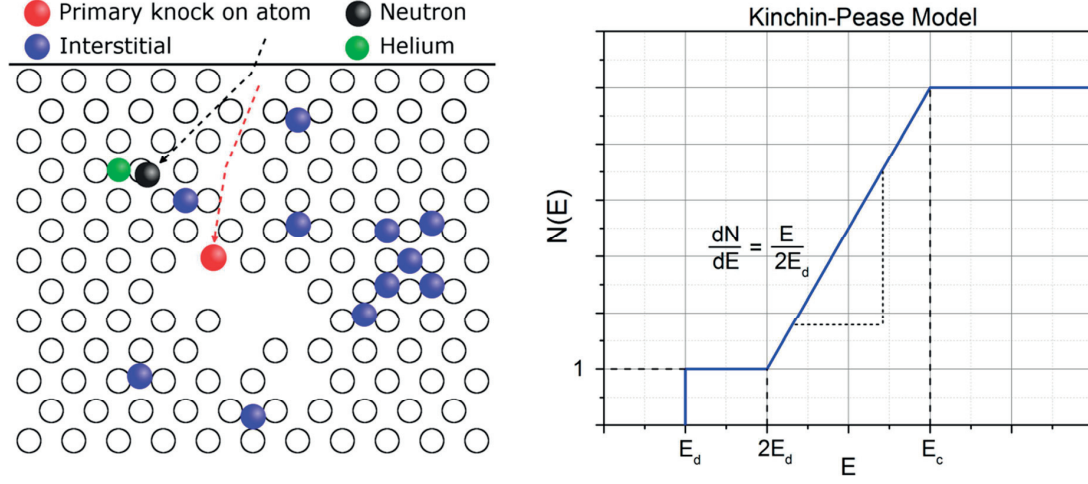


Figure 8: Left: Schematic representation of displacement damage. Right: Kinchin-Pease model indicating the number of displaced atoms N versus the energy of the PKA.

In case of a fusion reactor, high energy 14 MeV neutrons are created that penetrate into the first wall causing displacement cascades (see Figure 8). The amount of created FPs depends strongly on the energy of the PKA as illustrated in Figure 8 with the Kinchin-Pease model [31]. The high-energy fusion neutron produce most of PKAs with energies $> \text{keV}$, whereas the maximum is found to be in the MeV range. In addition, 14 MeV neutrons create transmutation reactions leading to hydrogen and helium production. Typically, about 40 appm H and 10 appm He are produced per 1 dpa in ferritic/martensitic steel. In Figure 9 the PKA energy distribution created in the first wall being exposed to the neutron spectra of DEMO is shown.

Once a PKA distribution is known, the produced damage can be calculated in terms of FPs (see Figure 9).

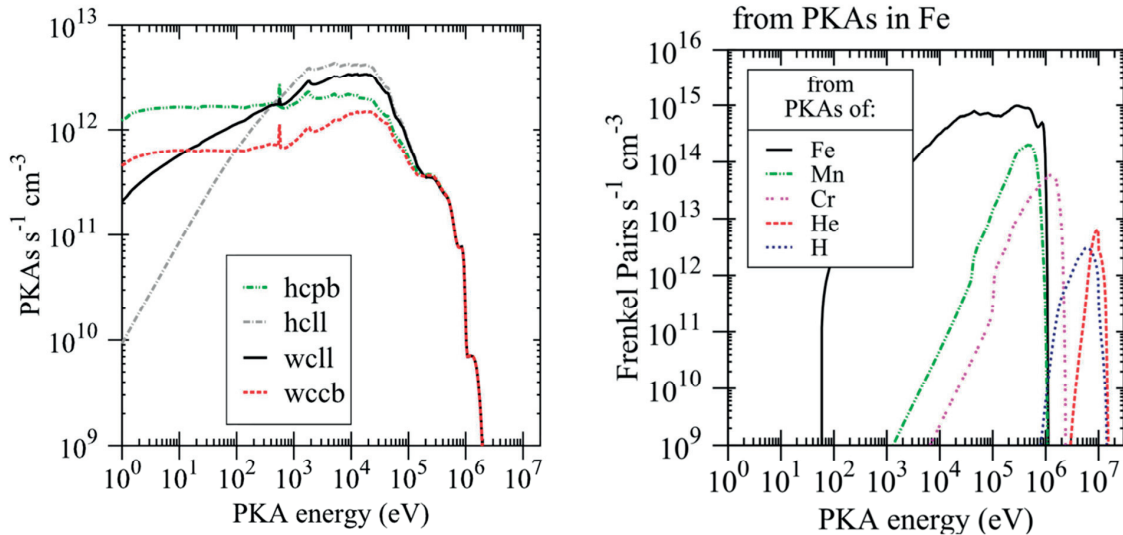


Figure 9: Left: Calculated total PKA spectra for pure Fe in the first wall of a DEMO (impact of the different TBMs is indicated). Right: Frenkel pair production in Fe under DEMO conditions (both from [32]).

Over a broad range of PKA energies, a significant amount of FP is created. However, the results were obtained by using the stopping and range of ions in matter (SRIM) binary collision approximation (BCA) code [32].

The above mentioned FPs are so called primary defects. Most of them recombine due to thermally activated motion of defects. Surviving defects accumulate in the form of secondary defects (clusters of defects) in the form of interstitial and vacancy dislocation loops, voids, stacking fault tetrahedra and precipitates. These microstructural changes are more stable than the initial point defects and lead to changes in the material properties.

Besides the mentioned defects, the high energy neutrons cause transmutation products such like H and He from (n,p) and (n, α) reactions. The threshold for (n,p) (~ 1 MeV) and (n, α) (~ 5 MeV) reactions in Fe is well exceeded by the 14 MeV neutrons in a fusion reactor [33]. Large amounts of He are also generated by thermal neutrons in Ni-bearing alloys [34]. However, the cross section for transmutation reactions varies considerably from element to element but cannot be avoided simply by selecting special elemental composition [35]. Due to the lower threshold than helium, even larger amounts of H will be produced in the first wall.

Hydrogen may get trapped among others at irradiation defects and affects mechanical behavior. It is also associated with the reduced cohesion of grain boundaries due to higher segregation rates compared to the bulk [2]. However, it is expected that H diffuses out at irradiation temperatures $T_i > 250$ °C [36] [37] [38]. Due to the fact that the operational temperature of a fusion reactor will be at 250-400 °C, the focus of current investigations lies in He effects. Nevertheless, H may affect the hardness and ductility and is still retained in martensitic stainless steels at elevated temperatures [36]. It is also possible that H may be stored in small bubbles, which were initially nucleated by He at lower temperatures (≤ 350 °C) [39]. Higher concentrations of H may also cause embrittlement in tempered martensitic steels [2].

Due to insolubility of He in solids, it diffuses in the material and forms bubbles at various microstructural trapping sites including grain boundaries [34]. Moreover, the He bubbles can interact with irradiation induced defects such as nucleation sites for growing voids. He induced microstructural changes have an impact on the mechanical behavior like embrittlement [40] [2]. Yet, the role of He has to be extensively studied, especially at higher He/dpa levels that will be reached in DEMO.

2.3.1 Irradiation effects on ferritic/martensitic steels

The fusion material community was initially inspired from materials being used in fission reactors, in particular the 12 % Cr martensitic steel HT9 from Sandvik. However, those ferritic/martensitic (FM) steels had to be modified to meet the requirements in a fusion environment. As already mentioned in section 2.2, some alloying elements had to be replaced or minimized to assure a short decay time of the induced radioactivity. So far, more than 30 years of research has been done on developing low or reduced activation FM steels. In the following, the recent research knowledge about irradiation effects on FM steels is presented with a focus on tensile behavior and hardening, irradiation creep and irradiation embrittlement. Results obtained mainly from the two FM steels developed by Japan (F82H) and Europe (Eurofer97) will be presented due to their large database.

2.3.1.1 Irradiation hardening

After neutron irradiation, the tensile behavior of FM steels is strongly modified due to the irradiation-induced secondary defects. The created dislocation loops, defect clusters, voids and bubbles contribute all to the strengthening of the material (see Figure 10), which can cause a significant increase of the yield stress. The irradiation hardening occurs for irradiation temperature up to about 450 °C. Beyond this temperature, irradiation softening may happen.

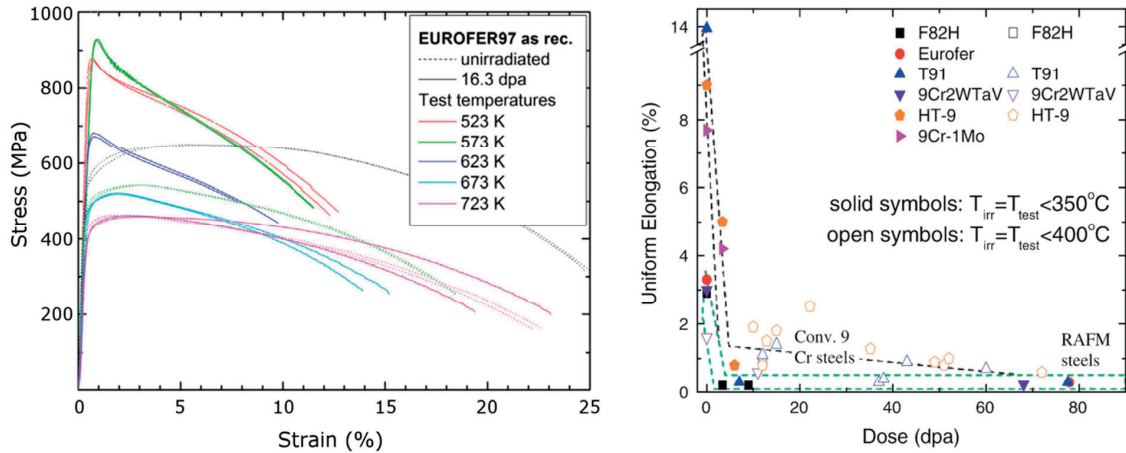


Figure 10: Left: Stress/strain diagram of Eurofer97 (from [41]). Right: Evolution uniform elongation with irradiation dose (from [42]). Dashed lines are guidance for the eyes.

However, in comparison to the yield stress the ultimate tensile strength (UTS) increases less. Simultaneously, a strong reduction of the uniform elongation (defined at the UTS) is observed. If the yield stress and UTS practically coincides, there is a complete loss of uniform elongation [43]. Figure 10 shows the loss of uniform elongation for different FM steels irradiated at $<400^\circ\text{C}$, which were tested at or around irradiation temperature. A sharp drop of uniform elongation can be recognized even at low irradiation doses. For the conventional 9Cr steels, the loss of ductility does not seem to saturate [44], whereas this appears improved for the newly developed FM steels.

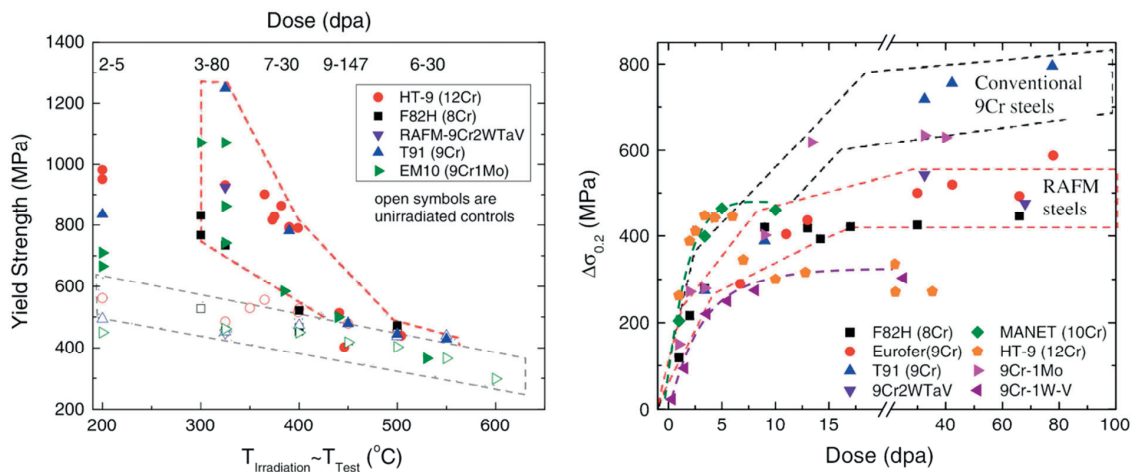


Figure 11: Left: Yield stress evolution with irradiation temperature. Right: Yield stress increase with irradiation dose at $T_i < 350^\circ\text{C}$ (both from [42]). Dashed lines are guidance for the eyes.

Irradiation hardening of FM steels is very sensitive to temperature and can vary significantly [42]. In Figure 11, the yield stress irradiation temperature dependence for several RAFM steels as well as conventional steels is shown.

Generally, the irradiation hardening is less pronounced for RAFM steels compared with conventional 9Cr steels whereas no hardening is observed for temperatures beyond 400 to 430 °C. However, depending on the fluence radiation enhanced softening may be observed [45].

Beside the mentioned temperature dependence, irradiation hardening shows dose dependence as well. As the doses on the first wall are much higher compared with fission irradiation, the irradiation hardening at higher doses is of great interest. Neutron irradiated FM steels do first show a steep increase in yield stress at lower doses (see Figure 11). However for some of the FM steels saturation in hardening at higher doses irradiated at 300 to 335 °C can be observed. On the other hand such saturation behavior was not found for Eurofer97 at the same temperature range [46] [47] [44] [48] [49].

2.3.1.2 Irradiation Creep

Creep is defined as a time dependent deformation of a metal under constant load and high temperature, typically above $0.5 T_m$. In general, creep is a thermally activated process and shows different stages characterized by different strain rate. It requires the thermal formation of vacancies and the motion of them by volume or grain boundary diffusion as well as the climb of dislocations over obstacles and glide along slip planes [50]. Therefore the thermal creep properties are defining among others the upper operating temperature (see Figure 12).

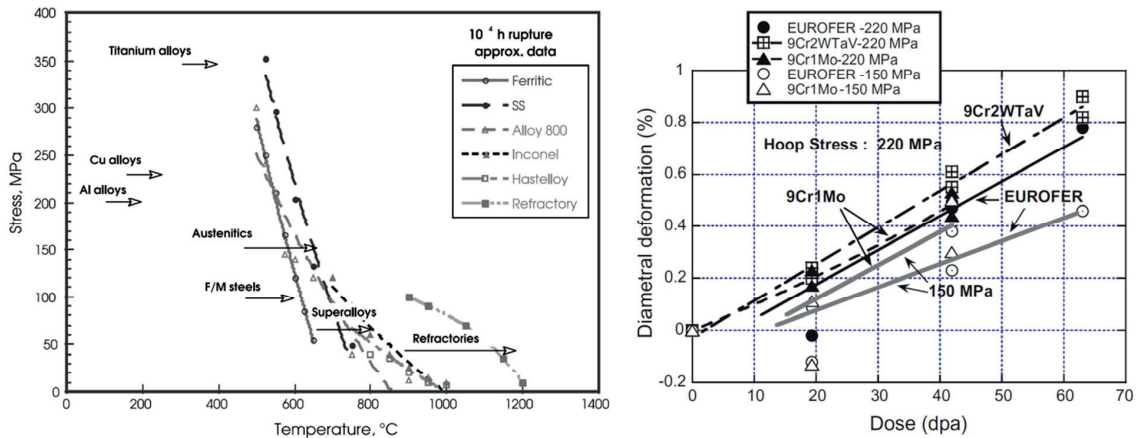


Figure 12: Left: Upper temperature limit for different steels based on a 10^4 h creep rupture time (from [51]). Right: Diametral strain of various 9Cr steels in dependence of irradiation dose at hoop-stresses between 150 - 220 MPa at 325 °C (from [52]).

Under irradiation the creep rate increases significantly and can induce creep at lower temperatures [50] whereas the microstructure of the material plays an important role. The induced point defects due to irradiation accelerate the kinetics of dislocation climb, coarsen the precipitates and enhance generally the diffusivity [24]. The 9Cr martensitic steels do show good irradiation creep stability under fission irradiation (see Figure 12).

2.3.1.3 Irradiation embrittlement

FM steels have a body centered cubic (BCC) structure and exhibit a ductile to brittle transition. Below a critical temperature, fracture toughness of the material decreases dramatically changing from the initial ductile behavior to brittle. The temperature at which the ductile to brittle transition temperature (DBTT) occurs can be defined either with Charpy impact tests or with fracture toughness tests. Charpy tests measure the energy absorbed to break notched specimens under impact loading. A typical Charpy curve consists of a lower shelf at low temperature and an upper one at high temperature, which are connected by a gradual increase of energy. The DBTT determined by Charpy, T_c , can be indexed in different ways but is always related to the transition between the two shelves. Even though T_c is a useful measure of brittleness, T_c cannot be safely used for quantitative assessments of structures containing loaded cracks, where fracture toughness K has to be considered. Similarly to the Charpy curve, the median fracture toughness-temperature curve $K_{med}(T)$ presents two shelves connected by a transition region. For fracture reactor pressure vessel (RPV) steels, Wallin demonstrated that the shape of the $K_{med}(T)$ curve in the transition has a constant shape for all unirradiated and irradiated low alloy bainitic RPV steel [53]. While developed for RPV steels, the method also applies to martensitic steels and perhaps to vanadium alloys [54] [55]. The $K_{med}(T)$ curve, for a reference $B = 25.4$ mm thick specimen with statically loaded deep crack, is described by the ASTM-E1921 standard Master-Curve expression [56]:

$$K_{med}(T) = 30 + 77 \exp(0.019(T - T_0)) \quad (1)$$

In this case, T_0 , the so-called reference temperature T_0 at a median toughness of 100 MPaVm, represents the DBTT but can be significantly different from that determined with Charpy tests T_c . However, the only difference between different steels is the reference temperature T_0 . This observation and basic hypothesis led to the development of the so-called master-curve method for measuring K_{Jc} in the cleavage transition and T_0 . The ASTM-E1921 establishes the requirements to determine the index T_0 , as well as $K_{Jc}(T)$ curves at specified confidence (probability) intervals (e.g., 1 and 99%) that reflect the inherent statistical variability in measured cleavage toughness, for the same steel and test conditions. The master-curve approach is generally applicable to ferritic, bainitic and tempered martensitic steels. However, based on the fracture toughness dataset of several unirradiated and irradiated ferritic-martensitic steels, Lucon [57] raised some doubts about the applicability of the master-curve method in this case, observing that intrinsic scatter of some toughness data in the transition region is greater than predicted, which is likely to be the consequence of a strong specimen size effect on toughness not properly taken into account. However, Odette et al. [58] assembled all the available fracture toughness data on F82H steel and showed that by adjusting these data to a common specimen size, the toughness behavior of F82H in the transition was consistent with the master-curve. Later on, the applicability of the master curve method to the unirradiated tempered martensitic steel Eurofer97 was also assessed by Mueller et al. [59]. This study was based on the analysis of a fracture toughness database of Eurofer97 steel obtained with sub-sized 0.18T, 0.36T and 0.88T CT specimens tested in the lower to middle transition region. The large number of data points of the analyzed database allowed recalculation of the master-curve coefficients. The data suggest an adjustment of the athermal part of master-curve equation (30 MPaVm in the standard Master-Curve) is sufficient to represent the data with a slightly modified equation as:

$$K_{med}(T) = A + (100 - A) \exp(0.019(T - T_0)) \quad (2)$$

An $A = 12 \text{ MPa}\sqrt{\text{m}}$ provided the best fit to the $K(T)$ data for Eurofer97 down to the lower shelf as can be seen in Figure 13. Without this adjustment it would be difficult to accurately define T_0 from data near the lower shelf.

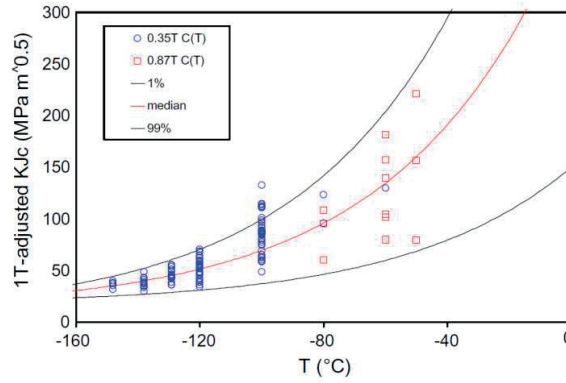


Figure 13: Modified master-curve of unirradiated Eurofer97 steel, $T_0 = 78 \text{ °C}$ (from [59]).

Many FM steels possess good fracture toughness in the upper shelf temperature region. Additionally, the DBTT before irradiation lies well below room temperature both in quasi-static and dynamic loading conditions [60] [61] [62] [63] [64] [65] [66]. However, the induced irradiation hardening in FM steels results in embrittlement, which shifts the DBTT (ΔT_c for Charpy tests or ΔT_0 for fracture toughness test) to higher temperatures and may be of great concern [61] [62]. Figure 14 illustrates the effect of irradiation on the shift of the $K_{med}(T)$ curve and corresponding ΔT_0 . In this example, K_{Jc} was measured with pre-cracked sub-sized compact tension 0.18T CT specimens of unirradiated and irradiated Eurofer97 steel.

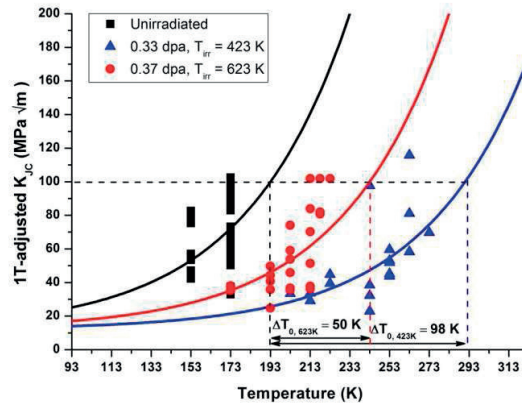


Figure 14: Fracture toughness results and corresponding master-curves in the unirradiated and irradiated conditions (from [67]).

Extensive evaluation of the DBTT shift for FM steels with different chemistry is shown in Figure 15 . The minimum around 9% Cr is very clear and is the main reason for 9 % Cr in F82H and Eurofer97. However, increasing the Cr content would improve the corrosion resistance [24].

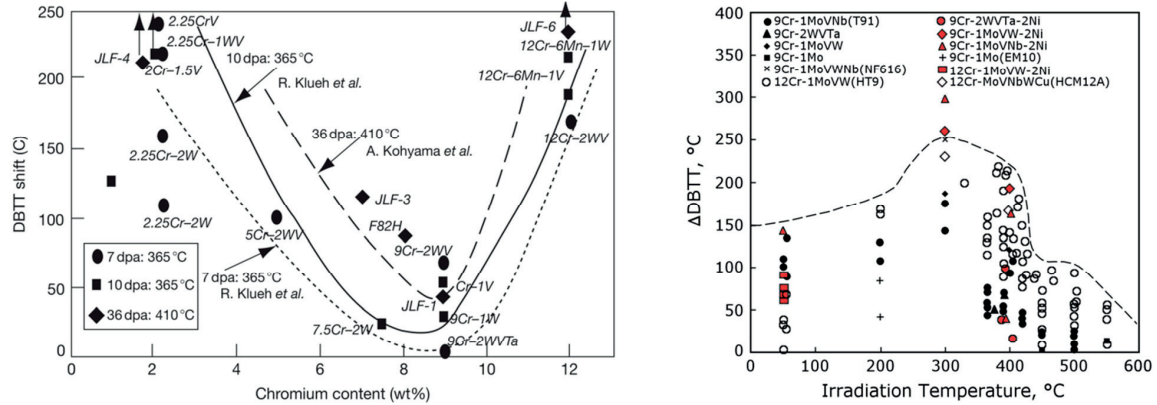


Figure 15: Left: DBTT measured by Charpy tests shift in relation to Cr content for different irradiation doses (from [24]). Right: DBTT measured by Charpy tests shift in FM steels at different irradiation temperatures (from [42]).

In Figure 15, the DBTT shift for different FM steels at various irradiation temperatures is shown. The data set involves different FM steels which were irradiated at distinct conditions. Therefore, more details on the shown material as well as irradiation process would be needed to describe the difference among them. Still, it can be observed that the 9Cr steels do show a smaller shift at $T_i > 100$ °C in comparison to the 12Cr steels [42].

Similar to irradiation hardening, embrittlement is pronounced at irradiation temperatures between 250 to 450 °C [42]. The maximum DBTT shift for 9 to 12 % Cr steels is observed at 250 to 300 °C. The RAFM steels do show a lower shift in comparison to the conventional steels which was explained by Klueh et al. with the different microstructure and chemical composition [61]. In addition the Cr content in relation to the irradiation temperature shows that for 9Cr steels the DBTT after irradiation remains below room temperature for $T_i > 375$ °C whereas for 12Cr steels T_i has to be > 450 °C. For 17Cr steels the DBTT falls always below room temperature for all irradiation temperatures [68] [69] [70] [71].

Simple linear correlations between ΔT_c or ΔT_0 and the ambient temperature $\Delta \sigma_y$ are often reported in literature, as $\Delta T_c = C_c \Delta \sigma_y$. A compilation and analysis of $\Delta \sigma_y$ and ΔT_c data for 9Cr tempered martensitic steel indicates an average value of C_c of about 0.38 ± 0.18 °C/MPa [2]. Similar to Charpy curves, it has been shown that $\Delta T_0 \approx C_y \Delta \sigma_y$ with $\sim 0.57 \pm 0.13$ °C/MPa proposed by Odette [72]. Charpy ΔT_c are somewhat lower than ΔT_0 and are consequently a non-conservative measure of embrittlement, and should not be used as a surrogate for fracture toughness ΔT_0 .

2.3.1.4 He effect

Structural materials in fission reactors are exposed to high neutron fluxes as well. However, the major difference lies in the neutron energy spectrum that shows a high portion of 14 MeV neutrons (≈ 20 %) and lower energy (≈ 80 %) for a deuterium tritium reaction in a fusion reactor [34]. As a consequence, the transmutation reactions in Fe differ from < 1 appm/dpa He in a fast fission spectrum to ~ 10 appm/dpa He in a fusion spectrum [73]. In Figure 16 the increase in cross section for the (n, α) reaction with increasing neutron energy is shown.

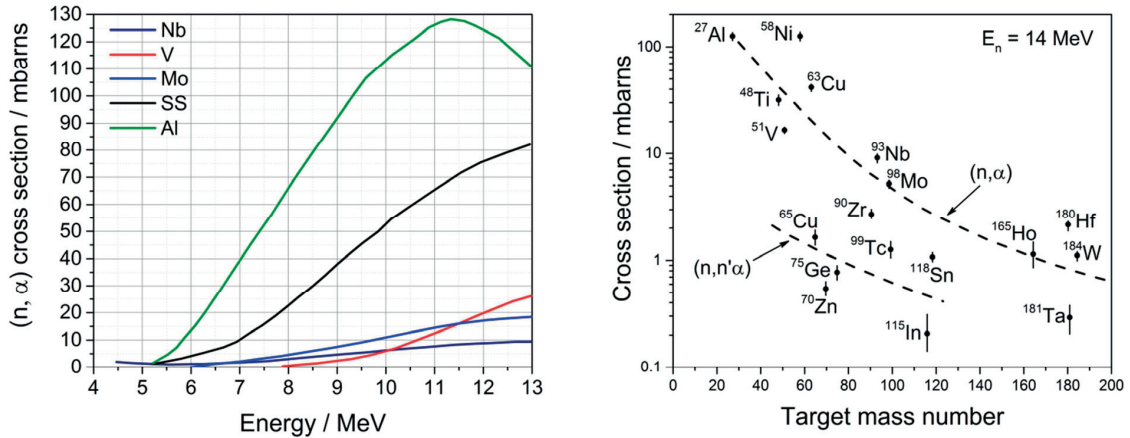


Figure 16: Left: Cross section for (n, α) reaction for neutrons with different energy (from [74]). Right: Cross sections for 14 MeV neutrons producing He in various elements. Dashed lines indicate the trends of the indicated reactions (from [75]).

Virtually any element can contribute to the (n, α) reaction but the cross sections vary considerably with the atomic number (see Figure 16). Therefore, He production cannot be avoided by changing the chemical composition of an alloy. Instead, elements with a large cross section, like Ni, can be replaced or the amount be reduced. The large accumulated He concentration in the first wall affects the mechanical behavior of the material and contributes among others to swelling, hardening and embrittlement. In this review the emphasis will be put on the He embrittlement.

Metals undergo void swelling if exposed to neutron irradiation due to clustering of vacancies produced by the displacement cascade. It is the most pronounced at irradiation temperatures at 425 °C for Fe-Cr alloys [22] but may differ a lot due to chemical composition. FM steels develop much less swelling compared with austenitic steels (see Figure 17). However, under the presence of He the swelling resistance can be affected [76].

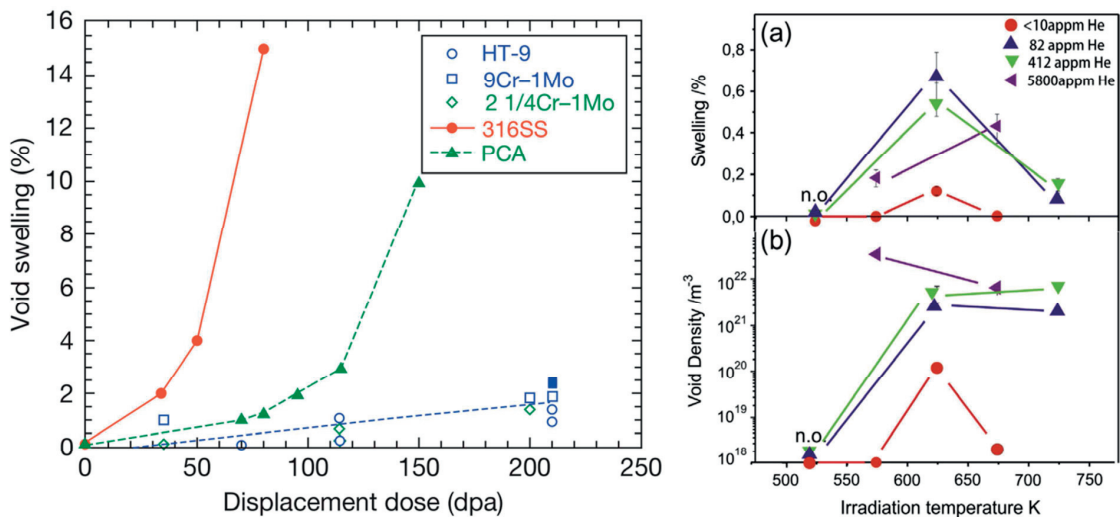


Figure 17: Left: Observed swelling with increasing dpa for austenitic and FM steels (from [34]). Right: Effect of He on swelling and void density at different He concentration for Eurofer97 irradiated to 16.3 dpa (from [77]).

FM steels show increased swelling at higher He/dpa ratios (see Figure 17). Helium acts as a stimulant for cavity swelling in FM steels at high He levels [78] [79]. The observed swelling rates suggest that void swelling may be of concern for doses above 25 dpa [80]. However, most studies used a high He/dpa ratio which may leads to non-conservative estimates of the critical dose for void swelling due to excessive cavity nucleation [80].

As already mentioned, neutron irradiation causes hardening of the material, which depends on the irradiation temperature. The hardening is usually represented by the increase in yield stress $\Delta\sigma_{YS}$, which follows a square root dose dependence at low dose and tends to saturate at higher doses. However, data obtained from spallation neutron irradiated material do not show saturation (see Figure 18).

Remarkable hardening was measured up to 700 MPa [81] [82]. The additional hardening above 10 dpa compared to the saturation behavior of fission irradiation is mainly attributed to He bubbles and possibly to the higher loop density [34].

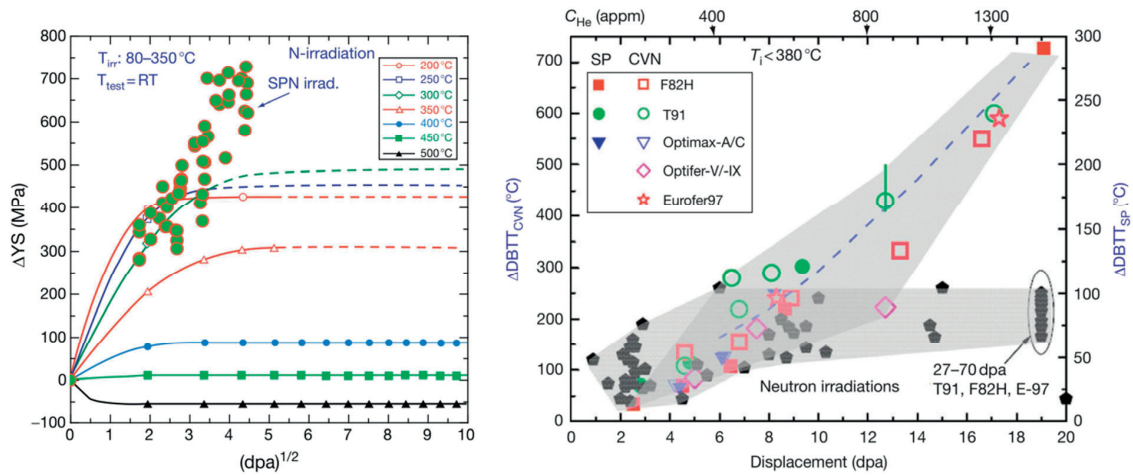


Figure 18: Left: Hardening induced by spallation irradiation (data points) and neutron irradiation (lines). Right: DBTT shift for FM steels irradiated by spallation in comparison with neutron irradiated (both from [34]).

Besides swelling and hardening, helium also can cause an additional embrittlement in materials that is typically characterized by a shift in DBTT. Similar to irradiation hardening, He embrittlement shows a temperature dependence. Initially it was thought that even small amount of He cause an increase in DBTT [83] [84] [85] but it has been shown that embrittlement at irradiation temperatures below 400 °C is mainly due to irradiation induced fine-scale dislocation obstacles [72] [86]. At lower irradiation temperatures single vacancies are almost immobile and He gets trapped in those. However, at elevated temperatures vacancies and He gets mobile and forms helium-vacancy clusters namely bubbles [87] [88].

The total shift of the DBTT can be estimated using a simple hardening-shift relation $\Delta T = C\Delta\sigma_{YS}$ [89] whereas as C shows an average value of ≈ 0.4 °C MPa⁻¹ for FM steels tested with sub-sized Charpy notch specimens. Consequently, this would mean that He contributes to embrittlement with the same amount as to hardening. Nevertheless, He implantation indicated that high concentration levels above ≈ 5000 appm are needed to observe significant hardening due to He [90] [91] [92]. Below ≈ 500 appm, He the hardening effects of He

are minimal [93] [87] [94]. This rough threshold was used in addition with a large database to derive a new simple equation to predict the DBTT shift of Charpy notched specimen irradiated at 300 °C

$$C = 0.4 + 7 \cdot 10^{-4} (X_{\text{He}} - 500) (^\circ\text{C MPa}^{-1}) \quad [34] \quad (3)$$

whereas X_{He} denotes the actual amount of He in the material in appm. In Figure 18 neutron and spallation proton irradiation results are shown whereas the dotted line represents the prediction calculated by equation (3).

The non-hardening contribution of He to embrittlement leads in a transition from cleavage fracture to a very brittle intergranular fracture [2] [95] as the He accumulates at the grain boundaries. Dai et al. explained the He induced grain boundary weakening with the sketch shown in Figure 19 [34].

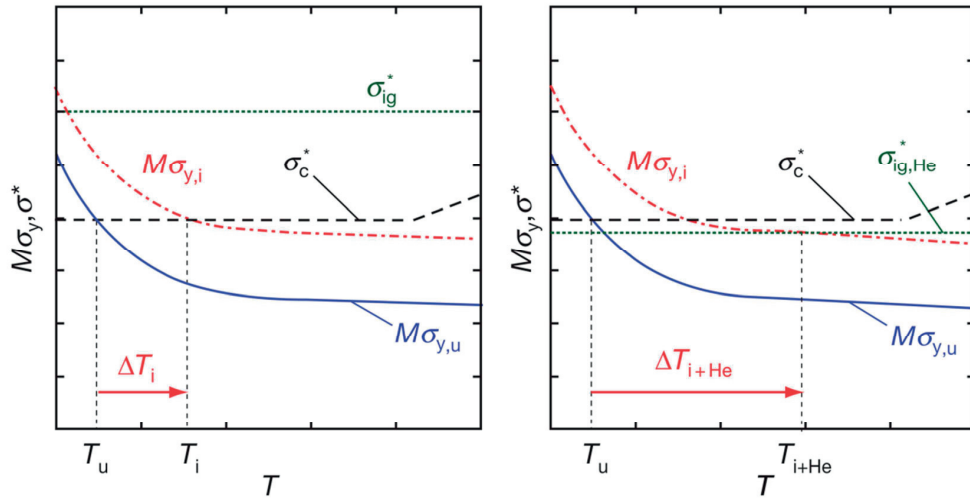


Figure 19: Sketch of the DBTT shift caused by irradiation hardening and He induced grain boundary weakening (from [34]).

Cleavage fracture is triggered when the crack tip stress $M\sigma_y$ exceeds a critical local stress σ_c^* over a critical volume [72] whereas M denotes a stress concentration factor. Intergranular fracture occurs when the crack tip stress exceeds the critical local stress σ_{ig}^* over a certain volume. Usually the σ_{ig}^* stress is higher than σ_c^* and therefore cleavage fracture would take place first. However, with increasing He concentration accumulated at the grain boundaries the σ_{ig}^* falls below the σ_c^* which leads to an intergranular fracture and σ_{ig}^* continues to decrease with increasing He concentration [34].

2.4 Irradiation techniques

In order to investigate irradiation effects under fusion condition to design a high performance structural material for DEMO, irradiation facilities that mimic accurately the PKA spectrum and He production rate of fusion neutrons are needed. So far a wide variety of irradiation facilities have been proposed and applied in research. However, every irradiation technique has its own advantages, limitations and drawbacks. In the following, the main irradiation techniques are presented and discussed. As the investigated specimens in this work were irradiated at the Swiss spallation neutron source, it will be covered in more detail. Finally, the International Fusion Materials Irradiation Facility (IFMIF) is discussed.

2.4.1 Ion accelerators

One option to produce irradiation damage in material is using ion accelerators. Therefore usually Fe^{3+} ion are accelerated into the material causing certain damage with depth (see Figure 20). As the damage profile is quite inhomogeneous, the beam energy can be varied with a degrader to obtain homogeneous irradiation damage. Besides single ion irradiation dual and triple irradiation is common which includes implantation of He^+ and H^+ .

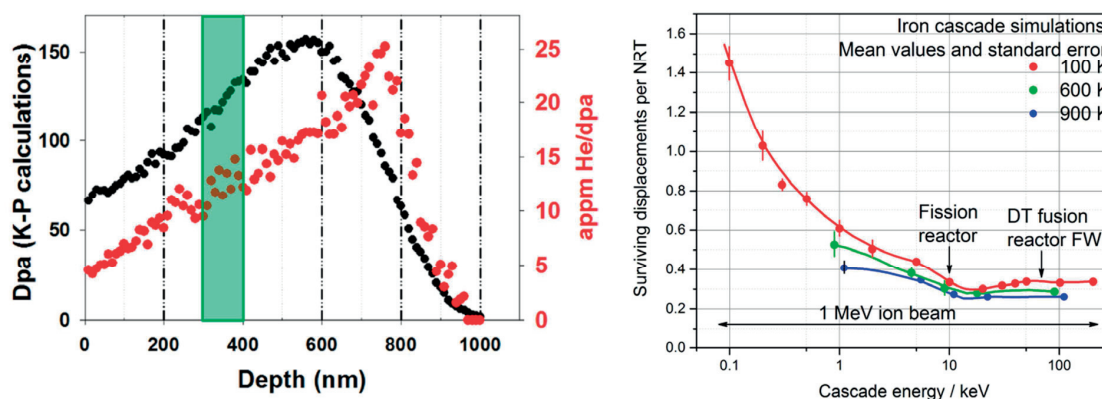


Figure 20: Left: Dpa and He profile obtained in Fe via dual ion beam irradiation at JANNUS using 2MeV Fe^{2+} and 2MeV He^{2+} (from [96]). Right: Surviving defect fraction as function of the PKA energy calculated from molecular dynamics [30]. Range of displacement cascade energies associated with a 1 MeV ion beam (from [80]).

The main advantage of ion beams lies in the fact that high damage rates can be achieved within days whereas it would need month or years in a fusion reactor. He concentrations up to several 1000 appm can be implanted uniformly in the material [97] [98]. Also the irradiation condition like temperature, dose rate, fluence and damaged thickness can be adjusted to cover a large range [99] and even in-situ investigations using a transmission electron microscope are possible [100].

The limited irradiation volume is clearly a drawback and does not allow obtaining bulk properties of the irradiated material. Many potential artefacts are created during the ion irradiation [96]. Furthermore the ion irradiation includes a higher fraction of low angle collisions which cause a much higher fraction of surviving defects compared to dpa values for fission and DT fusion conditions [30] (see Figure 20). Therefore the migration and interaction kinetics of the initial distribution of defects may be considerable different [80].

2.4.2 Fission reactors

Research of radiation effects in structural materials has been and is still advanced using fission reactors. A large range of irradiation temperature can be covered thanks to the strong steady-state volumetric heating [80]. Depending on the reactor type, damage levels of about 50 dpa up to 200 dpa in fast reactors can be achieved within a period of 2 to 4 years. The main advantage of fission irradiation lies in the fact that bulk properties can be obtained. Still, the irradiation volume is limited leading to the development of small specimen test technologies to increase the amount of specimens [101]. However, sodium-cooled fast spectrum reactors reach irradiation volume up to several liters [80].

Disadvantages of fission reactors include the difficulty to control the irradiation temperature and to perform in-situ experiments [96]. The primary reason why fission irradiation is insufficient to simulate fusion conditions can be addressed to the too soft neutron spectra (see Figure 21).

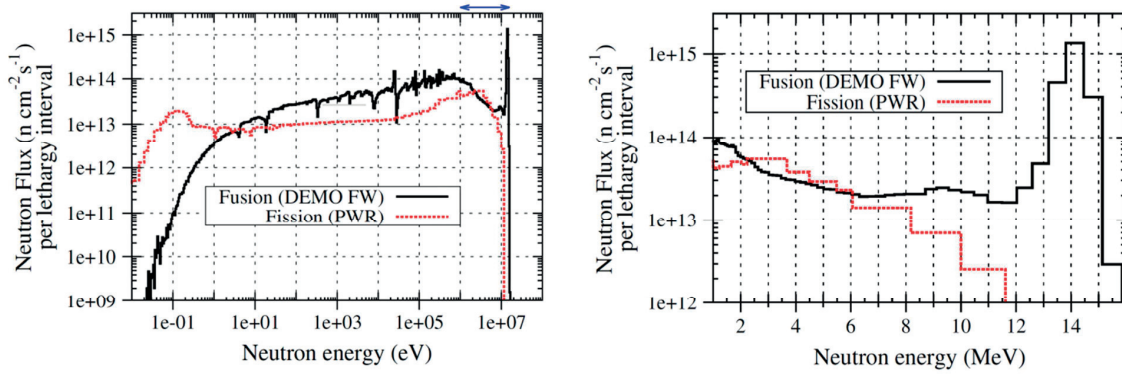


Figure 21: Neutron spectra of a fission (averaged spectra of pressurized water reactor) and fusion reactor. Left: Full energy range. Right: Spectra above 1 MeV as indicated by the blue arrow (both from [102]).

Particularly the fission neutron spectra cannot simulate the peak at 14 MeV energy. The lower amount of neutrons with energies > 5 MeV in fission irradiation causes a low generation of transmutation elements like H and He as the cross section for those reactions increases significantly at higher energies (see Figure 16). He production can be enhanced but only over a few μm in depth by using injector foils based either on Ni or U [103] [104]. Another approach which has been applied is solute doping of the irradiated material with Ni or B [105] [106]. However, doping with B can promote precipitation (as well as Ni), effect prior austenite grain size and produces lithium during the transmutation reaction [107]. Furthermore the addition of Ni or B produces high levels of He relatively early during the irradiation which affects the material behavior [108] [109].

2.4.3 Spallation neutron irradiation

A spallation neutron source is an accelerator based facility than can provide a pulsed or continuous neutron beam depending on the set up. Their main advantage are the high transmutation rates due to the high energy neutron tail (see Figure 22) allowing to investigate mechanical properties at He concentrations around 1000 appm [110] [111]. Also it is possible to induce irradiation damage of >10 -20dpa per year [80] over a large range of temperatures.

Similar to other irradiation techniques the available irradiation volume is limited but significantly bigger than for ion irradiation. Another difficulty which comes along with spallation facilities concerns the irradiation temperature control that varies with the beam current and may cause temperature fluctuation of $\pm 15\%$ [112]. Due to the high generation rates of H and He compared to fusion condition, the interpretation of obtained results can be difficult as the higher H/dpa and He/dpa ratios can affect the final microstructure [113].

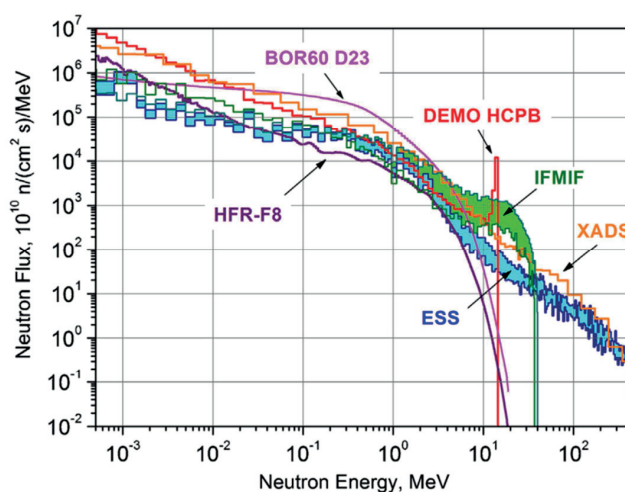


Figure 22: Neutron spectra from spallation sources (ESS, XADS) in comparison with spectra fission (HFR, BOR60) and fusion (DEMO). The international fusion materials irradiation facility (IFMIF) spectrum is given as well (from [114]).

2.4.3.1 Swiss spallation Neutron Source SINQ

SINQ is a steady-state neutron source driven by a proton beam from the Paul Scherrer Institute (PSI) ring cyclotron. The protons are accelerated in three steps (see Figure 23). First the proton beam is produced from an ion source and pre-accelerated in a Cock-croft-Walton column to energy of 870 keV. As a next step the beam is brought to 72 MeV in a 4-sector injector cyclotron. The final acceleration to 590 MeV occurs in a 8-sector mainring cyclotron receiving a stable proton beam of 1.3 mA [115](upgraded 2012 to 2 mA).

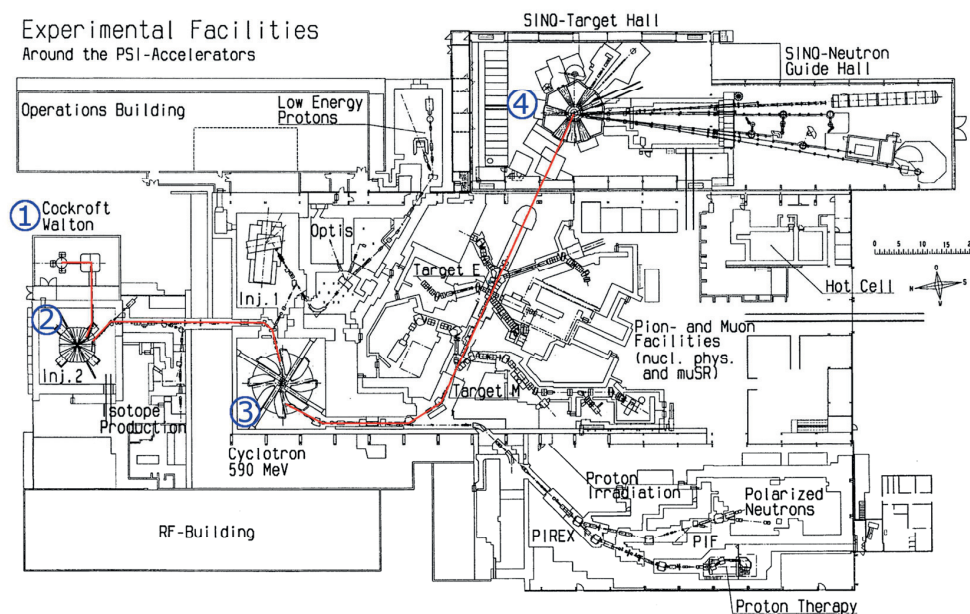


Figure 23: Neutron irradiation facility at Paul Scherrer Institute. Proton beam is indicated in red. 1) Cock-croft-Walton column, 2) 4-sector injector cyclotron, 3) 8-sector mainring cyclotron and 4) SINQ target (from [116]).

Neutrons are created through spallation which takes place when the generated proton beam strikes a heavy target (heavy nucleus). Nuclear spallation consists of two steps:

1. Inter- and intra-nuclear cascade and
2. The nuclear evaporation.

In step one, the striking proton shares its kinetic energy with the nucleons of the target causing a cascade of nucleon-nucleon collisions. Depending on the proton energy, nucleons of the target may have enough energy to escape the nucleus in the direction of the incident proton. The remaining energy is evenly distributed in the target nucleus, which is left in an excited state. In the second step, the nucleus loses its energy by evaporation where particles are emitted isotropically. The total number of neutrons liberated by a 600 MeV proton beam from a thick lead target is around 10 neutrons per incident proton [117].

The SINQ target consists of the target block which is surrounded by two aluminum magnesium shells which are 4 mm spaced (see Figure 24). In between the shells as well as through the target block D_2O coolant is flowing. The normal target rods consist of Pb clad whereas the tube is made of SS316L. Initially zircaloy rods were used but using SS316L increased the neutron production by 30 % [118]. Specimens are packed in the center of the target block in tubes made of SS316L (see Figure 24). The diameter of the specimen rods is 11 mm and the length about 123 mm. Irradiation rods are located at different positions in the targets, the further away from the beam entrance in the target, the lower the irradiation dose and temperature.

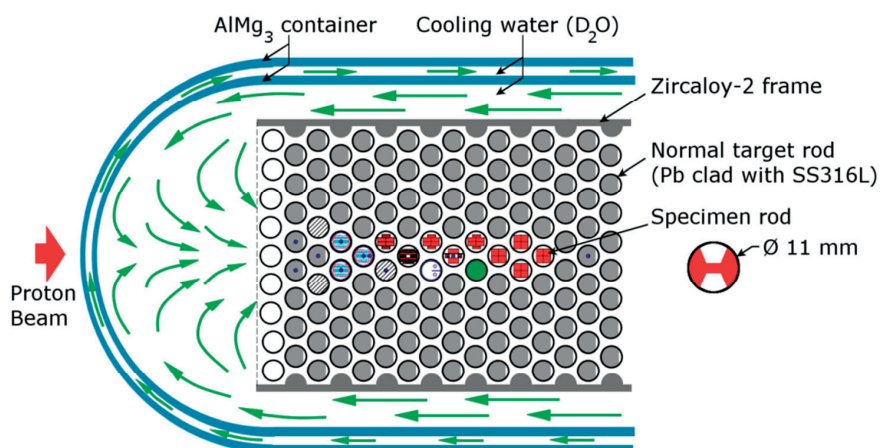


Figure 24: Sketch of the SINQ target indicating the specimen position. Dimension of a specimen rod is given (from [112]).

2.4.4 International fusion materials irradiation facility

From the irradiation techniques presented above, it is evident that currently there is no satisfying fusion relevant neutron source available. However, in order to qualify materials to be used in a real fusion reactor beyond ITER, the fusion materials research community needs an irradiation facility that produces a representative fusion neutron and pka spectra as well as adequate He and H production rate. The International Fusion Materials Irradiation Facility (IFMIF) was initiated in 1994 as a collaborative effort between Japan, the European Union, the United States, and Russia. Since 2007, the IFMIF project is currently pursued by Japan and European Union. IFMIF consists of an accelerator, a target and a test facility. Post-irradiation examination facilities are planned. IFMIF will generate neutrons with a broad peak at 14 MeV (see Figure 22).

seek for an alternative approach. In order to properly take into account specimen geometry and size effects on toughness, local approach models for brittle fracture have been developed over the past 35 years [123]. These local approaches relate the micro-mechanisms of cleavage fracture, which is triggered when a critical crack tip stress field has a high probability of causing cleavage. Evidently, some parameters characterizing the crack tip stress field have to be determined experimentally or calibrated numerically. The near tip stress fields are usually calculated with finite element simulations and have been found quite sensitive to many details of the model and on the constitutive behavior description of the material. Thus, a strategy to determine these parameters must therefore be clearly defined.

2.5.1 Cleavage fracture mechanism

Any crystalline material contains irregularities and deviations from perfect crystals. In ferritic materials, the microstructure consists of randomly orientated grains and second phase particles (carbides). Generally the microstructure affects the fracture process in terms of development and final failure. Cleavage in ferritic steels can be described by three steps:

- i. Formation of a micro-crack: At lower temperatures the initiation of micro-cracks is triggered by hard particles, like carbides, which break under loading [124] [125] [126].
- ii. Propagation: The formed micro-crack propagates into the ferrite.
- iii. Crack progression: In the final step the micro-crack propagates into adjacent grains and coalesces with other crack to create a macroscopic crack.

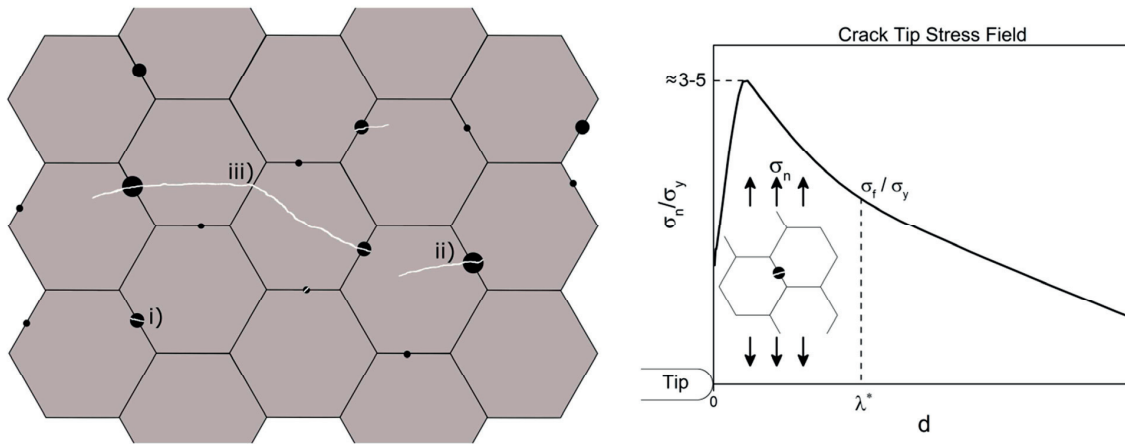


Figure 26: Left: Schematic representation of the cleavage fracture mechanism in ferritic steels. Right: Normal stress σ_n at a crack tip illustrating the critical distance λ^* at which the critical stress for failure σ_f is reached. Carbide cracking near the peak stress is indicated.

The cleavage formation process is schematically shown in Figure 26. In many cases the micro-crack arrest at or near the interface of the hard particle and the surrounding material [127]. However, experimental investigation revealed that micro-cracks can be arrested at grain boundaries and twins as well [124] [125] [128] [129] [130]. The cleavage mechanism involves then competition of two critical events which is either the nucleation or propagation of the micro-crack. At low temperature, cleavage is nucleation controlled but with increasing temperature the critical event is propagation controlled [123] [131]. However, which critical event is controlling cleavage is an ongoing controversy.

2.5.2 Local fracture models

Among the various local fracture models available, one class is based on the attainment of a critical fracture stress σ^* ahead of the crack tip. Before cleavage fracture takes place, a micro-crack has to be present in the material and certain loading conditions have to be applied. Griffith calculated the stress σ^* , which has to be exceeded to grow a micro-crack by setting up an energy criterion [132]. Ritchie, Knott and Rice (RKR) further advanced the requirements for cleavage failure by postulating that the critical stress has to be exceeded over a certain distance λ^* [133] (see Figure 26), which is related to the spacing between larger trigger particles. They proposed a microstructural distance of about two grain diameters in coarse grained mild steel. In the classical RKR model, it is assumed that both critical parameters, σ^* and λ^* , are insensitive to temperature.

The simple RKR model considering λ^* cannot fully describe the interactions of a number of crack-tip processes and therefore does not predict the critical fracture toughness K_{Jc} at higher toughness [72]. Therefore, an alternative approach was proposed that predicts cleavage, by a single or several propagating micro-cracks, or quasi-cleavage which includes extensive micro-cracking by critical stress σ^* which has to enclose a critical area A^* (see Figure 27) around the crack tip. Generally A^* can be substitute by a critical volume by $V^*=A^*B$, where B denotes the thickness [54] [134] [135] [136] [137] [138] [139] [140] [141] [142] [143] [144]. The σ^* - A^* model allows scaling fracture toughness from one specimen size to another by considering that the load level, represented by K , has to be such that the stress volume V^* is the same in each specimen but for two different respective K values. Considering the volume has the advantage that, besides the microstructural role of the trigger particles, it also better describes experimental observations where cleavage fracture is more expected to be triggered in the region of the peak stress rather than at a fixed distance from the tip (i.e., λ^*). Furthermore, considering V^* has the consequence that more potential trigger particles lie within the critical stress σ^* which has been estimated to be around 10^5 in total and ~ 100 of the largest particles [72].

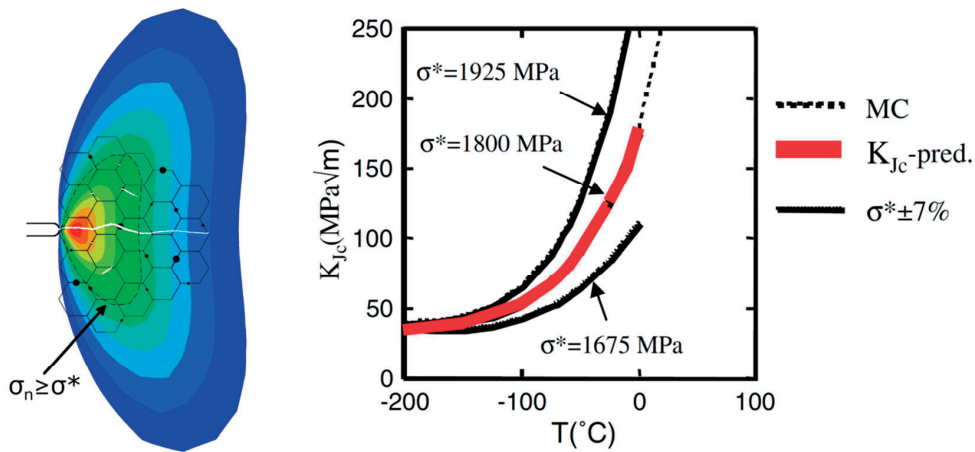


Figure 27: Left: Illustration of the local approach indicating the stressed area $\sigma_n \geq \sigma^*$ which includes several carbides. Right: Predicted K_{Jc} by the local approach in comparison to the master curve for a $T_0 = -45$ °C (from [72]).

Based on this approach, the critical stress intensity factor $K_{Jc}(T)$ is controlled by the stress field $\sigma(\epsilon, \epsilon', T)$, A^* and σ^* . The stress field $\sigma(\epsilon, \epsilon', T)$ depends on the strain ϵ , strain rate ϵ' and temperature T , where σ^* is controlled by the size of trigger particle and the micro-arrest toughness K_{μ} of the ferrite matrix [72]. V^* and σ^* are often assumed to be temperature independent. From blunt notch tests where cleavage is controlled by the broad peak stress supports the temperature insensitivity of σ^* [145] [125] [146] [147] [148]. However,

K_{II} depends on the plastic work dissipated during crack growth and should depend to some extent on temperature. As a matter of fact, at increasing transition temperature T_0 the model reaches a limit. It has been shown that for $T_0 > 0$ °C that the assumption for a temperature independent σ^* and K_{II} is not consistent with an invariant median toughness curve $K_0(T-T_0)$ [134]. In case of large $\Delta\sigma_y$ shifts, the temperature independence of σ^* and K_{II} would yield a reduced slope for the predicted $K_{Jc}(T)$ curve (see Figure 28) resulting from temperature dependence of σ_y [134]. This reduction is due to fact that the slope $d\sigma_y/dT$ decreases with increasing temperature. Therefore, a given $\Delta\sigma_y$ results in a bigger shift at higher temperatures (see Figure 28) and a decrease in slope of $K_{Jc}(T)$. Such big increases in σ_y can easily occur in irradiated material.

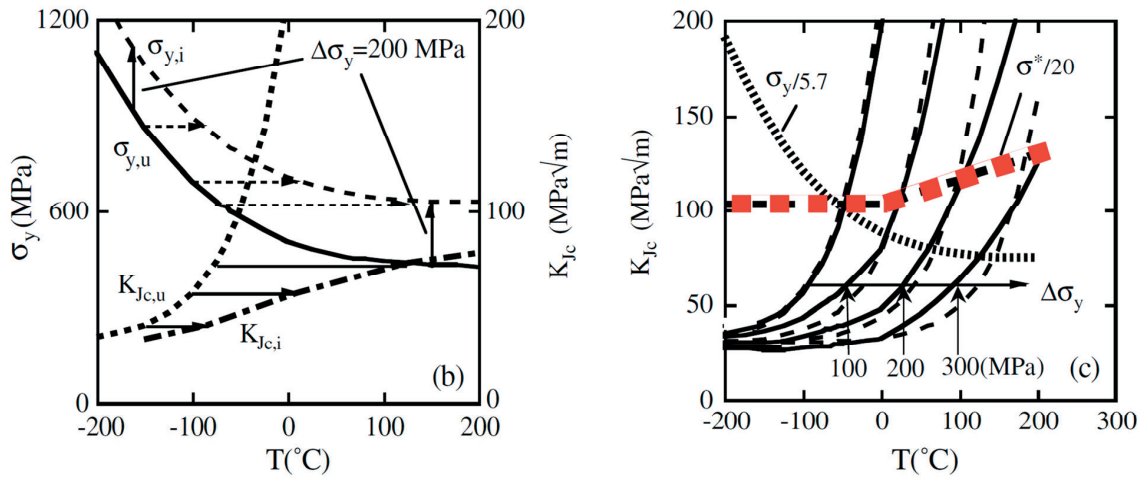


Figure 28: Left: Yield stress shift of 200 MPa and corresponding $K_{Jc}(T)$ curve considering σ^* is not a function of temperature. Right: Comparison of the predicted $K_{Jc}(T)$ by the local approach (dashed lines) and the master curve for different shifts in yield stress with the assumption that σ^* is a function of temperature (red curve) (from [72]).

For reactor pressure vessel steels, the $K_{Jc}(T)$ curve was effectively found constant for increased yield stresses up to $\Delta\sigma_y \approx 200$ MPa [148] and there is evidence of similar agreement for 9Cr martensitic steel that the shift can be even higher $\Delta\sigma_y \approx 350$ MPa [136]. However, at larger shifts of σ_y , a constant shape of the $K_{Jc}(T)$ is obtained by assuming a mild increase of σ^* beyond 0 °C [134] as illustrated in Figure 28. The applied temperature dependence of $\sigma^*(T)$ yields in a reasonable prediction of K_{Jc} in comparison to the dashed master curve result.

Note also that weakest link statistical models have been developed to account for the intrinsic larger scatter in measured fracture toughness and therefore the physics of cleavage fracture [149] [150] [151] [152]. Nevertheless the deterministic σ^* and V^* model approach is capable to predict the fracture toughness well. In Figure 27, the predicted K_{Jc} for an unirradiated martensitic steel which is used for pressure vessels is compared to the statistical master curve approach using $\sigma^* = 1800 \pm 125$ MPa and $A^* = 10^{-8} \text{ m}^{-2}$ as critical parameters [72]. Statistically variations from specimen to specimen can be addressed by the model simply by varying σ^* and V^* .

Weibull stress models for brittle fracture constitute another local fracture approach that has been extensively used. Such models are based on simple weakest link statistics as proposed by Beremin [149]. In this model, the cumulative failure probability of a cracked body loaded at a given loading K_I is calculated with a two-parameter Weibull distribution (σ_u-m)

$$P_f(\sigma_w) = 1 - \exp \left[-\frac{1}{V_0} \int_V \left(\frac{\sigma_n}{\sigma_u} \right)^m dV \right] = 1 - \exp \left[-\left(\frac{\sigma_w}{\sigma_u} \right)^m \right] \quad (5)$$

where the Weibull stress σ_w is defined as:

$$\sigma_w = \left[\frac{1}{V_0} \int_V \left(\frac{\sigma_n}{\sigma_u} \right)^m dV \right]^{1/m} \quad (6)$$

There are major differences between the σ^* - V^* approach and that based on the Weibull stress. In σ^* - V^* model, all the infinitesimal material volume dV with a stress higher than σ^* has the same weight in the fracture process, while in the Weibull stress model, the contribution of each volume element dV depends on the actual stress. Nonetheless, to calibrate the two parameters (σ_u - m) of the Weibull stress model is complicated due to the non-uniqueness of the solution but can be done with a cumbersome procedure proposed by Gao et al. [152], where fracture tests under different constraint conditions have to be performed and supplemented by tensile tests and 3D finite element calculations.

Chapter 3 Experimental Procedures

In this chapter, the tested materials as well as the applied experimental techniques are introduced first, and a description of the data evaluation follows. Finally the finite element models and analysis methods are presented in detail. Own developed data processing techniques and approaches are explained in more detail.

3.1 Materials

Eurofer97 is a reduced activation tempered martensitic steel envisaged as a structural material for Test Blanket Modules (TBMs) that will be applied in the International Thermonuclear Experimental Reactor (ITER). In this study, two different heats of Eurofer97 are investigated, which were produced by Böhler AG. They were provided in the form of plates of different thickness. In order to properly distinguish the two different batches they are renamed to Eurofer97-(14) and Eurofer97-(25). The “14” and the “25” refers to the rolled plates with 14 mm and 25 mm respectively. Besides the plate thickness, they differ slightly in composition (see Table 1). For both steels the Ta and Ni content is much higher than in the specifications for Eurofer97. Slight exceeding values can be found for Co and Nb as well.

Another difference can be found in the heat treatment. For both heats, normalization was performed at 980 °C followed by air cooling. However, the normalizing temperature was held for 27 min for the Eurofer97-(14) and 30.6 min for the Eurofer97-(25). Tempering was applied at a temperature of 760 °C for 90 min and air cooling.

Detailed investigations of the microstructure of the Eurofer97-(25) were already performed by Bonadé [153] and Mueller [154] for example. Eurofer97-(25) features small prior austenite grains (PAG) size characterized by a mean intercept length of approximately 10 μm [153]. The ductile to brittle transition temperature (DBTT) was found to be at $T_0 = -78$ °C whereas ASTM values were modified [154].

As in the work of Bonadé [153], the PAG size determination was conducted using optical microscopy images of chemically etched specimens (see section 3.3). The PAG was calculated by the linear intercept method following the ASTM E112-13 standard.

Table 1: Chemical composition of the two Böhler Eurofer97 batches used in this work.

	Eurofer97-(14)	Eurofer97-(25)	Specifications Eurofer97
Thickness	14 mm	25 mm	
Heat	E83698	E83697	
C	0.12	0.12	0.09-0.12
Si	0.04	0.06	≤0.05
Mn	0.49	0.46	0.20-0.60
P	<0.005	<0.005	≤0.005
S	0.004	0.004	≤0.005
Cr	8.93	8.9	8.50-9.50
Mo	<0.001	0.0023	≤0.005
Ni	0.02	0.022	≤0.005
V	0.2	0.2	0.15-0.25
W	1.08	1.07	1.0-1.2
Cu	0.0019	0.0039	≤0.005
Co	0.006	0.006	≤0.005
Ti	0.006	0.009	≤0.01
Al	0.009	0.008	≤0.01
Nb	0.0017	0.002	≤0.001
B	<0.001	<0.001	≤0.001
N	0.021	0.02	0.015-0.045
Pb	<0.0003	<0.0003	
Ta	0.15	0.15	0.05-0.09
O	0.006	0.0007	≤0.01
As	<0.005	<0.005	As + Sn + Sb + Zr ≤ 0.05
Sn	<0.005	<0.005	
Zr	<0.005	<0.005	
Sb	<0.005	<0.005	

Concerning the Eurofer97-(14) heat, microstructural investigations were performed in this work, which includes precipitation analysis, energy dispersive X-ray spectroscopy as well as electron back scatter diffraction maps. The detailed description of these techniques can be found in the next section.

3.2 Scanning electron microscopy

Scanning electron microscope (SEM) was used for topographical imaging, to determine the chemical composition of the precipitates and to examine the crystallographic orientation of the grains. Additionally, SEM investigation was applied to perform EBSD measurements.

Two different scanning electron microscopes (SEM) were used to investigate the microstructure of Eurofer97. A Zeiss NVision40 equipped with a Schottky field emission gun was used to acquire images with an Everhart-Thornley detector, a four quadrant backscatter detector (QBSD, Type 815, Cambridge), an Inlens and an energy dispersive X-ray detector (Model 8061, Oxford). Electron back scatter diffraction (EBSD) maps were acquired with a Zeiss ULTRA55 using an EDAX detector and TSL OIM Analysis 7 software.

Standard secondary electron (SE) imaging using the Everhart-Thornley (ET) detector was applied to investigate the fracture surface of the tested disk tensile specimens (DTS) as well as for the compact tension (CT) specimens. SE are low energy electrons (< 50 eV) and originate from a thin surface layer. Therefore they provide information about the topography of the specimen. Besides the ET, the in-lens detector was used as well. As the name already indicates the detector is placed in the electron column. It is mainly used at higher magnifications and can enhance among others the topographical contrast. The applied accelerating voltage was 15 kV with high current and an aperture size of 60 μm . Working distance (WD) during investigation varied between 10-12 mm.

The four quadrants back scattering detector (QBSD) is used to detect back scatter electrons (BSE). Those electrons possess higher energy and originate from elastic scattering interaction with the atoms of the specimen. Material specific information can be deduced because heavier elements yield more BSE than lighter ones causing a compositional contrast. The detector can also be used to show channeling contrast giving information about the grain orientation relative to the beam. In this work, the QBSD was used to investigate precipitates in the steel as well as grain and sub-grain boundaries. Once more the accelerating voltage was set to 15 kV with high current and an aperture of 60 μm . However the WD ranged between 5 - 7 mm.

Crystallographic information from the specimen can be obtained by EBSD. Therefore the electron beam interacts with the 70° tilted specimen causing an electron diffraction pattern that is detected by a fluorescent screen. From the formed pattern, the crystal structure and orientation can be determined. By scanning the electron beam across the specimen, the crystallographic orientation is measured at several points. The resulting data provide information about the grain orientation and boundaries. EBSD measurements were conducted at an accelerating voltage of 20 kV with high current and an aperture of 120 μm . EBSD maps at high magnification were obtained with a step size of 20 nm whereas the maps at low magnification used 0.4 μm .

In order to determine the elemental composition of the precipitates, an energy dispersive X-ray (EDX) spectroscopy was carried out. The electron beam focused on the surface of interest acts an excitation source. The electron beam may eject an electron of an inner shell of an atom leaving an electron hole. An electron from an outer shell, which has a higher energy, fills up the hole. The energy difference is then emitted in the form of a photon. Every element possesses a unique set of energy levels and therefore emits only x-rays that are characteristic to it. The used x-ray detector was an Oxford model 8061 Inca Penta FETX3 which has a resolution of 133 eV at 5.9 keV. Peak identification as well as EDX mapping was done with the INCA software. The accelerating voltage was varied between 20 and 10 kV due to the minimizing the interaction volume of the beam. High current settings were applied and a 60 μm aperture.

3.3 Sample preparation

Proper specimen preparation is crucial for any microscopy technique, optical or electron microscopy. Depending on the investigation method, different preparation methods were considered.

The optical microscopy analysis to measure the PAG size required first a coarse mechanical polishing with P1000 sandpaper followed by electrochemical etching (Kristall 620) with a solution of 10 g oxalic acid in 100 ml distilled water. Etching was applied at 10 V for 20 s at room temperature.

In order to examine the distribution and size of precipitates, the specimen was mechanically polished with P1000, P1500 and P2500 sandpaper followed by electropolishing (Kristall 620). The used polishing solution consists of 700 ml ethanol, 250 ml glycerol and 50 ml perchloric acid. At a voltage of 30 V the sample was polished for 10 s at room temperature.

Mechanical polishing was applied to EBSD samples using P1000, P1500 and P2500 sandpaper. As a next step diamond suspension with a grain size of 3, 1 and $\frac{1}{4}$ μm was used. The final polishing abrasive was a 40 nm colloidal silica (Struers OPS).

Investigation of the fracture surfaces simply required cleaning in acetone and ethanol in order to remove possible contamination.

3.4 Irradiation conditions

Irradiation of the specimens was realized in the fifth irradiation program (STIP-V) at SINQ (Swiss Spallation Neutron Source), Paul Scherrer Institute. The design of the samples as well as the temperature calculation was done by the group of Odette at University of California, Santa Barbara (UCSB). The specimens were put in 10 mm diameter and 150 mm long tubes, which were inserted in the target in place of lead tubes (see Figure 29)

The irradiation dose and temperature of the samples are depending on their position within the tube and on the position in the target array. The more distant from the position where the proton beam enters the target and from the beam axis, the lower is the received dose and temperature of the sample. Rod number 12 in row 11 was chosen as final position within the array (see Figure 29) which is slightly of the center of the beam.

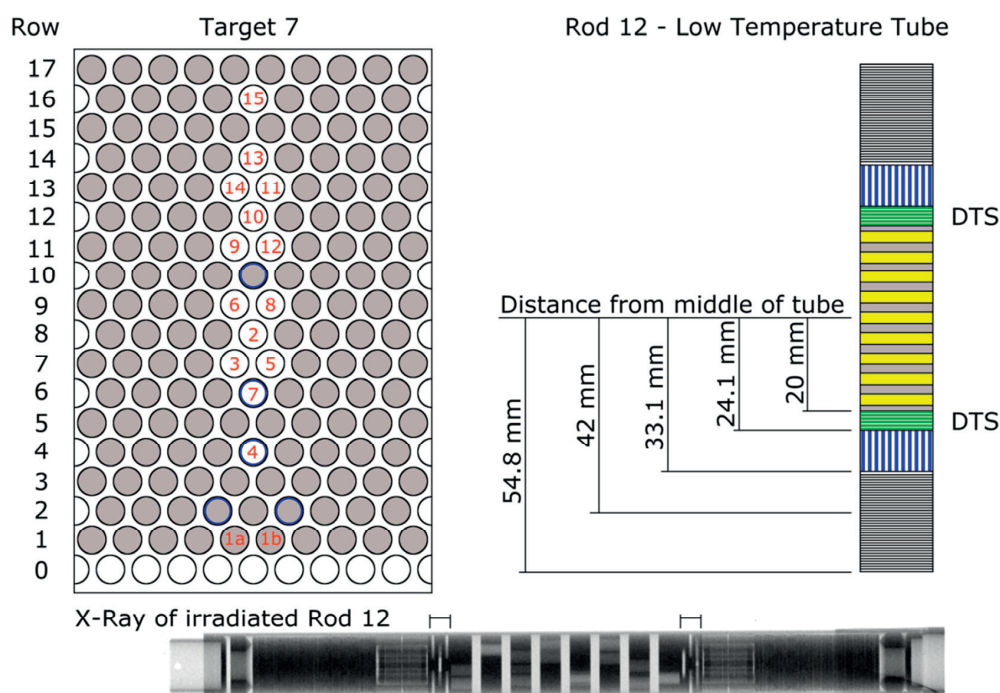


Figure 29: Left: Rod positions within the target array. Right: Sample layout within rod 12. Lower: X-ray image of rod 12 after irradiation (DTS positions are indicated).

The DTS were placed in the middle of the tube. The final irradiation damage in terms of dpa and He was calculated from the energy deposition of the beam (see Figure 2). In total, a proton charge of 9.56 Ah was delivered during the irradiation period from 2007 to 2008. It can be seen that the shown beam profile is not perfectly centred to the target. This slight shift off the centre has of course an impact on the damage distribution. Therefore, a range of these values is given in Table 2.

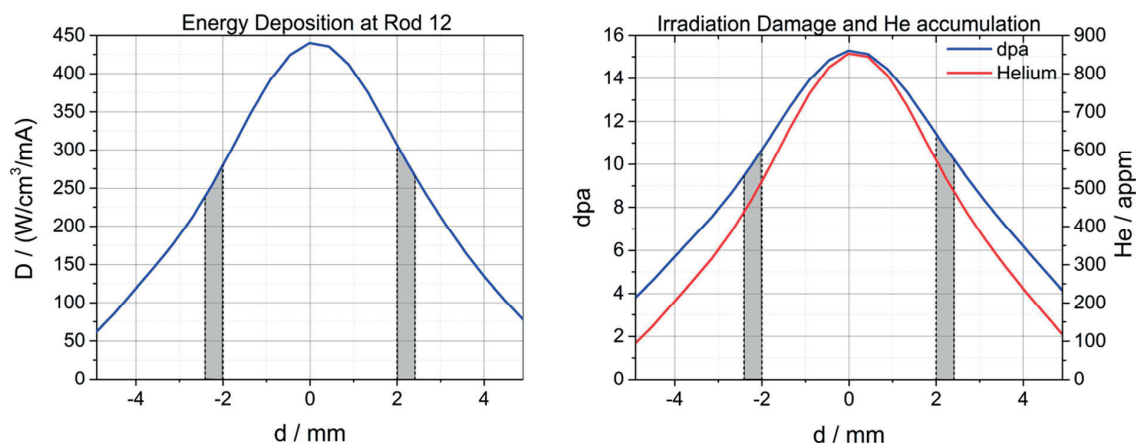


Figure 30: Beam properties: Deposited energy D , calculated irradiation damage and He accumulation for rod 12. Gray areas indicate the DTS position.

Table 2: Determined range of irradiation damages in Fe calculated by the energy deposition of the beam.

	dpa	He / appm
Min	9.5	440
Max	11.4	570

The final calculated dose is about 10.5 ± 1 dpa dose and the concentration of helium is 505 ± 65 appm. However, the proton beam position, intensity and size fluctuate in during irradiation (see Figure 31). As a consequence it is difficult to determine the irradiation damages precisely. However, a reasonable estimate can be made that yields an irradiation dose of about 11 dpa and a He accumulation of about 540 appm.

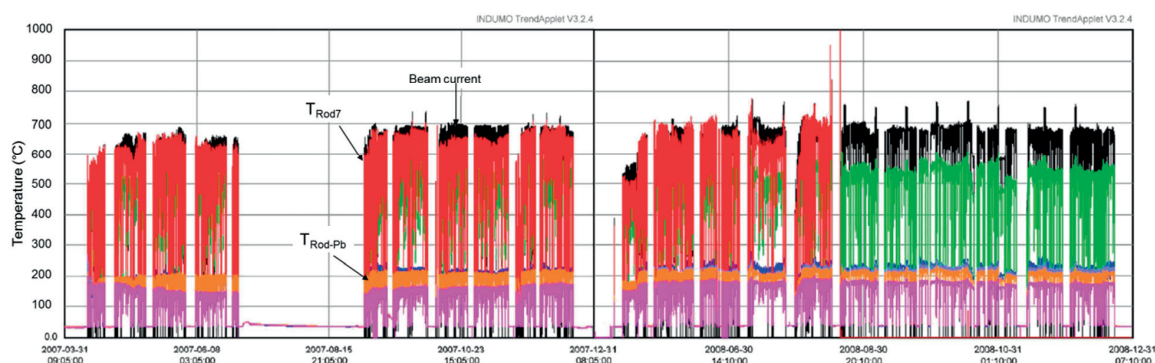


Figure 31: Beam current and temperature history of SINQ STIP-V during 2007-2008 (adopted from Dai. Y. unpublished).

The last irradiation parameter, which affects the accumulation of defects in materials, is the irradiation temperature. The irradiation temperature was not measured but calculated by finite element simulation (ref of UCSB report) by considering the beam energy deposition and heat transfer. As a consequence the

described specimen design was developed to minimize the temperature fluctuations. The calculated irradiation temperature based on the beam energy deposition is around $250 \pm 50^\circ\text{C}$.

3.5 Tensile tests, specimens and testing conditions

To determine the tensile properties of Eurofer97, tensile tests were performed with two types of specimen, namely standard round shaped and non-standard flat butterfly shaped specimens (disk compact tension DTS).

3.5.1 Standard round shaped specimen

The main purpose to conduct uniaxial tensile tests is to obtain the yield stress and the flow properties at different temperatures and various strain rates. Two different sizes were used (see Figure 32) whereas both were tested with a Schenck RMC100 at constant cross head speed ranging from 0.05 to 10 mm/min. Load and displacement were recorded by a load cell which calibrated to 30 kN and by compliance correcting the load train displacement respectively. For the tests done at room temperature, the displacement was measured with a clip-on extensometer (Sandner EXA10-5o).

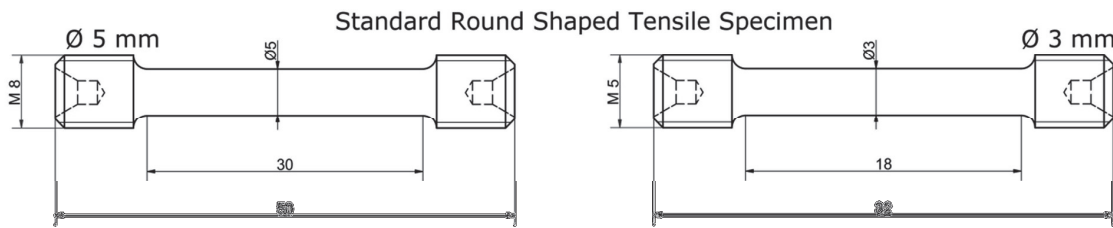


Figure 32: Standard round shaped tensile specimens (Dimensions in millimeters).

An environmental chamber from Noske-Kaeser (Tee40) was used for tests at low and high temperature within the range -150 to 250°C . Low temperatures were reached by liquid nitrogen flow provided by a PID controller whereas high temperatures were controlled by electric heating. The temperature of the specimen was measured using a thermocouple attached on its surface. In order to conduct tensile tests at -196°C , a tube was mounted around the load train which was completely filled with liquid nitrogen.

With the 5 and 3 mm diameter round shaped tensile tests, the flow properties, namely the true stress/strain curve, can be calculated up to necking straightforward. A developed inverse approach using a finite element model allowed extending the determination of the flow properties up to failure. Details can be found in section 3.7.1 and 3.7.3.

The $\varnothing 3$ mm standard round shaped tensile specimens were used to investigate strain rate effects onto the yield and flow stress with temperature. Strain rate jumps were applied by periodically varying the displacement rate between two values and conventional tests at various strain rates were performed.

3.5.2 Non-standard disk tensile specimen

The disk tensile specimens (DTS) were used to evaluate the irradiated and unirradiated yield stress and flow properties at different temperatures of Eurofer97-(14). As mentioned in section 3.4, the non-standard geometry (see Figure 33) was designed to fit the specimen on the radial plane of irradiation tube for SINQ irradiation. Due to the geometry of the target, a non-standard tensile specimen geometry, which minimizes the irradiation damage gradient and ensures a uniform center sample temperature, had to be designed.

The heat transfer is mostly radial since heat is generated inside the sample and is extracted only from the outer diameter of the tube. Therefore the aim was to create a sample where the heat flows through as few components as possible in the radial direction. In order to provide the radial heat flow and minimize the irradiation gradient thin samples with a circular geometry were chosen. Detailed thermal FE models were conducted with ABAQUS and revealed a sufficient temperature distribution using the developed specimen.

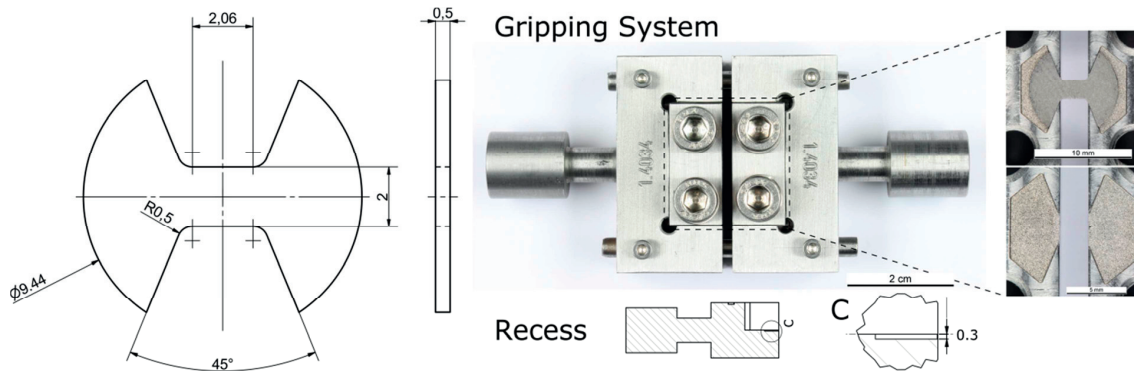


Figure 33: Non-standard disk tensile specimen geometry and dimensions as well as the designed DTS clamping system (dimensions in millimeters).

The nominal gage length l_0 and cross section A_0 of the DTS are respectively 2.06 mm and 1.03 mm^2 . A special gripping system was developed to clamp the specimen that guaranteed a proper alignment of the DTS. The grips have a 0.3 mm deep recess that enables a pure clamping of the 0.5 mm thick specimen preventing at the same time the specimen from slipping (see Figure 33).

In order to check the functionality and reproducibility of the designed grip system, several tensile tests of unirradiated material at room temperature were conducted. Three results in terms of engineering stress/strain curve are shown In Figure 34, showing good reproducibility.

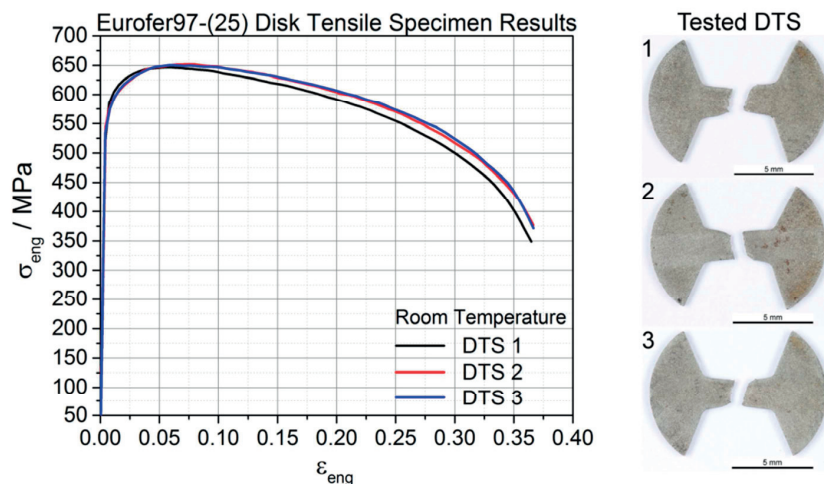


Figure 34: Engineering stress/strain curves of tested DTS specimens at room temperature and corresponding image of tested specimens.

The uniaxial tensile tests were conducted with a Zwick Z010 at constant cross head speed of 4 mm/h. An environmental chamber from Instron (ECD86 D) was used to conduct tests at low and high temperature.

The temperature was measured at both clamps, upper and lower. Measurements of the load were recorded by a load cell which was calibrated to 10 kN. Due to the size and geometry of the specimen, it was not possible to mount a clip extensometer to measure the displacement directly. Therefore the strain was calculated from load train displacement which was compliance corrected using results obtained by a DTS finite element model (see section 3.7.3).

A related difficulty with non-standard geometry resides in the fact the constitutive behavior, or equivalently the true stress-strain curve, cannot be obtained in a straightforward procedure due to the inhomogeneity of the stresses and strains along the gage length. To extract the constitutive behavior from non-standard specimens, one has to rely on modeling. An inverse method was developed in this work to determine the elastic and plastic flow properties of DTS, which described in detail in section 3.7.3.

3.6 Fracture toughness tests

The fracture toughness of Eurofer97 was experimentally determined with two different sizes and shaped compact tension (CT) specimens (see Figure 35). CT and disk CT (DCT) specimen were fabricated from the two different Eurofer97 heats.

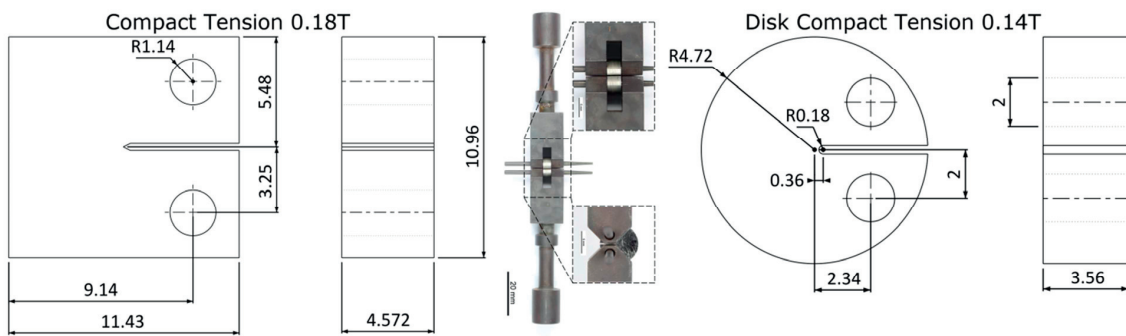


Figure 35: Fracture compact tension specimens; Left: 0.18T CT and Right: 0.14T DCT specimen as well as the developed gripping system is shown (dimensions in millimeters).

The rectangular shaped CT specimens were manufactured from the Eurofer97-(25) batch whereas the disk shaped CT specimens were manufactured from the Eurofer97-(14) batch. Prior to testing, the fracture specimens were pre-cracked by fatigue at room temperature with a resonant testing machine Cracktronic/Rumul. Both specimen types were tested with a Schenck RMC100 at a constant cross head speed. For CT specimens of Eurofer97-(25), dynamic fracture toughness measurements were performed. The loading rate was applied in cross-head controlled mode at a displacement rate of 52 mm/min. Quasi-static loading rates were applied for the DCT specimens Eurofer97-(14) with a displacement rate of 0.1 mm/min. Measurements of the load and displacement were recorded by a load cell which calibrated to 30 kN. Lower temperature tests ranging between -160 and -70 °C were done using the same environmental chamber and control unit as for the standard tensile tests. The testing temperatures were chosen to have enough tests in the lower ductile-to-brittle transition to determine the reference transition temperature T_0 of the master-curve. The transition temperature T_0 was determined according to the ASTM standard E1921 – 17a [56]. Per definition T_0 is the temperature at which the median fracture toughness $K_{Jc(\text{med})}$ equals $100 \text{ MPam}^{1/2}$ for a 1T specimen (see Figure 37). In the following the procedure to evaluate T_0 from experimental CT test is described. First the critical stress intensity factor K_{Jc} for each test has to be calculated from the experimental load/displacement curve using

$$K_{Jc} = \sqrt{\frac{J_c E}{1 - \nu^2}} \quad (7)$$

where E is the Young's modulus and ν the Poisson's ratio. The J-integral at the onset of cleavage fracture can be calculated by

$$J_c = J_e + J_p \quad (8)$$

with J_e being the elastic and J_p the plastic component. For both specimen types, CT and DCT, the elastic component is obtained by

$$J_e = \frac{(1 - \nu^2) K_e^2}{E} \quad (9)$$

$$K_e = \frac{P}{B\sqrt{W}} f\left(\frac{a_0}{W}\right)$$

P denotes the fracture load, a_0 is the initial crack size, and B and W are the thickness and the so called width of the specimen respectively (see Figure 36).

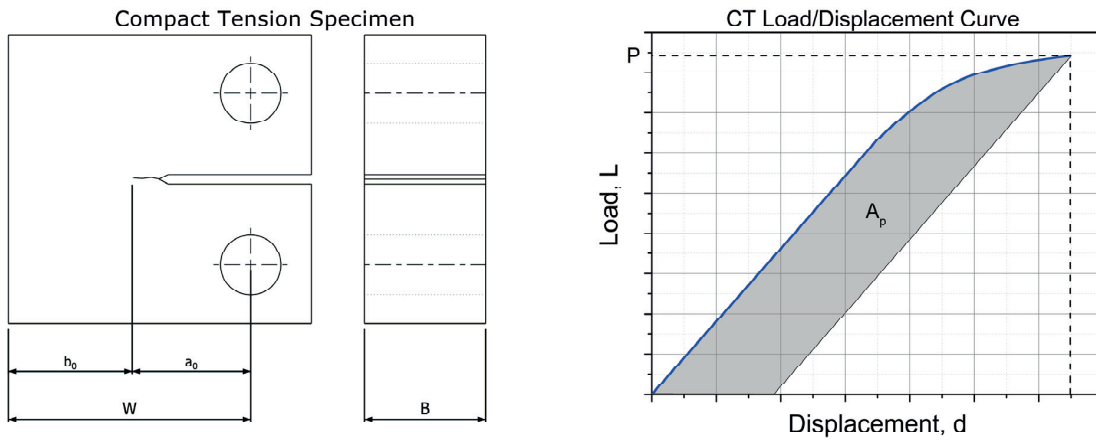


Figure 36: Left: Compact tension specimen sketch Right: Plastic area A_p determination.

The initial crack size a_0 of the fractured specimen is measured at nine equally spaced points in thickness and averaged according to the ASTM standard E1921 – 17a. The function $f(a/w)$ is dimensionless and depends on the geometry of the specimen. In equation (10) the geometric functions for CT and DCT specimens are shown.

$$f_{CT}\left(\frac{a_0}{W}\right) = \frac{2 + \frac{a_0}{W}}{\left(1 - \frac{a_0}{W}\right)^{3/2}} \left(0.886 + 4.64\left(\frac{a_0}{W}\right) - 13.32\left(\frac{a_0}{W}\right)^2 + 14.72\left(\frac{a_0}{W}\right)^3 - 5.60\left(\frac{a_0}{W}\right)^4 \right) \quad (10)$$

$$f_{DCT}\left(\frac{a_0}{W}\right) = \frac{2 + \frac{a_0}{W}}{\left(1 - \frac{a_0}{W}\right)^{3/2}} \left(0.76 + 4.8\left(\frac{a_0}{W}\right) - 11.58\left(\frac{a_0}{W}\right)^2 + 11.43\left(\frac{a_0}{W}\right)^3 - 4.08\left(\frac{a_0}{W}\right)^4 \right)$$

The plastic component of the J-integral can be calculated using

$$J_p = \frac{\eta A_p}{B b_0} \quad (11)$$

$$\eta = 2 + 0.522 \frac{b_0}{W}$$

where $b_0 = W - a_0$ is the initial remaining ligament and A_p denotes the plastic area below the load/displacement curve (see Figure 36).

K_{Jc} values have to be converted to a so called 1T size which corresponds to a CT specimen of 25.4 mm in thickness (1 inch). Generally, a conversion is necessary if the tested specimens are different from 1T size in order to account for the statistical size effect. The used CT and DCT specimens do have a size of 0.18T and 0.14T respectively. The following equation adjusts the $K_{Jc(xT)}$ value from any size to 1T.

$$K_{Jc(1T)} = K_{\min} + (K_{Jc(xT)} - K_{\min}) \left(\frac{B_x}{B_{1T}} \right)^{1/4} \quad (12)$$

K_{\min} denotes the minimum threshold toughness value and equals $20 \text{ MPa m}^{1/2}$. B_x is the thickness of the tested CT specimen and B_{1T} is the thickness of a 1T sized CT specimen. The obtained K_{Jc} values shall be considered valid if the following maximum K_{Jc} is not exceeded

$$K_{Jc(\text{limit})} = \sqrt{\frac{E b_0 \sigma_{ys}}{M(1-\nu^2)}} \quad (13)$$

σ_{ys} is the yield stress at 0.2% of plastic strain at the test temperature. M is the deformation limit and per ASTM definition equal to 30. If the limit is violated, the K_{Jc} value gets censored and replaced by the $K_{Jc(\text{limit})}$. The mentioned censoring limit accounts indirectly for constraint loss effects [155].

After converting and censoring of the K_{Jc} data the transition temperature T_0 can be iteratively determined with

$$\sum_{i=1}^N \delta_i \frac{\exp(\alpha(T_i - T_0))}{\left(\frac{(A - K_{\min})}{(\ln 2)^{1/4}} + \frac{(100 \text{ MPa m}^{1/2} - A)}{(\ln 2)^{1/4}} \exp(\alpha(T_i - T_0)) \right)} - \sum_{i=1}^N \frac{(K_{Jc(i)} - K_{\min})^4 \exp(\alpha(T_i - T_0))}{\left(\frac{(A - K_{\min})}{(\ln 2)^{1/4}} + \frac{(100 \text{ MPa m}^{1/2} - A)}{(\ln 2)^{1/4}} \exp(\alpha(T_i - T_0)) \right)^5} = 0 \quad (14)$$

where $A = 30 \text{ MPa m}^{1/2}$ and $\alpha = 0.019$ are parameters which define the shape of the master curve (see equation (15)). The Kronecker delta δ_i equals one for valid $K_{Jc(i)}$ entries and zero for censored ones. T_i denotes the test temperature corresponding to $K_{Jc(i)}$ and N is the number of tested specimens. The test temperatures from the individual experimental CT tests should be close to the transition temperature fracture toughness value $K_{Jc} = 100 \text{ MPa m}^{1/2}$ for 1T. In that case, only six valid tests are needed to properly define T_0 . However, for small specimens like the used 0.18T CT and 0.14T DCT testing close to T_0 may cause an in-

creased amount of tests exceeding $K_{Jc(\text{limit})}$. Therefore tests should be conducted below T_0 with the drawback of increasing the uncertainty of the T_0 determination as closer the lower-shelf toughness is approached. One can counteract this problem by simply increasing the number of tests.

Once the transition temperature has been determined the median fracture toughness versus temperature can be calculated using the master curve equation

$$K_{Jc(\text{Med})} = A + (100 \text{ MPa m}^{1/2} - A) \exp(\alpha(T - T_0)) . \quad (15)$$

Usually an upper and lower bound are calculated as well using

$$K_{Jc(0.x)} = K_{\min} + \left(\ln \left(\frac{1}{1-0.x} \right) \right)^{1/4} \left(\frac{(A - K_{\min})}{(\ln 2)^{1/4}} + \frac{(100 \text{ MPa m}^{1/2} - A)}{(\ln 2)^{1/4}} \exp(\alpha(T - T_0)) \right) \quad (16)$$

where the 0.x represents the selected cumulative probability level. In Figure 37 the median, the lower and the upper bound master curve is shown using the standard values proposed by ASTM. Lower bound is usually set to 1 % failure probability and upper one to 99 %.

The reasons to use two different CT specimen geometries for the two Eurofer97 heats are the following. The static fracture toughness behavior of the Eurofer97-(25) was extensively characterized in literature with rectangular shape CT specimens (among which 0.18T CT) so that one can rely on a huge database. Therefore it was chosen to analyze the loading effects using rectangular 0.18T CT specimen for comparison. For the Eurofer97-(14) the DCT shaped specimen with a size of 0.14T results from the geometric constraint of the irradiation tube used for SINQ irradiation.

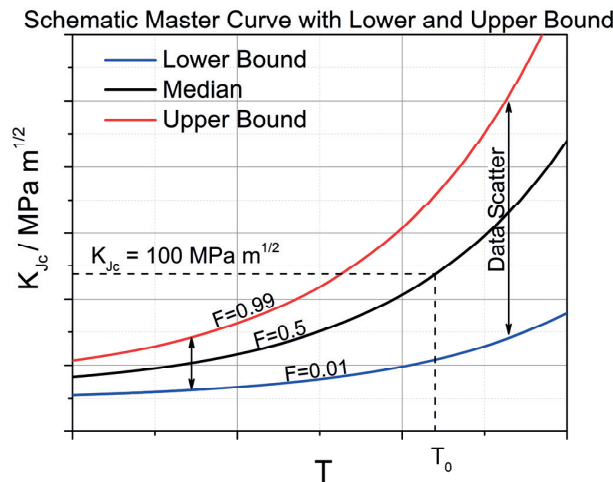


Figure 37: Schematic master curve shape for the lower and upper bound as well as the median. The transition temperature definition is indicated.

For the dynamic CT tests obviously the loading rate is from great interest. Since most specimens broke practically in the macro-elastic regime where K_{Jc} is proportional to P , which in turn is proportional to the loading rate linear with the cross-head velocity, the loading rate was approximated by the following equation

$$\frac{dK_{JC}}{dt} = \frac{K_{JC}}{t_f} \quad (17)$$

where t_f denotes the time of failure of the CT specimen.

3.7 Finite element modelling

Several finite element models (FEM) were built with the commercial software Abaqus in order to analyze and reconstruct experimental results. Standard and non-standard tensile models were used to determine the mechanical properties at quasi static tests as well as dynamic tests to assess the effect of strain rate and thermal effects on the deformation behavior. 2D and 3D FE models of CT specimens and a plain strain small scale yielding (SSY) model were used to calibrate and analyze the local approach. The impact of strain rate and thermal effects on the local approach was studied with 2D plain strain models. A 2D disk CT specimen was considered to reconstruct the lower bound of the master-curve by considering a local approach to fracture. All models were implemented in Abaqus 6.14-1 using an implicit solution method.

3.7.1 Standard round shaped tensile FEM

An axisymmetric model was developed for the standard round shaped tensile specimen with a diameter of 5 mm. Due to symmetry only a quarter had to be considered. The model contains 16'000 linear quadrilateral elements of type CAX4RT. The applied boundary conditions are shown in Figure 38).



Figure 38: Axisymmetric FE model of the standard round shaped tensile specimen. Boundary conditions are indicated.

A reference point (Ref. P. in Figure 38) which is constrained to the surface nodes at the cross section of the gage length was used to load the specimen in displacement control. The applied load can be calculated from the reaction forces acting on the reference point. A single node approach to calculate the load/displacement curve is more advantageous for processing the obtained data in the developed algorithm (see section 3.7.3).

The elastic properties of the material were considered by a Young's modulus of $2.1 \cdot 10^5$ MPa and a Poisson's ratio of 0.3. Isotropic hardening was implemented in Abaqus by simply entering the true flow stress as a function of plastic strain in a tabular form. In other words, the flow properties are represented by means of true stress and plastic strain pairs. Besides the mentioned work hardening strain rate hardening and thermal softening was considered as well. Strain rate hardening can be included in the FE analysis by adding true stress versus plastic strain values at different plastic strain rates. Thermal effects can be considered by adding true stress and plastic strain pairs at different temperatures.

The axisymmetric standard round shaped tensile FEM model was built for two purposes. The first objective was to do a post necking investigation by reconstructing the experimental load/displacement curve. The intention to do post necking investigation is that irradiated Eurofer97 shows premature necking close to the yield stress. Therefore the flow properties could be directly determined only up to a small amount of plastic strain. In order to extend the range of flow properties extraction a FEM guided inverse approach was

used (see section 3.7.3). To simplify the problem neither strain-rate nor thermal effects were considered in the model.

The second objective was to analyze thermal effects at higher strain rates. A temperature increase can be observed when metal is deformed as most of the energy is dissipated as heat [156]. Depending on the deformation speed and localization, the temperature increase can be large and causes thermal softening. Usually this phenomenon is considered in metal forming processes [157] as well as in impact studies [158] where high strain rates are present. However, in literature it can be found that even at low strain rates ($\dot{\epsilon} = 10^{-3} \text{ s}^{-1}$) a considerable increase in temperature can be measured [159]. Therefore, a strain rate and temperature dependent model is in principle needed to account for the increase in temperature originating from the heat dissipated by plastic deformation. As the temperature distribution of the specimen depends on the stress/strain solution and vice versa, the thermal and mechanical solution has to be obtained simultaneously instead of sequentially. In Abaqus such an analysis was implemented using a fully coupled thermal-stress analysis. In order to consider both strain rate and thermal effects, the flow property input has to be modified as described above and extended by the material density ρ , the conductivity k , the specific heat c_p and the inelastic heat fraction η (see Table 3). The thermal properties were adopted to be constant over temperature and were taken from literature ([160] [161]).

Table 3: Material properties of Eurofer97 which were used as an input for Abaqus.

$\rho / \text{kg m}^{-3}$	$k / \text{W (mK)}^{-1}$	$c_p / \text{J (kgK)}^{-1}$	η
7887	28	400	0.9

η defines the amount of inelastic energy which is dissipated as heat. By default η is set to 0.9 but η may show a plastic strain dependence [162].

3.7.2 Non-standard disk tensile specimen FEM

As already mentioned in section 3.5.2, the constitutive behavior cannot be obtained straightforward from the non-standard DTS. This is due to the inhomogeneous stress and strain distribution within the gage length (see Figure 39). Plastic deformation initially takes place in the shoulders of the DTS followed by a strain concentration in the center of the gage length whereas for the standard tensile specimen a homogeneous deformation within the gage occurs.

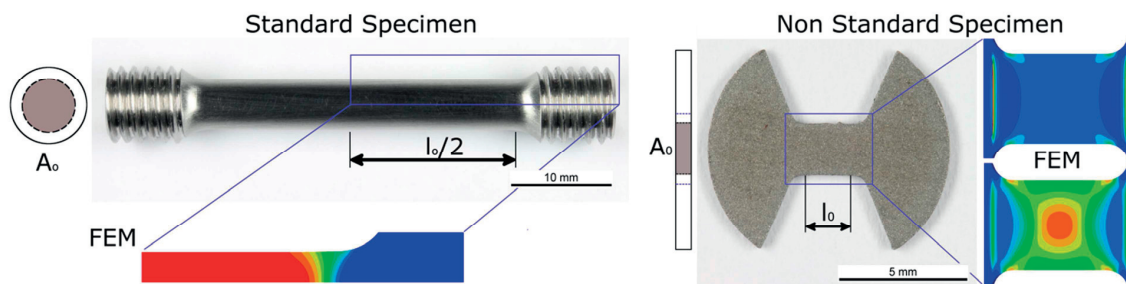


Figure 39: Illustrative comparison of plastic strain distribution within a standard round and a non-standard DT specimen at low loading level.

Neither the Young's modulus nor the flow properties up to necking can be obtained from the DTS experimental load/displacement curve in a straightforward procedure due to this inhomogeneity. To overcome this problem, one has to rely on modeling and apply a so called inverse approach. Therefore, a 3D FE model of the DTS was built that contains 52'892 linear hexahedral elements with reduced integration (type

C3D8R). Due to huge stress/strain gradients in the vicinity of the shoulders, it is essential that the mesh is refined there (see Figure 40). The boundary conditions are shown in Figure 40. Again a reference point is used to calculate the load/displacement curve in order to easily access and process the data with the inverse algorithm.

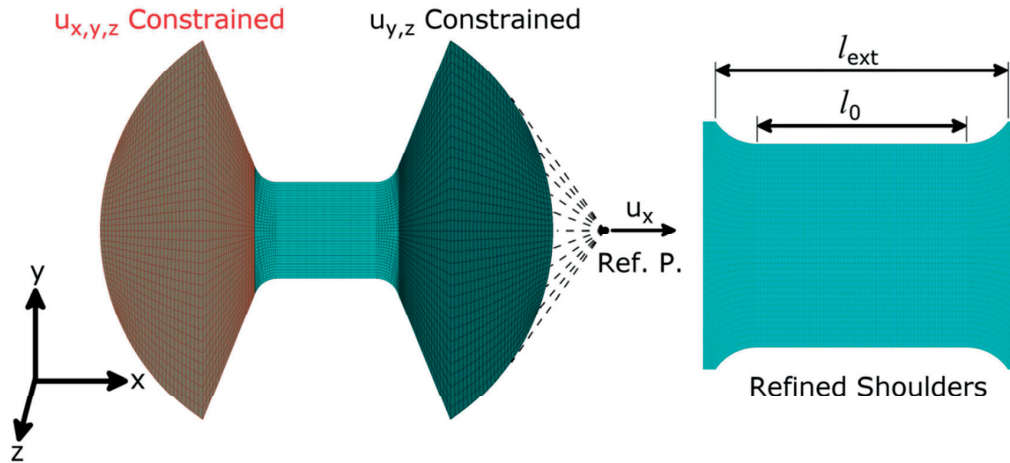


Figure 40: Left: 3D FE model of the non-standard DTS. Boundary conditions are indicated. Right: Refined mesh at gage section.

The DTS FE model simply considers isotropic work hardening, which is considered by true stress versus plastic strain values in tabular form.

3.7.3 Inverse approach

In conventional stress analysis studies, the material elastic and plastic properties are usually known and used as input parameters for FE simulations, along with others boundaries and initial conditions. The output consists of calculated stress and strain fields as well as reaction forces and/or displacements. An inverse approach uses the opposite direction to this conventional way, i.e., it determines the elastic and plastic properties of the material to use as input for the FE model to reconstruct the measured forces and displacements, e.g. [163] [164] [165] [166]. There are several options to implement an inverse approach. One can adjust the different parameters of a given constitutive equation to fit the measured material behavior, or one can reconstruct the constitutive equation in a piece-wise manner by connected small linear segments. Using an analytical expression has the advantage of low computational cost but requires the ability to describe the material by a functional law like Hollomon's or Ludwig's law. An analytical expression for the tempered martensitic was already proposed [167] but such laws are not always well established for technical alloys and are a priori not known for materials after irradiation. Therefore, the advantage of reconstructing the constitutive behavior by segments is that it is applicable to a large class of materials without doing any assumptions on the possible analytical expression of constitutive law.

The DTS FE model in combination with the experimental results is used to iteratively determine the elastic and plastic flow properties to reconstruct the experimental engineering stress/strain curve. If a good match is found the material properties are considered determined, but the accuracy depends significantly on the used implementation method. A piece-wise linear reconstruction of the material parameters was chosen due to the unknown irradiated plastic behavior. Initially the inverse piece-wise determination of the true

stress-strain curve was performed by considering three different regions of the load-displacement curve of the DTS deformations (see Figure 41):

- Region I: Elastic deformation.
- Region II: Plastic deformation up to maximum load and necking onset.
- Region III: Necking to failure.

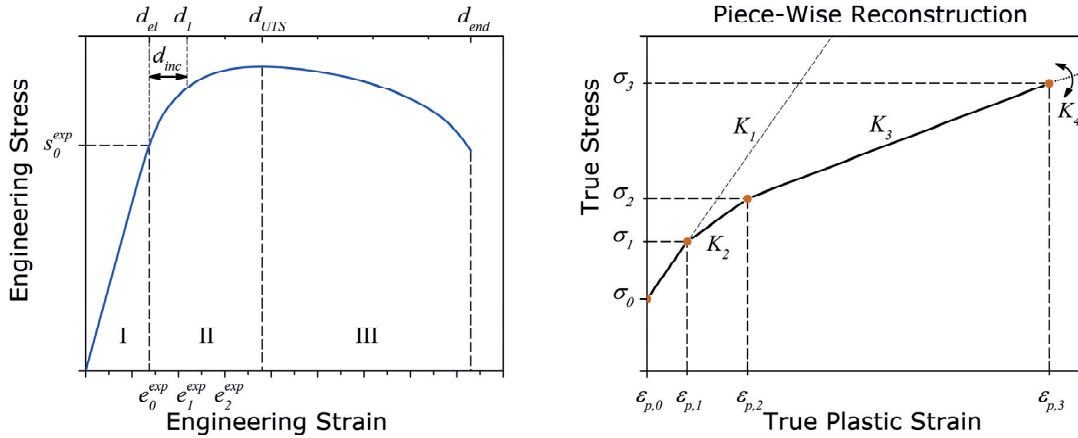


Figure 41: Left: Engineering stress/strain curve with the three regions indicated. Right: Piece-wise reconstruction of the material properties as (true stress, plastic strain) pairs.

For ABAQUS FE simulations, the elastic and plastic material properties have to be given as input. In the case of isotropic material like Eurofer97, the elastic properties are fully characterized by two elastic constants. In the region I, the Young's modulus was determined by fitting while the Poisson's ratio was taken as a constant. The plastic flow properties were inferred from region II and III, where extensive plasticity occurs. Note that the implementation of isotropic hardening in ABAQUS is simply given by the true flow stress as a function of plastic strain in a tabular form. In other words, the flow properties are represented by means of true stress and plastic strain pairs. To start the inverse algorithm, the following initial data are required:

- The experimental engineering stress/strain curve.
- An estimate of the Young's modulus E and proportional limit σ_0 .
- The ABAQUS input file describing the specimen with the boundary and loading conditions.

In the following, the engineering stress and strain are represented by s and e , and the true stress, true strain and plastic true strain by σ , ϵ and ϵ_p . The experimental and simulated engineering stress engineering strain are calculated by

$$\begin{aligned} s^{exp} &= \frac{P^{exp}}{A_0}, & e^{exp} &= \frac{d^{exp}}{l_0} \\ s^{sim} &= \frac{P^{sim}}{A_0}, & e^{sim} &= \frac{d^{sim}}{l_0} \end{aligned} \quad (18)$$

where P is the load, d the displacement, A_0 the initial specimen cross section and l_0 the initial gage length.

Region I: As mentioned above, for isotropic materials only two elastic constants are necessary to characterize the elastic properties completely. In this work, the Poisson's ratio ν was taken equal to 0.3, in agreement with the experimental determination on a similar tempered martensitic steel [161]. On the contrary, the elastic slope was determined with the inverse method. The experimental maximum elastic engineering stress e_0^{exp} is naturally defined at the point of the experimental curve where the linearity between s^{exp} and e^{exp} is lost (see Figure 41 left). This point is defined by the pair $(s_0^{\text{exp}}, e_0^{\text{exp}} = d_{\text{el}}/l_0)$. In an iterative manner, the region I of the $s^{\text{sim}}(e^{\text{sim}})$ curve is generated by adjusting the value of the Young's modulus until the following criterion is met:

$$\Delta s = (s_0^{\text{sim}} - s_0^{\text{exp}}) \leq \alpha \quad \text{at} \quad d_{\text{el}} \quad (19)$$

where s_0^{sim} corresponds to the simulated engineering stress at d_{el} and α determines the maximum allowable error. This procedure is schematically shown in the left part of Figure 42. The dots correspond to results from the simulation and the blue line to the experimental curve. First a too low elastic slope E_1 was chosen with results in a too flat response of the FE model giving an error of Δs_1 at d_{el} . Then elastic slope is increased until a too steep curve with an error of Δs_2 between the simulation and the experimental curve. This process is repeated until the error falls below the desired tolerance. An ideal case is shown in Figure 42 represented by the red dots. Thus, at the end of the fitting in region I, one has adjusted the Young's modulus to determine s_0^{sim} , which is finally converted to σ_0^{sim} .

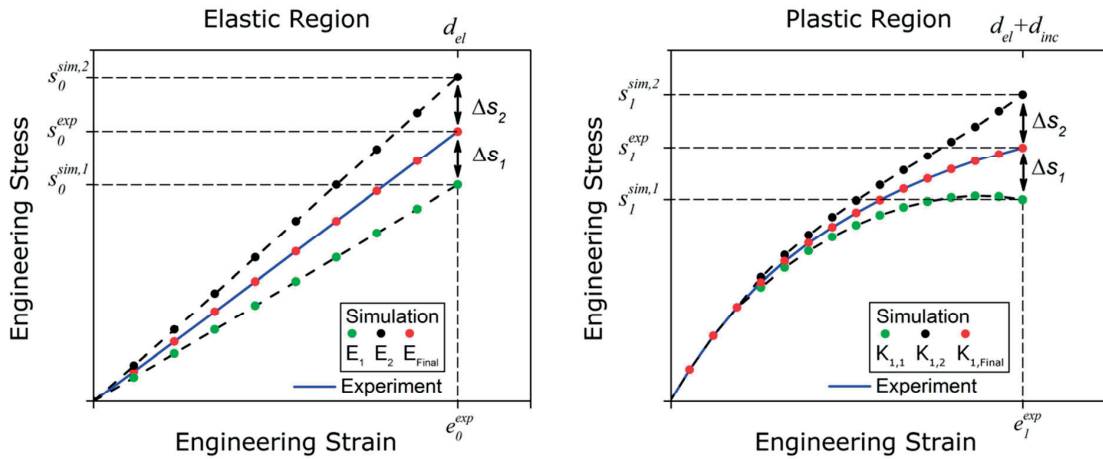


Figure 42: Schematic explanation of the inverse approach in the elastic and plastic region.

σ_0^{sim} corresponds to proportional limit but it is not the standard 0.2% offset yield strength. It is important to note here once more that a direct determination of the Young's modulus from the engineering stress/strain curve of the DTS specimen is not possible, because from the very beginning of the loading the stress state in the specimen is not homogenous and a significant amount of deformation takes place in the specimen shoulders. Hence the slope of linear loading represents only an apparent elastic modulus but not the Young's modulus.

Region II & III: The experimental engineering stress/strain curve is now divided into n small segments, each of them corresponds to a certain displacement increment d_{inc} in the load/displacement curve, which of course causes an increment of plastic deformation. For each increment, a corresponding pair of true stress/true plastic strain values can be determined. For the sake of clarity, one provides hereafter the details of the algorithm for the first increment. The FE model is updated by imposing a total displacement

such as $d=d_{el}+d_{inc}$, and by considering a constitutive behavior with a proportional limit equal to σ_0^{sim} followed by plastic behavior characterized by a linear strain hardening K_1 (see Figure 41 right). Similar as in Region I the slope of K_1 is adjusted until

$$\Delta s = (s_1^{sim} - s_1^{exp}) \leq \alpha \quad \text{at} \quad d_1 \quad (20)$$

is fulfilled. In the right of Figure 42 the optimization process is being sketched. If the linear slope is too flat the response of the FE model will be too soft (represented by the green dots). An increased slope of $K_{1,2}$ resulted into a too stiff response. The ideal case is represented by $K_{1,Final}$ shown by the red dots. Knowing K_1 is not enough at that point because we are essentially interested in the pair $(\sigma_1, \epsilon_{p,1})$. The true stress/true plastic strain is actually deduced from the FE model by calculating the average von Mises stress $\bar{\sigma}_i^{sim}$ and true plastic equivalent strain $\bar{\epsilon}_{p,i}^{sim}$ from the elements that contribute to deformation. To better illustrate and explain how the averaging elements are chosen, a deformation state of the gage section beyond necking is used (see Figure 43). In such a case the deformation gets highly localized and deformation takes place only in a confined volume.

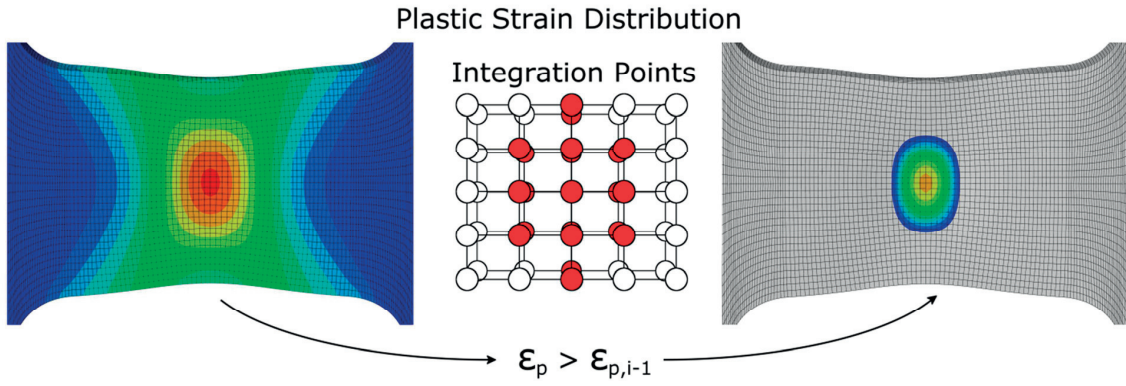


Figure 43: Plastic strain distribution within the extended gage length including an illustration of the confined deformation beyond onset of necking.

A similar effect is seen for the DTS at the onset of plastic deformation but not as pronounced as beyond the onset of necking. If equation (20) is fulfilled, a true stress/true plastic strain pair for the current incremental deformation can be extracted by only considering elements with deformation exceeding that of the previous increment $i-1$, as illustrated in Figure 43. In other words, one considers only the region of the specimen that contributes to deformation by simply checking the deformation state at the integration point. Those elements are then used to derive the average plastic equivalent strain $\bar{\epsilon}_{p,i}^{sim}$ and true stress $\bar{\sigma}_i^{sim}$ as

$$\begin{aligned} \bar{\epsilon}_{p,i}^{sim} &= \frac{\sum_{j=1}^N \epsilon_p^j (\epsilon_p^j > \epsilon_{p,i-1}) \cdot V^j (\epsilon_p^j > \epsilon_{p,i-1})}{\sum_{j=1}^N V^j (\epsilon_p^j > \epsilon_{p,i-1})} = \epsilon_{p,i} \\ \bar{\sigma}_i^{sim} &= \frac{\sum_{j=1}^N \sigma^j (\epsilon_p^j > \epsilon_{p,i-1}) \cdot V^j (\epsilon_p^j > \epsilon_{p,i-1})}{\sum_{j=1}^N V^j (\epsilon_p^j > \epsilon_{p,i-1})} = \sigma_i \end{aligned} \quad (21)$$

where V^j is the volume of element j and σ^j is the von Mises stress in the element. N denotes the number of nodes within the extended gage length l_{ext} (see Figure 40). The extension of the gage section includes the shoulders because a significant amount of deformation takes place there as well. As the mesh size is not constant within the extended gage length, the volume of the elements is used to weight and average the plastic equivalent strain and true stress. For the first increment in Region II, $\epsilon_{p,i-1}$ is equal to zero as desired from Abaqus.

In Region III, the same determination method is used with the only difference that the increment size can be increased significantly. After passing the ultimate tensile strength, the hardening curve does not show a strong gradient anymore. Therefore, the increment size can be increased to reduce the computational costs for reconstructing the flow properties without any drawback.

The implementation of the method consists of the finite element code ABAQUS to calculate the stress/strain and force/displacement fields in the specimen, and of the numerical computing environments MATLAB and FORTRAN. The MATLAB program is the main controlling program that assures the interface between ABAQUS and FORTRAN routine, which calculate the average stress and strain within the DTS extended gage length.

The final output of the inverse program yields the proportional limit σ_0 and the pairs of true stress/plastic strain in tabular form. It is well known that the elastic-plastic transition of martensitic steels is very smooth and gradual so that there is a relatively large difference between the proportional limit and yield strength, of the order of 100-150 MPa at room temperature. Therefore, it is important to develop an inverse method that permits to catch the details of the elastic-plastic transition. The quality of the reconstruction depends not only on σ_0 . Another parameter which affects the inverse result is the increment size d_{inc} . The larger d_{inc} , the fewer data points of the flow curve are obtained resulting in a coarse determination of the flow behavior. If an experimental engineering curve which should be reconstructed shows strong gradients, an insufficient number of true stress/strain points will result in a low-quality reconstruction. However, to keep the computational time reasonable while assuring a precise simulation, d_{inc} should be not chosen too small. For an optimum computational time and precise reconstruction, the increment size is not kept constant over the entire process. At higher gradients the incremental size is kept small but is increased at flatter parts of the curve. The development of this inverse method on unirradiated DTS is reported in [168] and slight adjustments for irradiated DTS in [169].

Before applying the above described technique to the irradiated and unirradiated material, a proof of concept was conducted with standard uniaxial tensile tests of \varnothing 5 mm round shaped specimen. The standard tensile tests were conducted at room temperature with a displacement rate of 0.05 mm/min. From the load/displacement curve, the flow properties up to necking can be readily calculated. However, the inverse technique was applied on the standard tensile results beyond necking (see Figure 45) to extend the flow property range.

The DTS results show a very good reproducibility, indicating that the developed gripping system was adequate (see section 3.5.2). Therefore the engineering curve from only one DTS test is shown in Figure 44 in comparison to the \varnothing 5 mm round shaped specimen result. As expected, the main difference between the tensile behavior between the DTS and the standard ones resides in the development of the neck. It is however clear that the engineering strain at failure of the standard specimens is much lower than that for the DTS.

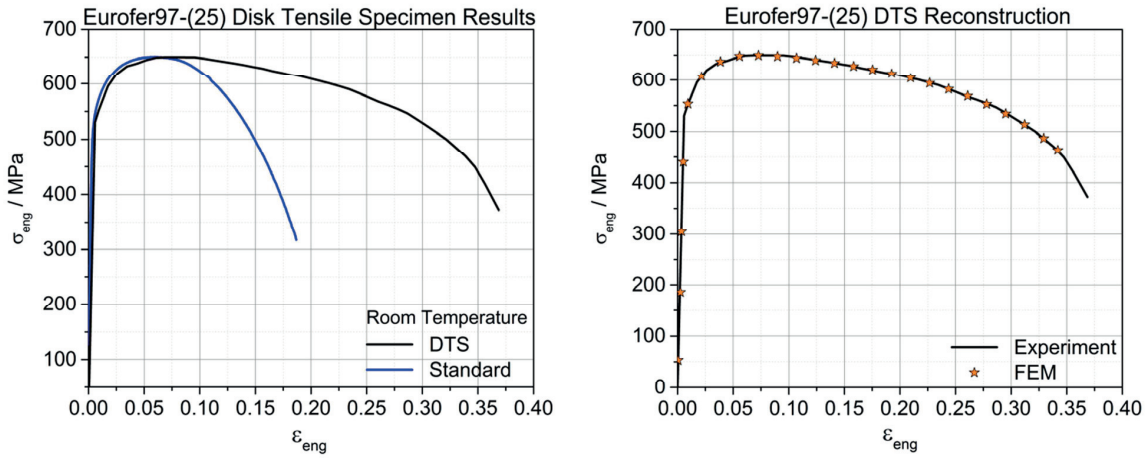


Figure 44: Left: Disk tensile specimen test in comparison with a standard \varnothing 5 mm round shaped tensile specimen. Right: Reconstructed experimental DTS curve.

The engineering strain at failure of the standard specimen is around 20%, in good agreement with published data [170], while it is slightly over 35% for the DTS. This observation is actually expected as it is well known that the total elongation is not a material property but depends on the specimen geometry: the shorter the specimen gage length the larger the relative contribution of the necking region to the total elongation [171]. Reconstruction of the experimental DTS curve using the inverse approach yielded in a good match in terms of engineering stress/strain (see Figure 44).

In Figure 45 the corresponding flow properties obtained by the inverse approach are shown. The increase in increment size appears in increasing spacing between the data points. At the transition of elastic to plastic deformation the increment is rather small whereas beyond necking the increment size increased in two orders of magnitude.

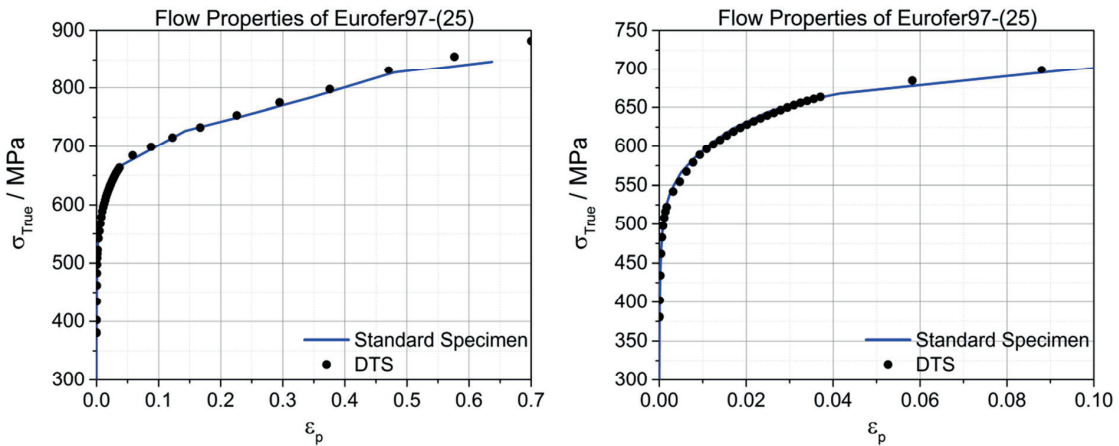


Figure 45: Flow property curves in terms of true stress/true plastic strain obtained by the inverse approach in comparison with the experimental data from a standard tensile test.

At the transition of elastic to plastic deformation the increment is rather small whereas beyond necking the increment size increased in two orders of magnitude. For the sake of comparison, we also plot in Figure 45 the true stress/strain curve obtained by the inverse method on the standard specimen. The inverse method

is clearly consistent, namely yielding the same $\sigma(\epsilon_p)$ curve for two tensile specimen geometries that exhibit very different necking behavior.

The mentioned inverse method was applied to the experimental DTS curves for the irradiated and unirradiated Eurofer97-(14). Note that it was also applied to obtain flow properties from the standard round shaped tensile tests in the post necking region. Therefore the above axisymmetric standard tensile FE model is used in the inverse algorithm. The experimental obtained flow properties from the standard tensile specimen were inserted in order to be able to skip Region I and II.

3.7.4 Fracture FEM

The local approach to fracture used in this work is based on the attainment of a critical stress σ^* within the critical volume V^* around the crack tip as a function of K . These values were determined through different FE models in 3D and 2D, which are described below.

3.7.4.1 3D Compact Tension FE Model

First, two 3D models of compact tension specimens of different size were developed. Taking advantage of the specimen symmetry, only one quarter of the CT specimen model was considered to minimize computational costs. The two models were built according to the dimensions of a 0.18T and 0.88T specimen (see Table 4). For the computations, a stationary deep crack was modelled with an initial root radius ρ_0 (see Figure 46 c)). For both CT sizes the root radius was equivalent to $0.1 \mu\text{m}$ which was necessary to obtain an accurate description of the near tip stress field at low loading. The crack length to specimen width ratio was chosen as $a/W=0.52$. In order to catch the strong stress and strain gradients just ahead of the crack tip as precise as possible, a fine mesh around the crack tip was used. It consists of two different element types, namely 20-node quadratic brick elements with reduced integration (C3D20R) in the domain around the crack tip (see Figure 46 b) and c)) and 8-node linear brick elements with reduced integration (C3D8R) at the remaining domain (see Figure 46 a)).

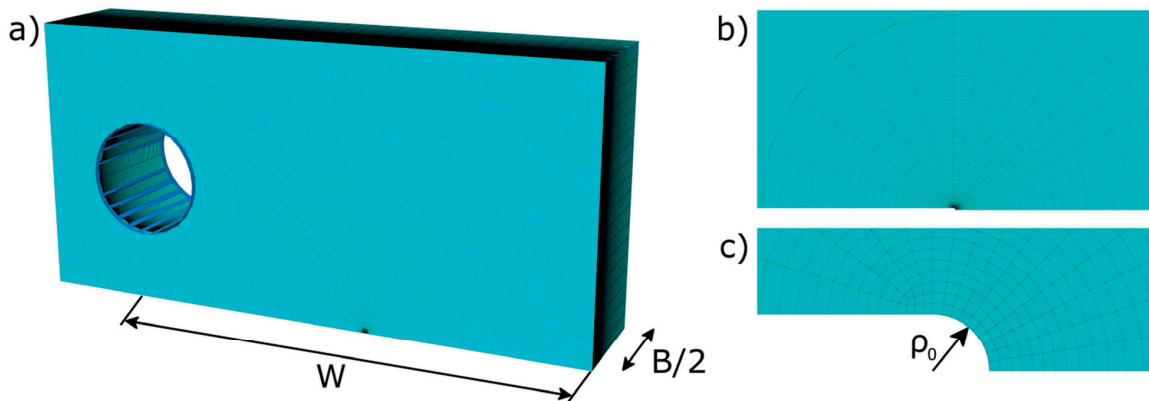


Figure 46: 3D FE CT mesh with details of the initial crack root.

A combination of these two elements is used, because the C3D20R elements showed a better resistance against mesh deformation than the C3D8R. Besides the better performance at higher loading the C3D20R elements do show a higher accuracy but demand higher computational cost. Therefore the major volume of the model consists of C3D8R elements. However, as the mesh around the crack tip has to be finer, the amount of elements does not differ so much. It emerged that a circular mesh around the crack tip with a slight increasing mesh size with the distance from the crack tip provides the best results in terms of accuracy.

cy and computational cost. The final amount of elements for both CT models is shown in Table 4 and obviously depends on the size of the model.

Table 4: Measure and amount of elements being used for the FEM model for 0.18T and 0.88T CT.

Model Size	Dimension		Elements	
	B / mm	W / mm	C3D8R	C3D20R
0.18T	4.5	9	170700	130650
0.88T	22.2	44.4	70320	140520

For the 0.88T model, the limit of the PC memory was reached with the settings mentioned above. Therefore no further refinement of the mesh was possible.

Loading of the C(T) specimen was implemented by an analytical rigid pin with a node to surface discretization method and normal interaction properties. A reference point on the rigid pin was used to extract the resulting reaction force F in the model versus the displacement D . The calculated stress intensity factor K was deduced from the calculated P-D curve using the standard equations given in the ASTM standard E1921-17a:

$$K = \sqrt{J \frac{E}{(1-\nu^2)}} \quad \text{with} \quad J = J_e + J_p = \frac{(1-\nu^2)}{E} \left[\frac{P}{B\sqrt{W}} f(a/W) \right]^2 + \frac{\eta A_p}{Bb} \quad (22)$$

where a is the crack length and b the ligament length.

The elastic properties of the material were considered by a Young's modulus of $2.1 \cdot 10^5$ MPa and a Poisson's ratio of 0.3. Isotropic hardening was implemented in Abaqus by simply entering the true flow stress as a function of plastic strain in a tabular form. Neither strain rate nor thermal effects were considered in the 3D models.

The main purpose of the 3D model was to determine the critical parameters for the local approach and provide reference values which can be compared to the simplified models. Due to the enormous computational costs of the 3D models, only static FE analysis was performed considering the flow properties at quasi-static condition. In order to obtain the critical parameter, it is necessary to extract the stressed volume V encompassed by a given maximum principal stress σ_I . A FORTRAN routine was used, which determines the nodes with a stress exceeding σ_I . Due to the non-uniform mesh size within the model the volume per elements differs significantly. In order to account for this, the stressed volume per element is weighted by the nodes exceeding σ_I divided by the total number of nodes of the element

3.7.4.2 2D Compact Tension FE Model

The first simplification in comparison to the 3D model was to build a 2D plane strain model of 0.18T CT in size. Obviously the symmetry of the specimen allows modeling the half of the specimen (see Figure 47 a)). A static crack was considered with a root radius equivalent to $0.1 \mu\text{m}$ and a crack length to specimen width ratio of $a/W=0.52$. As the computational costs for a 2D model are much lower in comparison to 3D, the mesh density around the crack tip was increased (see Figure 47 c)).

The model consist of 2040 4-node bilinear plane strain quadrilateral elements (CPE4R) and 43031 8-node biquadratic plane strain quadrilateral elements (CPE8R), both with reduced integration, as well as 39 3-node linear plane strain triangle elements (CPE3).

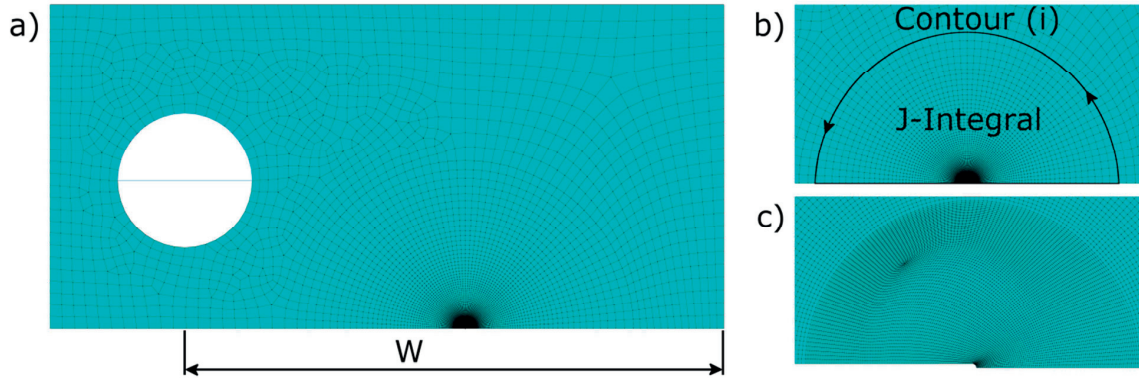


Figure 47: 2D FE CT mesh indicating the J-integral path and refined mesh at the crack tip.

Loading was applied through a rigid pin whereas a reference point on the rigid pin was used to extract the resulting reaction force F in the model versus the displacement D . A surface to surface discretization method and normal interaction properties were used between the pin and the specimen. The stress intensity factor K was calculated by the J-integral results obtained from Abaqus (see Figure 47 b)) and equation (22).

The 2D FE plane strain model allows analyzing strain rate and thermal effects during a CT test which may affect the critical parameters. However, first a static FE analysis was performed with the same flow properties as in 3D. The stressed area encompassed by a certain maximum principal stress σ_1 was determined with a FORTRAN algorithm following the same principal as for 3D. The volume is simply obtained by multiplying the obtained stressed area by the thickness of the CT specimen times two, as only the half of the specimen is modeled.

Similar to the standard round shaped FEM analysis thermal effects in combination with strain rate were analyzed. The implementation in Abaqus to address thermal effects was realized as described in section 3.7.1 with the material properties in Table 3. Two different loading scenarios were considered:

1. Quasi-Static: Even at quasi-static loading conditions one may has to consider strain rate effects as the crack tip shows a strong strain gradient.
2. Dynamic Loading: At higher loading rates the strain rate as well as thermal effects has to be considered in a FE model.

For both scenarios, an Abaqus FE model, which considers strain rate and a fully coupled thermal-stress analysis, was realized. Additionally, an adiabatic analysis was applied for the dynamic loading. Due to the high loading rate it may occurs that the dissipated heat has no time to transfer to the surroundings. Therefore the thermal conductivity is not considered in an adiabatic FE analysis.

3.7.4.3 Modified boundary layer model

The most simplified approach realized in this work were crack tip small scale yielding (SSY) conditions which were reproduced with the so-called boundary layer model (BLM) using a 2D full circular shaped plane strain FE model having a stationary crack with $p_0 = 0.1 \mu\text{m}$ (see Figure 48). The model contains 4142 quadratic quadrilateral elements with reduced integration (CPE8R).

A detailed description of the model can be found in [172]. Loading was applied by imposing displacements of the elastic Mode I singular field with a T-stress equal to zero at the nodes on the outer circular boundary.

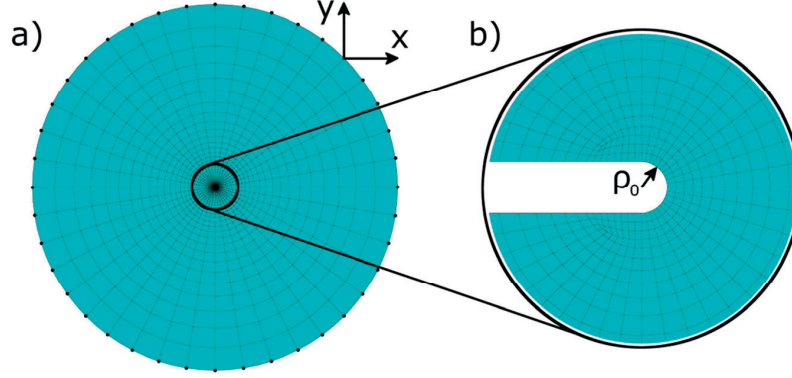


Figure 48: 2D FE SSY mesh indicating the nodes where boundary conditions were applied and details of the initial crack tip root.

The x and y displacements for each node (indicated in Figure 48) can be calculated by

$$\begin{aligned}\Delta x &= K \frac{1+\nu}{E} \sqrt{\frac{r}{2\pi}} \cos\left(\frac{\theta}{2}\right) (3-4\nu - \cos\theta) \\ \Delta y &= K \frac{1+\nu}{E} \sqrt{\frac{r}{2\pi}} \sin\left(\frac{\theta}{2}\right) (3-4\nu - \cos\theta)\end{aligned}\quad (23)$$

where r is the radial distance from the crack tip and θ is the angle between the crack plane and the node. The above relations hold for plastic regions R_p limited to a small fraction of the circular model radius R , typical $R_p < R/20$.

The SSY-mesh was employed to investigate the near crack tip stress/strain fields at much lower computational cost than the full 3D and 2D CT model. However, it was already shown that the stresses in the process zone calculated in SSY without a T-stress are somewhat different from those existing in a real specimen or component where non-zero T-stress is present. In particular, the positive T-stress of CT specimens [173] tends to elevate the crack tip stresses. In order to improve the stress/strain fields at the crack tip with the proposed SSY model the T-stress has to be taken into account. This can be simply implemented by

$$\begin{aligned}\Delta x &= K \frac{1+\nu}{E} \sqrt{\frac{r}{2\pi}} \cos\left(\frac{\theta}{2}\right) (3-4\nu - \cos\theta) + T \frac{1-\nu^2}{E} R \cos\theta \\ \Delta y &= K \frac{1+\nu}{E} \sqrt{\frac{r}{2\pi}} \sin\left(\frac{\theta}{2}\right) (3-4\nu - \cos\theta) - T \frac{\nu(1+\nu)}{E} R \sin\theta\end{aligned}\quad (24)$$

where T is the T-stress. In the present work the T-stress was evaluated using an approach proposed by Larson et al [174]. Therefore the stress/strain fields of the used specimen geometry have been calculated first. In this study the 2D 0.18 CT model is used. Additionally, a model being under SSY conditions without T-stress consideration has to be loaded to the same amount as the corresponding specimen. The T-stress for each specimen can be simply obtained by

$$T = \sigma_x(r, \pi)_{CT} - \sigma_x(r, \pi)_{SSY} \quad (25)$$

where $\sigma_x(r, \pi)$ can be determined from the two FEM results (see Figure 49). The described procedure can be applied to any crack geometry like bend bars, center and double edge-cracked specimens.

The SSY model approach in combination with equation (23) and (24) allows analyzing the impact of the T-stress onto the stress/strain fields at the crack tip. Therefore static FE analyses were performed with the same flow properties as in 3D and 2D CT. From the results it should be deduced if the SSY model approach can substitute the more complex 3D and 2D models.

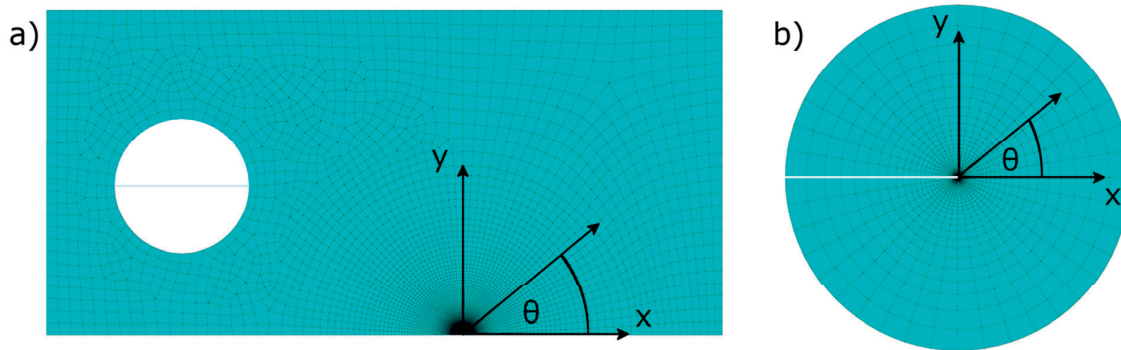


Figure 49: a) 2D CT model and b) Modified boundary layer model including coordinate system.

3.7.4.4 Disk Compact Tension FE Model

Also a 2D disk compact tension (DCT) FE plane strain model was built to analyze the obtained experimental results in more detail. The symmetry of the specimen allows to simply considering the half of the specimen (see Figure 33 a)). In accordance to the above mentioned fracture models the initial root radius was equivalent to $0.1 \mu\text{m}$ considering a stationary crack with a crack length to specimen width ratio of $a/W=0.52$ (see Figure 50 c)).

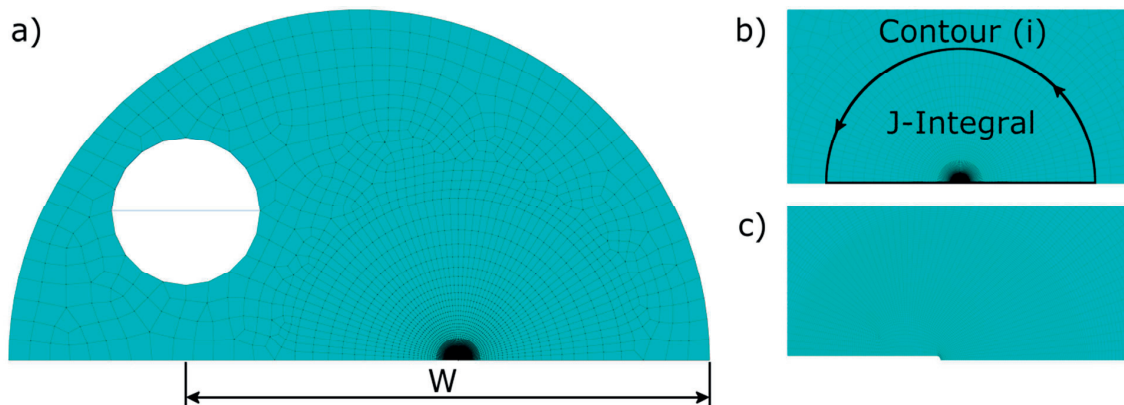


Figure 50: 2D FE DCT mesh indicating the J-integral path and refined mesh at the crack tip.

The model consist of 632 4-node bilinear plane strain quadrilateral elements (CPE4R) and 17951 8-node biquadratic plane strain quadrilateral elements (CPE8R) both types with reduced integration as well as 15 3-node linear plane strain triangle elements (CPE3).

Loading was applied through a rigid pin whereas a reference point on the rigid pin was used to extract the resulting reaction force F in the model versus the displacement D . A surface to surface discretization method and normal interaction properties were used between the pin and the specimen. The stress intensity factor K was calculated using the J-integral result obtained from Abaqus (see Figure 50 b)) and equation (22).

Main purpose of the model was to determine the critical parameters for the local approach to fracture for the Eurofer97-(14) heat. Therefore the unirradiated flow properties obtained from the DTS tests were used as an input in tabular form. Moreover the irradiated flow properties obtained from the DTS tests were used in combination with the model to give a T_0 prediction by applying the local approach parameters.

Chapter 4 Results

In this chapter, the experimental and simulation results are presented. First, the microstructural investigations are shown, followed by the experimental tensile and fracture test results. Fractographic observations of the tested tensile and fracture specimens are shown after the corresponding tests. Subsequently, the finite element modelling results are reported and compared with the experimental results.

4.1 Microstructure of Eurofer97-(14)

The microstructure of the Eurofer97-(14) base material was investigated using different SEM techniques and optical microscopy, including characterization of precipitates, and grain size determination. The above mentioned analyses were only applied to the unirradiated material. Concerning the Eurofer97-(25) base material the microstructure was characterized previously in the work of Bonadé [153] and Müller [154].

4.1.1 Grain size determination

Tempering of martensitic steels is needed to reduce the hardness and therefore the brittleness. In the as-quenched state, the microstructure consists of laths of martensite, which is supersaturated with carbon [175]. However, the size of the austenite grains prior to quenching in relation to mechanical properties is of great interest for metallurgist. In Figure 51, the grain boundary structure of Eurofer97-(14) after etching can be seen.

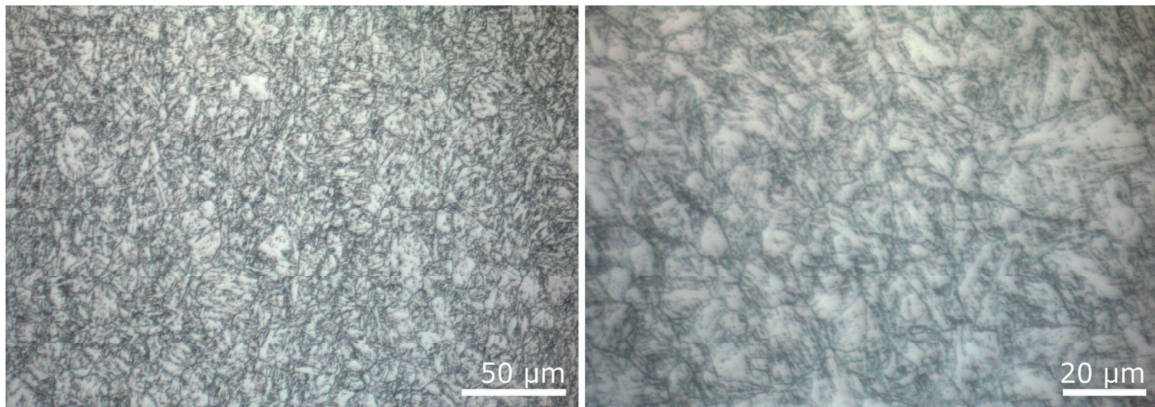


Figure 51: Optical microscope images from etched Eurofer97-(14).

From the optical micrographs, the grain size was determined according to the ASTM line interception method. Since PAG size may vary with the position within the plate, images were taken over the entire cross section of the plate. The average value from all measurements was then taken and is given in Table 5.

Table 5: Determined grain size number G and corresponding grain diameter d both according to ASTM 112-13.

Batch	G	d / μm
Eurofer97-(14)	9.51	13.36 ± 0.08

Compared to literature, the determined grain size is slightly bigger. Fernández observed a grain size for the same batch and 14 mm plate of 6.7 -11 μm [176]. The difference may arise from the fact that the grain size within a manufactured steel plate varies with the position in the plate. Also the etching may not resolve the PAG boundaries well leading to some uncertainty.

4.1.2 PAG, lath and sub-grain analysis

Prior austenite, packet, block and lath boundaries characterize the microstructure of reduced-activation ferritic/martensitic steels [177]. The microstructural investigations of the Eurofer97-(14) using SEM revealed the typical complex tempered martensitic structure (see Figure 52 and Figure 53). The EBSD results and in the SEM images obtained with the QBSD reveals the typical lath like structure. From the obtained EBSD map at lower magnification, it is not possible to identify properly the PAG boundaries by considering the misorientation between neighboring data points. No preferable microstructure orientation was found.

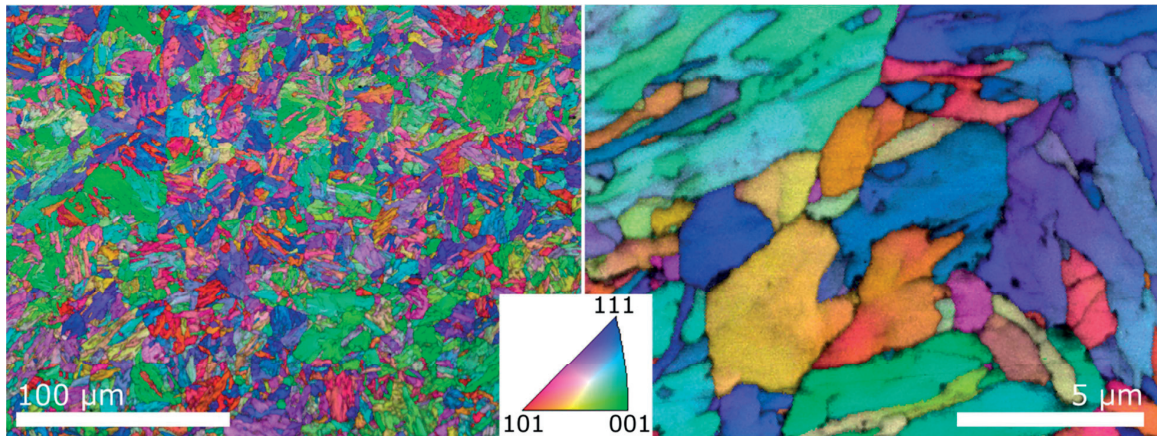


Figure 52: EBSD results of Eurofer97-(14). Left: Overview image of the martensitic structure. Right: Image at higher magnification showing the grain and sub-grain structure.

PAG boundaries and packet boundaries are indicated in the right upper image in Figure 53. Inside the PAG the above mentioned complex structure is found. The lath type structures originate from the as-quenched condition and their size ranges between 150 – 600 nm in width (see right lower image in Figure 53). Sub-grains, which form during the tempering process [178], were found in the lath type structure (see Figure 52 and lower two images in Figure 53). The size of the sub-grains ranged from few hundred nm to few μm in size. Similar results were obtained from EBSD records.

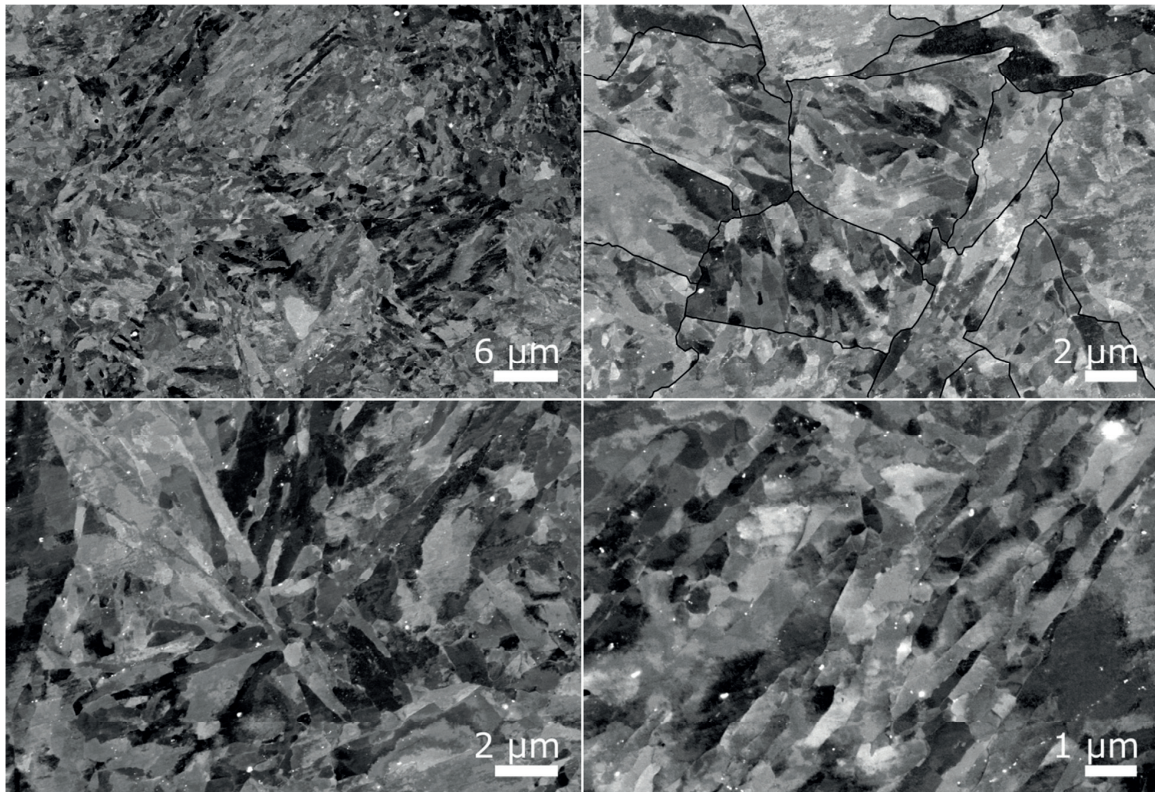


Figure 53: Microstructural investigation of Eurofer97-(14) using SEM. All images were taken using the QBSD. In the right upper image some PAG and packet boundaries are indicated.

4.1.3 Precipitates analysis

In order to analyze the precipitates in the unirradiated Eurofer97-(14), the specimens were electro-polished. This preparation method allowed a quick and easy investigation by SEM. In Figure 54, the typical distribution and size can be seen. The precipitates decorate the prior austenite grain boundaries (see Figure 54 upper two images). Medium and smaller sized precipitations can be found inside the PAG at the sub-grain boundaries. The smallest detectable precipitates with the SEM were about 10-20 nm in size whereas the biggest ones ranged up to 970 nm (see Figure 55 and Figure 57).

It has to be pointed out that the largest particles do have an elongated needle like shape. Other shapes of particles were circular and rectangular in almost any size in the above mentioned range. In Figure 55, an overview of the different precipitates that were found in Eurofer9-(14) can be seen. Beside the bright iron matrix, the particles appear in different darker contrast, associated with a higher atomic number Z . A few particles were found having a sharp transition of contrast within the grain (see arrow in lower mid image in Figure 55). Some of the precipitations are entirely black indicating an even higher Z . These particles appear in a roundish shape in sizes ranging from as small as 10-20 nm to the mentioned 970 nm and are randomly distributed. The black contrast indicates that those precipitations are most probably W or Ta rich particles (see alloying elements in Table 1). Concerning the particles located at the grain boundaries, several alloying elements are possible as the contrast appears similar.

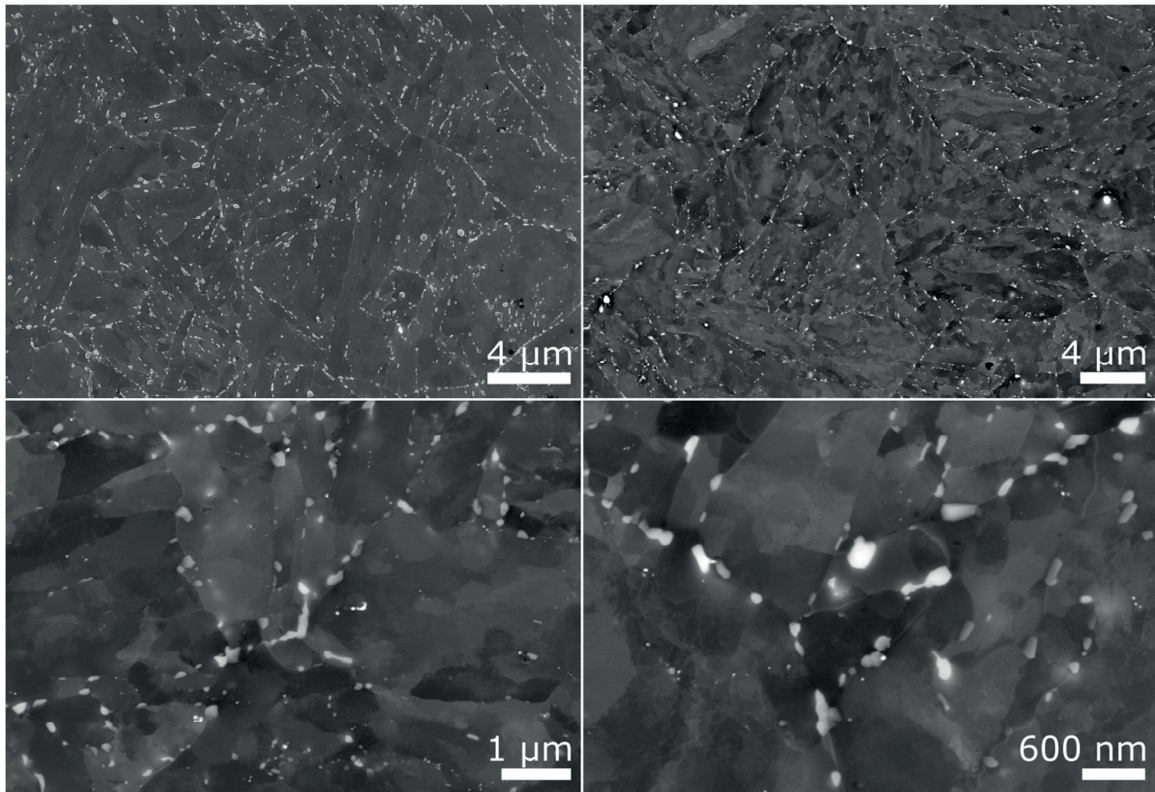


Figure 54: Analytical investigation of precipitates in Eurofer97-(14) using SEM. Left upper image was taken with an In-lens detector and others with the QBSD.

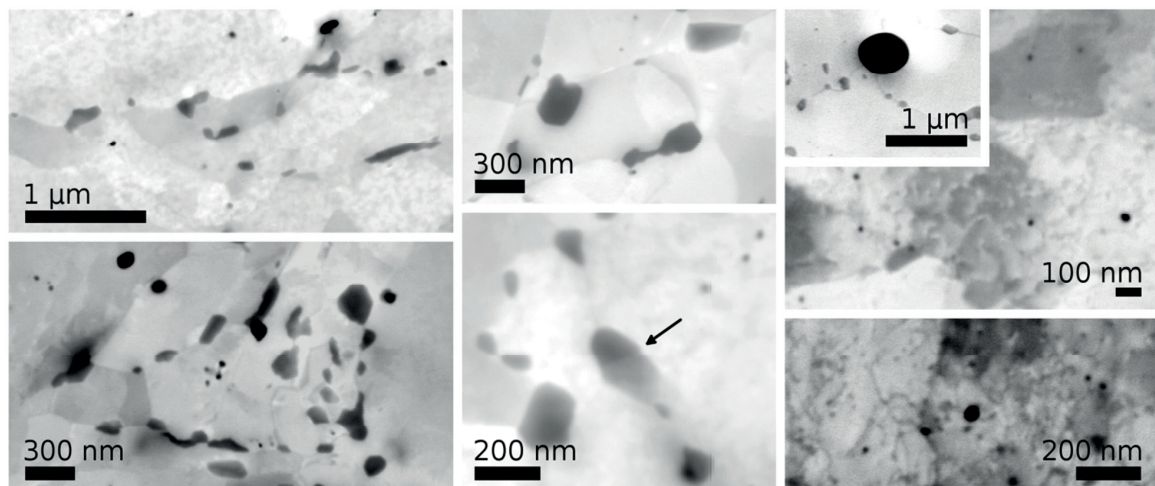


Figure 55: Various precipitations investigated in Eurofer97-(14) using SEM. All images show the inverted recorded contrast.

Therefore the precipitates were further analyzed by EDX spectroscopy. It was found that the majorities of the precipitates are Cr-rich and located at the PAG boundaries. In Figure 56, an EDX-mapping of two Cr rich particles can be found. Besides Cr, the particles consist of carbon and tungsten and are Fe depleted. Another result which can be concluded from the EDX map is the limit of the investigation method. The larger the particles are, the better the signal of the detected elements. The size dependence originates from the fact that the SEM EDX analysis is limited among others by the interaction volume. At higher accelerating volt-

age, the interaction volume is bigger. However, by reducing the voltage the interaction volume reduces as well but with the drawback that elements with higher electron binding energy will show fewer or non-ionization events.

Another EDX mapping was applied to an almost spherical Ta-rich particle of 460 nm in size (see Figure 56 right). The elemental maps show besides Ta, Ti and C and a depletion in Fe. The particle is surrounded by some Cr particles which are close to the detection limit using this technique and mentioned parameters. Therefore mostly noise is detected besides one or two spots where Cr particles are big enough. Most of the time, the Ta-rich particles appear in a spherical shape but can occur in different shapes as well.

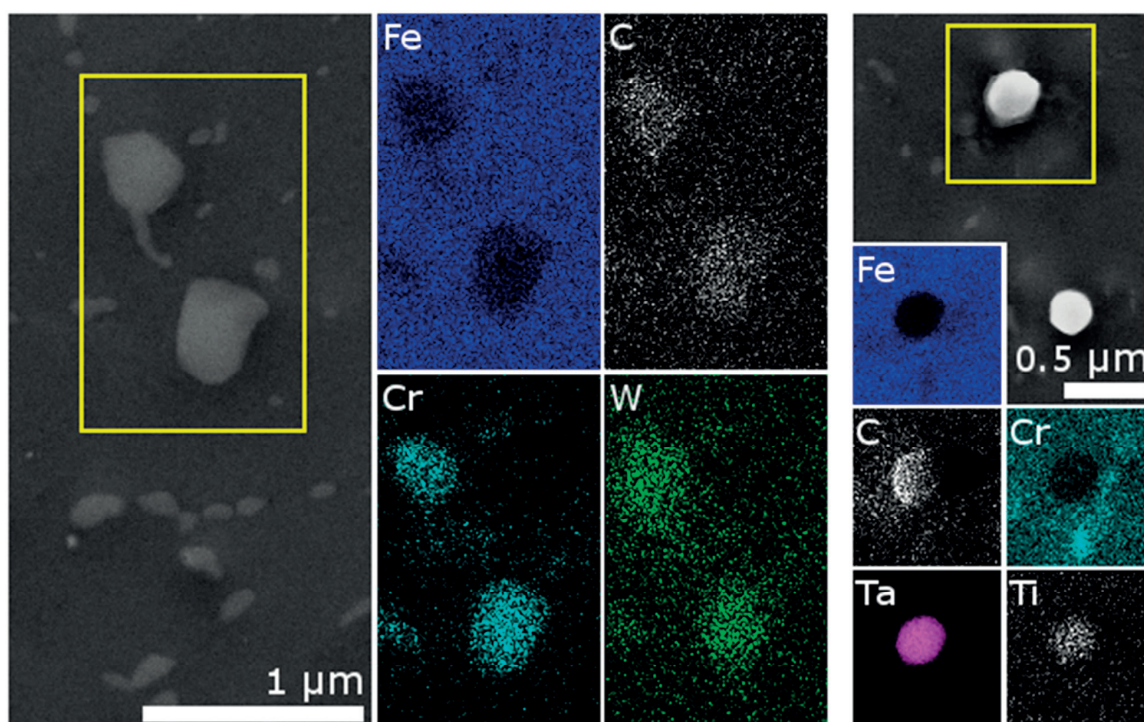


Figure 56: SEM EDX analysis of precipitations. Left: EDX-mapping of two Cr rich particles. Right: EDX-mapping of a tantalum rich particle.

Point EDX analyses were also applied to several precipitates in order to determine all elements present. From the Ta-rich particles C and Ti were found in the EDX mapping analysis. However, in the spectrum a low amount of V was detected as well. From literature it is known that Ti forms complex particles which also contain V and Ta [179]. In Figure 57, the result of a point EDX spectrum of a bigger Ta particle is shown.

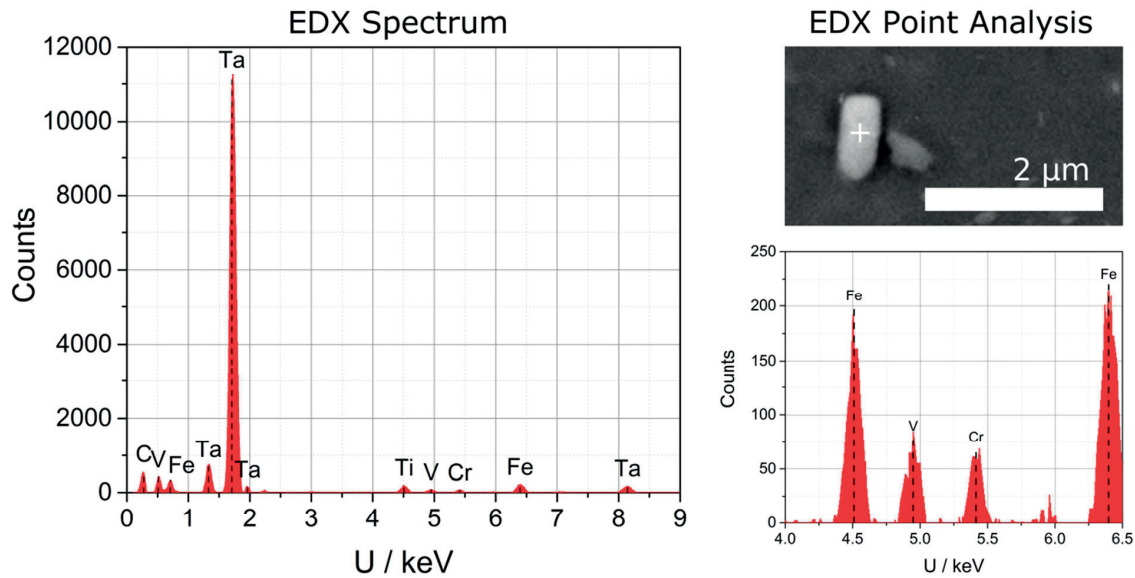


Figure 57: EDX point spectrum of a Ta rich particle. Vanadium peak is magnified in the lower right spectrum.

Besides Ta, Ti can be found but a small amount of V is also present (see inset in Figure 57). In order to determine the elemental distribution within such a complex precipitate, TEM EDX analysis would be required. Nevertheless, the presence of Ti and V suggests that a complex TiN-VN-TaC precipitate was detected. Even though the analyzed Ta particle is rather big, a low signal of the Fe matrix as well as from a neighboring Cr particle can be recognized but at a very low signal to noise ratio.

Also several Cr-rich particles were analyzed in more detail using point EDX spectroscopy. The spectrum for a larger Cr-rich particle can be seen in Figure 58.

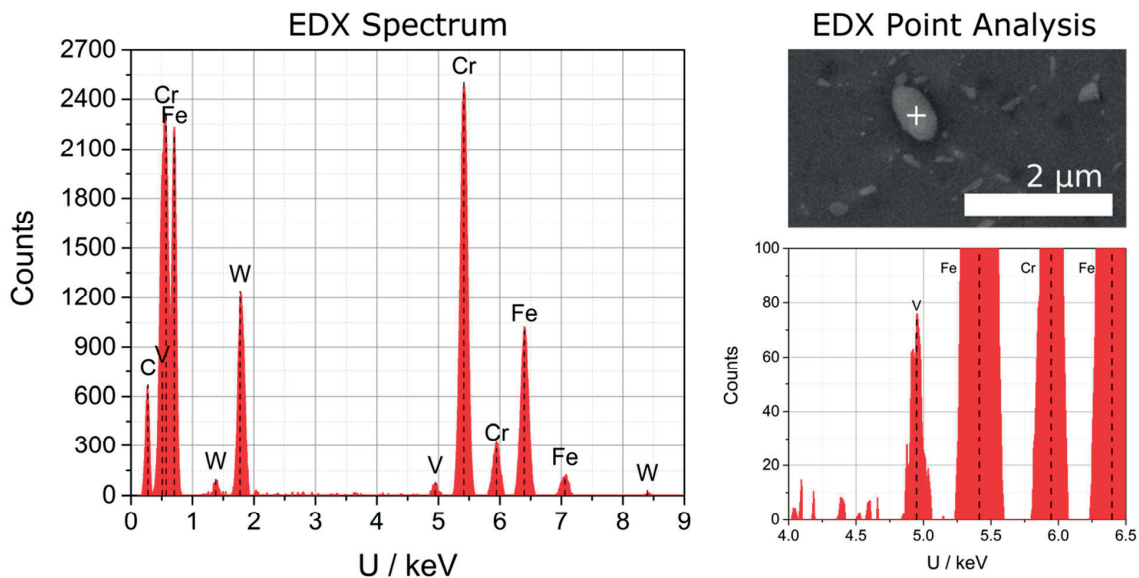


Figure 58: EDX point spectrum of a Cr rich particle. Vanadium peak is magnified in the lower right spectrum.

In accordance to the EDX mapping results, W was found in the particle as well. Again the analysis revealed a small amount of V present in the analyzed particle. However, several other Cr-rich particles did not show

any V. In literature it was reported that Cr carbides may precipitate around VN precipitates, which are also preferentially located at grain boundaries [179]. The proper spatial location could not be determined as the SEM EDX analysis simply approaches the limit. Nonetheless, it can be said that V is present at the investigated Cr rich particle. $M_{23}C_6$ type precipitations which contain W and V were also found in [179] and [180]. In the work of [179] it was found that the boundaries which were free of VN precipitates were also free of $M_{23}C_6$.

4.2 Tensile properties of Eurofer97-(25)

Two different sizes of round shaped tensile specimen of Eurofer97-(25) were tested to determine the flow properties versus temperature and strain rate.

4.2.1 Ø 5 mm tensile specimen tests

Tensile tests with the Ø 5 mm round shaped specimen were carried out at three different displacement rates, namely 0.05, 0.5 and 5 mm/min at temperatures ranging from -196 to 200 °C. The resulting 18 tensile curves are shown as engineering stress/true strain in Figure 59. Most specimens were tested up to failure as indicated with a vertical dashed line. Every uniaxial tensile tests at room temperature, the 0.5 mm/min test at -100 °C, and the 0.05 and 0.5 mm/min tests at 200 °C were realized using a clip-on extensometer. Those tests were therefore interrupted after passing the UTS followed by unloading. The nominal engineering strain rates corresponding to the applied displacement rates are shown in Table 6.

Table 6: Applied displacement rates and corresponding engineering strain rates.

\dot{d} / (mm/min)	0.05	0.5	5
$\dot{\epsilon}$ / s ⁻¹	$2.8 \cdot 10^{-5}$	$2.8 \cdot 10^{-4}$	$2.8 \cdot 10^{-3}$

A strong temperature and strain rate dependence of Eurofer97 can be recognized. From room temperature down to -196 °C, the yield stress increase is about 500 MPa. At -196 °C, the strain rate hardening effect between the different displacement rates is manifested by a an upper shift of the curves. However, test being conducted at higher temperatures do show a different behavior, for instance the test series at -150 °C. Initially, the strain rate hardening effect is observed but, with increasing strain, the amplitude decreases. Actually the two curves at $2.8 \cdot 10^{-3} \text{ s}^{-1}$ and $2.8 \cdot 10^{-4} \text{ s}^{-1}$ get closer to each other and merge at around 8 % of strain (see right in Figure 60). Similar results were found at higher temperatures. This phenomenon is likely to be the consequence of thermal softening due to dissipation of the plastic work into heat.

This assumption was confirmed by measuring the specimen temperature with a thermocouple attached to the gage length. At the test at -150 °C with a strain rate of $2.8 \cdot 10^{-3} \text{ s}^{-1}$, a temperature increase of about 20 °C during the test was measured. Even though measuring the temperature distribution in the tensile specimens with a thermocouple on the surface is not suitable to detect fast and locally confined temperature increase properly, the result remains a good indication of possible thermal softening. At higher temperatures and other strain rates, where the heat released in the specimen has more time to diffuse out, the measured increase in temperature was not so pronounced. This behavior was studied in more detail using a FEM model with consideration of temperature variation induced from plasticity and is presented in section 4.5.2.

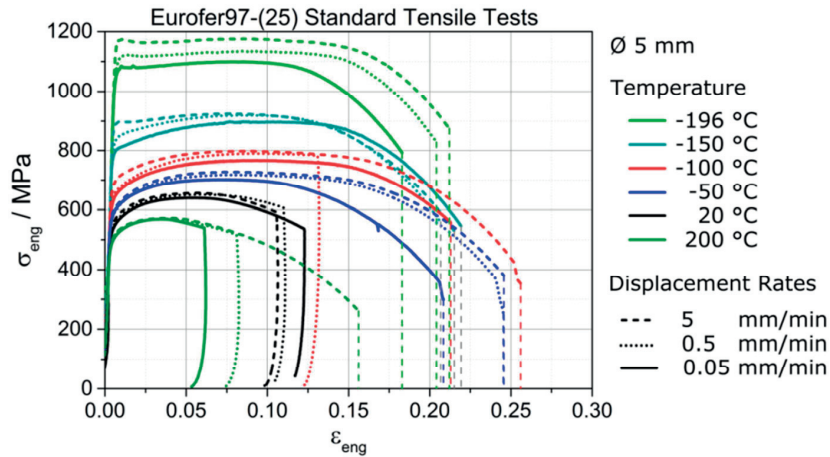


Figure 59: Tensile curves of Eurofer97-(25) at different temperatures and displacement rates conducted with the standard \varnothing 5 mm round shaped specimens.

Another feature in the tensile results can be found at the tests conducted at -150 °C and lower (see Figure 60). At low true plastic strains just beyond the yield point, the curves show a small region where the engineering stress remains almost constant. It is more pronounced at higher strain rates and can even be found at -150 °C.

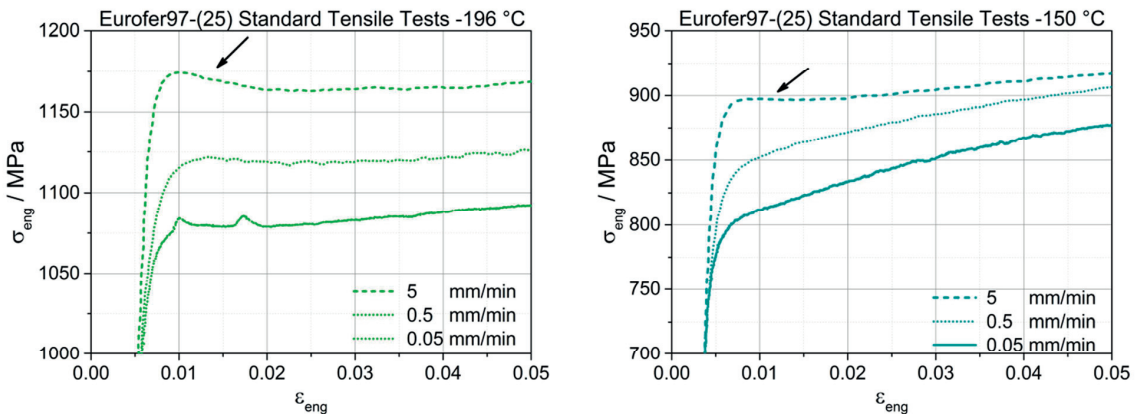


Figure 60: Tensile curves of Eurofer97-(25) at -196 and -150 °C. Deformation at almost constant stress is indicated.

For the highest strain rate at the lowest temperature even a short drop in stress can be observed whereas at an engineering strain of 4 % the stress increases again. This phenomenon was already reported in previous investigations as well [181]. However, the physical reason for this behavior remains unclear.

4.2.2 \varnothing 3 mm tensile specimen tests

The impact of strain rate on the flow properties of Eurofer97-(25) was also investigated with tensile tests carried out with \varnothing 3 mm specimens. The idea was to increase the specimen surface to volume ratio in comparison with the \varnothing 5 mm specimens, to minimize the thermal softening effect. Specimens were loaded at different displacement rates, namely 0.1, 1 and 10 mm/min. At each temperature, three tests were performed whereas for one test strain rate jumps were applied. To do so, the displacement rate is periodically varied between two values and was applied at -50 , -100 and -150 °C between a displacement rate of 0.1 and 1 mm/min. The temperature range was chosen in accordance to the \varnothing 5 mm tensile tests where the strain rate effect on the tensile properties was the most pronounced. In Figure 61 the obtained tensile

curves in terms of true stress/strain can be seen. Similarly to the $\varnothing 5$ mm specimens, a strain rate effect on the tensile curves can be observed. All uniaxial tensile tests were conducted up to failure which is indicated in Figure 61 with a vertical dashed line. The engineering strain rates corresponding to the applied displacement rates are shown in Table 7.

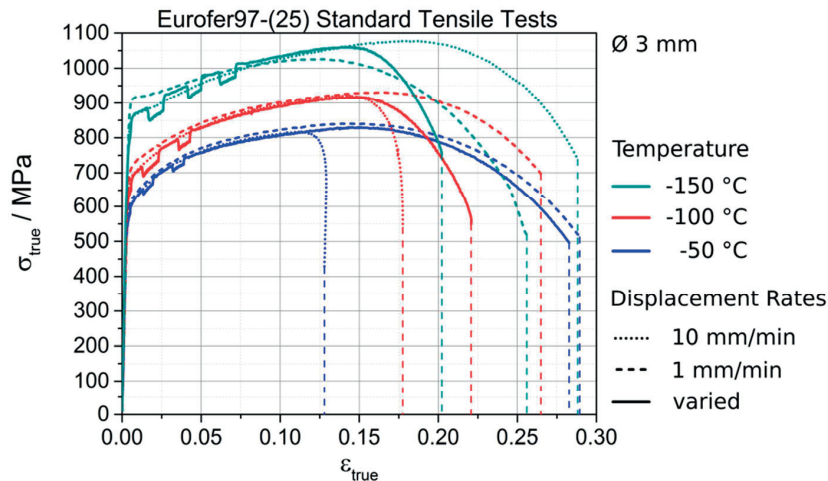


Figure 61: Tensile curves of Eurofer97-(25) at different temperatures and displacement rates performed with the standard $\varnothing 3$ mm round shaped specimen.

Table 7: Applied displacement rates and corresponding engineering strain rates.

$\dot{d} / (\text{mm/min})$	0.1	1	10
$\dot{\epsilon} / \text{s}^{-1}$	$9.3 \cdot 10^{-5}$	$9.3 \cdot 10^{-4}$	$9.3 \cdot 10^{-3}$

In Figure 62 the range where strain rate jumps were applied is enlarged. It can be seen that for -50 and -100 °C the strain rate change from 0.1 to 1 mm/min superimposes almost immediately with the curve obtained at a constant displacement rate of 1 mm/min. However, at -150 °C the flow stress right after the strain rate jump is higher than that obtained at constant rate, only close to yielding the two curves overlap after the strain rate jump. This flow stress difference is likely to arise from thermal softening occurring in the high strain rate tests at constant velocity, where the temperature rises due to dissipation of plastic work into heat. For the tensile curve at -150 °C with 10 mm/min, a similar trend is observed. Shortly after yielding the stress difference is well marked but reduces constantly with increasing strain. The same behavior was found for the $\varnothing 5$ mm tensile results.

However, this effect reduces with increasing temperature and cannot be seen anymore at -50 °C. In order to reduce the effect of thermal softening, the shift in stress associated with strain rate was determined at lower true strains. In other words, the shift caused at $9.3 \cdot 10^{-3} \text{ s}^{-1}$ was simply measured close to the onset of plastic deformation. The resulting measured shifts were about constant in the tested range of $9.3 \cdot 10^{-5}$ - $9.3 \cdot 10^{-3} \text{ s}^{-1}$ at each temperature which is indicated in Figure 62 as arrows with the same length. In Table 8 the shift in stress $\Delta\sigma_{\text{true}}$ at -50, -100 and -150 °C is shown.

From the obtained results a trend of decreasing $\Delta\sigma_{\text{true}}$ with increasing temperature was found which is shown in the right diagram in Figure 62. However at temperatures above -50 °C the effect of strain rate hardening was not determined as the measurable shift is vanishing in the standard deviation of a tensile test. Also the standard $\varnothing 5$ mm round shaped specimen results did not show a clear strain rate effect at

temperatures > -50 °C. Therefore, it is assumed that the strain rate effect at temperatures > -50 °C is not pronounced and can be neglected.

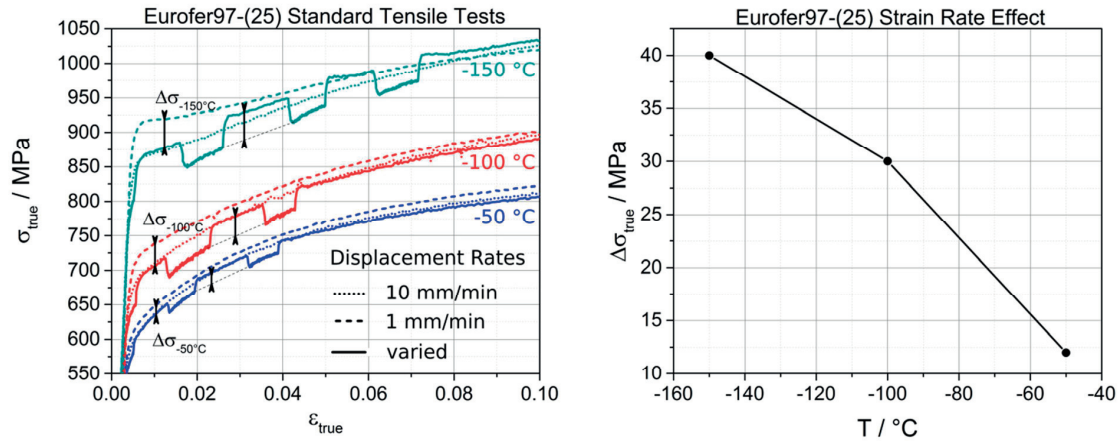


Figure 62: Strain rate analysis of Eurofer97-(25). Left: Tensile curves at different temperatures and displacement rates. Right: Determined shift in stress caused by an increase in strain rate by factor 10 at different temperatures.

Table 8: Determined shift in stress due to a change in strain rate of factor 10 for Eurofer97-(25).

T / °C	$\dot{\epsilon}_1 / \dot{\epsilon}_2$	$\Delta\sigma_{true}$ / MPa
-150	10	40
-100	10	30
-50	10	12

The determined strain rate sensitivity of the true stress (Table 8) will be applied in the FEM analysis in section 4.5.2 and 4.5.4.

4.3 Tensile properties of Eurofer97-(14)

Unirradiated and irradiated disk tensile specimens (DTS) of Eurofer97-(14) were tested at temperatures ranging from -137 to 370 °C. The irradiation impact on the yield stress and on the true stress/strain relationship obtained with the developed inverse method is reported. The necking shapes of the tested specimens as well as the fracture surface at -100 and 200 °C were studied to identify possible irradiation effects.

4.3.1 DTS tensile tests results

For both irradiated and unirradiated DTS, a displacement rate of 4 mm/h was applied, which corresponds to a loading nominal strain rate of $5.56 \cdot 10^{-4} \text{ s}^{-1}$. Due to the limited volume in the irradiation rod, only five irradiated specimen were tested whereas nine tests were conducted for the unirradiated ones. Figure 63 shows the tensile curves for the unirradiated Eurofer97-(14) as well as the irradiated curves in terms of engineering stress/strain.

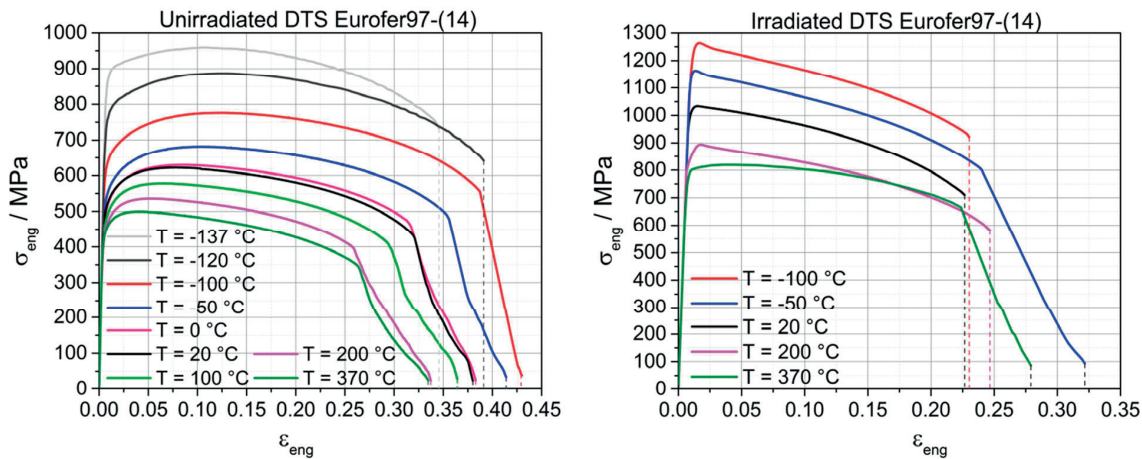


Figure 63: Non-standard DTS tensile curves of the Eurofer97-(14) at different temperature. Left: Unirradiated Right: Irradiated.

The irradiation induces profound changes of the shape of the tensile curves. In the unirradiated case, a gradual transition between elastic and plastic deformation can be found with significant uniform elongation. The tensile curves of the irradiated specimens conducted between -100 and 200 °C are characterized by a premature necking that occurs just beyond the yield point followed by a continuous decrease of engineering stress (or load). At 370 °C, the tensile behavior of the irradiated specimen is somewhat different from the other specimens. In this case, the tensile curve presents a low strain-hardening rate, which persists up to several percent of engineering strain.

For the tests performed on unirradiated specimens from -100 °C up to 370 °C, the failure of the specimens, regarded as the total separation of the specimen in two parts, occurs over a range of strain that follows the sudden load drop characterized by an abrupt slope change of the tensile curve towards the end of the test. This behavior arises from the fact that the specimens fail only partly at this point but a remaining ligament still holds the two specimens halves together, which continue to plastically deform. At lower testing temperatures, i.e. -120 °C and -137 °C, the unirradiated DTS failed at high stress in a total macroscopic brittle manner as indicated by a vertical dashed line (see Figure 63 left). A similar result was found for the irradiated DTS. However, there was not such a clear trend of this phenomenon versus temperature. From five conducted active tests, only two show such a behavior.

A well-marked temperature dependence of the yield stress at 0.2% of plastic strain below room temperature is observed for both unirradiated and irradiated Eurofer97, which is characteristic of BCC metals and alloys. However, at higher temperatures the decrease in yield stress with temperature becomes weaker. The yield stresses for the irradiated and the unirradiated DTS results are compared in Figure 64 at 0.2 and 1% of plastic strain. Due to the flow behavior of the irradiated Eurofer97-(14) right after yielding the yield stress was determined at 0.2 and 1% of plastic strain. However, the trend as well as difference between unirradiated and irradiated yield stress is unaffected.

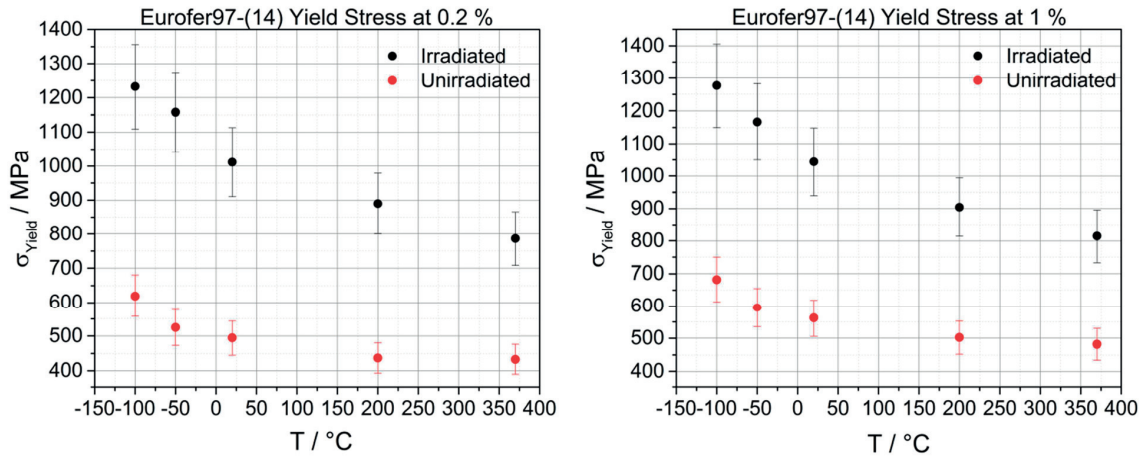


Figure 64: Yields stress at 0.2 % and 1 % of plastic strain for the irradiated and unirradiated Eurofer97-(14).

Significant irradiation-hardening was determined as can be seen in Figure 65. The irradiation increased the yield stress about two times. From the left diagram in Figure 65, a temperature dependence of the irradiation hardening was found that cannot be explained by the temperature dependence of the elastic constant (see right Figure 65).

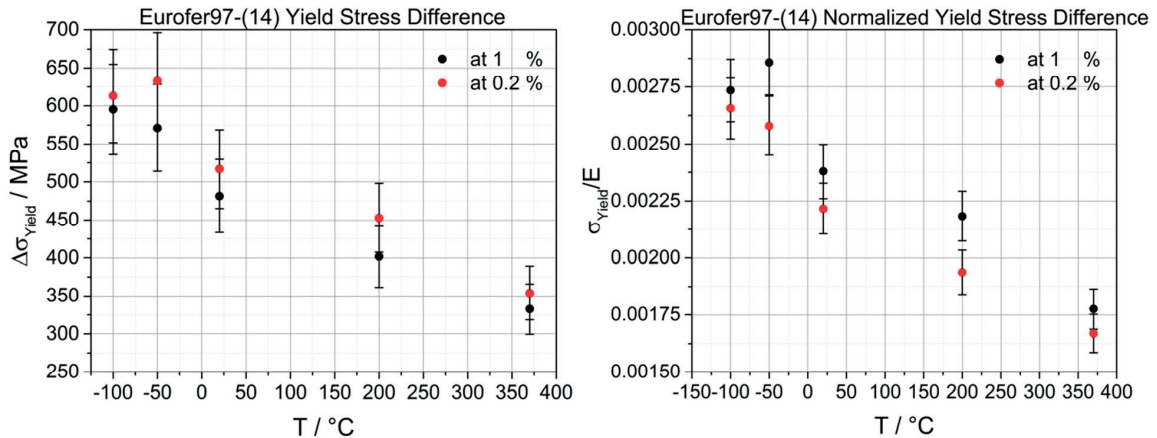


Figure 65: Yield stress difference between unirradiated and irradiated at 0.2 and 1 % of plastic strain.

Due to the above described phenomenon of partial failure, the fracture strain and stress of the DTS were chosen as those at the abrupt slope change of the tensile curve. In the following, the analysis of the stress/strain state using the FE modeling at failure was done at the fracture stress/strains as defined above. In Figure 66 the failure strains and stresses for the irradiated and unirradiated Eurofer97-(14) are shown.

Regarding the fracture strain of the unirradiated DTS, a strong decrease with increasing temperature can be seen reaching a plateau about $\epsilon_f=0.26$ at 200°C. There is no such clear trend for the irradiated DTS. The fracture strain varies in between 0.22 and 0.25 over the entire temperature range and shows always a lower value than the unirradiated.

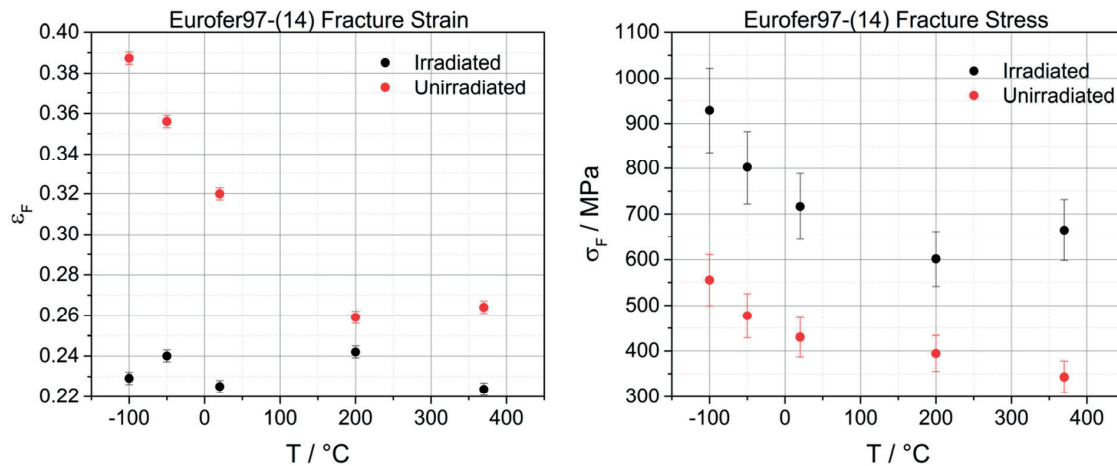


Figure 66: Engineering failure strain and stress for the irradiated and unirradiated Eurofer97-(14) DTS.

Concerning the fracture stress, a similar behavior as for the yield stress can be found. The irradiated fracture stress (engineering stress) is higher than that of the unirradiated specimens.

4.3.2 Optical microscopy and fractography

In order to analyze possible effects of irradiation on the failure mode of the DTS, specimens were investigated by optical microscope to identify the necking shape. Scanning electron microscopy was used to investigate the overall pattern of fracture as well as characteristic features.

4.3.2.1 Optical microscopy

The necking behavior was characterized by optical microscopy of both the unirradiated and irradiated specimens at each testing temperature. Top view images of the gage section of the tested DTS are presented in Figure 67. All the unirradiated DTS exhibit a diffuse necking behavior and failed at a fracture plane normal to the loading axis. From the curved shape of the fracture surfaces, it appears that fracture initiated in the middle of the specimens and propagated towards the edges of the gage section, analogous to cup-cone fracture in round tensile specimens.

Qualitatively, the shape of the necked region of the irradiated specimens is similar to those in the unirradiated condition, except that the specimens tested at 20 °C and 200 °C show a more localized necking, with fracture inclined with respect to the loading axis. At -50 °C, a slight inclination of the fracture plane is also observed. It is well known that for sheet tensile specimens, like those used in this work, tensile instability is manifested either by a diffuse or by a localized necking, where the latter typically succeeds the former.

Plastic deformation occurs in a narrow band inclined with respect to the tensile axis in a localized neck. Thus the irradiated specimens tested at 20 °C and 200 °C indicate that the ultimate stage of failure can be associated with a localized neck. On the contrary, in all the other specimens, diffuse necking prevails up to failure. The criteria for onset of the two types of necking are different while both are related to the balance between strain-hardening capacity and geometrical softening.

From a pure continuum approach, the criteria for diffuse and localized necking to begin reads $\sigma=\theta$ and $\sigma=2\theta$ respectively. Localized neck develops if diffuse neck does not terminate in fracture. The physical reason for which diffuse or localized necking occurs in the DT specimens remains unclear.

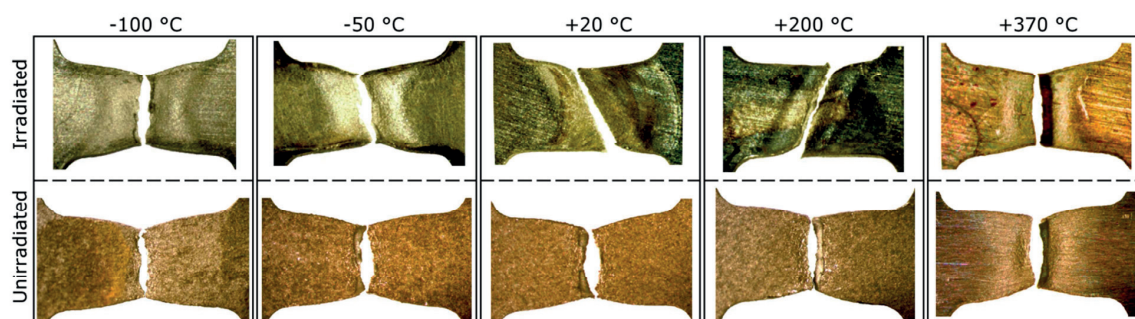


Figure 67: Comparison of the gage section of the tested irradiated as well as unirradiated DTS at various temperatures.

4.3.2.2 SEM analysis

The unirradiated as well as the irradiated DTS tested at -100 and 200 °C were examined by scanning electron microscope in order to assess possible irradiation effects on fracture mechanisms. To do so, a fracture surface overview image was made for all four specimens. From the entire surface, six regions were chosen to examine specific features at higher magnification.

4.3.2.2.1 DTS tested at 200 °C

In Figure 68 the fracture surfaces of an unirradiated DTS at 200 °C is presented. The general view shows a typical flat fractured surface normal to the tensile axis. The higher magnifications in Figure 68 - 2,3,4 and 6 show that the surface is covered with small equiaxed shallow dimples (Figure 68 - 6). Some areas near the center of the gage section exhibit more complex, rougher fracture surfaces, consisting of shallow equiaxed dimples along with deeper conical dimples and micro-void coalescence (Figure 68 - 4). This behavior can be attributed to higher and more triaxial stresses that initiate the first damage that ultimately form a central crack, which propagates to the specimen edges at the point of final fracture. At the edges of the fracture surface so called featureless regions can be found (Figure 68 - 5).

Figure 69 shows the fracture surface of an irradiated specimen tested at 200 °C which failed on a plane inclined by $\sim 70^\circ$ with respect to the tensile axis. The appearance of the surface is more irregular than that of the unirradiated specimen. A major difference between the unirradiated and irradiated fracture surface is that in the latter case, quasi-cleavage facets up to $\sim 50 \mu\text{m}$ are observed (see Figure 69 - 2). The quasi-cleavage facets are distributed over the whole fracture surface, with the largest located off the loading axis as illustrated in Figure 69 top. The irradiated surface is also covered with equiaxed dimples which are deeper than in the unirradiated case. Thus irradiation decreases the proportion of fracture surface with ductile dimple features which are largely replaced by inducing numerous cleavage facets. The brittle fracture events are also responsible for the sudden load drop on the macroscopic deformation curve at final failure. Featureless regions can be found at the edges.

4.3.2.2.2 DTS tested at -100 °C

The fracture surfaces were also investigated at -100 °C. The unirradiated fracture surface has a normal orientation with respect to the tensile axis and appears quite irregular (Figure 70). There are many cleavage

facets with size and shape corresponding to laths and lath blocks (Figure 70 - 4). Interestingly, numerous secondary cracks are visible on most of the surface. The secondary cracks are orientated along the long transverse direction, reach a length of about 120 μm in height and some are wide open. The biggest of them are located off the tensile axis. Besides the small cleavage facets, some regions exhibit ductile tearing manifested by the presence of small dimples as can be seen (Figure 70 – 3,4 and 6).

The fracture surface of the irradiated specimen tested at -100 °C present many similarities with the unirradiated one (Figure 71). It is also irregular and normal to the tensile axis. Here again, a noticeable difference to the unirradiated surface are the big secondary cracks that are arranged parallel to the width of the specimen or resemble smaller sized wedges with a random arrangement. The biggest crack measures around 200 μm in length and 29 μm in width (Figure 71 – 3). Wide areas of the fracture surface can be reported as cleavage facets and appear at the edges as well as in the center of the specimen. Only few dimples were occasionally observed (Figure 71 – 6).

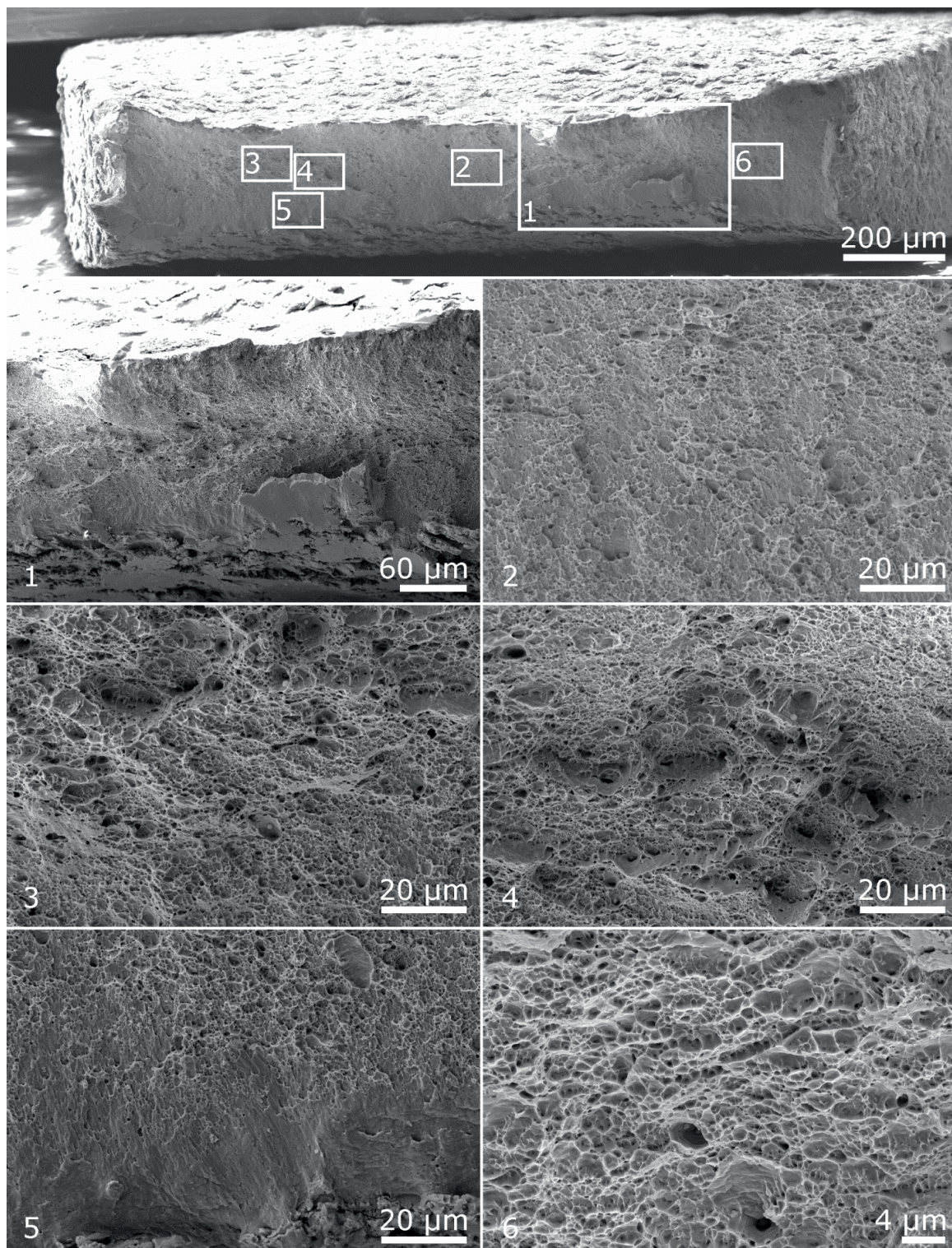


Figure 68: Fracture surface of the unirradiated DTS of Eurofer97-(14) at 200 °C using SEM. Lower right image was taken with the In-lens detector and others with ET detector.

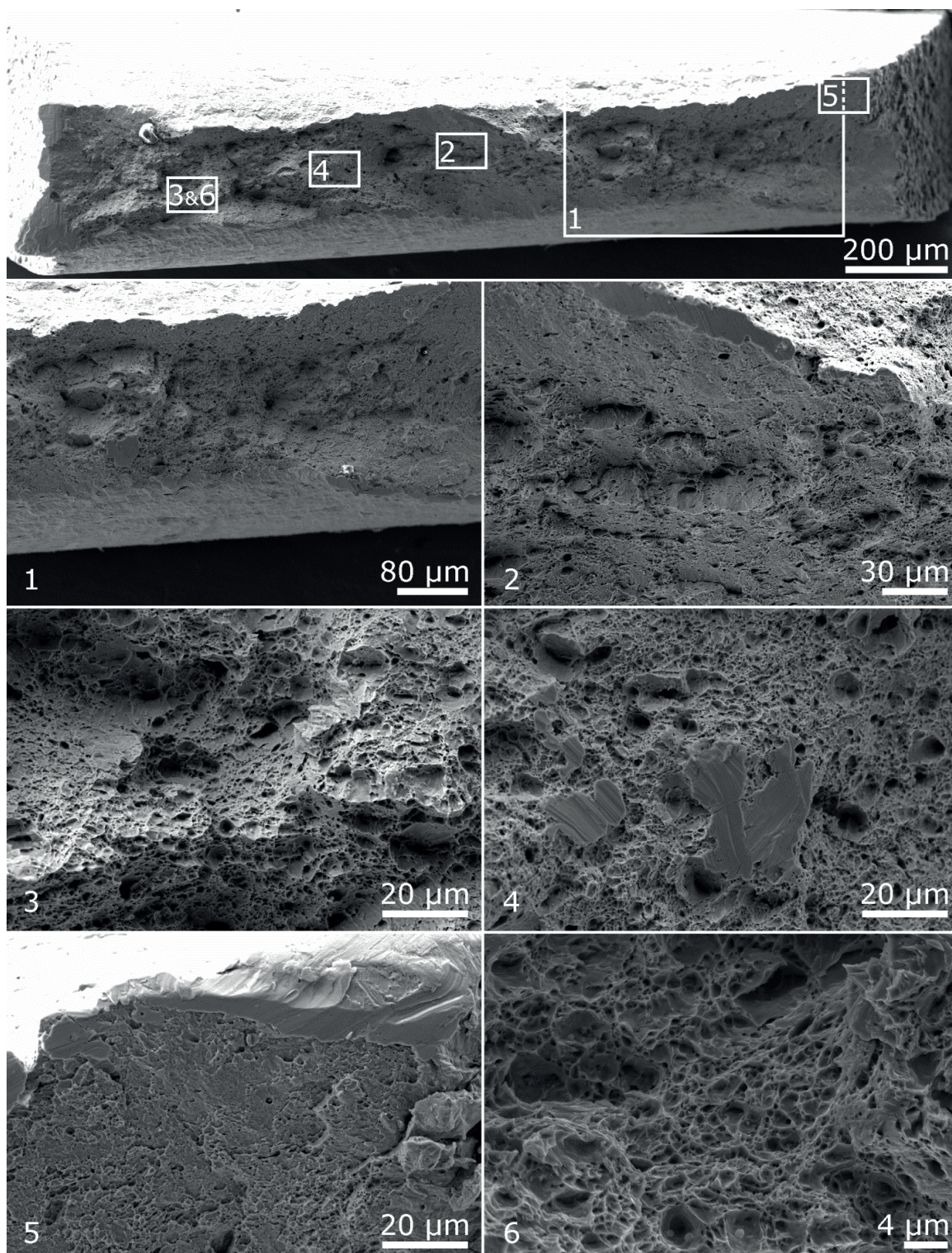


Figure 69: Fracture surface of the irradiated DTS of Eurofer97-(14) at 200 °C using SEM. Lower right image was taken with the In-lens detector and others with ET detector.

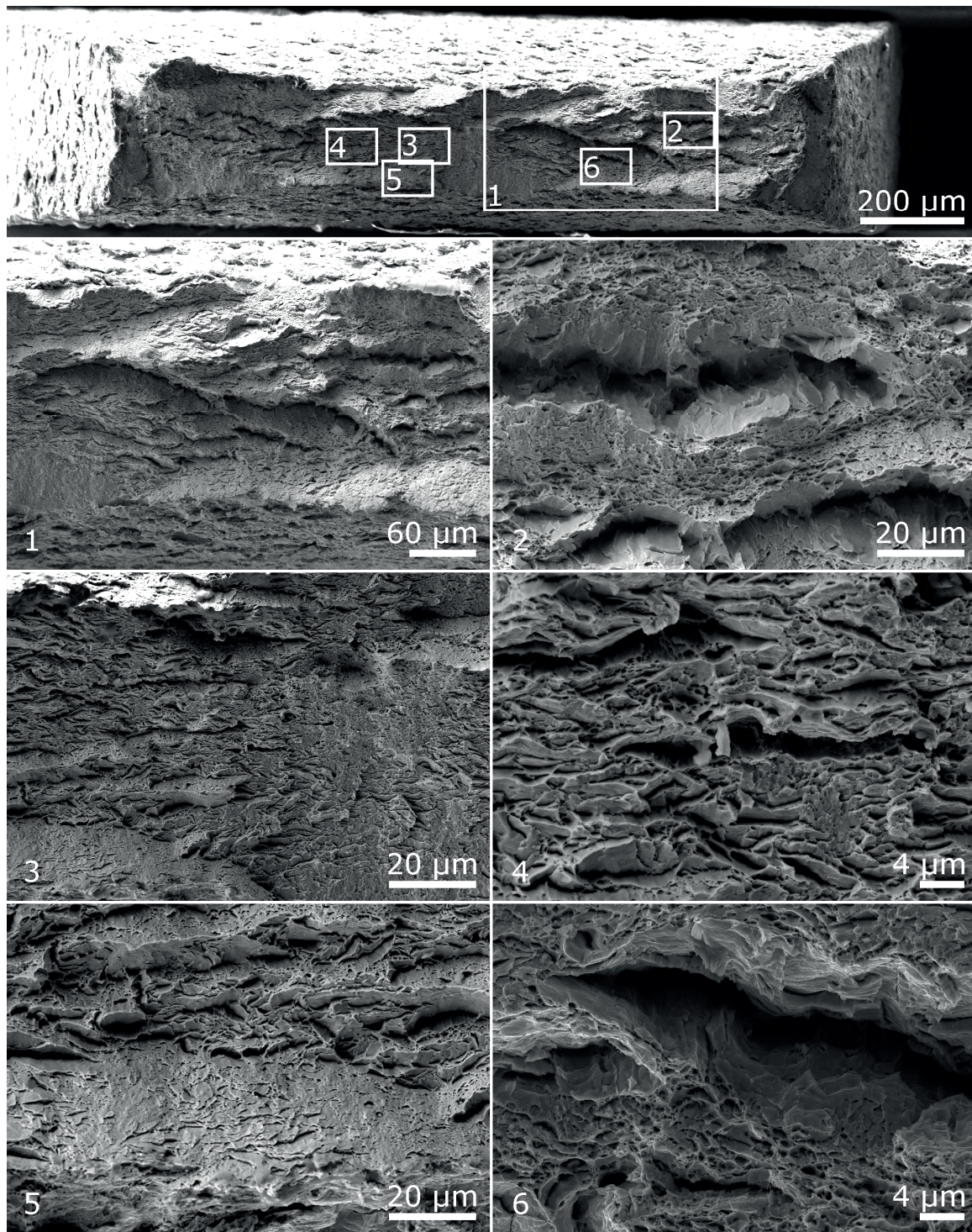


Figure 70: Fracture surface of the unirradiated DTS of Eurofer97-(14) at -100 °C using SEM. Lower right image was taken with the In-lens detector and others with ET detector.

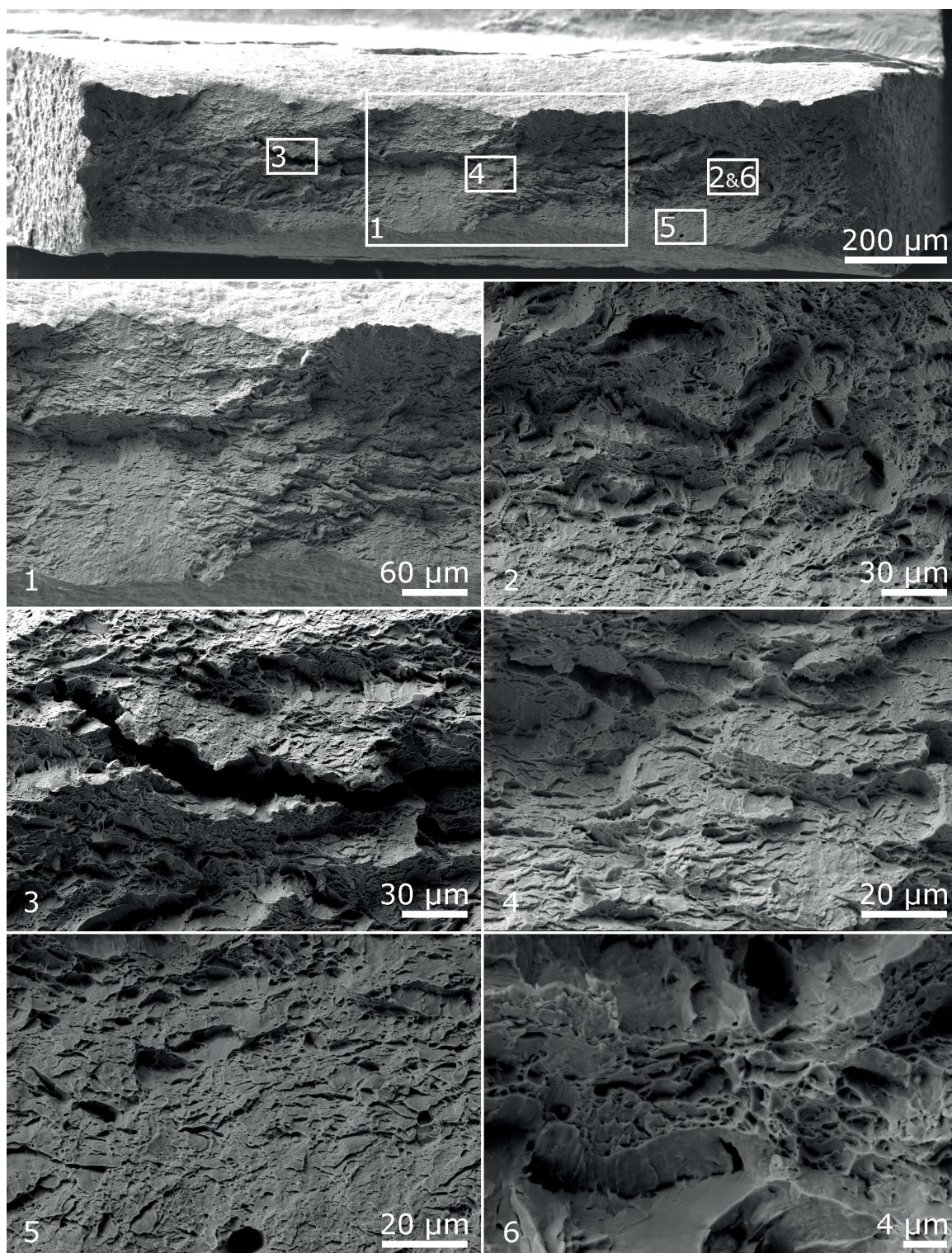


Figure 71: Fracture surface of the irradiated DTS of Eurofer97-(14) at -100 °C using SEM. All images were taken with the ET detector.

4.4 Fracture toughness measurements

Two different shaped and sized compact tension specimens were tested in order to compare the fracture toughness of Eurofer97 under quasi-static and dynamic loading conditions. The obtained results were analyzed using the ASTM standard E1921 – 17a, which is described in detail in section 3.6. Analysis of the fracture surface of the quasi-statically and dynamically tested CT specimens was conducted to identify possible loading rate effects on fracture mechanisms.

4.4.1 Quasi static fracture tests on Eurofer97-(14)

In order to determine the ductile to brittle transition temperature T_0 from the Eurofer97-(14) base material, fracture tests were done using 0.14T sized disk shaped CT specimen. In total 11 tests were performed at temperatures ranging between -160 to -100 °C. For all tests, the traverse displacement velocity was set to 0.1 mm/min. In Figure 72, the temperature dependence of fracture toughness (K_{Jc}) is presented. The lower and upper bounds refer to the 1% and 99% failure probability respectively.

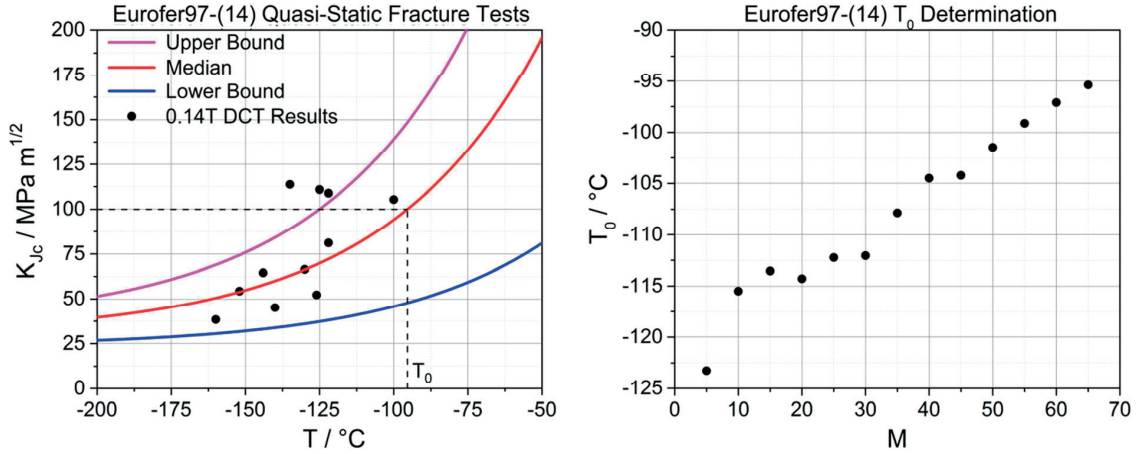


Figure 72: Left: Fracture toughness results for the quasi-static 0.14T DCT tests of Eurofer97-(14) adjusted to 1T. Transition temperature is indicated. Right: Determined transition temperature at increasing M value.

The presented values are already adjusted to 1T using a minimum threshold toughness value of 20 $\text{MPa m}^{1/2}$ in accordance to the ASTM standard E1921 (see equation (12)). From the initial 11 fracture tests, four exceeded $K_{Jc(\text{limit})}$ calculated with $M=30$. We just recall here that $K_{Jc(\text{limit})}$ is defined as $K_{Jc(\text{limit})} = (Eb_0\sigma_{YS}/(M(1-v^2)))^{1/2}$. In Figure 72, the 7 lowest values lie below $K_{Jc(\text{limit})}$ and the 4 highest ones are above.

T_0 was determined with equation (14) using the 1T-adjusted values. However, in order to investigate the effect of M on T_0 , a Matlab routine was written to determine T_0 as a function of M. The routine stops the evaluation if there are fewer than six valid tests, which is in accordance to the ASTM standard E1921. In the right diagram in Figure 72, M-dependence on T_0 is shown.

A clear dependence is seen. Around $M=10$ to 30 there is a short plateau of T_0 with a value of about -113 $^{\circ}\text{C}$. At larger M values, T_0 increases up to -95.4 $^{\circ}\text{C}$ at $M=65$, which is the last value with six valid test. This is consistent with previous studies with CT specimens indicating that T_0 increases up to about $M=100$, [154] and [181]. The ASTM M-value of 30 is indeed too low and not restrictive enough to assure a high level of constraint. The difference in T_0 between the ASTM M value of 30 and 65 is 16.6 $^{\circ}\text{C}$. Therefore, the reference

temperature T_0 of the master-curve and the lower and upper bound shown in Figure 72 was calculated with a transition temperature of -95.4°C obtained at $M = 65$.

Note that the ASTM standard recommends a minimum of six tests, if the 1T adjusted data are between $K_{Jc}=83$ and $212\text{ MPa m}^{1/2}$. However, if subsize CT specimens are tested close to the transition temperature, the $K_{Jc(\text{limit})}$ can be easily violated yielding too many censored values. Hence, it is advisable to perform tests below T_0 to increase the number of uncensored results. The drawback is that the uncertainty in T_0 increases as the lower-shelf toughness is approached [56] and that more tests must be carried out for a precise determination of T_0 .

4.4.2 Dynamic fracture tests on Eurofer97-(25)

Fracture toughness measurements are usually conducted using standard 1T CT specimens loaded in quasi-static condition. To simulate possible fast loading conditions that may happen in a fusion reactor, dynamic fracture tests with 0.18T CT specimen were carried out. In total 19 tests were done at temperatures ranging between -70 to -120°C . The displacement rate was set to 50 mm/min , which corresponds to the maximum traverse velocity of the testing machine. The resulting fracture toughness values adjusted to 1T are shown in Figure 73.

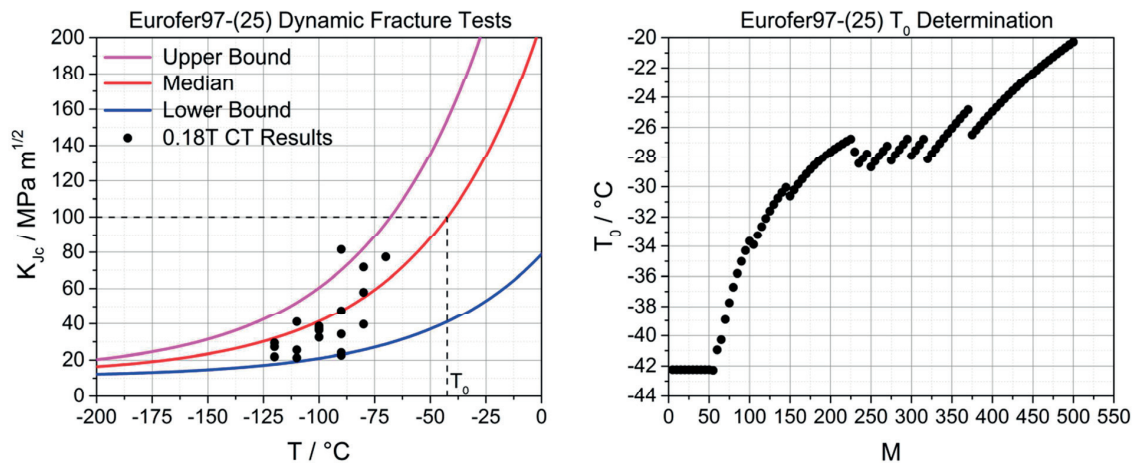


Figure 73: Left: Fracture toughness results for the dynamic 0.18T CT tests of Eurofer97-(25) adjusted to 1T. Transition temperature is indicated. Right: Determined transition temperature at increasing M value.

In the following T_0 evaluation, the ASTM master-curve modifications proposed by Müller et al. for Eurofer97-(25) after analyzing a rather large data base [59] were implemented. First, the median toughness A on the lower shelf was taken at $12\text{ MPa m}^{1/2}$, instead of 30 as recommended in the ASTM E1921 standard (see equation (15)). Second, a K_{\min} value of $10\text{ MPa m}^{1/2}$ was considered.

To evaluate the transition temperature in dependence of M , the same procedure as for the quasi-static tests was applied. As the number of tests conducted is higher and all of them were valid, the M value could be increased up to 500 before less than six valid tests were left (see Figure 73). The determined transition temperature at a M value of 5 to 50 is -42.24°C . After exceeding $M=50$ the transition temperature increases strongly. Between $M=195$ and 350 a plateau value of about -27°C established. At high M values, T_0 determination becomes unreliable because the valid data are obtained at testing temperature lower than $T_0-50^\circ\text{C}$, i.e., out the temperature range where the data for T_0 determination should be.

The loading rate in terms of $\text{MPa m}^{1/2} \text{s}^{-1}$ corresponding to the traverse velocity of 50 mm/min was estimated with equation (17), yielding loading rates of about $87 \text{ MPa m}^{1/2} \text{s}^{-1}$ with a standard deviation of $21 \text{ MPa m}^{1/2} \text{s}^{-1}$ (see Figure 74). This is due to the different nature of failure mechanisms from specimen to specimen, i.e. fully elastic loading or elastic-plastic loading.

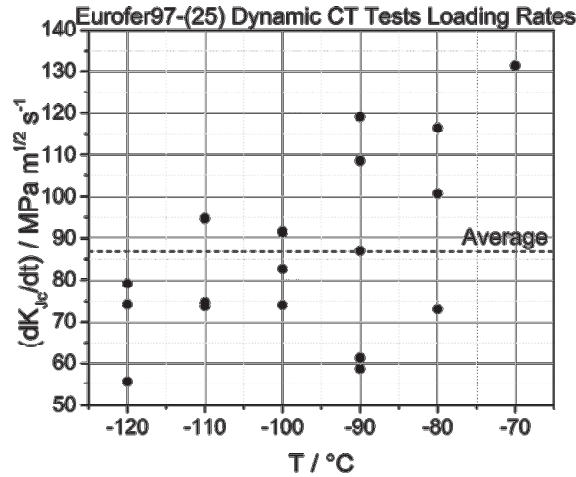


Figure 74: Loading rate in terms of dK_{IC}/dt for the dynamic 0.18T CT tests of Eurofer97-(25) at different temperatures. Average value is indicated.

In comparison, the quasi-static CT tests from Müller [154] were conducted at loading rates from $0.09 \text{ MPa m}^{1/2} \text{s}^{-1}$ for the 0.18T and $0.1 \text{ MPa m}^{1/2} \text{s}^{-1}$ for the 0.88 T sized specimens. Roughly speaking, the difference in dK_{IC}/dt between the quasi-static and dynamic tests is about 1000 which yielded in an increase in T_0 of about 36°C .

4.4.3 Fractographic observations on 0.18T CT specimen, Eurofer97-(25)

To reveal possible effects due to dynamical loading on the fracture behavior, the dynamically tested 0.18T CT specimen at -120°C was investigated using SEM. The temperature was chosen in accordance to the observed softening behavior at the standard tensile tests, where we may expect some influence of heating in the fracture process zone. As a reference, a specimen of the same size and same temperature at quasi-static condition tested by Bonadé was examined as well [182]. Since possible loading rate effects arise close to the crack tip, the investigation was conducted along the entire crack front.

4.4.3.1.1 Quasi-Static Tests

In Figure 75 the fracture surface along the entire crack tip width for the quasi-static CT test is shown. The fatigue pre-crack can be easily identified. In comparison to the rest of the fracture surface, the fatigue pre-crack areas appear smoother. At the crack front, which shows a curvature, an immediate change to a rougher surface appearance takes place. Around the center of the crack, the transition is characterized by a bigger step perpendicular to the fracture surface that is covered with dimples (see 1 and 2 in Figure 75). Off the center and at the edges, the transition is smoother and appears either with a smaller or no gap (see 3 and 4 in Figure 75). Inward from the crack front, cleavage fracture dominates in form of river patterns and cleavage steps. However at some areas still a few dimples can be found that appear mostly at gaps vertical to the fracture surface (see white arrows in Figure 75). Besides the mentioned features, out-of-plane cracks were also found (see red arrows in Figure 75). The fracture mechanism is clearly brittle, with small cleavage facets connected by ductile ridges characteristics of the so-called quasi-cleavage.

4.4.3.1.2 Dynamic Tests

The dynamic tested CT specimen fracture surface can be seen in Figure 76. In opposition to the quasi-static test, the dynamic CT fracture surface does not show a pronounced gap in the center of the specimen at the crack front. Overall the transition is smoother over the entire crack width. Only at one position a bigger gap normal to the fracture surface was found, which is covered with dimples (see white arrows in 4 in Figure 76). Similarly to the quasi-static tests, dimples can be seen at gaps vertical to the crack surface (see white arrows in Figure 76). Out-of-plane cracks (see red arrows in Figure 76) as well as cleavage features like river patterns and cleavage steps cover mainly the surface indicating once more brittle failure.

From the obtained results, a clear difference between the quasi-static and dynamic tested CT cannot be seen. Besides the mentioned gap at the crack front for the quasi-static CT, no other feature which would indicate a different fracture behavior was found. The micro-mechanisms of fracture in dynamic loading are then the same as those in quasi-static loading.

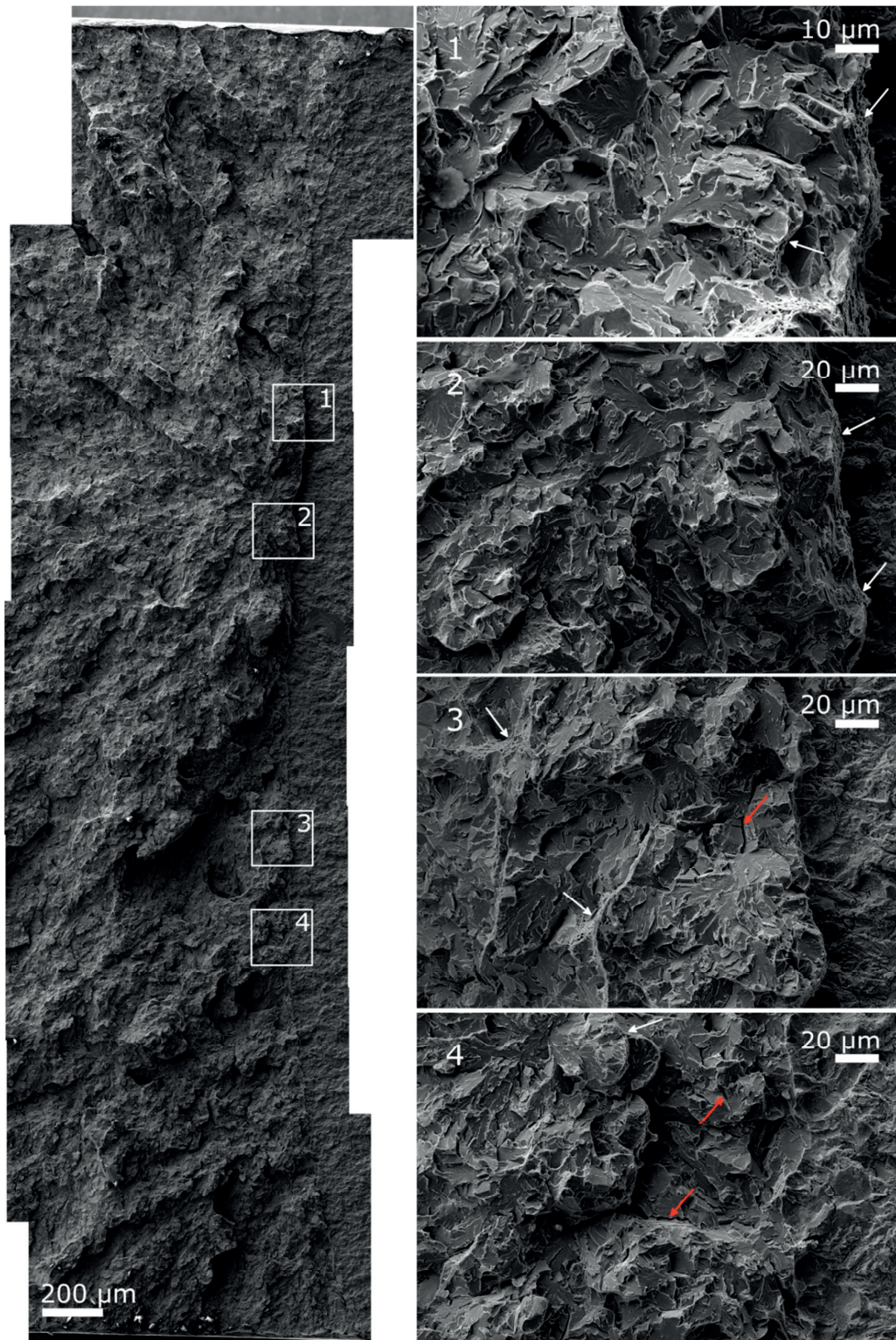


Figure 75: Fracture surface of the quasi-static tested 0.18T CT specimen of Eurofer97-(25) at -120 °C. SEM images were taken with the ET detector.

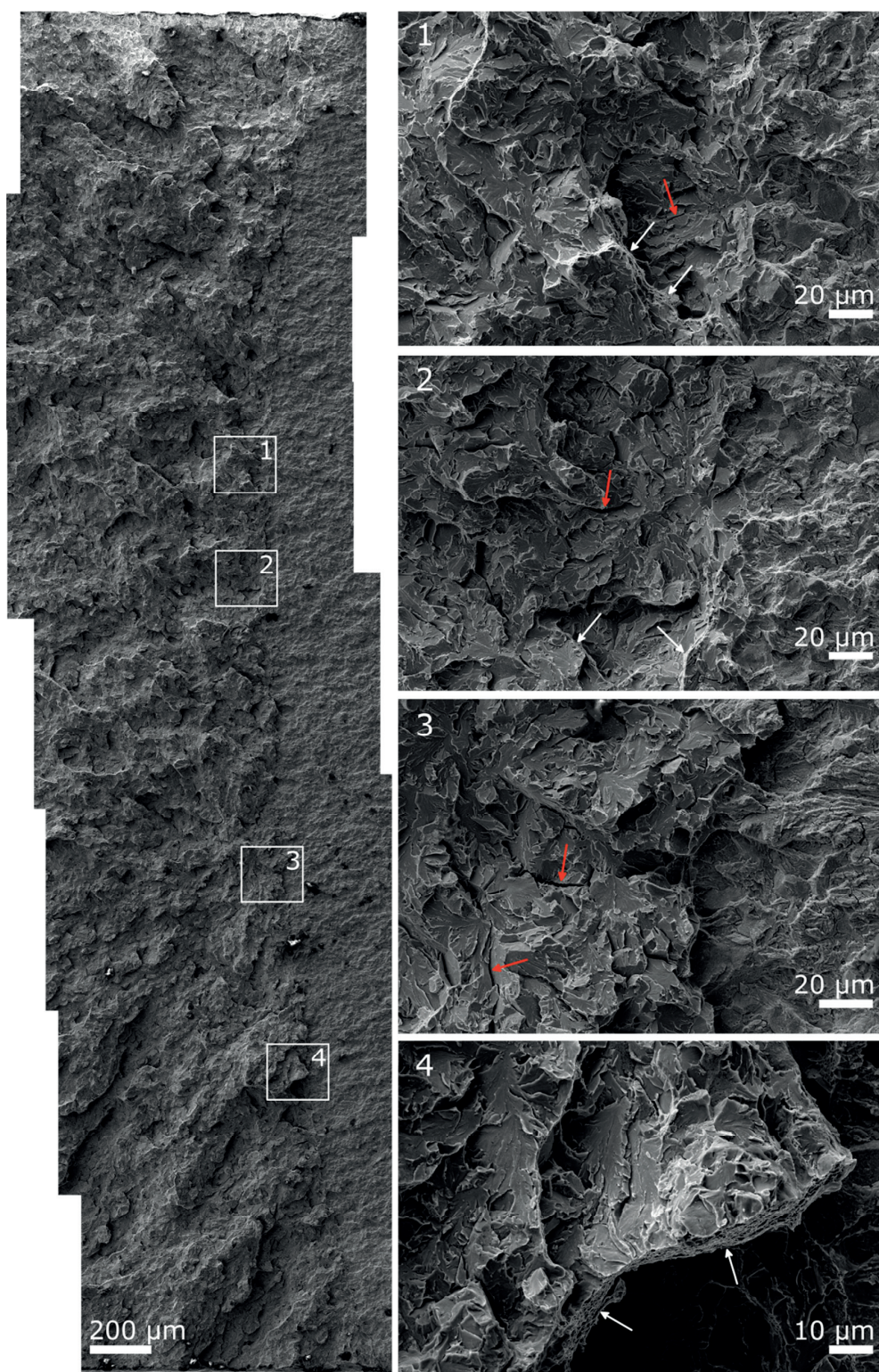


Figure 76: Fracture surface of the dynamic tested 0.18T CT specimen of Eurofer97-(25) at -120 °C. SEM images were taken with the ET detector.

4.5 Finite element modeling results

Several FE models were developed for the standard and non-standard tensile specimens as well as for fracture specimens. The experimental results presented in the previous sections were modeled. For the tensile specimens, the true stress-strain curve beyond the onset of necking was determined with the inverse method for unirradiated and irradiated specimens. The near tip stress/strain fields of the fracture specimens were calculated to determine the sensitivity to strain rate, thermal effects and irradiation on critical parameters of a local approach model to fracture.

4.5.1 Post-necking analysis of Ø 5 mm standard tensile specimen, Eurofer-(25)

In section 4.2.1, tensile curves of 18 uniaxial standard Ø 5 mm round shaped tensile specimens were presented at temperatures ranging from -196 °C to 200 °C. From the obtained tensile results the true stress-strain curve up to necking can be immediately calculated. To determine flow properties beyond the onset of necking, our developed FEM inverse approach was applied to reconstruct the experimental results increment by increment. The reconstruction of the engineering stress/strain curves was realized satisfactorily well for all tests. In Figure 77, a comparison between the experimental and FEM calculated curves is shown. As the 18 tensile curves overlap, only the reconstruction and the corresponding experimental curve at a displacement rate of 5 mm/min for each temperature is shown. The true stress-strain curve determined for the reconstruction of the 18 tests can be found in Figure 78 and Figure 79.

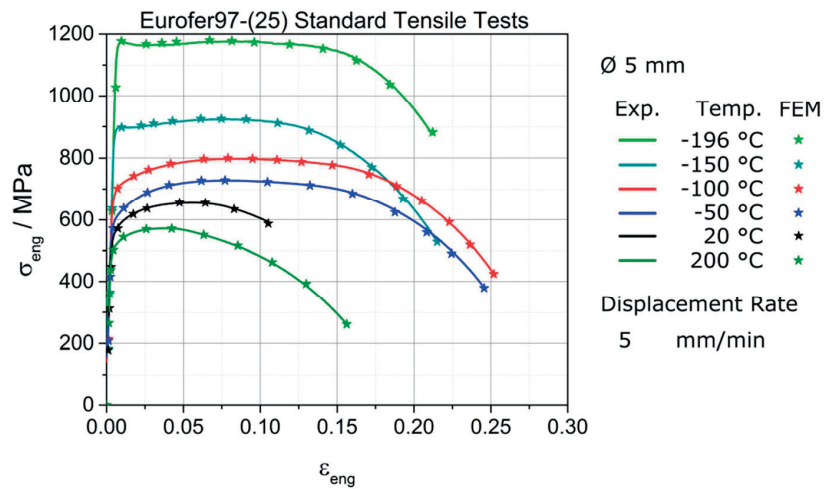


Figure 77: Experimental engineering curves and corresponding FEM results of the Ø 5 mm round shaped standard tensile specimen of Eurofer97-(25).

Due to the fact that the hardening slope at high plastic strains does not change significantly, the increment size can be set large and therefore allows a fast completion of the inverse determination process. The resulting true stress/plastic strain curves are shown in Figure 78 and Figure 79. Note that the inverse method allows determination of the plastic flow properties to much higher strain than the uniform strain. Let's emphasize that the true stress/plastic true strain at -196 °C obtained at different strain rates show only a shift to higher stresses in good agreement with the engineering curve that are also shifted in stress. On the contrary, at -150 °C, the shift in stress, for the two elevated strain rates at $2.8 \cdot 10^{-3} \text{ s}^{-1}$ and $2.8 \cdot 10^{-4} \text{ s}^{-1}$, can only be found at the onset of yielding, then the curves merge at higher plastic strain. Note also that the shift to higher stresses due to the strain rate decreases at higher temperatures.

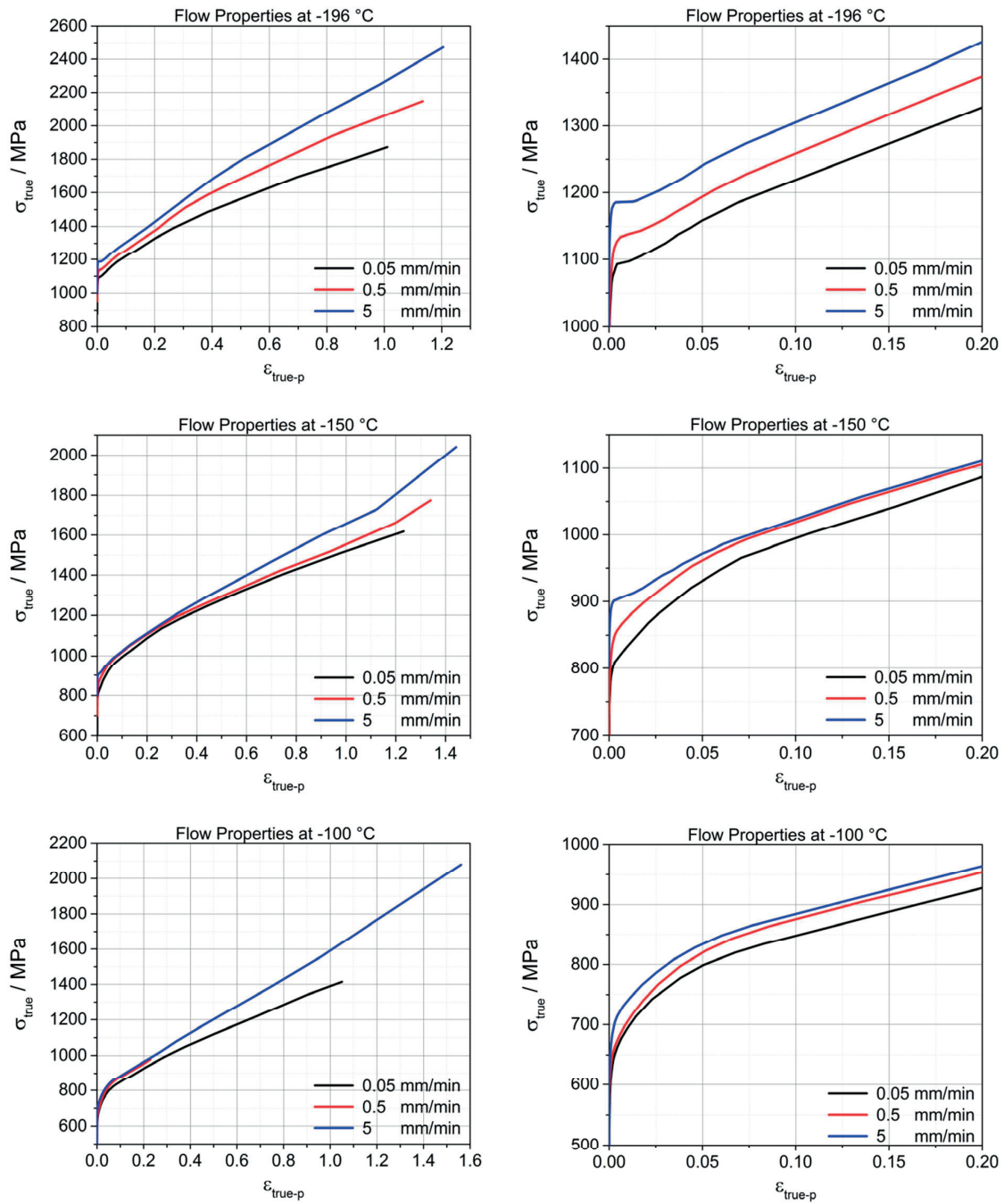


Figure 78: Determined flow properties of Eurofer97-(25) at -196, -150 and -100 °C using the standard tensile \varnothing 5 mm round shaped tensile test results. Values beyond UTS were obtained by an inverse method.

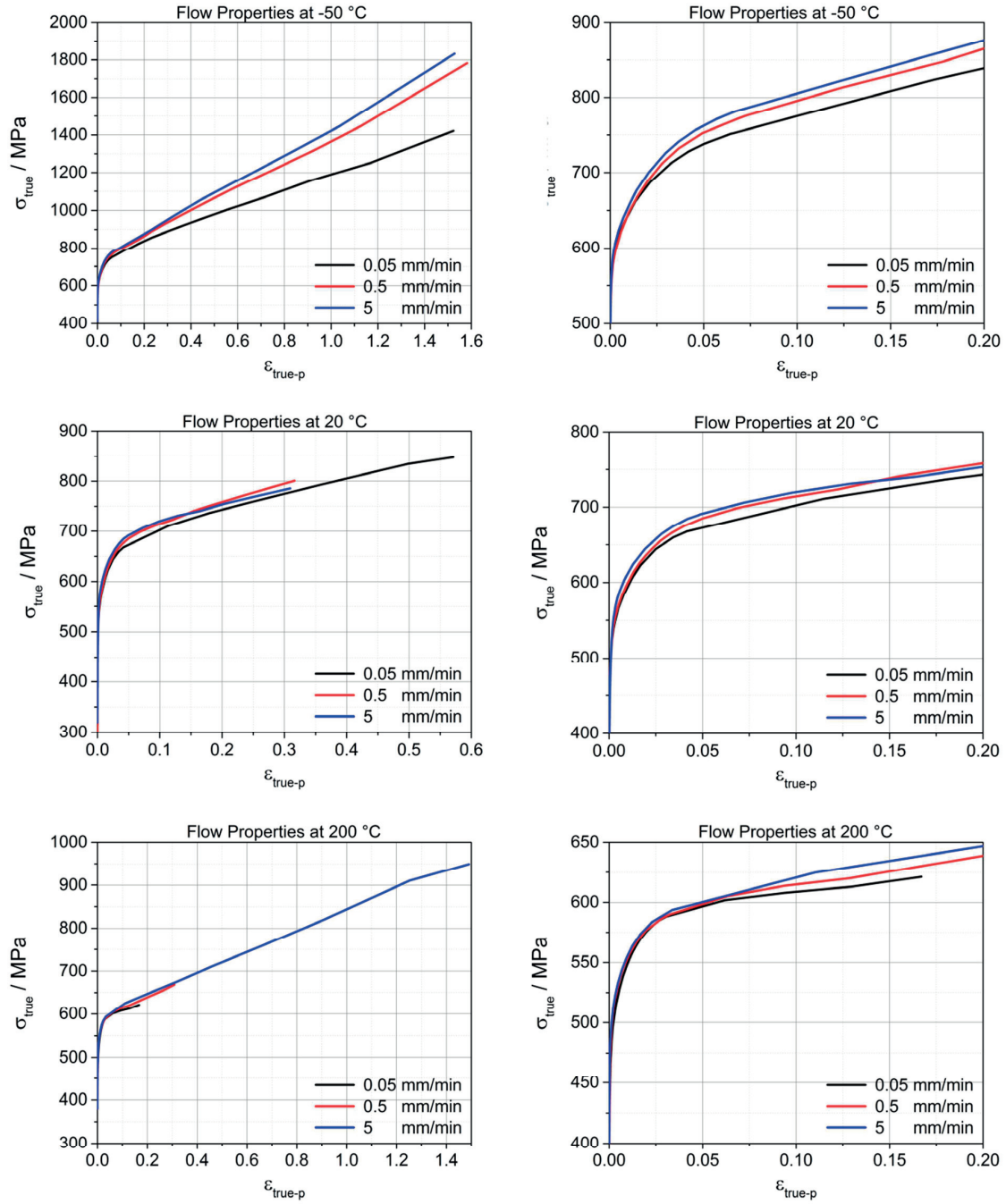


Figure 79: Determined flow properties of Eurofer97-(25) at -50, 20 and 200 °C using the standard tensile \varnothing 5 mm round shaped tensile test results. Values beyond UTS were obtained by an inverse method.

4.5.2 Strain rate effect including thermal effects on tensile tests of Eurofer97-(25)

From the experimental \emptyset 5 mm round shaped tensile specimen results conducted at a displacement rate of 5 mm/min, softening could be observed that is likely caused by thermal effects (see left in Figure 80). These thermal effects are characterized by a temperature increase in the specimens resulting from a conversion of the plastic work into heat, which at high strain rate is not extract fast enough out the specimen. To analyze this phenomenon in detail, the axisymmetric \emptyset 5 mm round shaped tensile FE model was extended to account for strain rate along with thermal softening effects. In order to identify the impact of thermal softening on the calculated tensile curves, two different models were run: one which accounts for strain rate sensitivity of the flow stress, and one which accounts for strain rate sensitivity of the flow stress and thermal effects. Here below, we refer to the first as “non-thermal” and to the second as “thermal”. In the thermal model, the temperature increase between simulation increments is calculated as:

$$\Delta T = \int_0^{\epsilon} \frac{\beta}{\rho c_p} \sigma(\epsilon) d\epsilon \quad (26)$$

where β is the Quinney-Taylor coefficient, ρ is the mass density and $\sigma(\epsilon)d\epsilon$ represents the plastic work increment. β was set to 0.9 and the values for c_p and ρ can be found in Table 3.

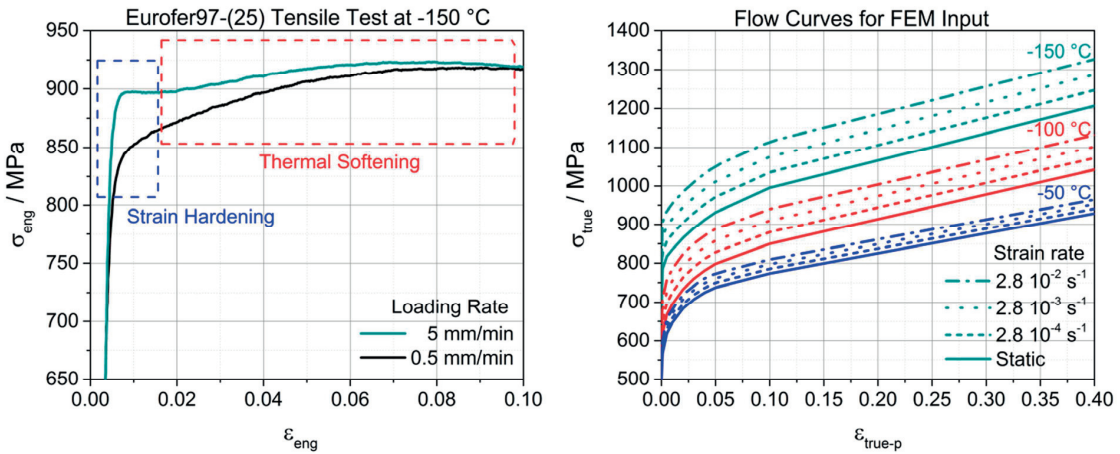


Figure 80: Eurofer97-(25) obtained results and FEM approach. Left: Experimental tensile curves. Right: Flow curves used as input for FEM.

The strain-rate sensitivity input in the FE model was introduced as follows; the flow curve from the \emptyset 5 mm round shaped tensile specimen at the lowest strain rate was used as a reference static curve at zero strain rate (in reality this is the curve obtained at of $2.8 \cdot 10^{-5}$ s $^{-1}$), and the flow stress was simply shifted to higher stresses for corresponding increase of one order of magnitude strain rate according to the determined $\Delta\sigma_{true}$ values in section 4.2.2. The resulting flow curves at -50, -100 and -150 °C are shown in the right diagram in Figure 80.

The FEM outputs are compared with the experimental curves in Figure 81. From the “non-thermal” FEM the obtained output only matches close to the onset of plastic deformation and then yields a too stiff response, namely a difference in true stress $\Delta\sigma^*$ which increases with increasing plastic strain. In contrary, the “thermal” FEM yields a less stiff response and shows a good match with the experimental curve up to 15 % of engineering strain. At larger strains, the thermal model becomes inaccurate. Nevertheless, the overall match of the experimental curve and the thermal FEM output is good, especially in the range of

onset of yielding up to 15 % of engineering strain. All flow curves were calculated from the load/displacement curve for displacement corresponding to a homogenous distribution of strain. The flow curves in Figure 81 are plotted up to 10 % of plastic strain. However, since necking takes place around 7 % of plastic strain, the true stress values beyond necking are not strictly correct.

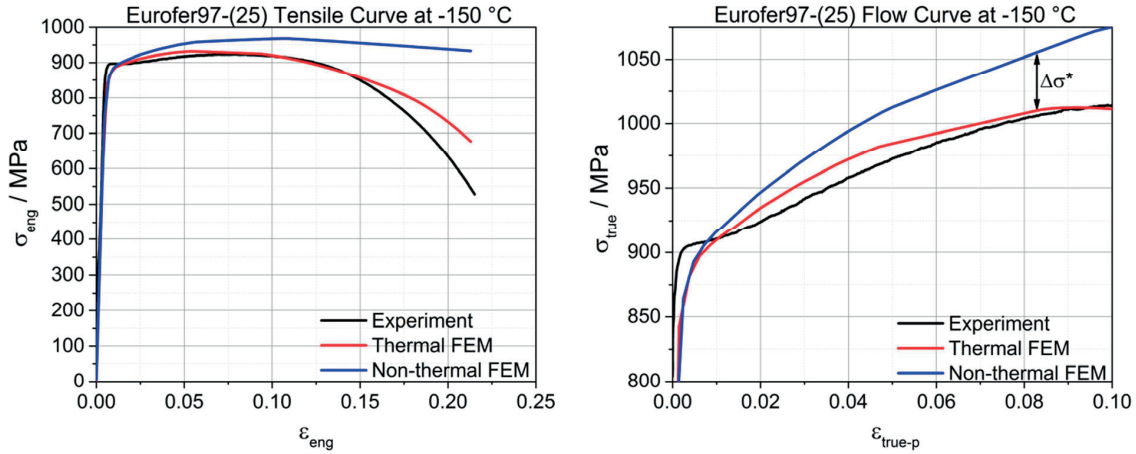


Figure 81: Tensile and flow curve of Eurofer97-(25) in comparison to the FEM results. Non-thermal FEM considers only strain rate; thermal FEM includes strain rate and thermal effects.

As expected, the thermal softening is opposing strain rate hardening which gets more dominant at higher deformation due to the increasing amount of dissipated heat. The thermal FE model was able to reduce the hardening due to strain rate by thermal softening in the range up to 15 % of engineering strain well. Beyond the discrepancy between the FEM and experimental result increases. A more detailed analysis of the stress/strain fields, the strain rate as well as the temperature distribution was performed at 10 % of engineering strain (see Figure 82).

Although necking has already started at 10% engineering strain, the stress distribution in terms of maximum principal stress is quite homogeneous over the entire gage section. In contrary, the plastic equivalent strain already shows an inhomogeneous distribution where the maximum strain can be found in middle of the gage section. The temperature has a rather strong gradient from the thread of the specimen to the gage section, where the maximum temperature was obviously found at the same position as the maximum of plastic equivalent strain.

The established temperature gradient promotes local softening, which in turn can trigger premature localization of deformation even at such low strain rates of $2.8 \cdot 10^{-3} \text{ s}^{-1}$. Similar results were obtained in [159]. From the FEM results the logarithmic strain rate (ER) was determined as well (see Figure 82). Interestingly, the ER distribution in the middle of the gage section increased already by 75 %. In the experimental results of the $\varnothing 5 \text{ mm}$ round shaped tensile specimen it was reported that for the test done at a displacement rate of 5 mm/min a temperature increase of about 20 °C could be measured. Compared to the FEM results which gave a ΔT of 17 °C at 10 % of engineering strain the obtained values match pretty well. At 10% of engineering strain a temperature increase of 25 °C was calculated with equation (26) which is slightly higher in comparison to the FEM and experimental obtained results.

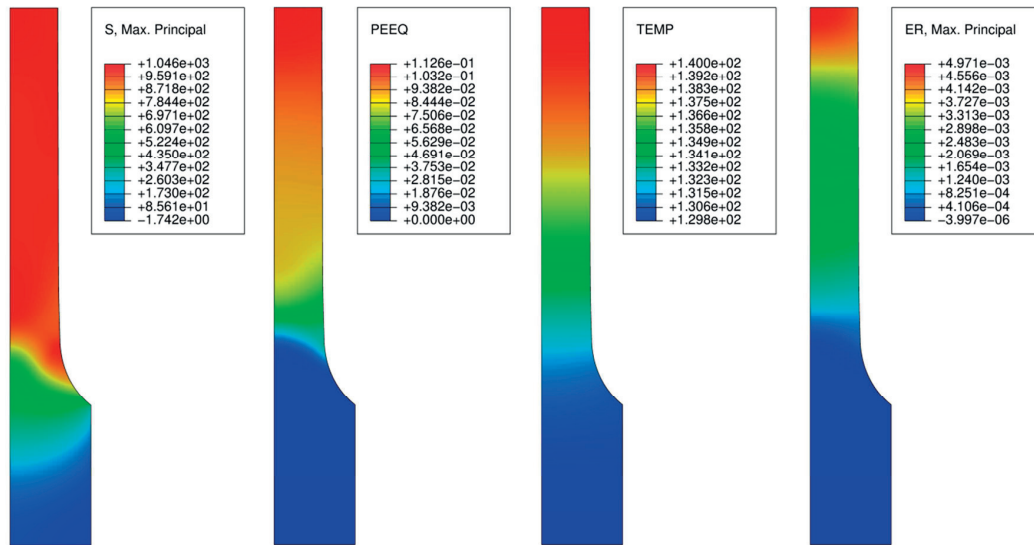


Figure 82: Calculated FE distributions of the standard tensile model which included strain rate and thermal effects at 10 % engineering strain. From left: Maximum principal stress in MPa, plastic equivalent strain, temperature in K and logarithmic strain rate in s^{-1} .

4.5.3 Flow properties determination of disk tensile specimens, Eurofer97-(14)

The experimental tensile DTS results were also analyzed with the inverse method. For each engineering stress/strain curve, the yield stress σ_0 was chosen close to the point where the curve deviates from the elastic response. As already mentioned in section 3.7.3, σ_0 does not correspond to the standard offset yield strength. Actually σ_0 was predefined to a lower value to be able to catch the gradual transition between elastic and plastic deformation. The initial displacement increment size was set to $d_{inc}=0.001$ mm. Such a small initial increment is required as the slope of the experimental engineering stress/strain curve at the elastic/plastic transition is steep. After exceeding 0.005 of plastic strain, the increment size is increased to 0.005 mm followed by the next increase in increment after passing the UTS to 0.01 mm. As the FE model considers non-damaged specimen, the reconstruction of the experimental engineering stress/strain curve is stopped at the fracture stress and strain defined in section 4.3.1.

In Figure 83, the reconstructed engineering stress/strain curves of unirradiated and irradiated DTS using the described inverse method in comparison to the experimental curves are shown. FEM results are indicated as stars in the figure. At all temperatures the inverse approach obtained a good reconstruction of the experimental curves. The corresponding determined flow properties can be found in Figure 84.

The unirradiated flow curves show a gradual transition from the onset of plastic deformation. Almost all flow curves do show a softening at very large plastic strains. This softening observed for the test temperature -50 °C to 370 °C probably accounts for the occurrence of damages in the form of micro-voids and or micro-cracks in the neck region that cause an apparent softening of the material. Only at -100 °C, a very low hardening rate was found close to failure. Interestingly, at this temperature only a few dimples and micro-voids were found on the fractographic observations, supporting the interpretation of softening due to micro-void initiation.

For the irradiated flow curves a gradual transition from the elastic to plastic regime was found at 370 °C only. At lower temperatures, the elastic-plastic transition is quite abrupt. At 200 °C and 20 °C, a short deformation range of perfectly plastic behavior emerged.

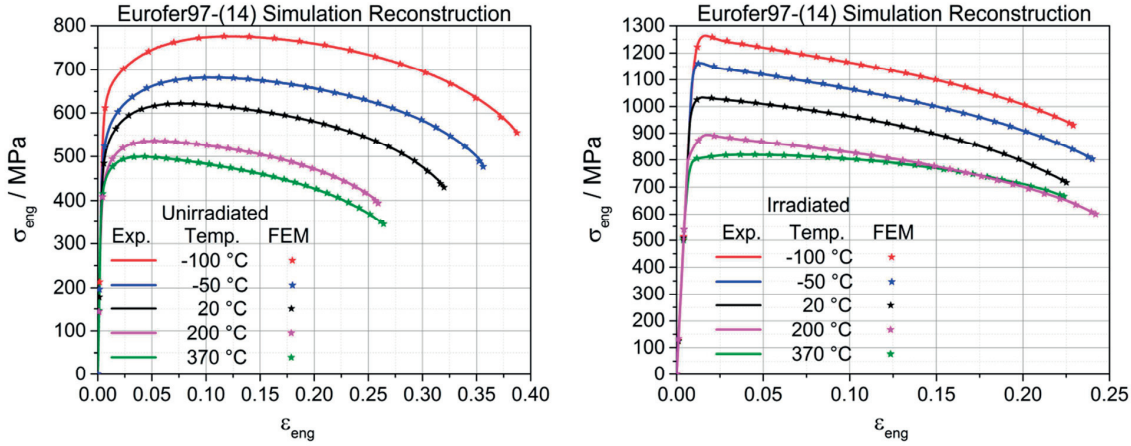


Figure 83: Experimental engineering curves of the DTS tests and corresponding FEM reconstruction results. Left: Unirradiated. Right: Irradiated Eurofer97-(14).

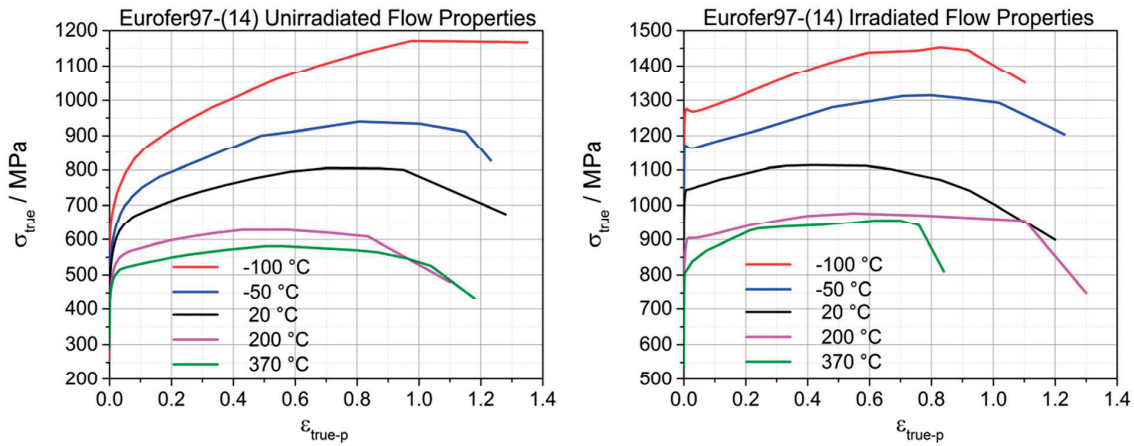


Figure 84: Inverse determined flow properties in terms of true stress and true plastic strain for Eurofer97-(14). Left: Unirradiated. Right: Irradiated Eurofer97-(14).

The lowest two temperatures -50 and -100 °C even show a feature similar to a yield drop followed by strain-hardening (see Figure 85). In the softening part a drop in flow stress of 9 MPa at -100 °C and 8.8 MPa at -50 °C can be measured. It has to be mentioned that if the softening behavior is replaced by a perfectly plastic or low hardening slope the FE model cannot reproduce the experimental result well and simply cuts off the small hump in the curve immediately after yielding. For the irradiated case, a strong softening at higher plastic strains close to failure can also be seen. This can be attributed to damage, which initiates and accumulates in the neck region before failure.

A direct comparison of the irradiated and unirradiated flow properties is found in Figure 85. Clearly the different strain hardening behavior at low plastic strain due to irradiation can be seen. The black horizontal bars indicate where the inverse algorithm approached necking and post necking analysis started by increasing the increment size. In the unirradiated case flow properties up to 9 % of plastic strain could be deter-

mined whereas for the irradiated DTS only flow properties up to 1 % of plastic strain were obtained before necking took place.

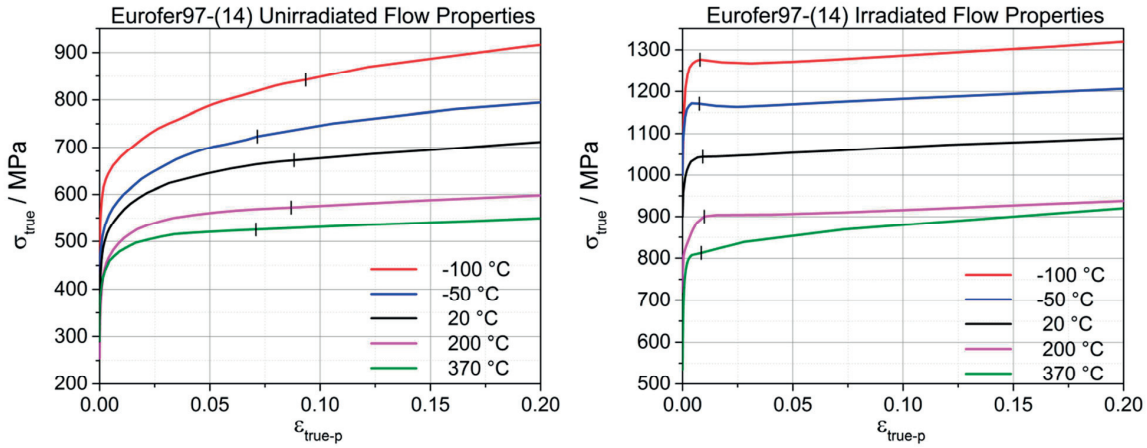


Figure 85: Inverse determined flow properties of the unirradiated and irradiated DTS of Eurofer97-(14).

4.5.4 Local Approach to Fracture

In the following the critical parameters of a local approach to fracture are determined using 3D and 2D FE models of CT specimen as well as a the modified boundary layer model (MBL) used in small scale yielding (SSY) conditions. These models were presented in detail in section 3.7. It has to be recalled that all FE model do have an initial root radius of $0.1 \mu\text{m}$ which is representative of a real radius of a pre-crack. The results from these models are compared and the limitations are discussed. In particular, the impact of loading rate, strain rate and thermal effects on these critical parameters are analyzed.

4.5.4.1 3D and 2D CT model, Eurofer97-(25)

In order to have results, as reference to the simplified 2D and MBL models, FE simulations in 3D of the 0.18T and 0.88T CT specimens were done. In this section, the FE simulations were run with a simple elastic-plastic material model, where the plastic flow properties are the true stress/plastic strain curves of the $\varnothing 5$ mm round shaped tensile specimens at a nominal strain rate of $2.8 \cdot 10^{-5} \text{ s}^{-1}$. In other words, no strain rate dependence of the flow stress is considered.

In Figure 86, the fracture toughness data versus temperature obtained by Bonadé [182] and Müller [59] are plotted along with the so-called lower bound of the master-curve indexed at $T_0 = -80 \text{ °C}$ determined for the 0.18T CT specimen size. The lower bound is here defined as the 1% cumulative failure probability. Fracture toughness values shown in the figure are not sized adjusted to 1T and therefore show a strong size effect. The stars highlighted on the lower bound in Figure 86 indicate the fracture toughness values at which the stress/strain fields of the 0.18T CT models were analyzed and reported. As the K_{Jc} values from the 3D FE model are determined from the calculated load/displacement curves, the resulting loading of the model in terms of K_{Jc} is slightly different from the theoretical values of the lower bound (see Table 9). Similarly, the 1% lower bound values correspondings to the 0.88T CT specimens are given in Table 6. We recall that the difference in the lower bound values is the consequence of the crack front length adjustment (see equation (12)).

Table 9: K_{Jc} lower bound values at different temperatures for the 0.18T sized specimen and the corresponding K_{Jc} values where the stress/strain fields were calculated from the 3D CT model. D is the difference between those in percent.

T / °C	$K_{Jc(0.01)} / \text{MPa m}^{1/2}$	$K_{Jc-FEM(0.01)} / \text{MPa m}^{1/2}$	D / %
-196	16.26	16.42	1
-150	23.52	22.92	-2.6
-100	43.26	44.03	1.8
-50	94.30	94.45	0.2

Table 10: K_{Jc} lower bound values at different temperatures for the 0.88T sized specimen and the corresponding K_{Jc} values where the stress/strain fields were calculated from the 3D CT model. D is the difference between those in percent.

T / °C	$K_{Jc(0.01)} / \text{MPa m}^{1/2}$	$K_{Jc-FEM(0.01)} / \text{MPa m}^{1/2}$	D / %
-196	14.20	14.57	2.6
-150	19.07	18.66	-2.1
-100	32.32	32.66	1.1

As mentioned above the 3D model does not account for strain rate effects and simply uses flow properties which were obtained at a strain rate of $2.8 \cdot 10^{-5} \text{ s}^{-1}$. This choice is justified by the following consideration. In Figure 86 are plotted the maximum principal stress σ_1 and the equivalent plastic strain $\varepsilon_{p,eq}$ within the so-called process zone ahead of the crack tip, in the middle of the specimen, as calculated by FE simulations at their respective lower bound value. At the position of the peak stress, $\varepsilon_{p,eq}$ is around 0.01 and it drops rapidly with the distance leading to typical loading rates for quasi-static loading of the order of few $\text{MPa m}^{1/2} \text{ s}^{-1}$. Hence, fracture initiation in quasi-static loading conditions is done within several minutes. Based on this, a rough but reasonable estimate of the plastic strain rate in the process zone yields values in the range of 10^{-5} to 10^{-4} s^{-1} , providing the reason for our choice of the tensile test strain rate in this first set of simulations. It must be noted that the height of the stress peak decreases and the width increases with temperature. On the contrary the equivalent plastic strain shows increasing values acting over a larger distance with increasing temperature.

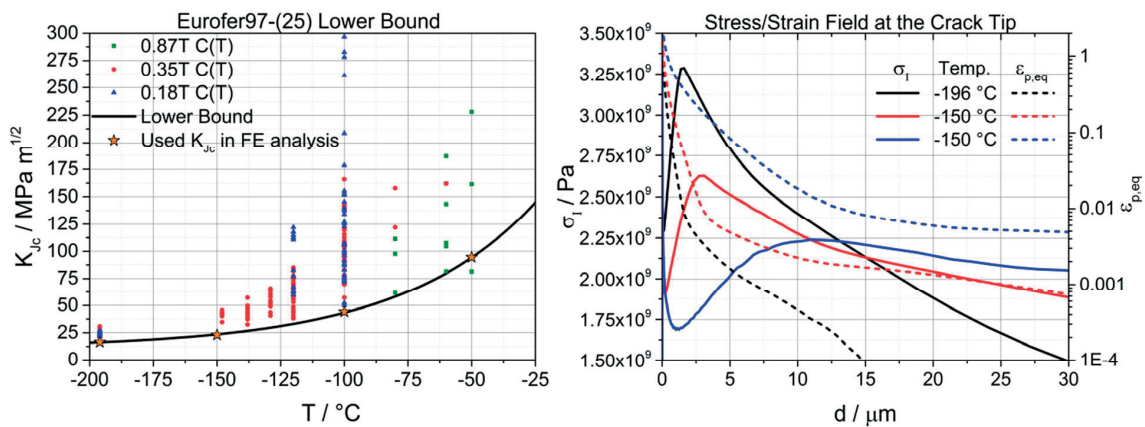


Figure 86: Left: Fracture toughness data with corresponding lower bound of the 3D 0.18T CT specimen. The stars indicate the FEM results. Right: Maximum principal stress σ_1 and plastic equivalent strain $\varepsilon_{p,eq}$ at the crack tip.

Among the different fracture local approaches proposed, the so-called “critical stress–critical volume” model, σ^*-A^* , developed by Odette et al. [140] is based on the two following assumptions:

- brittle fracture is triggered when a critical area A^* of material encompasses a critical stress level, and
- the critical values σ^* and A^* are usually assumed to be material properties independent of temperature.

It naturally follows from this model that, for a given specimen size characterized by thickness B , one can associate a critical volume $V^*=BA^*$. Using the 3D 0.18T and 0.88T CT FE results conducted at four temperatures, the dependence of the stressed volume encompassed by the maximum principal stress was calculated. In Figure 87, the results of the FE models of size 0.18T and 0.88T CT are shown.

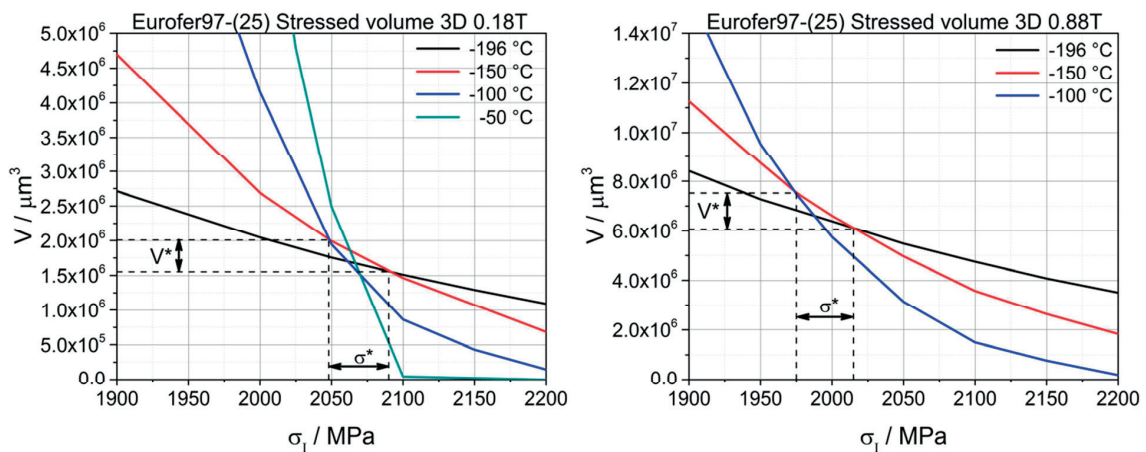


Figure 87: Stressed volume encompassed by the maximum principal stress at different temperatures for the 0.18T and 0.88T model loaded to $K_{Jc(0.01)}$ (see Table 9 and Table 10).

A perfect cross over as expected by the model was not found for both sizes. Instead a range of the critical parameters can be determined (see Table 11).

Table 11: Determined critical parameter σ^* - V^* range for the 3D 0.18T and 0.88T model.

Specimen size	σ^*_{\min} / MPa	σ^*_{\max} / MPa	V^*_{\min} / μm^3	V^*_{\max} / μm^3
0.18 T	2048	2090	$1.55 \cdot 10^6$	$2.01 \cdot 10^6$
0.88 T	1975	2015	$6.07 \cdot 10^6$	$7.52 \cdot 10^6$

From the data in Table 11, it can be seen that the critical stress is a little lower for the 0.88T CT. Indeed, for the 0.18T CT specimens, the upper critical stress range reaches 2090 MPa whereas for the 0.88T CT model a value of 2015 MPa was determined. As far as the critical volume is concerned, the two models resulted in V^* values of the same magnitude but they differ about factor 4. This apparent contradiction with the predictions of the σ^* - V^* model is discussed in detail in the next chapter. There is no result shown from the FE simulation for the 0.88T model at -50 °C as the desired load level was not reached due to excessive distortion of the elements at the crack tip. However, from the 0.18T model results, one can conclude that in principle FEM calculations obtained at three temperatures ranging from -196 and -100 °C are enough to define the critical parameters (see left in Figure 87).

As a next step, a 2D 0.18T CT model was used to determine the critical parameters σ^* - V^* to be compared with the 3D model. The material properties input were the same as for the 3D model. However K_{Jc} was determined by the J-integral around the crack tip by Abaqus. For comparison the K_{Jc} values were calculated as in the 3D model from the load/displacement curve as well (see Table 12).

Table 12: K_{Jc} lower bound values at different temperature for the 0.18T sized specimen and the K_{Jc} values where stress/strain fields were calculated from the 2D CT model. D is the difference between those in percent. $K_{Jc-FEM1(0.01)}$ was calculated by the J integral and $K_{Jc-FEM2(0.01)}$ by the load/displacement curve.

T / °C	$K_{Jc(0.01)} / \text{MPa m}^{1/2}$	$K_{Jc-FEM1(0.01)} / \text{MPa m}^{1/2}$	D / %	$K_{Jc-FEM2(0.01)} / \text{MPa m}^{1/2}$	D / %
-196	16.26	16.27	<0.1	16.07	-1.2
-150	23.52	23.52	0	23.24	-1.2
-100	43.26	43.30	<0.1	42.77	-1.2

In Table 8, it can be seen that the fracture toughness values obtained from the J integral are slightly larger than those from the load/displacement curve but in excellent agreement. Thus, the K_{Jc} values obtained from the J-integral are used. Due to the lower computational costs of the 2D model, it was possible to reduce the increment size to reach K_{Jc} values very close to the intended ones (see Table 12). Again the stress/strain fields at the crack tip at each temperature were analyzed.

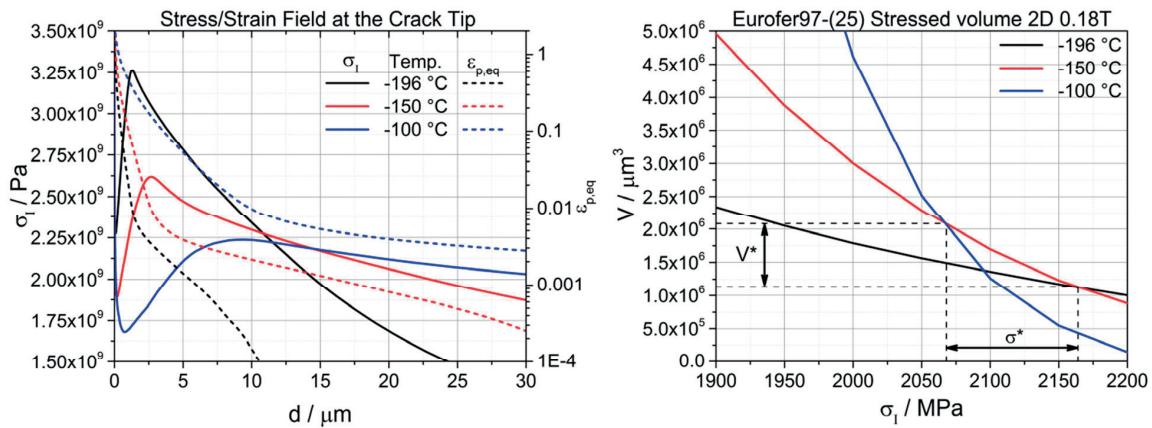


Figure 88: Results of the 2D 0.18T FE model loaded to $K_{Jc(0.01)}$ (see Table 12). Left: Maximum principal stress σ_1 and plastic equivalent strain $\epsilon_{p,eq}$ at the crack tip. Right: Stressed volume encompassed by the maximum principal stress at different temperatures.

Compared to the 3D 0.18T CT stress/strain fields, only one major difference can be seen which concerns the stress field at -196 °C. The 2D model calculates a slightly lower peak but the decrease in stress is more pronounced in the 2D model yielding in an overall narrower curve. In comparison the 2D curve reaches a stress of 1.5×10^9 Pa at a distance of about 24 μm whereas the 3D model reaches the same stress at 30 μm . However, the impact on the stress fields at -150 and -100 °C is much smaller and is manifested by a slight shift from the crack tip of the entire curve. The stressed area encompassed by the maximum principal stress at -196, -150 and -100 °C was calculated (see Figure 88). Similar to the result obtained for the 3D model, a perfect cross over of the three curves was not found. The resulting critical parameter ranges are given in Table 13.

Table 13: Determined critical parameter σ^* - V^* range for the 2D 0.18T model.

Specimen size	$\sigma^*_{min} / \text{MPa}$	$\sigma^*_{max} / \text{MPa}$	$V^*_{min} / \mu\text{m}^3$	$V^*_{max} / \mu\text{m}^3$
0.18 T	2068	2164	$1.13 \cdot 10^6$	$2.08 \cdot 10^6$

In order to compare the 2D model with the 3D one in terms of the V^* , the critical area A^* of the 2D model was multiplied by the thickness B of the 0.18T specimen. The determined critical volume V^* was found very

close to that obtained with the 3D model, see Figure 89 . In Figure 89 the difference in the stressed volume versus the maximum principal stress between the 3D and 2D for all three temperatures is plotted.

Besides the mentioned downward shift of the curve at -196 °C, the 2D stress curves at -150 and -100 °C are slightly shifted to higher stresses. For both models, the cross over range can be indicated as a triangle. In Figure 89, both triangles are shown illustrating the range of the critical parameters.

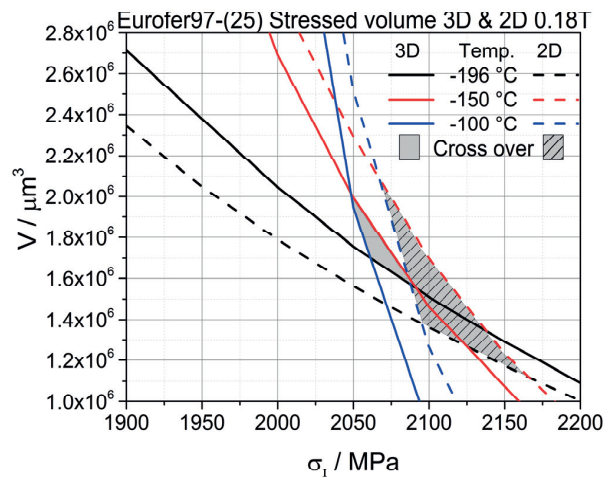


Figure 89: Stressed volume encompassed by the maximum principal stress at different temperatures for both 3D and 2D model loaded to $K_{Jc(0.01)}$ (see Table 9 and Table 12). Cross over range is indicated.

4.5.4.2 Modified boundary layer model with T-stress consideration

In order to simplify even more the 2D FE model, a modified boundary layer (MBL) model was run in small scale yielding (SSY) conditions. The boundary conditions were applied in accordance to the first two terms of the Williams expansion which takes the elastic T-stress into account [183] (see equation (24)). Using the T-stress approach, the stress field at the crack tip of the 2D 0.18T CT model was calculated. The same material constitutive behavior as for the 3D and 2D models was used. One advantage of the MBL model is that the desired K_{Jc} can be applied exactly through the boundary conditions (see equation (24)). To illustrate the impact of the T-stress on the stress fields, small scale yielding boundary conditions with and without T-stress were considered. The level of the T-stress selected is justified hereafter. In Figure 90, the maximum principal stress at the crack tip for the different models at -196, -150 and -100 °C are shown.

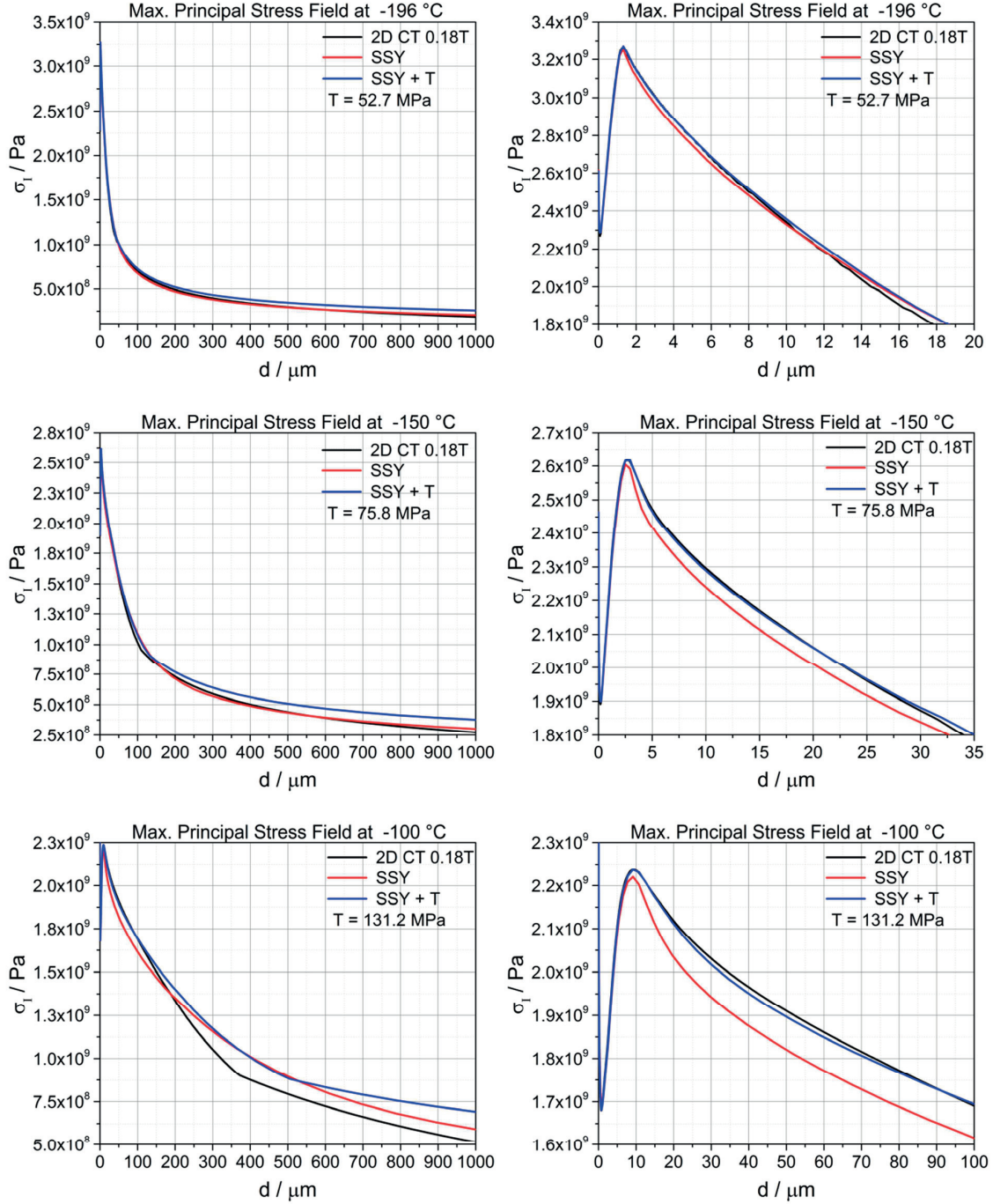


Figure 90: Maximum principal stress at the crack tip at different temperatures of the 2D 0.18T CT model, the MBL model without T-stress (SSY) and the MBL model considering T-stress (SSY+T).

As expected, the positive T-stress shifts the near tip stress field to higher values. At -196 °C the difference between the 2D 0.18T CT model and the MBL model without T-stress consideration is the smallest and increases with increasing temperature or K_{Jc} . Including the T-stress in the MBL model improves the match in comparison to the 2D CT model considerably. At large distance from the crack tip, the MBL stress field without T-stress and the 2D CT stress match each other better than the SSY+T model. However, the intention was to reconstruct the 3D stress/strain field in the process zone near the crack tip, which is the zone of

interest for the local approach to fracture. It was found that SSY model with a positive T stress can well reproduce the stress fields of CT specimen close to the crack tip.

The trend of the T-stress in the range of -196 to -100 °C is shown in Figure 91. We recall that here the T-stress was calculated according to equation (25). At -196 °C, the T-stress shows a rather low value and the impact on the stress is small as it can be seen in Figure 90. However, the T-stress increases with temperature and has the biggest value at -100 °C where the T-stress is more than two times greater as the corresponding value at -196 °C.

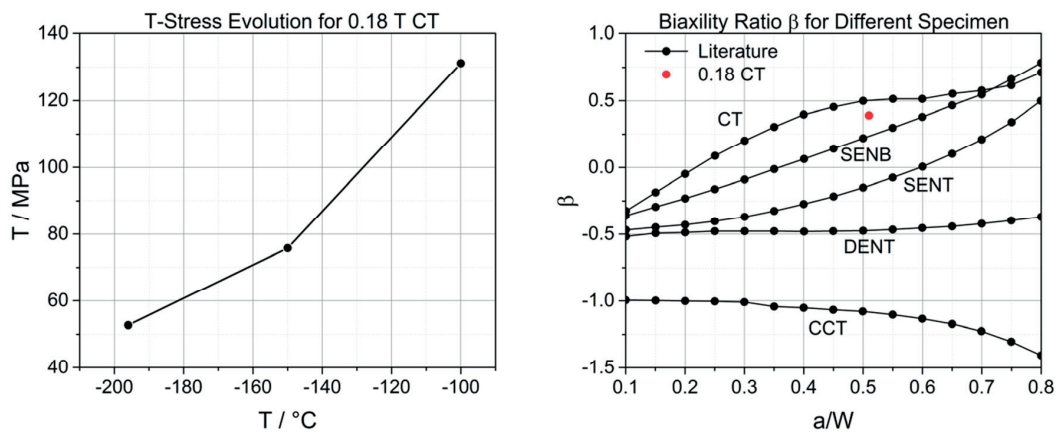


Figure 91: Left: Determined T-stress at different temperatures to fit the stress field of a 0.18T CT specimen at the lower bound. Right: Biaxiality ratio for different specimen including 0.18T CT result. Literature values adapted from [184] for homogeneous material.

In literature, the dimensionless representation of the T-stress which was introduced by Leever and Radon [185] is often used

$$\beta = \frac{T\sqrt{\pi a}}{K_I} \quad (27)$$

where a is the crack length and K_I represents the fracture toughness value in mode I. The obtained values can be found in Table 14.

Table 14: Calculated biaxiality ratio for the 0.18T CT specimen at different temperature.

T / °C	-196	-150	-100
β	0.39	0.39	0.37

For all temperature more or less the same β is calculated. In relation to literature, our values for the CT specimen are slightly lower but are consistent with the data in [185] (see right in Figure 91).

The critical parameters σ^* - V^* were determined for both the SSY with and without considering the T-stress. Both resulting curves can be found in Figure 92. As expected from the stress fields, the T-stress has an impact on the critical parameter range (see also Table 15). The critical stress range is shifted about 60 MPa to higher stresses for the SSY+T-stress model. In contrary, the critical volume was shifted to lower values reducing the range by 17 %.

The critical range values of the SSY+T model are similar to the 3D 0.18T CT model ones. However, the triangle shaped cross over area for the 3D model covers the smallest area whereas both simplified approaches in 2D increased it.

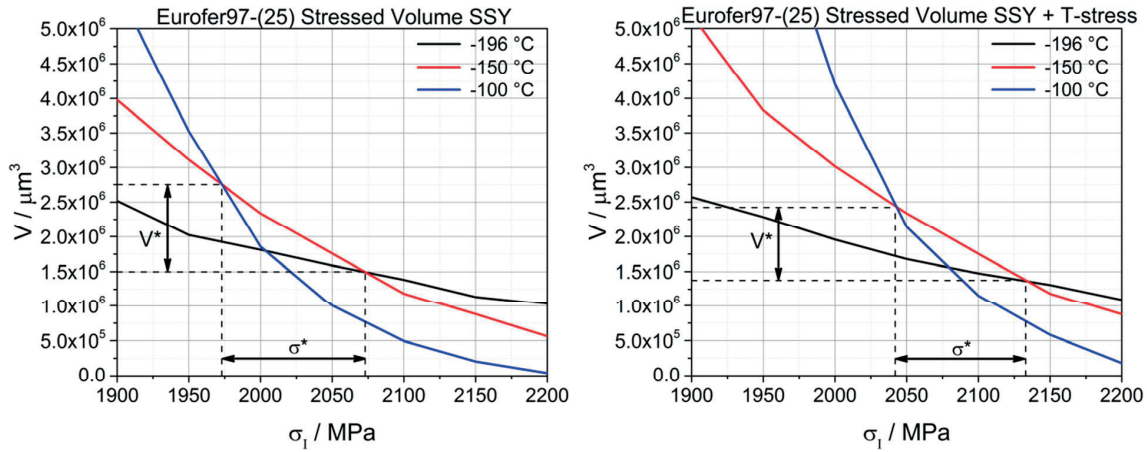


Figure 92: Stressed volume encompassed by the maximum principal stress at different temperatures. Left: MBL model without T-stress consideration Right: MBL model with T-stress consideration loaded to $K_{JC(0.01)}$ (see Table 12).

Table 15: Determined critical parameter σ^* - V^* range for the SSY model with and without T-stress consideration.

SSY Model	σ^*_{min} / MPa	σ^*_{max} / MPa	V^*_{min} / μm^3	V^*_{max} / μm^3
No T-stress	1973	2073	$1.50 \cdot 10^6$	$2.75 \cdot 10^6$
T-stress	2042	2133	$1.38 \cdot 10^6$	$2.42 \cdot 10^6$

This circumstance is illustrated in Figure 93 where the 3D and 2D model results are compared with the SSY+T model. Similar to the result obtained from the 3D and 2D CT model, the SSY+T model causes a shift of the cross over area to higher stress whereas the volume range is stretched in both directions in relation to the 3D CT reference. Compared to the 2D result, the SSY+T model shifts cross over area to lower volume and slightly lower stresses.

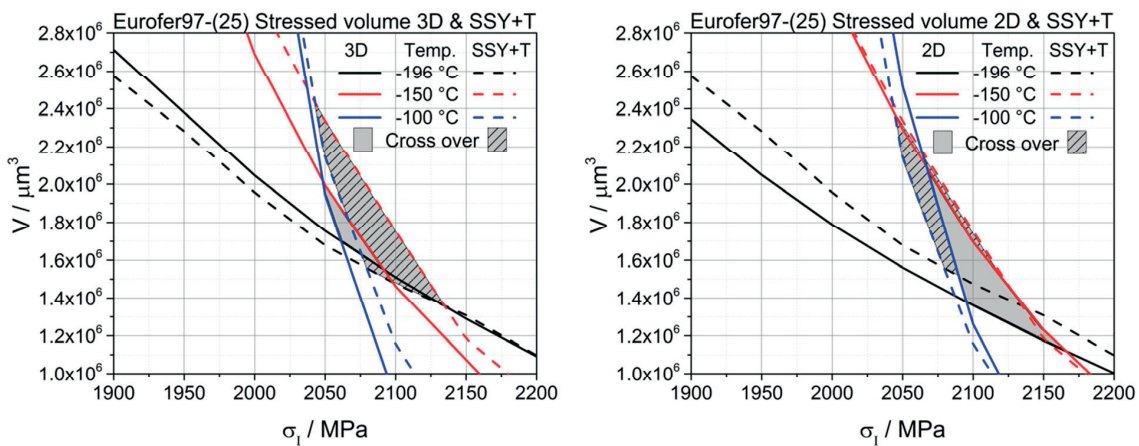


Figure 93: Stressed volume encompassed by the maximum principal stress at different temperatures for 3D and 2D model in comparison with the MBL model which considers the T-stress loaded to $K_{JC(0.01)}$ (see Table 12). Cross over range is indicated.

4.5.4.3 2D CT model with loading rate and thermal effects consideration

The strong plastic strain gradient that develops at the crack tip in a CT specimen evidently results in a corresponding plastic strain rate gradient. To address the influence of plastic strain rate on the stressed volume, a series of simulations were carried out by considering the strain rate dependence of the flow stress explicitly. From the previous results, the 2D 0.18T CT model was considered to study the impact of loading rate on the fracture parameters σ^* - V^* . Loading rate includes not only the strain rate dependence but also possible thermal effects due to heat dissipation from plastic deformation.

4.5.4.4 Quasi-static loading model with strain rate effects included

First, the impact of the strain rate gradient was studied for the 0.18T CT tests being done at quasi-static loading conditions. The specimen was loaded at a constant pin displacement rate of 0.1 mm/min. Implementation of the material properties was made in accordance to the standard tensile FE model described in section 3.7.1. The same strain rate data as for the standard tensile FE model (see section 4.5.2) were used, covering a strain rate range from $2.8 \cdot 10^{-5}$ up to $2.8 \cdot 10^{-1}$. Two different FEM analysis methods were applied for the same 0.18T CT model, namely a model which only considers the strain rate effect and a thermal one which considers both thermal and strain rate effects. In the following the two models will be named as "strain rate" and "thermal" respectively.

FEM calculations were done at -150 and -100 °C and were compared with the previous 2D 0.18T CT FE results, which will be referred to as "no strain rate" as no strain rate sensitivity of the flow stress is considered in the Abaqus input. The resulting stressed volume curves versus maximum principal stress for "no strain rate", "strain rate" and "thermal" model can be found in Figure 94. In both analyses, the implementation of loading rate sensitivity in the FE model caused a considerable shift stress of the cross-over of the two curves.

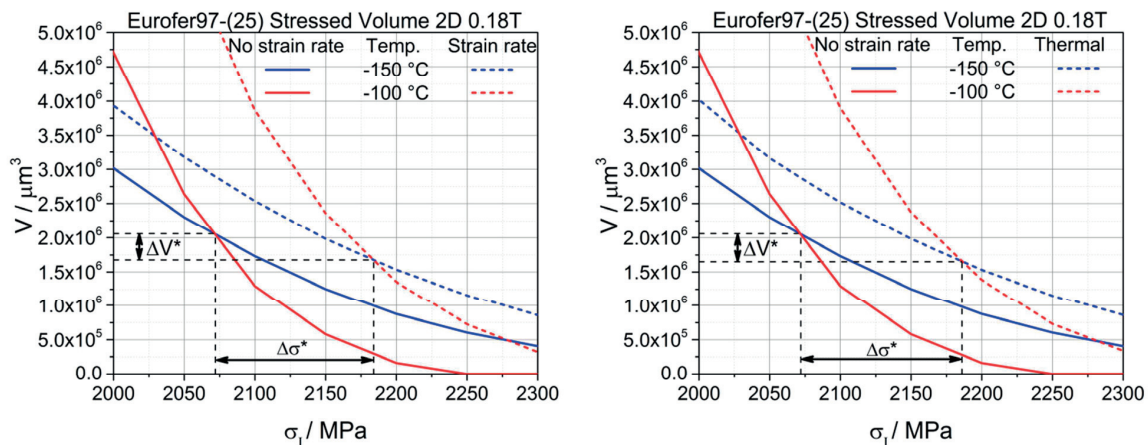


Figure 94: Stressed volume encompassed by the maximum principal stress at different temperatures loaded to $K_{Jc(0.01)}$ (see Table 17). Comparison of "no-strain rate", "strain rate" and "thermal" FEM analysis. Left: Only strain rate is considered Right: Strain rate and thermal effects are considered.

The critical stress is shifted at the most by $\approx 6\%$ to a higher value which causes the critical volume to reduce by only $\approx 1\%$ (see Table 16). A comparison between the two loading rate models reveals that the thermal effect does not play an important role in quasi-static loading.

Table 16: Determined critical parameters σ^* - V^* for the quasi-static 0.18T CT FEM analysis. Difference between the “strain rate” and “thermal” model to the “no-strain rate” model is given.

2D 0.18T CT FEM	σ^* / MPa	V^* / μm^3	$\Delta\sigma^*$ / MPa	ΔV^* / μm^3
Strain rate	2184	$1.68 \cdot 10^6$	116	$0.4 \cdot 10^6$
Thermal	2186	$1.65 \cdot 10^6$	118	$0.43 \cdot 10^6$

Clearly and as expected, in quasi-static loading the energy dissipated into heat has enough time to conduct from the plastic zone at the tip to the bulk of the specimen which acts as a heat sink. Therefore, the plastic zone does not heat up significantly. As before, the stress and strain rate fields at the crack tip were analyzed at K_{Jc} values that slightly differ from the intended ones ($K_{Jc(0.01)}$) (see Table 17).

Table 17: K_{Jc} lower bound values at different temperature for the 0.18T sized specimen and the K_{Jc} values where stress/strain fields were calculated from the 2D CT “strain rate” and “thermal” model. D gives the maximum difference between those in percent.

T / °C	$K_{Jc(0.01)}$ / $\text{MPa m}^{1/2}$	$K_{Jc\text{-FEM Strain rate}}$ / $\text{MPa m}^{1/2}$	$K_{Jc\text{-FEM Thermal}}$ / $\text{MPa m}^{1/2}$	D _{max} / %
-150	23.52	24.46	24.63	4.7
-100	43.26	44.33	42.41	2.5

In Figure 95, the strain rate effect on the stress fields at the crack tip is shown. The stress fields at both temperatures are shifted to higher stresses. At -150 °C, the peak stress increases by about 217 MPa whereas the shift is lower at larger distance to the crack tip. The same behavior was found at -100 °C but less pronounced yielding in an increase of about 140 MPa. At larger distance from the crack tip, the loading rate effects do not show any influence anymore. This is due to the fact that the plastic strain rate gradient is confined at the crack tip (see right in Figure 95). For instance, the mechanical strain rate at -150 °C drops within less than 10 μm from 0.1 s^{-1} to a constant value around $2.8 \cdot 10^{-4}$ which is within the rough estimate done for the 3D FEM analysis. In Figure 95, only the thermal result obtained at -150 °C is presented due to the fact that the curve perfectly matches with the “strain rate” results. The thermal effects do not have any significant impact onto the stress field at the tip.

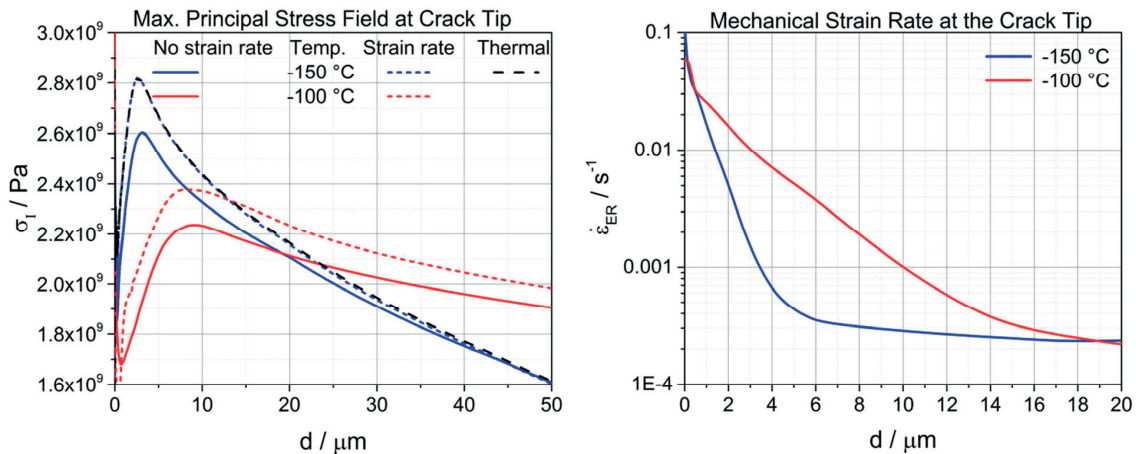


Figure 95: Comparison of static and quasi-static FEM analysis of the 2D 0.18T CT FE model at different temperatures loaded to $K_{Jc(0.01)}$ (see Table 17). Left: Maximum principal stress at the crack tip. Right: Mechanical strain rate at the crack tip.

From the obtained results it is concluded that even at a slow displacement rate of 0.1 mm/min the strain rate effects do show an impact on the critical parameters.

4.5.4.5 Dynamic Loading

From the experimental 0.18T CT tests conducted at dynamic loading conditions, the T_0 reference transition temperature was increased by about 36 °C. In order to assess the predictability of the σ^* - V^* model under dynamic conditions, 2D 0.18T CT FE analyses at high loading rates were conducted. The FE model was loaded with a speed of 9.6 mm/min. The displacement rate was chosen in order to reach a similar loading rate as in the experimental CT tests of about $90 \text{ MPa m}^{1/2} \text{ s}^{-1}$. As such loading rates, high strain rates exist at the crack tip so that the input for Abaqus had to cover a strain rate range up to 28 s^{-1} .

Four different FEM analyses were conducted to highlight loading rate effects on the critical parameters. As a reference, the results obtained from the quasi-static loaded 2D 0.18T model with strain rate effects were used and called "Quasi+SR". Three variants of the dynamic model were run: one that takes into account only the strain rate ("strain rate"), one which consider strain rate and thermal effects ("thermal") and an additional one called "adiabatic". The difference between these last two models is that for the adiabatic model the thermal conductivity was set to zero. In the adiabatic model, the dissipated energy remains in the elements where it is generated. For the "thermal" model the same thermal conductivity as in section 4.5.2 was used.

To assess the impact of the four different FEM analyses, an examination at -150 °C was executed. This temperature selection was done because it was found from the standard tensile tests that the thermal effects are most pronounced at this temperature. The stress fields of the FE models were extracted as close as possible of the lower bound of the dynamic master-curve (see Table 18).

Table 18: K_{Jc} lower bound values at -150 °C for the 0.18T sized CT specimen and the K_{Jc} values where stress/strain fields were calculated from various the 2D CT models. D is the difference between those in percent. $K_{Jc-FEM(0.01)}$ was calculated by the J integral.

FE Model	$K_{Jc(0.01)} / \text{MPa m}^{1/2}$	$K_{Jc-FEM(0.01)} / \text{MPa m}^{1/2}$	D / %
Strain Rate	17.12	17.38	1.5
Adiabatic		17.39	1.6
Thermal		17.39	1.6

In Figure 96 the extracted maximum principal stresses at the crack tip are shown.

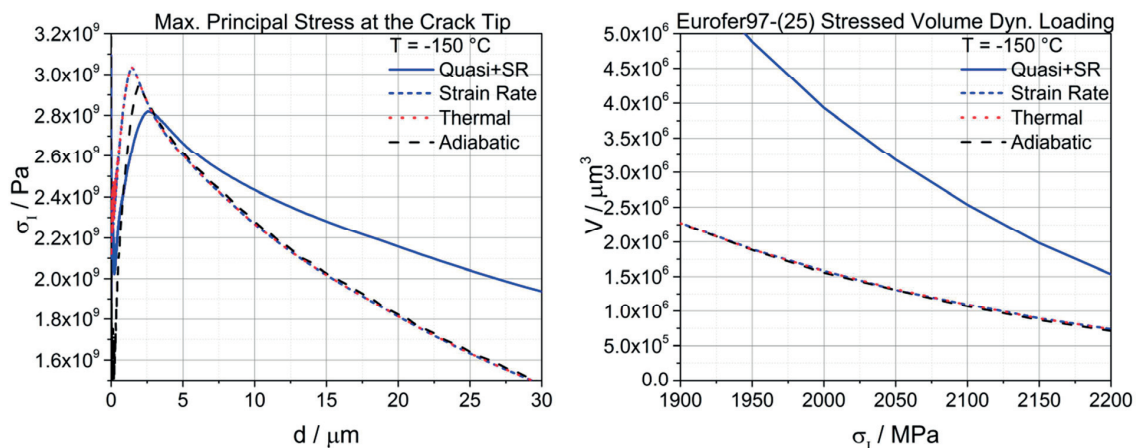


Figure 96: Comparison of the dynamic loaded 2D 0.18T CT models with "Quasi+SR", "strain rate", "adiabatic" and "thermal" analysis at -150 °C loaded to $K_{Jc(0.01)}$ (see Table 18). Left: Maximum principal stress at the crack tip. Right: Stressed volume encompassed by the maximum principal stress.

Similar to the quasi-static test, the strain rate effect shifts the peak to higher stresses of about 210 MPa in comparison to the “Quasi+SR” model. Therefore an increase in loading rate of about 100 times causes a 50 % higher peak stress.

The two other models “adiabatic” and “thermal” shifted the stress field. For the “thermal” analysis no difference to the “strain rate” model can be seen. However, the “adiabatic” result shows a slight decrease of the peak stress in comparison to the strain rate model in the order of 90 MPa (see Table 19). In addition the peak is positioned about 37 % further distant to the crack tip.

Table 19: Maximum principal stress at the peak and position for the four FEM analyses at -150 °C. d_p is the peak position and σ_{Ip} the peak stress.

FE Model	$d_p / \mu\text{m}$	σ_{Ip} / Pa
Static	2.56	$2.82 \cdot 10^9$
Strain Rate	1.46	$3.03 \cdot 10^9$
Thermal	1.46	$3.03 \cdot 10^9$
Adiabatic	2.00	$2.94 \cdot 10^9$

Although a difference in the stress field between the “thermal”, “adiabatic” and “strain rate” models can be seen, the impact on the stressed volume is marginal (see Figure 96). The dynamic loading clearly decreased the stressed volume due to the narrower peak. As seen in the stress field at the crack tip the stressed volume for the “strain rate” and “thermal” analysis do not show any difference and are on top of each other. For the “adiabatic” analysis the lower peak stress in the stress field has almost no impact. The “adiabatic” stressed volume is only slightly lower than the strain rate and thermal analysis volume and can be therefore neglected.

Thus the main effect of dynamic loading on the stressed volume is related to strain rate mainly. In order to better understand this result the temperature and plastic strain at the crack tip of both the “thermal” and the “strain rate” model were analyzed (see Figure 97).

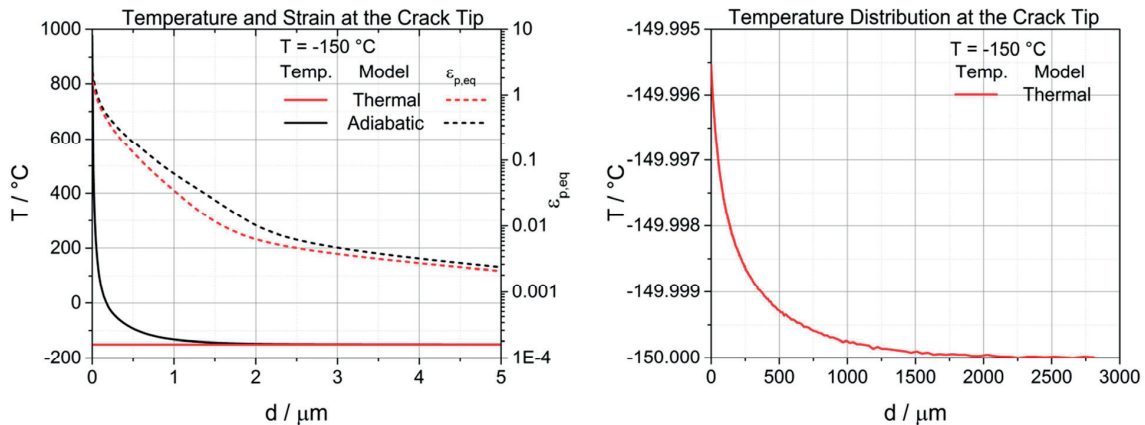


Figure 97: Comparison of the dynamic loaded 2D 0.18T CT models with “adiabatic” and “thermal” analysis at -150 °C. Left: Temperature and plastic strain at the crack tip in Kelvin. Right: Temperature field from the “thermal” analysis.

Due to the large difference in the temperature distribution at the crack tip between the thermal and adiabatic models, the two temperature distributions are presented in separated graphs. The “adiabatic” model result is represented by the black line and shows at the crack tip an extreme temperature gradient with a maximum unrealistic value of 977 °C at the very tip. However, at about 2 μm distant from the crack tip, the

“adiabatic” model shows again the test temperature value of $-150\text{ }^{\circ}\text{C}$. The dynamic loading caused an increase in temperature of $1127\text{ }^{\circ}\text{C}$ at a very confined area. In contrary the “thermal” model gives an almost negligible increase in temperature of about $0.005\text{ }^{\circ}\text{C}$ at the crack tip. Noticeable is that the test temperature of $-150\text{ }^{\circ}\text{C}$ for the “thermal” model is reached at a distance of $2000\text{ }\mu\text{m}$ which is 1000 times further distant to the crack tip as for “adiabatic” model. The heat dissipated in the very confined plastic zone at the crack tip is not large enough to increase the temperature significantly: main body of the CT specimen acts as a heat sink.

The mechanical strain rate at the crack tip is compared in the left diagram in Figure 98. Concerning the “adiabatic” model the maximum strain rate (12.92 s^{-1}) represents a 40 % increase at the tip in comparison to the “strain rate” and “thermal” model. Similar to the quasi-static loading result, the strain rate stabilizes within $10\text{ }\mu\text{m}$ to a constant value of about 0.036 s^{-1} , which is three orders of magnitude lower as that at the crack tip. Although the temperature differs a lot between the two investigated models, the impact onto the strain rate seems to be small. However, it has to be noted that only flow curves up to $-50\text{ }^{\circ}\text{C}$ were used as an input. Still, it is not expected that further input will affect the result as the “thermal” model in fact did not heat up at all but shows a similar output as the “adiabatic” model.

From the obtained results mentioned above it was decided to conduct another 2D 0.18T CT “strain rate” model at -100 and $-50\text{ }^{\circ}\text{C}$ to analyze the impact of dynamic loading onto the critical parameters of the local approach to fracture (see Figure 98).

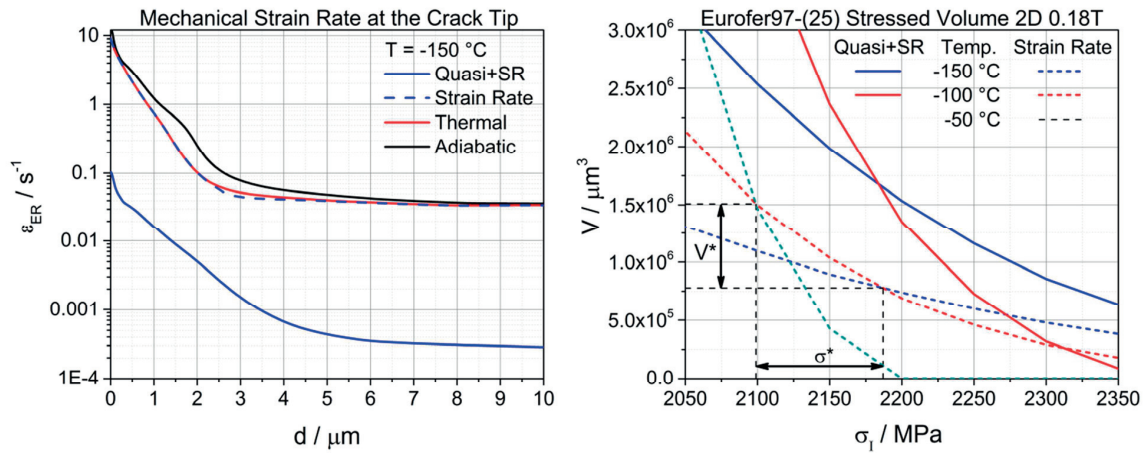


Figure 98: Left: Mechanical strain rate at the crack tip for the different models loaded to $K_{Jc(0.01)}$ (see Table 17). Right: Stressed volume encompassed by the maximum principal stress at different temperatures. Comparison of the “Quasi+SR” and “strain rate” FEM analysis.

Considering the strain rate shifted the crossover of the resulting stressed volume encompassed by the maximum principal stress at -150 and $-100\text{ }^{\circ}\text{C}$ to a similar stress value as for the “Quasi+SR” analysis but to lower volume (see Table 20). The cross over between the -100 and $-50\text{ }^{\circ}\text{C}$ shows a volume which is closer to the “Quasi+SR” result but at a lower stress.

The difference in volume can be explained with the difference in the stress field. For the dynamic condition a higher but much narrower peak was obtained compared to the quasi-static FEM which causes a reduction in stressed volume.

Table 20: Determined critical parameters σ^* - V^* for the dynamic test using the “strain rate” 2D 0.18T CT FEM analysis. Difference D between the dynamic and quasi-static results is given in %.

Specimen size	σ^*_{\min} / MPa	σ^*_{\max} / MPa	V^*_{\min} / μm^3	V^*_{\max} / μm^3
0.18 T	2099	2187	$0.78 \cdot 10^6$	$1.51 \cdot 10^6$

This result may indicate the more brittle behavior of the dynamic tested CT. The FE models taking into account the thermal effects indicate that the impact on the critical parameters at dynamic loading conditions studied here is limited.

4.5.4.6 2D Disk CT model, Eurofer97-(14)

Fracture toughness tests for the Eurofer97-(14) batch were carried out with 0.14T disk CT (DCT) specimens. To determine the critical parameters σ^* and V^* of the Eurofer97-(14) batch, a 2D plane strain DCT FE model was developed.

The critical parameters had to be recalculated for the unirradiated Eurofer97-(14) because it shows a lower T_0 as the Eurofer97-(25). We recall that T_0 (≈ -94.5 °C) was experimentally determined with 0.14T DCT specimens. A 2D model was used to reduce computational costs and simulations were done at four temperatures, -137, -120, -100 and -50 °C, where the plastic flow properties obtained from the unirradiated DTS were used as input. From the previous quasi-static FEM analysis results, it is known that the effect of strain rate on the critical parameters is not completely negligible. However, as the detailed strain rate dependent flow stress analysis was conducted for the Eurofer97-(25) batch, only the flow curves obtained at a strain rate of $5.56 \cdot 10^{-4} \text{ s}^{-1}$ were used and no modelling of strain rate and thermal effects were done.

The stressed volume encompassed by σ_I was determined at the lower bound calculated with $T_0 = -95.4$ °C, using the ASTM standard master-curve parameters (equation (15)). In Figure 99, the cross over range of the $V(\sigma_I)$ curves is shown. The result at -50 °C is not given as the determined stressed volume is almost zero around 2000 MPa. The observation indicates that 0.14T DCT specimens suffer from significant constraint loss at -50 °C. Actually, the M-value associated with K on the lower bound at -50 °C is about 30, which is way too low to ensure plane-strain condition as simulated by the 2D model.

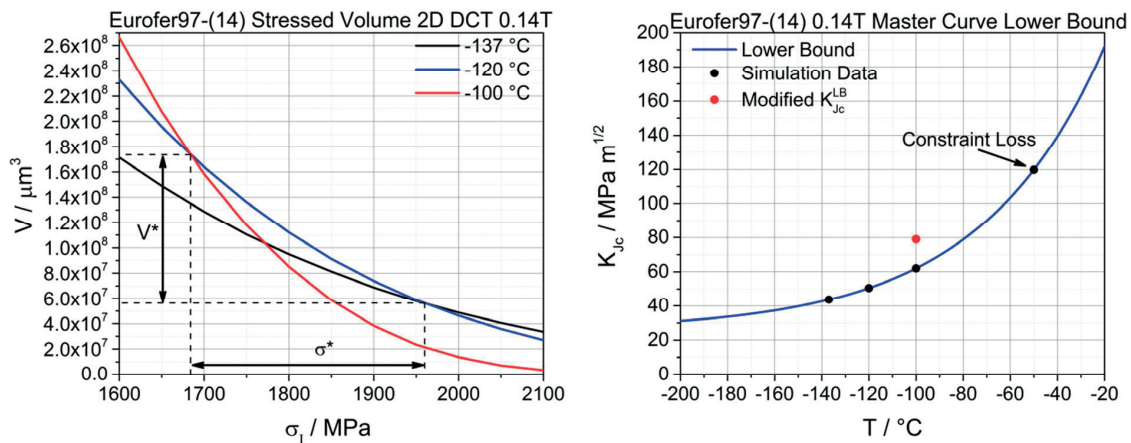


Figure 99: Left: Stressed volume encompassed by the maximum principal stress at different temperatures for the 2D DCT 0.14T model. Right: 1% Lower bound for the 0.14T CT indicating the data extraction from simulation.

Table 21: Determined critical parameter range σ^* - V^* for the 2D 0.14D CT FEM analysis.

DCT Model	σ^*_{\min} / MPa	σ^*_{\max} / MPa	V^*_{\min} / μm^3	V^*_{\max} / μm^3
0.14T	1684	1960	$5.63 \cdot 10^7$	$1.74 \cdot 10^8$

From the three curves $V(\sigma_I)$ at the lowest temperatures, a rather extended cross over is obtained (see Table 21). This is likely to be due to the curve at -100°C which crosses the other two curves at a relatively low maximum principal stresses, with a minimum of 1684 MPa. One possible and reasonable reason is that the lower bound considered is a little bit too conservative (too low values). In section 4.4.1, we assumed that Eurofer97-(14) is well described by the standard master-curve, which may not be strictly correct. In fact, the correct Eurofer97-(14) master-curve and related lower bound may be a little steeper, similar to Eurofer97-(25). However, no shape assessment of the Eurofer97-(14) master-curve shape has been done yet. Assuming a lower bound slightly steeper, by increasing the lower bound value at -50°C by $17 \text{ MPa m}^{1/2}$ (see right diagram in Figure 99) is sufficient to produce a unique cross over (see Figure 100). In this case, the determined critical parameters for Eurofer97-(14) can be found in Table 22. Note also that the critical volume increased roughly by one order in magnitude in comparison to the Eurofer97-(25) batch.

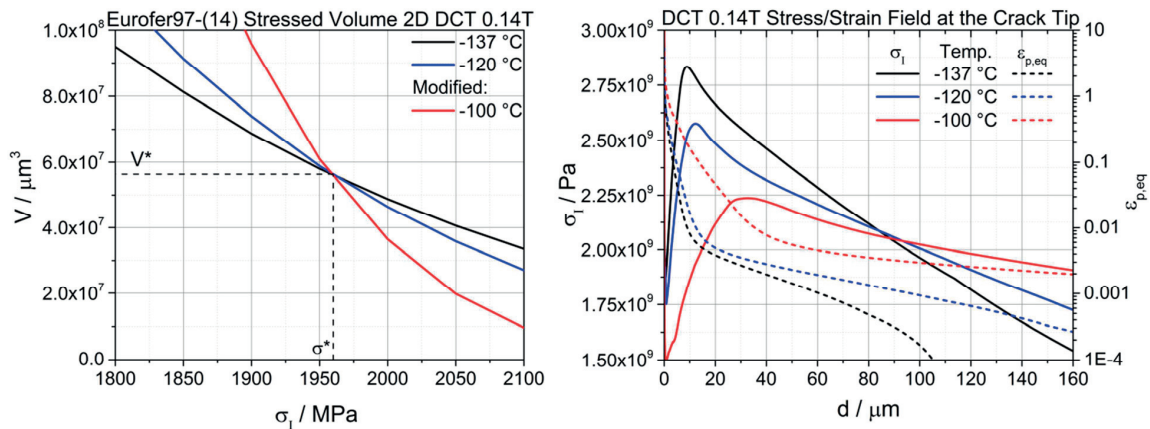


Figure 100: Left: Stressed volume encompassed by the maximum principal stress at different temperatures for the 2D DCT 0.14T model using the modified result loaded to $K_{Jc(0.01)}$ (see Table 23). Right: Maximum principal stress σ_I and plastic equivalent strain $\varepsilon_{p,eq}$ at the crack tip.

Table 22: Determined critical parameter range σ^* - V^* for the 2D 0.14D CT FEM analysis using the modified cross over.

DCT Model	σ^* / MPa	V^* / μm^3
0.14T	1960	$5.63 \cdot 10^7$

Concerning the stress/strain fields at the tip, it can be seen that the peak stress decreases with increasing temperature (see right diagram in Figure 100). The stress fields were extracted close to the desired lower bound K_{Jc} value (see Table 23). Similar to the 3D and 2D 0.18T CT results, the three maximum principal stress curves join each other but at different values. In terms of σ_I , the Eurofer97-(25) batch analysis showed an intersection of the three temperature curves around 2250 MPa whereas for the Eurofer97-(14) a value of 2050 MPa is obtained. Even more pronounced is the difference in distance to the crack tip where the three σ_I curves join each other at $\sim 88 \mu\text{m}$ which is almost nine times bigger than for the Eurofer97-(25) result.

Table 23: K_{Jc} lower bound values at different temperatures for the 0.14T sized specimen and the corresponding K_{Jc} values where the stress/strain fields were calculated from the 2D CT model. D is the difference between those in percent. The K_{Jc} at -100 °C is the modified one.

T / °C	$K_{Jc(0.01)} / \text{MPa m}^{1/2}$	$K_{Jc-FEM(0.01)} / \text{MPa m}^{1/2}$	D / %
-137	43.69	43.58	<0.1
-120	50.56	50.38	<0.1
-100	79	78.94	<0.1

Chapter 5 Discussion

This chapter begins with a discussion on the tensile properties of Eurofer97, including the temperature dependence, the strain rate and the effect of irradiation. Local approach models to fast fracture are discussed in more detail to assess the difference and similarity of different finite element models of stationary loaded crack models on the structure of the near tip stress field and their capacity to predict dynamic brittle fracture and embrittlement due to irradiation.

5.1 Tensile properties of Eurofer97

Standard and non-standard tensile test were conducted to determine the tensile properties of Eurofer97 in unirradiated and irradiated condition. In this section, the temperature and strain rate dependence of the yield stress is discussed. Hardening due to irradiation obtained from the DTS tests are compared with literature data. The strain hardening behavior is briefly discussed for unirradiated and irradiated Eurofer97.

5.1.1 Temperature and strain rate dependence of the yield stress

The tensile tests were performed to derive as completely as possible the constitutive behavior of the two heats of Eurofer97 investigated in this work. A precise description of the constitutive behavior in terms of temperature and strain rate is critical to determine the temperature and loading rate effects on the near tip stress/strain fields of fracture specimens, which are in turn used to calibrate the critical parameters of local fracture criteria. The structure of these fields was already shown to be quite sensitive to the strain-hardening law [141]. In addition, a large gradient of equivalent plastic strain exists at the crack tip that yields a corresponding plastic strain rate gradient. Thus, not taking into account the strain-rate dependence of the constitutive behavior remains a priori a simplification. With the current computing power, it is not justified any more to neglect the loading and strain rates, which we found to have an impact on the structure of the near tip stress field.

Temperature and strain rate dependence of the yield stress is presented in Figure 101. On the left, the data obtained in this work are plotted where one can see a strong temperature dependence below 200 K, which is typical of BCC metals and alloys. At higher temperature, the weak temperature dependence reflects essentially the decrease of the elastic constants. Note also that our yield stress data of Eurofer97-(14) is about 40 MPa lower than that of Eurofer97-(25). This is consistent with the fact that T_0 of Eurofer97-(14) is 17 °C lower than Eurofer97-(25), and with the simple relation $\Delta T_0 \approx C \Delta \sigma_y$ with $C \sim 0.57$.

The low temperature regime is the signature of the strong Peierls lattice friction acting on the screw dislocation segments as it was proven with a complete thermal activation analysis of the yield stress on two similar tempered martensitic steels [186]. The strain rate effect is also well marked in the low temperature, while practically absent above 200 K.

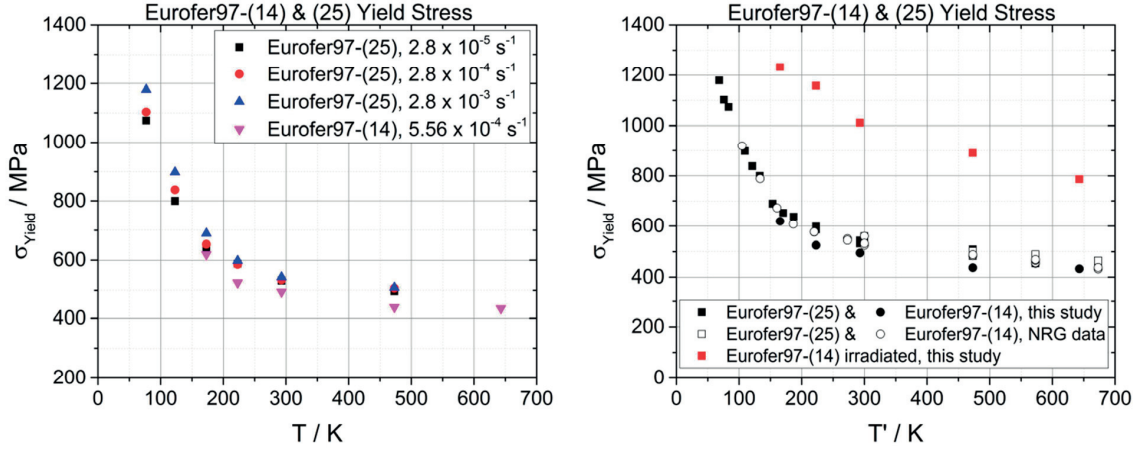


Figure 101: Eurofer97-(25) and Eurofer97-(14) yield stress versus temperature T and strain rate compensated temperature T' . Data from this study and from NRG [187].

This low temperature plastic strain rate behavior is well characterized by an Arrhenius equation of the plastic strain rate at the yield point:

$$\dot{\epsilon}_p = \dot{\epsilon}_0 \exp\left(-\frac{\Delta G(\sigma(T))}{kT}\right) \quad (28)$$

where ΔG is the activation energy of the dislocation rate controlling mechanisms, which is the nucleation of double kink on the screw dislocation [188]. $\dot{\epsilon}_0$ is only weakly dependent on σ and T and is usually considered constant. Thus, for a series of tests performed at different temperatures with $\dot{\epsilon}_p = \text{constant}$, it follows immediately that

$$\Delta G = kT \ln\left(\frac{\dot{\epsilon}_0}{\dot{\epsilon}_p}\right) = \alpha(\dot{\epsilon}_p) kT \quad (29)$$

The two previous equations allow defining the concept of strain rate compensated temperature T' in order to derive a single curve of σ versus T' . For a given σ , or equivalently for a given ΔG , obtained at different strain rates $\dot{\epsilon}_1$ and $\dot{\epsilon}_2$, one shows readily that the two temperature T_1 and T_2 are related by,

$$T_1 = T_2 \left[1 + \frac{1}{\alpha(\dot{\epsilon}_1)} \ln\left(\frac{\dot{\epsilon}_1}{\dot{\epsilon}_2}\right) \right] \quad (30)$$

$\dot{\epsilon}_1$ can be arbitrarily selected and referred as to a reference strain rate $\dot{\epsilon}_r$, to finally write the equation of the strain rate compensated temperature T' with respect to the chosen $\dot{\epsilon}_r$ as:

$$T' = T \left[1 + \frac{1}{\alpha(\dot{\epsilon}_r)} \ln\left(\frac{\dot{\epsilon}_r}{\dot{\epsilon}}\right) \right] \quad (31)$$

Determination of $1/\alpha$ on tempered martensitic steel was previously done [189]. For a reference strain rate equal to $2 \times 10^{-4} \text{ s}^{-1}$, $1/\alpha$ was equal to about 0.042. The value is close to that obtained by Cao al. on ferritic steels, who found 0.036 [190]. Using the equation (31) above, the strain rate compensated temperature

were calculated with respect to a reference strain rate of $2 \times 10^{-4} \text{ s}^{-1}$ and are plotted in Figure 101-Right. All the data obtained at different strain rates fall along the same curve as well as other data published [187]. Note that only the temperatures lower than 200K were strain rate compensated as the equation (31) is valid only for the Peierls mechanism at low temperature. Finally, we remind here that the irradiated data suggest that the temperature dependence of the yield stress is affected by irradiation to some extent (see Figure 101). In other words, the irradiation hardening $\Delta\sigma_y$ seems to depend on temperature. The irradiated data are however too scarce to draw firm conclusions regarding this issue.

In presence of thermally activated dislocation mechanisms, the strain rate is usually related to the activation volume V_a defined as:

$$V_a = -\frac{\partial \Delta G(\tau)}{\partial \tau} = kT \left(\frac{\partial \ln(\dot{\epsilon})}{\partial \tau} \right) \quad (32)$$

Note that in the previous the applied uniaxial stress σ was converted into a shear stress τ acting on gliding dislocation by dividing σ by the Taylor's factor M equal to 3. On the one hand, V_a and its stress dependence characterize the dislocation rate controlling process. On the other hand, as equation (32) shows, V_a is a measure of the strain rate sensitivity of the stress. V_a can be determined with our data shown in

Table 8 of section 4.2.2, where we indicated the stress change associated with a change of one order of magnitude in strain rate. A comparison of the activation volume of Eurofer97 with those obtained on the tempered martensitic steels F82H [186] is presented in Figure 74.

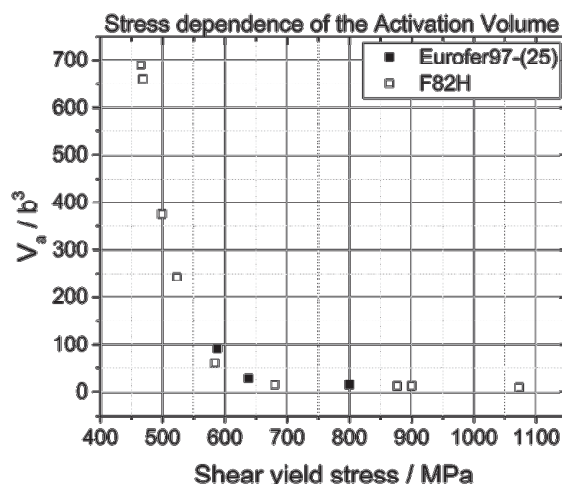


Figure 102: Activation volume in dependence of the shear yield stress for Eurofer97-(25) and F82H (from [186]).

The high stress corresponds to the low temperature regime with small value of V_a of the order of few tens of b^3 , where b is the amplitude of the Burgers vector of the $a/2\langle 111 \rangle$ dislocation, equal to 0.268 nm. Such small values of V_a are fully consistent with the models of double kink nucleation and propagation along the screw segments, which effectively controls the strain rate.

5.1.2 Irradiation-hardening

Our irradiation hardening data $\Delta\sigma_y$ at 20 °C and 200 °C could be compared to previously published data in Figure 103, [34]. At $T_{\text{test}} = 20 \text{ °C}$, the increase in yield stress is about 517 MPa, which is in good agreement with the dataset obtained after irradiation at SINQ from Y. Dai. The lines in the left plot of Figure 103 represent neutron irradiation hardening with saturation at high dose. From the single data point of this study,

only a small amount of additional hardening may be present. However, for the irradiation conditions considered here (11 dpa and 540 appm He) the hardening is essentially in line with neutron irradiation. A similar conclusion can be drawn from the DTS tested at 200 °C. The irradiation-hardening is about 453 MPa, which lies close to the dashed saturation curve (Figure 103 - right), [2]. Thus, we conclude that the He contribution to irradiation-hardening, if any, is quite small at 540 appm He.

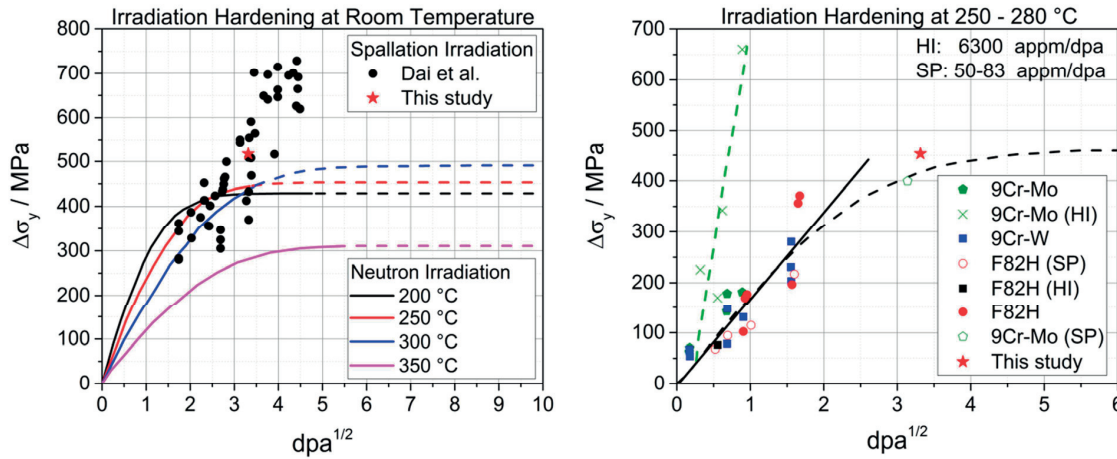


Figure 103: Yield stress increase due to irradiation compared with literature values. Left: At room temperature [34]. Right: At 200 °C [2].

5.1.3 Strain-hardening

The unirradiated tempered martensitic steels present a relatively low uniform elongation. We remind that only several percent (< 10 %) of plastic strain can be reached on the reduced activation tempered martensitic steels with standard specimens, independently of temperature. This situation arises because these steels have simultaneously low strain hardening rate and elevated flow stress, which yield rapidly to necking instability by lack of strain-hardening. Strain-hardening laws were previously established on unirradiated reduced activation tempered martensitic steels [167]. These laws were derived in the frame of the phenomenological model of Kocks, based on the competition between storage and annihilation of dislocations in the microstructure [191, 192]. In this approach, the increase of the flow stress stems from the accumulation of dislocations in the microstructure. A very good description of the strain-hardening rate from the yield point to the necking initiation was found. The dislocation storage rate was associated with the mean free path of dislocation taken as 1 μm representative of the dimensions of sub-blocks of tempered martensite laths. The annihilation rate was shown to increase with temperature, reflecting the thermally activated nature of these processes [167]. The strain-hardening laws were found consistent with a hardening rate characteristic of stage III that predict a saturation of the flow stress at strain extrapolated beyond the uniform strain. However, the strain-hardening of the tempered martensitic steel at large strain remains experimentally unexplored. While the inverse method was initially developed to determine the constitutive behavior of irradiated materials with low or even quasi-inexistent uniform elongation, the method was used to extract the true stress-strain curve of unirradiated non-standard and standard well beyond the strain at necking onset. Our results, presented in Figure 78 and Figure 79 of the previous chapter clearly indicated that there is actually no saturation of the flow stress. Indeed, to reconstruct the load-displacement curve after initiation of necking, true stress-strain curve with practically constant strain-hardening rate were employed up to large strain. This finding is in line with the results of Fang and Dahl [193] who showed by using a special tensile test technique applied on ferritic steels that the flow stress does not saturate at large

strains but increases linearly with strain. The deformation is then characterized by a linear strain-hardening, referred as to stage IV.

Interestingly, the tensile true stress-strain curves of the irradiated DTS specimens obtained with the inverse approach (see Figure 84) clearly demonstrate that, even after a dose of 11 dpa, the tempered martensitic steel keep their strain-hardening capacity. Indeed, the true stress-strain curves present a significant strain hardening rate up to a strain of at least 0.4 at every investigated temperature. We emphasize here again that obtaining the tensile true stress-strain curves of the material in irradiated conditions is a must to perform numerical stress calculations with finite element calculations.

5.2 Local approach to brittle fracture

Several FE models were considered in this work to determine, in the frame of a local approach of fracture, the critical stress state for fast fracture. Even with very detailed numerical models, the calibration of the critical parameters of any local approach of fracture remains challenging. In the following, issues and suggestions concerning the calibration are discussed in detail. Furthermore, the criterion calibrated on statically loaded unirradiated fracture tests is used to predict the transition temperature shift due to high loading rate and irradiation.

5.2.1 Specimen size dependent calibration

The σ^* - V^* model predicts brittle fracture when a critical stress σ^* encompasses a critical volume V^* , independent of temperature. In addition, the σ^* - V^* calibrated values should be independent of the specimen size used to calibrate them. From the 3D CT analysis, we found however that V^* of the 0.88T CT specimen was about 4 times higher than that of the 0.18T model (see Figure 87 and Table 11 previous chapter). We recall here that we calibrated the σ^* - V^* values to reconstruct the 1% failure probability bound of the master-curve, calculated for the corresponding specimen sizes and indexed at $T_0 = -80$ °C. The discrepancy between σ^* - V^* values of 0.18T and 0.88T CT specimens is believed to be the consequence of an improper specimen size scaling law. Initially, the critical parameters σ^* - V^* were determined for the 0.18T CT specimens and were compared with those of the 0.88T CT specimens on their respective lower bound, which were size adjusted according to the ASTM standard E1921 – 17a, i.e.:

$$K_1 = K_{\min} + (K_2 - K_{\min}) \left(\frac{B_2}{B_1} \right)^{1/4} \quad (33)$$

K_{\min} denotes the minimum stress intensity factor needed to trigger fracture, introduced in a Weibull statistical model to avoid a non-zero probability at an infinitesimal K value [194, 195]. However, for the σ^* - V^* model, there is a priori no K_{\min} threshold foreseen and therefore the size adjustment has to be done simply as:

$$K_1 = K_2 \left(\frac{B_2}{B_1} \right)^{1/4} \quad (34)$$

Note that these scaling laws derive from the fact that the stress area A scales with K^4 [196] so that the stressed volume V is equal to

$$V = B A = B c K^4 \quad (35)$$

In Table 24, the K_{Jc} values at the lower bound for the 0.18T model and the corresponding to 0.88T adjusted values with each scaling equation (33) and (34) are shown. It can be seen that with increasing K_{Jc} value the discrepancy between the two adjustment approaches reduces.

Table 24: K_{Jc} lower bound values for different CT sizes. The 0.88T sizes were adjusted from the 0.18T model by the master-curve (MC) equation (33) and by the local approach (LC) equation (34).

T / °C	0.18T $K_{Jc(0.01)} / \text{MPa m}^{1/2}$	0.88T MC adjusted $K_{Jc(0.01)} / \text{MPa m}^{1/2}$	0.88T LC adjusted $K_{Jc(0.01)} / \text{MPa m}^{1/2}$
-196	16.26	14.20	10.89
-150	23.52	19.07	15.75
-100	43.26	32.32	28.98

Depending on the specimen size adjustment considered (equation (33) or equation (34)), the predicted toughness is different, which in turn leads to a significant effect on σ^* - V^* . For the sake of completeness, the stressed volumes for both adjustment approaches are shown in Figure 104.

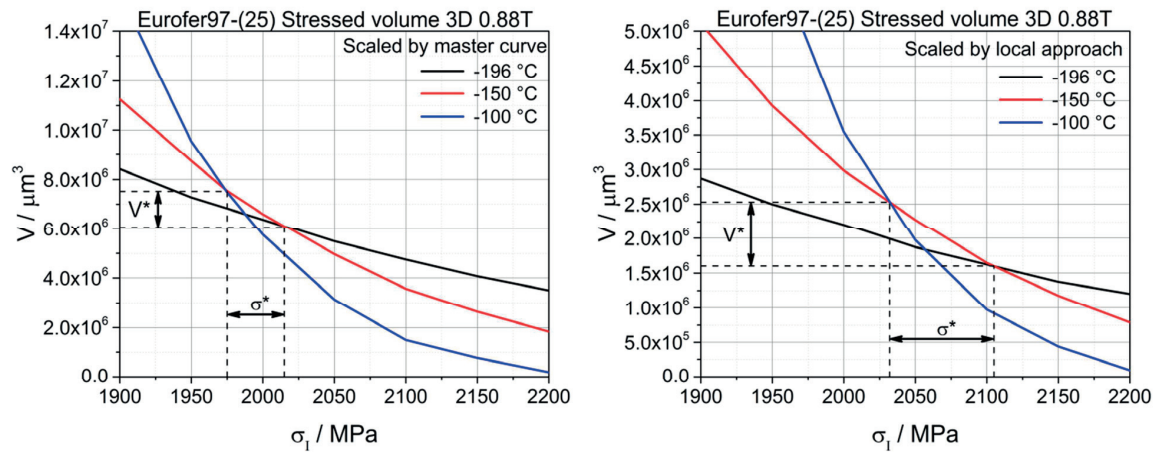


Figure 104: Stressed volume encompassed by the max principal stress at different temperatures for Eurofer97-(25) obtained from a 3D 0.88T FE model loaded to $K_{Jc(0.01)}$ (see Table 24). Left: Size was adjusted according to ASTM, equation (33). Right: Size was adjusted by local approach, equation (34).

The 0.88T CT adjusted K_{Jc} values according to equation (34) are lower than those obtained with equation (33) which causes a downward shift of the stressed volume curves at each temperature. As a consequence the crossover range is shifted considerably (see Table 25). The new crossover range for the 0.88T matches overall well with the 0.18T.

Table 25: Determined critical parameter range σ^* - V^* for the 3D 0.88T and 3D 0.18T CT FEM analysis.

CT Model	$\sigma^*_{\min} / \text{MPa}$	$\sigma^*_{\max} / \text{MPa}$	$V^*_{\min} / \mu\text{m}^3$	$V^*_{\max} / \mu\text{m}^3$
0.18T	2048	2090	$1.55 \cdot 10^6$	$2.01 \cdot 10^6$
0.88T	2032	2105	$1.60 \cdot 10^6$	$2.53 \cdot 10^6$

Applying the σ^* - V^* size adjustment (equation (34)) shows that the local approach to fracture gives consistent σ^* - V^* parameters for different CT sizes. Thus, it is clear that a consistent pair critical parameters σ^* - V^* can be obtained from any CT size but care has to be taken in the size adjustment.

We emphasize that the adjustment given by equation (34) does not consider a minimum toughness value K_{\min} , which basically leads to unphysical low toughness values for very thick specimen. Furthermore, it is known from experimental observation that CT specimens tested at the lower shelf (< -150 °C) do show a minimum toughness value. In order to account for this circumstance, we propose here a method which includes a minimum fracture toughness threshold in the frame of the σ^* - V^* model. The critical volume for a certain specimen size can be calculated by

$$V_1 = B_1 A^* = B_1 c K_1^4 \quad (36)$$

where B_1 is the thickness, K_1 the fracture toughness and c denotes a constant which depends on σ^* and constitutive behavior. Under plane strain and small scale yielding (SSY) condition, the critical areas shows a dependence on K_1 by $A^* = c K_1^4$. The SSY condition is met for the lower bound close to the lower shelf. At K_{\min} , where SSY conditions are present, A^* is therefore the same for any specimen size which leads to

$$V_{1,\min} = B_1 c K_{\min}^4 \neq V_{2,\min} = B_2 c K_{\min}^4. \quad (37)$$

Thus, V_{\min} is specimen size dependent. However, K_{\min} mediates the minimum critical area (or distance) ahead of the crack tip to propagate cracks [194] The toughness scaling between specimen sizes can then be done on the stressed volume increment. In other words, specimens of two different sizes will have the same failure probability if the stressed volume increment is the same:

$$\begin{aligned} V_1 - V_{1,\min} &= V_2 - V_{2,\min} \\ B_1 c K_1^4 - B_1 c K_{\min}^4 &= B_2 c K_2^4 - B_2 c K_{\min}^4 \end{aligned} \quad (38)$$

Therefore the new scaling law between two specimens can be written

$$K_1 = \left(K_2^4 \frac{B_2}{B_1} + K_{\min}^4 \frac{B_1 - B_2}{B_1} \right)^{1/4}. \quad (39)$$

In order to visualize the impact of the new proposed scaling law, the adjustment factor $c = K_1/K_2$ was calculated and compared to the corresponding c from the master-curve and local approach, where a conversion from 0.18T to 0.88T was calculated (see Figure 105).

For the master-curve and the proposed scaling laws, K_{\min} of $10 \text{ MPa m}^{1/2}$ was assumed. As the σ^* - V^* adjustment does not have a minimum threshold value, c shows a constant value of 0.67 for any K_{1c} (equation (34)). Therefore, a toughness value of $K_2 = 10 \text{ MPa m}^{1/2}$ obtained from a 0.18T CT specimen would lead to a toughness value of $K_1 = 6.3 \text{ MPa m}^{1/2}$ for the 0.88T specimen which is unrealistic low. On the contrary, the master-curve and proposed size adjustment would scale the toughness to $K_2 = K_1 = 10 \text{ MPa m}^{1/2}$. At fracture toughness values $K_{1c} > 40 \text{ MPa m}^{1/2}$, the size scaling according to equation (40) shows the same c as for the local approach. Following the size adjustment for the master-curve, different c values are obtained leading to different toughness values. The c value for the master-curve is about 12 % bigger as the other two scaling laws for a $K_1 = 40 \text{ MPa m}^{1/2}$.

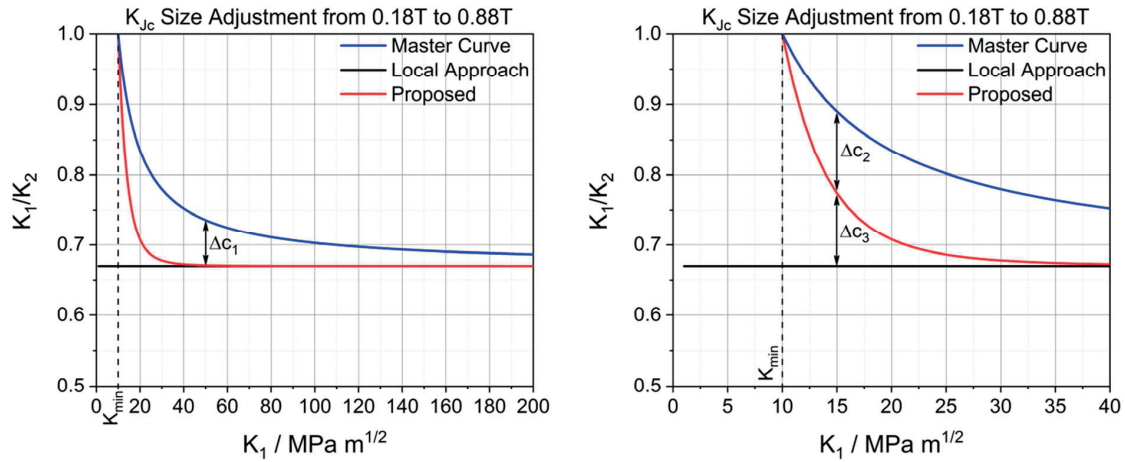


Figure 105: Adjustment factor $c=K_1/K_2$ in dependence of K_1 for the master-curve, local approach and the proposed method. K_{min} is indicated; K_1 correspond to 0.18T CT and K_2 to 0.88T CT.

Of course, the biggest discrepancy between the different scaling laws is observed at low K_{Jc} values close to K_{min} (see Figure 105). Owing to the minimum threshold value, the master-curve and proposed scaling law approach deviate from the adjustment factor of 0.67. Thus, if a minimum fracture toughness threshold has to be considered, a physically sound and well-established size scaling law must be used. This is especially true close to the lower shelf, where fracture tests on small irradiated specimens have to be performed to avoid excessive constraint loss. This requires a precise determination of K_{min} and extended testing with various specimen sizes to verify any postulated scaling law.

5.2.2 Impact of flow properties, strain rate and thermal effects

The impact of the different FE model approaches was studied and analyzed. The results indicate that plain strain 2D models introduce a certain but moderate discrepancy with 3D models as far as the calibration of the σ^* - V^* values are concerned, provided that the focus is done in the lower transition region. Other possible sources of uncertainty lie in the details of the plastic flow properties. The impact of these details was assessed. First, the sharpness of transition from elastic to plastic behavior was studied by considering a smooth and an abrupt transition in the flow curve at -150°C (see Figure 106).

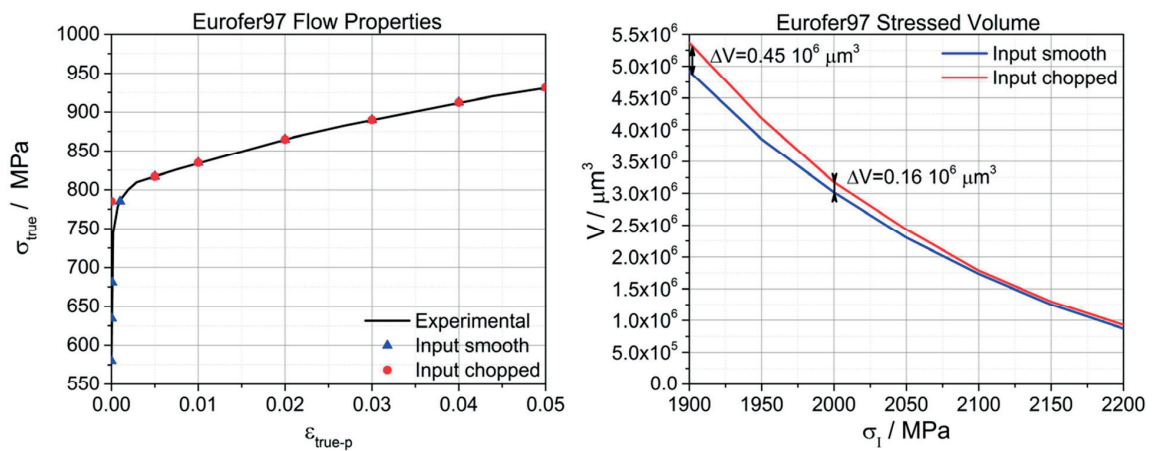


Figure 106: Left: Determined flow properties at -150°C with different elastic/plastic transition used as an input for Abaqus. Right: Impact of the different input on the stressed volume.

FEM analyses with these two different flow curve inputs were run and the stressed volume was extracted at $K_{Jc} = 23.52 \text{ MPa m}^{1/2}$, which corresponds to the lower bound for a 0.18T sized specimen with $T_0 = -78 \text{ °C}$ (see Figure 106). It was found that the stressed volume at high principal stresses is not affected. However, at low principal stresses, the two curves deviate from each other and do show a difference in volume of about $0.45 \cdot 10^6 \text{ } \mu\text{m}^3$ at 1900 MPa. An inaccurate transition from elastic to plastic deformation by neglecting the smooth transition in the flow curve has an impact on the stressed volume up to about 10 % for principal stress values very close to the local fracture stress.

In literature, most of the reported numerical simulations of the crack tip stress fields do not consider strain rate effects. However, we showed in this work that, at a quasi-static loading rate of 0.1 mm/min for a 0.18T CT specimen, the strain rate has to be considered. Considering strain rate effects in a FEM is more demanding as the strain rate sensitivity has to be determined and the computational costs increase. In order to simplify the approach it was investigated if the quasi-static 0.18T CT analysis is dominated by a certain strain rate. In other words, it was tried to find a single strain rate which allows reproducing the stress/strain fields at the crack tip sufficiently. To do so a rough estimate was made by considering the plastic strain at the peak stress at the lower bound. For the quasi-static 0.18T analysis at -150 °C the plastic strain is about 1 % at the peak stress which corresponds to a strain rate of $4 \cdot 10^{-4} \text{ s}^{-1}$. Two different strain rates were chosen, as input close to the estimated one (see Figure 107).

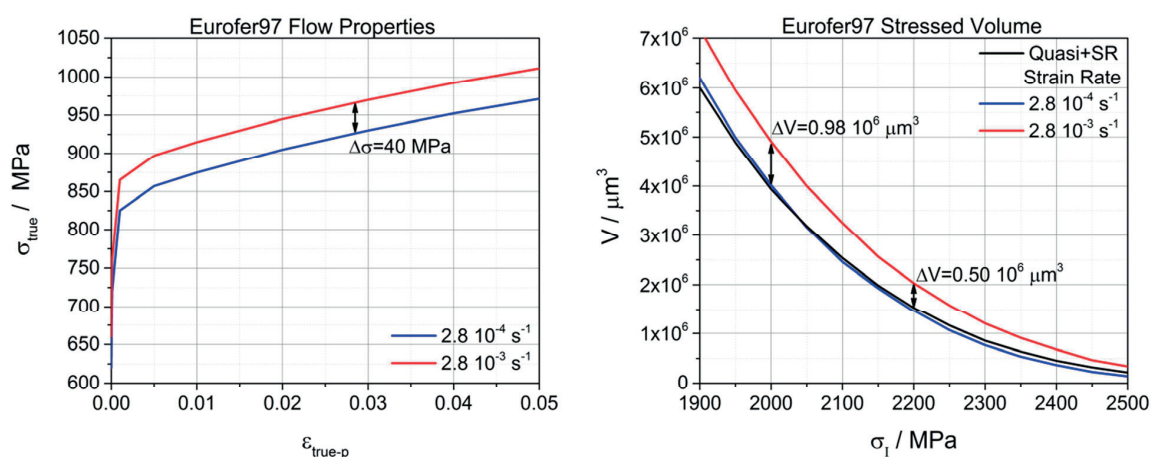


Figure 107: Left: Flow properties at -150 °C for two strain rates. Right: Stressed volume caused from the quasi-static loading FEM considering strain rate effects in comparison to FEM results obtained from a single strain rate.

From the two conducted simulations with only a single flow curve as an input the stressed volume at the corresponding lower bound was extracted and compared to the quasi-static FEM which considers strain rate effects (see Figure 107). Interestingly, the flow curve at a strain rate of $2.8 \cdot 10^{-4} \text{ s}^{-1}$ reproduces well the reference stressed volume (= black curve in Figure 107, FE simulation with strain-rate effect) over a large range of principal stresses. On the contrary the strain rate of $2.8 \cdot 10^{-3} \text{ s}^{-1}$ causes a considerably increase in the stressed volume. The discrepancy between the reference stressed volume is bigger at lower principal stresses and decreases with increasing stresses. In comparison to the previous discussed yield stress issue, the impact is much bigger. At 2000 MPa, the volume of the single strain rate analysis differs about $0.98 \cdot 10^6 \text{ } \mu\text{m}^3$.

These results show that considering only one representative strain rate for the FEM analysis is sufficient to reproduce the stressed volume calculated from the strain rate dependent FEM. However, this does not

imply that the structure of the stress field is reproduced. Therefore the maximum principal stresses for the three different FE models at the crack tip were compared (see Figure 108). The two models, which simply use a single strain rate as an input, do not reproduce the stress field well. In case of the $2.8 \cdot 10^{-4} \text{ s}^{-1}$ strain rate input, the peak stress is not reached and lies about 3.5 % lower than the reference field. On the other hand the $2.8 \cdot 10^{-3} \text{ s}^{-1}$ strain rate input is able to reproduce the peak stress well.

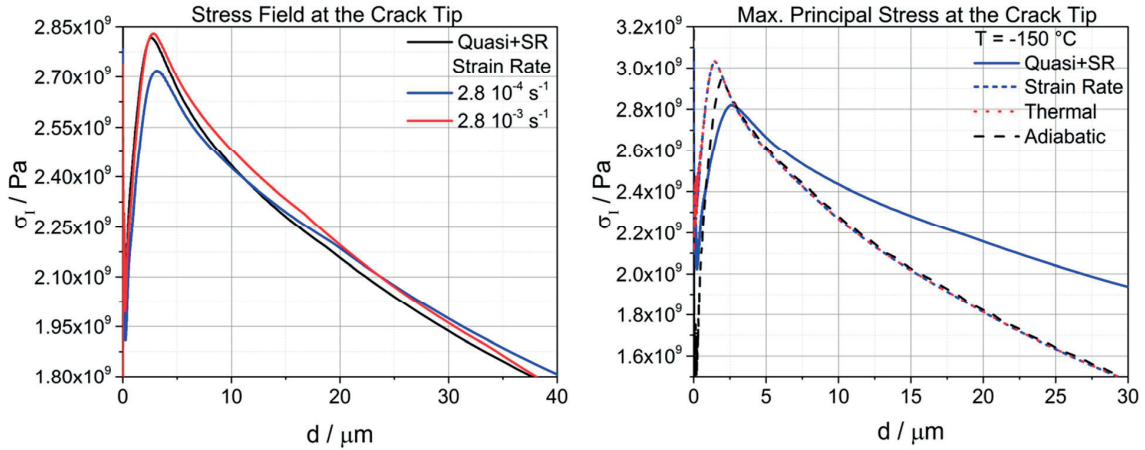


Figure 108: Maximum principal stress at the crack tip. Left: Quasi-static loading FEM considering strain rate effects in comparison to FEM with a single strain rate. Right: Impact of dynamic loading and thermal effects.

However both strain rates do not match well with the reference stress field at large distance from the crack tip. The plastic strain rate gradient at the crack tip requires to use a constitutive behavior strain rate to properly evaluate the structure of the stress field.

Finally, the impact of thermal effects was analyzed as well. As expected, thermal effects, which may cause softening of the material due to heat dissipation, can be neglected for quasi-static toughness tests. For the dynamic loading conditions considered in this work, it was found that the stress field is slightly modified by a lower peak stress (see Figure 108) if adiabatic conditions are assumed. However, the impact on the stressed volume is marginal and can therefore be neglected as well.

5.2.3 Prediction of dynamic toughness of Eurofer97-(25)

For the dynamically tested 0.18T CT specimens, the reference temperature T_0 ($= -42 \text{ }^\circ\text{C}$) of the master-curve was determined experimentally and the critical parameters $\sigma^* \cdot V^*$ were extracted from the FE simulations at the corresponding lower bound. $\sigma^* \cdot V^*$ parameters slightly differ from those obtained at quasi-static loading as was already shown in Figure 98. We remind here that the pair of $\sigma^* \cdot V^*$ was about ($2180 \text{ MPa} / 1.68 \cdot 10^6 \mu\text{m}^3$) for quasi-static loading, while it is around ($2140 \text{ MPa} / 1.15 \cdot 10^6 \mu\text{m}^3$) for dynamic loading. The capability of the $\sigma^* \cdot V^*$ to predict the shift in ΔT_0 associated with the dynamic loading was evaluated. To do so, the critical parameters at quasi-static loading were considered. We used $V^* = 1.68 \cdot 10^6 \mu\text{m}^3$ and four different σ^* around the quasi-static value of 2180 MPa to account for uncertainty and possible temperature dependence of $\sigma^*(T)$. The applied K_{Ic} values necessary to reach the corresponding stressed volume $1.68 \cdot 10^6 \mu\text{m}^3$ are shown in Figure 109.

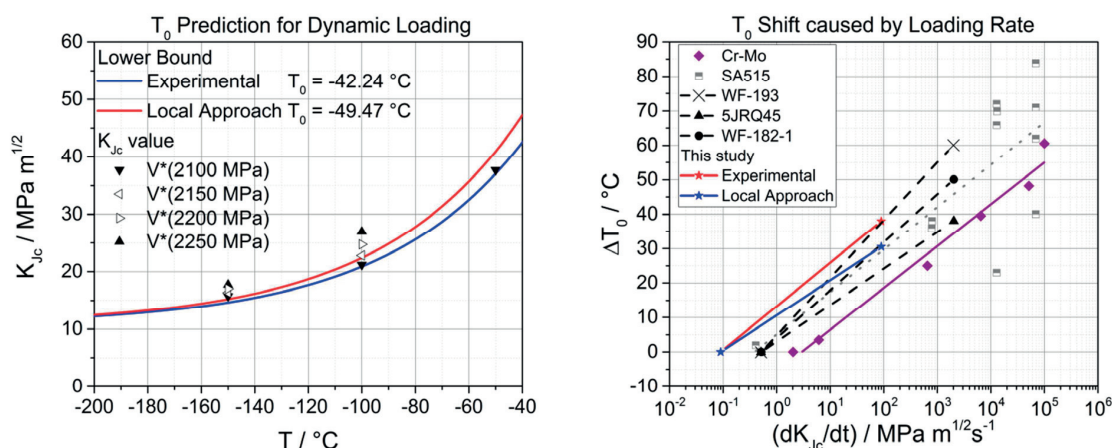


Figure 109: Left: Predicted T_0 using the local approach to fracture in comparison with the experimental result. K_{Jc} values obtained at different σ^* at $V^*=1.68 \cdot 10^6 \mu\text{m}^3$ are indicated. Right: Transition temperature shift ΔT_0 due to increased loading rate obtained from Eurofer97 in comparison with literature data (from [197, 198, 199]).

At -150 and 100 °C four different K_{Jc} were determined but at -50 °C, K_{Jc} could only be determined at $\sigma^*=2100 \text{ MPa}$ as the 0.18T specimen because the higher stresses are not reached. Still, the single data point at -50 °C was included in the least square fit to determine T_0 , which resulted in a value of -49.47 °C. This value is in excellent agreement with $T_0 = -42.24 \text{ °C}$ obtained from the experimental data. Obviously, the σ^* - V^* criterion calibrated on static loading is capable to predict ΔT_0 shifts resulting from loading rate.

In Figure 109, the ΔT_0 shift induced by loading rate on Eurofer97 was compared with literature data obtained experimentally on various ferritic steels with different chemical compositions. Both determined shifts of Eurofer97 present a loading rate dependence well in line with the published data.

5.2.4 Prediction of the Eurofer97-(14) toughness after irradiation

The critical parameters σ^* - V^* calibrated on 0.14T DCT specimens of unirradiated Eurofer97-(14) can be used to estimate the expected shift of the reference temperature T_0 . σ^* and V^* were respectively equal to 1960 MPa and $5.63 \cdot 10^7 \mu\text{m}^3$. In order to do so, the irradiated flow properties determined from the disk tensile specimens were used. The simulations were run at five temperatures -100, -50, 20, 200 and 370 °C and the output in terms of stressed volume $V^*(\sigma^*)$ was analyzed to extract the K_{Jc} values, calculated by the J-integral obtained by Abaqus, at which the criterion σ^* - V^* is attained. The corresponding result can be seen in Figure 110.

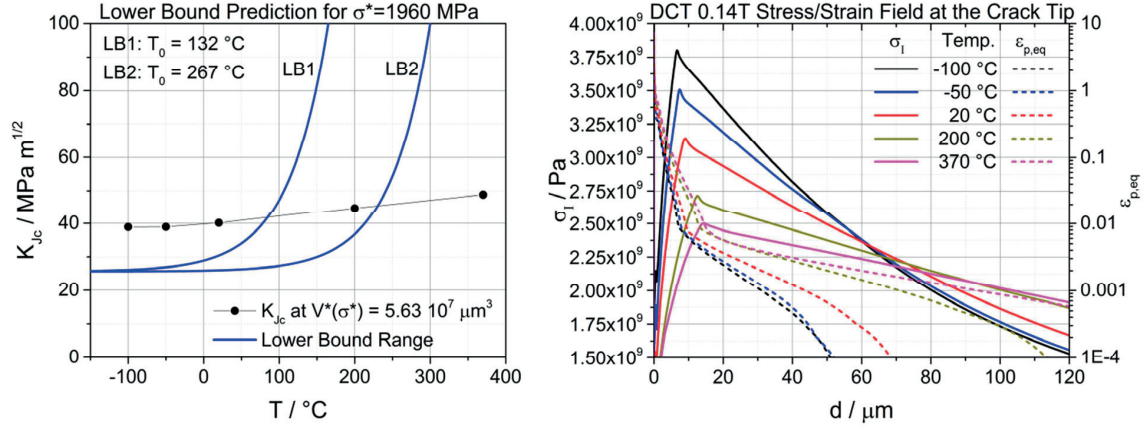


Figure 110: Left: Determined K_{Jc} values for the irradiated FEM including the 1 % lower bound for $T_0=132$ and $267^{\circ}C$ for 0.14T CT. Right: Corresponding stress/strain fields at K_{Jc} .

The transition temperatures were chosen in accordance to the estimated $\Delta T_0/\Delta\sigma_y \sim 0.57 \pm 0.13^{\circ}C/MPa$ proposed by Odette [72], where $\Delta\sigma_y$ is measured at room temperature. Having $\Delta\sigma_y = 511$ MPa at $20^{\circ}C$, ΔT_0^{min} and ΔT_0^{max} are respectively $227^{\circ}C$ and $362^{\circ}C$, which finally correspond to $T_0^{min} = 132^{\circ}C$ or $T_0^{max} = 267^{\circ}C$. In Figure 110, the lower bound corresponding to these last two temperatures are plotted. In the same Figure, the corresponding stress/strain fields do show a crossover around 2280 MPa which is comparable to the unirradiated result. However, the curves intersect each other about 25 % closer to the crack tip at a distance of $66 \mu m$. Furthermore, the peak stress positions as well as the width of the peaks do not change significantly with increasing temperature. Only the decrease in peak height is pronounced. Interestingly the peak height at $200^{\circ}C$ does show a similar magnitude as the peak for the unirradiated FEM simulation at $-137^{\circ}C$.

As observed in Figure 110, the lower bounds with the two chosen T_0 do not fit well with the calculated K_{Jc} data points to meet σ^*-V^* criterion. The K_{Jc} values are about 50 % higher in comparison to the calculated lower bound, suggesting a slight irradiation and/or temperature dependence of the σ^*-V^* values. For the high dose irradiation condition of this study (11 dpa, 500 appm), it is clear that fracture toughness at -100 and $-50^{\circ}C$ must be on the lower shelf. The fact that the predicted toughness values are too high can be the consequence of:

1. A moderate decrease of V^* at constant σ^* following irradiation is possible. This assumption would lead to a smaller predicted K_{Jc} value. It can be assumed that the transmutation product He affects the density of potential microcrack triggering particles by accumulation at carbide/matrix interfaces increasing the density of potential crack initiation sites. In this situation, a small decrease of V^* , which in turn leads to a corresponding decrease in toughness.
2. If V^* is assumed constant, a decrease of the critical stress σ^* leads to lower K_{Jc} values. A possible explanation for a decrease in σ^* lies in the accumulation of He at the grain boundaries which reduces the critical stress for intergranular fracture σ_{ig}^* . Therefore σ_{ig}^* replaces the transgranular critical stress σ_{tg}^* which has an lower value.

5.2.5 Impact of different FE models on the local approach

The goal in developing different fracture FE models in 3D and 2D was to analyze the impact of the applied model on the critical parameters of the local approach. The models were designed to reproduce as closely

as possible the near tip stress field at low loading. To do so, the initial crack root radius was equal to 0.1 μm , representative of the actual root radius after fatigue pre-cracking. By doing so, there is no issue related to possible effects of initial root radius on the development of the stress field against loading. The use of a small initial root radius in combination with a fine mesh around the crack tip to catch the stress/strain gradients precisely in 3D models requires a significant increase of computational costs with respect to 2D models. However, the implications on the stress/strain fields and on local fracture criteria were not studied in detail yet.

In total 5 different FE model approaches were used to calculate the stress/strain fields ahead a crack tip with an initial root radius of 0.1 μm . The local approach analysis was focused to the 1% lower bound of a 0.18T CT specimen. The determined critical parameters σ^* - V^* for the different FEM approaches are summarized in Figure 111.

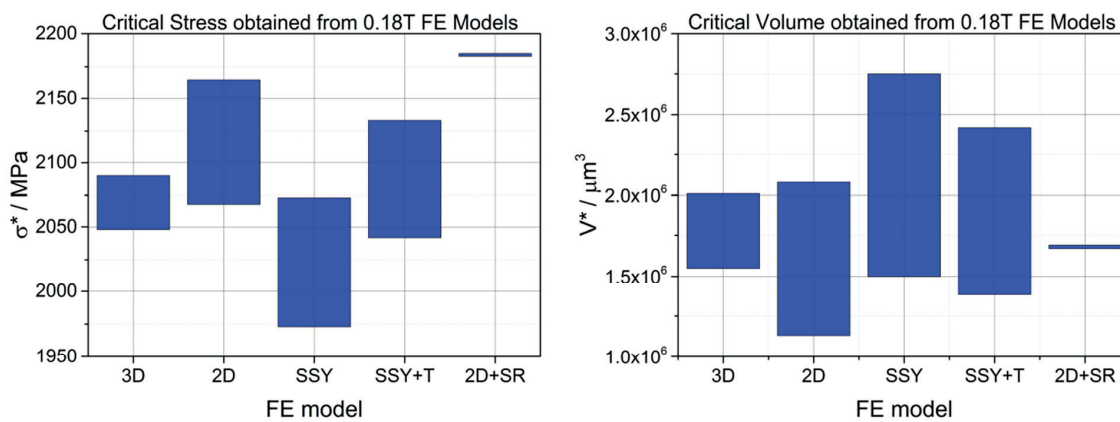


Figure 111: Determined critical parameter ranges from different 0.18T FE model approaches. Left: Critical stress. Right: Critical volume.

The critical stress σ^* does not show a large variation between the different FE models. Averaging the values of all models yields $\sigma^*_{\text{avg}}=2096$ MPa with a maximum deviation of about 6%. The minimum $\sigma^*_{\text{min}}=1973$ MPa was obtained from the MBL in SSY conditions and the maximum $\sigma^*_{\text{max}}=2185$ MPa from the 2D 0.18T model which considered strain rate. As far as V^* is concerned, the average value is $V^*_{\text{avg}}=1.82 \cdot 10^6 \mu\text{m}^3$ but the scatter is much bigger and is at maximum 51 %. The uncertainty in the calibration of σ^* - V^* depends on the selected temperatures considered.

The rather large uncertainty in V^* has a moderate impact on T_0 . For instance, if one considers $2V^*$ instead of V^* for the same σ^* , the impact on T_0 is to shift it by about 15 °C. This is about the same uncertainty in T_0 determination when deduced with 6 valid tests according to the master-curve standard.

In Figure 111 one can see that the simplified models are capable to replace the 3D FEM in terms of the σ^* - V^* parameters. However, it was found that the stress field can vary considerably between the different models (see Figure 112). In particular, for the MBL model in SSY without T-stress the structure of the stress field deviates significantly from that of the 2D CT. Considering the T-stress in the MBL model reduces considerably the discrepancy with the 2D CT model. However, one observes that the MBL/SSY conditions reproduces well the peak but the peak width is narrower (see Figure 112 left). Therefore the critical stress acts over a shorter distance λ^* . An opposite result is obtained from the quasi-static loaded 2D 0.18T CT model when effect of strain rate is taken into account. In this case, the peak stress is higher than in the model without strain rate sensitivity of the flow stress (see Figure 112 right), which reflects the strain rate

hardening effect. Let's point out that the stress fields are quite similar at increasing distance from the crack tip.

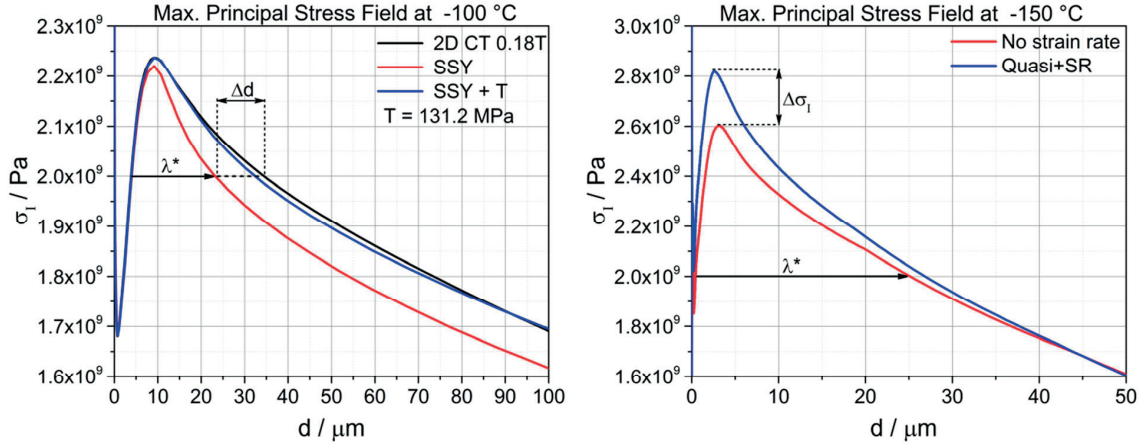


Figure 112: Stress field at the crack tip. Left: 2D 0.18T CT and MBL model under SSY condition at -100 °C. Right: 2D 0.18T CT models whereas no strain rate and strain rate effect were considered at -150 °C.

Thus, even if the simplified FE models, namely MBL and CT model without strain rate sensitivity, give reasonable results, the structure of the stress field at the crack tip is not satisfactory. For the σ^* - V^* model, the impact is minor on the calibrated values. However, this appears to be a more crucial issue for the calibration of the Weibull parameters as derived in the approach proposed by Beremin [149], where the cumulative failure probability dependence on the Weibull stress that intrinsically account for the spatial dependence of the stress within the process zone. In other words, the two stress fields shown in Figure 112 right would result in different Weibull stress. Therefore the local approach to brittle fracture based on the critical stressed volume $V^*(\sigma^*)$ is less sensitive to some details of the constitutive behavior but appears in the same time less powerful to accommodate the 3D variation of the stress field in failure prediction. The major drawback of the Weibull stress is the complicated procedure to calibrate the parameters over a range of temperatures. As a rule, it is advisable to use FE models of real specimens with very precise description of the constitutive behavior in terms of strain hardening and strain rate sensitivity to calculate the stress field the most realistically.

5.2.6 DTS stress field analysis at fracture

The local fracture stress σ^* for Eurofer97-(14) is 1960 MPa. Again, this stress was calibrated to reconstruct the master-curve lower bound at 1% failure probability. Slightly different values would be needed to reconstruct master-curve bounds at other failure probability. Difference in σ^* would be of the order of few hundred MPa. The variation in σ_f reflects the intrinsic scatter of measured fracture toughness resulting from the distribution inhomogeneity of micro-crack initiators in the vicinity of stress concentrators. In other words, each fracture specimen is characterized by its own fracture stress, in the same way as it has a specific fracture toughness value. The stress fields at fracture for unirradiated and irradiated DTS were calculated by FE analysis to verify whether the fracture stress in tensile specimen is consistent with that of the fracture specimens, at temperatures where the tensile specimens failed in a brittle manner. For completeness, the fracture stress of DTS tests at 200 °C and that failed essentially according to a ductile mode is also presented.

The true stress-strain curves derived with the inverse method at 200 and -100 °C were used as input in FE models to calculate the stress state at failure of the DTS. As it can be seen in Figure 113, the cross sectional matches at 200 °C, at failure, are not perfect. The specimens at 200 °C failed according to ductile mode of fracture. From the fracture surface analysis, it was shown that mainly dimples and voids were found on the unirradiated and irradiated DTS fracture surfaces. It has to be pointed out that the used FEM is not capable to consider dimple and void formation. The formation of voids does represent a reduction in cross section and the FEM tries to reconstruct the tensile behavior by softening. From Figure 113, one deduces that the fracture stress in the unirradiated and irradiated specimen is respectively 880 and 1500 MPa.

Concerning the DTS FEM at lower temperature, a better match was found (see Figure 114). Since at -100 °C, the fractographic observations show a dominance of small cleavage facets, the calculated fracture stress, was compared to the calibrated fracture stress from fracture toughness tests. The nominal fracture stress values of the unirradiated and irradiated DTS was respectively found equal to 1700 and 2100 MPa. In this case, these data are in good agreement with the value of local fracture stress determined with fracture toughness tests. This result indicates that for the irradiation conditions of this study, 11 dpa and 540 appm He, the micro-mechanisms of fracture are not significantly affected by helium. This is in general consistent with the embrittlement analysis done by Yamamoto et al. on tempered martensitic steels that indicate that the so-called He non-hardening embrittlement effect emerges for concentration higher than 400-600 appm [200]. Thus, the He concentration attained in our specimen is likely to be too low to induce a strong change in the local micro-mechanisms of fracture, from transgranular cleavage to intergranular cleavage. Our tensile test data are also in good agreement with the conclusion drawn by Wang et al. [201] who showed for F82H steel that only specimens with a dose and He content greater than 15 dpa and 1370 appm respectively present intergranular fracture mode along with pure elastic loading up to fracture.

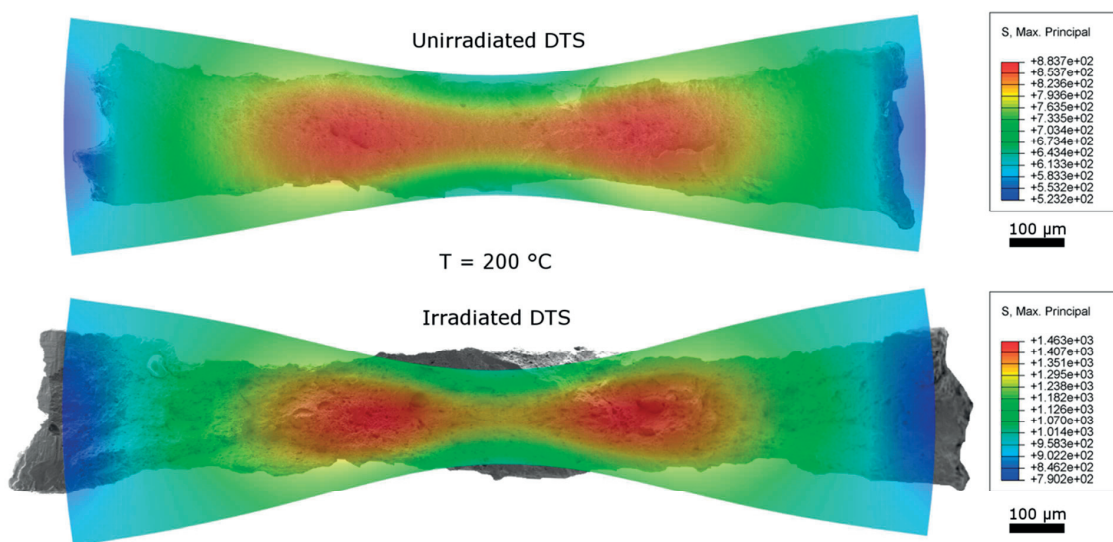


Figure 113: Maximum principal stress distribution overlaid with the experimental fracture surface for the irradiated and unirradiated DTS tests at 200 °C. Units are in MPa.

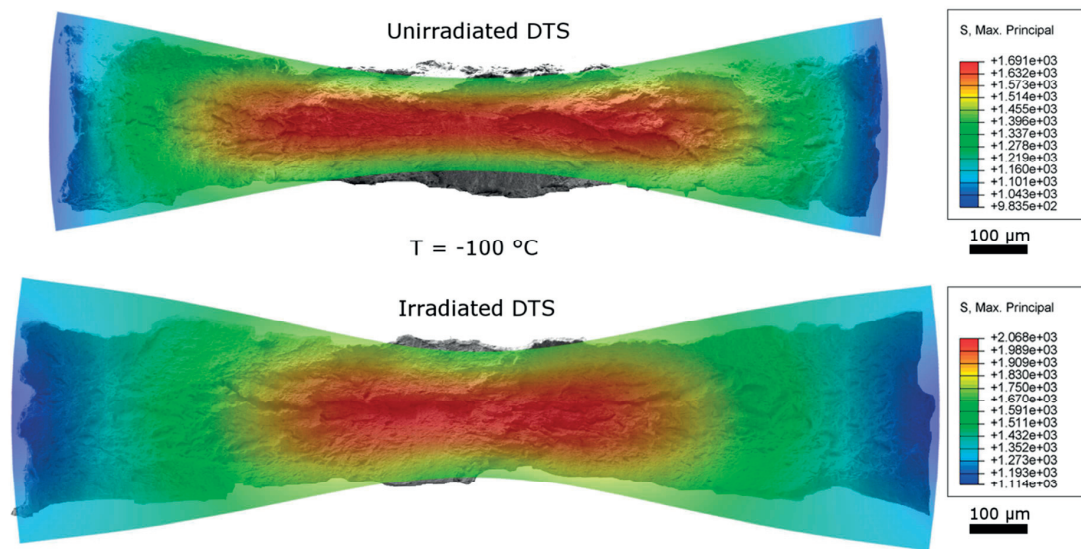


Figure 114: Calculated maximum principal stress on the fracture at -100 °C of unirradiated and irradiated specimens. Units are in MPa.

Chapter 6 Conclusions

Investigations of the mechanical properties before and after irradiation of two heats of Eurofer97, a reduced activation tempered martensitic steel developed for fusion reactors structural applications were conducted. These two heats were referred as to Eurofer97-(25) and Eurofer97-(14) in relation their original plate thickness, 25 mm and 14 mm respectively. The effects of irradiation were studied only used on Eurofer97-(14). The focus of this work was put on the tensile and fracture properties in the ductile to brittle transition region. The conclusions drawn from the experimental and modeling activities are the following:

Standard tensile tests on round specimens were performed over a broad range of temperatures (-196 °C to 200 °C) at different strain rates to evaluate the plastic flow properties of unirradiated Eurofer97-(25). A strong temperature and strain rate dependence was reported at cryogenic temperature (< -100 °C). Small activation volume determined from strain rate jumps were found in this temperature regime. This behavior was shown to be fully in line with other body-centered cubic metals and alloys, and consistent with the mechanism of formation and propagation of double kinks on screw dislocation that controls the dislocation mobility at low temperature. The comparison of the curves obtained at high strain rate with those at low strain rate revealed a competition between strain rate hardening and thermal softening, which arises from the plastic work dissipation into heat in the specimen. This effect was particularly well pronounced at -100 and -150 °C and was successfully modeled by finite elements simulations taking into account the plastic work dissipation into heat. To properly reconstruct the tensile curves at high strain rate with thermal softening, we found that the Quinney-Taylor coefficient has to be equal to 0.9 (this coefficient quantifies the amount of plastic work converted into heat). To separate the effect of hardening rate from those of thermal softening, strain rate jumps along the deformation curves were performed that show that the strain rate sensitivity of the flow stress is in good approximation independent of the strain.

The constitutive behavior (= the true stress-strain curve) was determined at strain significantly greater than uniform elongation. Such information is important because the constitutive behavior is used as input for the finite simulations of fracture specimens where large plastic strains are introduced near the crack tip. Owing to the limited uniform strain of Eurofer97 in the unirradiated conditions, and even practically absent uniform strain after irradiation, an inverse method was developed. This method was based on finite elements, where the input constitutive behavior is fitted to reconstruct the measured load displacement curves of the tensile specimens. It was shown that, with the inverse method, the entire deformation curves can be modeled with true stress-strain relations fitted up to strain of at least 0.5. The advantage of the proposed inverse method resides in the fact that it adjusts the true stress strain by small linear segments without assuming an analytical expression, which does not exist for tempered martensitic steels at large strains. The fitted true stress-strain curves indicated that there is actually no saturation of the flow stress. Indeed, to reconstruct the load-displacement curve after initiation of necking, true stress-strain curve with practically constant strain-hardening rate were employed up to large strain.

The constitutive behavior of Eurofer97-(14) was investigated before and after irradiation in SINQ, the Swiss spallation source at Paul Scherrer Institute, for a dose of 11 dpa and a helium content of 500 appm. As non-standard disk tensile specimens had to be used, we emphasize that the development of the inverse method was necessary to analyze the deformation behavior of these specimens, which do not deform homogeneously due to their very short gage length. Interestingly, it was also observed that the irradiated specimens, tested between -100 and 370 °C keep their strain hardening capacity. The irradiation hardening, defined as the increase of the yield stress, seemed to be dependent on testing temperature.

The unirradiated as well as the irradiated non-standard disk tensile specimen tested at -100 and 200 °C were examined by scanning electron microscope in order to identify possible irradiation effects on fracture mechanisms. At 200 °C, irradiation caused the appearance of quasi-cleavage facets and a large reduction of dimple features in comparison to the unirradiated surface, which was dimple dominated. As far as the fracture surface at -100 °C is concerned, large secondary cracks and wide areas were covered with cleavage facets, while very few areas were characterized by dimples. Intergranular fracture features were not observed indicating that the helium non-hardening embrittlement at concentration of 500 appm is still not present.

Fracture toughness tests were carried out on unirradiated Eurofer97-(25) and Eurofer97-(14) in the transition region with sub-sized compact tension specimens. The fracture behavior was analyzed in the frame of the master-curve approach, which allows defining a reference temperature T_0 at a median toughness of $100 \text{ MPa}\sqrt{\text{m}}$. T_0 depends on a number of factors such as loading rate, specimen size, specimen type, irradiation dose for example. Knowing T_0 as function of these factors is crucial. Dynamic fracture tests with 0.18T compact tension specimens were carried out on unirradiated Eurofer97-(25) and a reference temperature T_0 at -42 °C was determined, which compared with T_0 at -78 °C for static tests (the loading rate was 1000x faster). This upper shift of the transition temperature is in good agreement with literature data on a variety of ferritic alloys. Static fracture tests with 0.14T disk compact tension specimens of Eurofer97-(14) were also performed and T_0 was found at -95 °C. With a reference temperature 17 °C lower than that of Eurofer97-(25), Eurofer97-(14) appears a little tougher, which is consistent with the fact that the Eurofer97-(14) yield stress is somewhat lower than Eurofer97-(25).

Different finite element models of the compact tension specimens were developed and used to reconstruct the toughness dependence in the lower transition of both Eurofer97 heats and to study the structure of the tip stress field as a function of specimen size, loading rate and constitutive behavior. A simple criterion for brittle fracture was considered, which was based on local approach of fracture. According to this model, brittle fracture is triggered when critical volume V^* encompassed a critical stress σ^* . The impact of different finite element models on the critical parameters σ^* - V^* were assessed by considering 3D and 2D plain strain compact tension models as well as the modified boundary layer model (MBL) under small scale yielding (SSY) condition. In case of the MBL model, SSY conditions were applied with and without T-stress. Since the toughness level considered was in the lower part of the transition, a good agreement between the 3D model and the 2D models in terms of σ^* - V^* criterion and stress field structure was found. However, for the MBL model without T-stress, the stress field at the crack tip was not well reproduced, highlighting the beneficial effect of the positive T-stress of tension specimens to maintain constraint.

Furthermore, strain rate sensitivity of the constitutive behavior and thermal effects on σ^* - V^* were investigated using a 2D 0.18T plain strain model. At quasi-static loading rate condition, the thermal effects can be neglected as the energy dissipated into heat has enough time to flow from the plastic zone at the tip to the

bulk of the specimen that acts as heat sink. On the contrary, strain rate sensitivity of the constitutive behavior clearly increases the stress field while decreasing slightly the critical volume. Still, it was concluded that strain rate effects do show an impact on the stress field in the fracture process zone and should be therefore considered. Additionally, strain rate and thermal effects were studied at dynamic loading condition representative to those of the experimental dynamic fracture tests. Two different models were developed to account for thermal effects namely: one which considers thermal conductivity and an adiabatic model where the dissipated heat remains in the elements where it is generated. It was found that the adiabatic model had an impact mainly onto the stress field due to unrealistic high heat dissipation at the very crack tip. However, it was found that the impact onto the critical parameters σ^*-V^* is marginal and a simple strain rate consideration is sufficient to address increased loading rate effects, at least to the loading rate considered in this work.

Reference

- [1] A. Molvik, A. Ivanov, G. L. Kulcinski, D. Ryutov, J. Santarius, T. Simonen, B. D. Wirth and A. Ying, "A Gas Dynamic Trap Neutron Source for Fusion Material and Subcomponent Testing," *Fusion Science and Technology*, vol. 57, pp. 369-394, 5 2010.
- [2] T. Yamamoto, G. R. Odette, H. Kishimoto, J.-W. Rensman and P. Miao, "On the effects of irradiation and helium on the yield stress changes and hardening and non-hardening embrittlement of a 8Cr tempered martensitic steels: Compilation and analysis of existing data," *Journal of Nuclear Materials*, vol. 356, pp. 27-49, 15 9 2006.
- [3] F. W. Aston, "LIX.The mass-spectra of chemical elements," *Philosophical Magazine Series 6*, vol. 39, pp. 611-625, 5 1920.
- [4] A. S. Eddington, "The Internal Constitution of the Stars," *The Scientific Monthly*, vol. 11, pp. 297-303, 1920.
- [5] INTERNATIONAL ATOMIC ENERGY AGENCY, Fusion Physics, Vienna, : International Atomic Energy Agency, 2012.
- [6] L. Spitzer, "The Stellarator Concept," *Physics of Fluids*, vol. 1, p. 253, 1958.
- [7] R. Mitteau, B. Calcagno, P. Chappuis, R. Eaton, S. Gicquel, J. Chen, A. Labusov, A. Martin, M. Merola, R. Raffray, M. Ulrickson and F. Zacchia, "The design of the ITER first wall panels," *Fusion Engineering and Design*, vol. 88, pp. 568-570, 10 2013.
- [8] A. R. Raffray and M. Merola, "Overview of the design and R&D of the ITER blanket system," *Fusion Engineering and Design*, vol. 87, pp. 769-776, 8 2012.
- [9] L. M. Giancarli, M. Abdou, D. J. Campbell, V. A. Chuyanov, M. Y. Ahn, M. Enoeda, C. Pan, Y. Poitevin, E. R. Kumar, I. Ricipito, Y. Strebkov, S. Suzuki, P. C. Wong and M. Zmitko, "Overview of the ITER TBM Program," *Fusion Engineering and Design*, vol. 87, pp. 395-402, 8 2012.
- [10] M. Zmitko, Y. Carin, N. Thomas, M. Simon-Perret, A. LiPuma, L. Forest, J. Tosi, G. Aiello, L. Cogneau, J. Rey, H. Neuberger, J. Aktaa, E. Gaganidze, K. Zhang, N. Pierredon, Y. Lejeail, P. Lamagnere and Y. Poitevin, "The European ITER Test Blanket Modules: EUROFER97 material and TBM's fabrication technologies development and qualification," *Fusion Engineering and Design*, vol. 124, pp. 767-773, 11 2017.
- [11] G. Shatalov, "DEMO blanket testing in ITER. Influence on reaching DEMO," *Fusion Engineering and Design*, Vols. 56-57, pp. 39-46, 10 2001.

- [12] G. Federici, W. Biel, M. R. Gilbert, R. Kemp, N. Taylor and R. Wenninger, "European DEMO design strategy and consequences for materials," *Nuclear Fusion*, vol. 57, p. 092002, 2017.
- [13] G. G. Dolgov-Savelev, V. S. Mukhovatov, V. S. Strelkov, M. N. Shepelev and N. A. Yavlinskii, "Investigation of a toroidal discharge in a strong magnetic field," *Zhur. Eksptl'. i Teoret. Fiz.*, vol. Vol: 38, 2 1960.
- [14] M. Lehnen, G. Arnoux, N. Hartmann, S. Brezinsek, S. Devaux, A. Huber, S. Jachmich, U. Kruezi, G. F. Matthews, C. Reux, V. Riccardo, B. Sieglin, M. F. Stamp and P. C. Vries, "Disruption heat loads and their mitigation in JET with the ITER-like wall," *Journal of Nuclear Materials*, vol. 438, pp. S102--S107, 7 2013.
- [15] A. Hassanein, "Prediction of material erosion and lifetime during major plasma instabilities in tokamak devices," *Fusion Engineering and Design*, vol. 60, pp. 527-546, 7 2002.
- [16] J. Blanchard, C. Martin and W. Liu, "Effect of ELMS and disruptions on FNSF plasma-facing components," *Fusion Engineering and Design*, 8 2017.
- [17] S. Pak, H. Jhang, D.-K. Oh and D. Y. Ku, "Electromagnetic load calculation of the ITER machine using a single finite element model including narrow slits of the in-vessel components," *Fusion Engineering and Design*, vol. 88, pp. 3224-3237, 12 2013.
- [18] I. A. Maione and A. Vaccaro, "Analysis of electromagnetic loads on EU-DEMO inboard and outboard blanket vertical segments," *Fusion Engineering and Design*, vol. 89, pp. 1314-1318, 10 2014.
- [19] H. Tanigawa, T. Hirose, D. Hamaguchi, T. Nakata, H. Sakasegawa, M. Enoda, Y. Someya, H. Utoh, K. Tobita, K. Ochiai, C. Konno, M. Ando, S. Nogami, R. Kasada, A. Moslang, E. Diegele, M. A. Sokolov, L. L. Snead, Y. Katoh, R. E. Stoller and S. Zinkle, "Research and Development Status of Reduced Activation Ferritic/Martensitic Steels Corresponding to DEMO Design Requirement," Vienna, 2012.
- [20] R. Kasada, D. Ishii, M. Ando, H. Tanigawa, M. Ohata and S. Konishi, "Dynamic tensile properties of reduced-activation ferritic steel F82H," *Fusion Engineering and Design*, vol. 100, pp. 146-151, 11 2015.
- [21] K. Ioki, A. Bayon, C. H. Choi, E. Daly, S. Dani, J. Davis, B. Giraud, Y. Gribov, C. Hamlyn-Harris, C. Jun, B. Levesy, B. C. Kim, E. Kuzmin, R. L. Barbier, J.-M. Martinez, H. Pathak, J. Preble, J. W. Sa, A. Terasawa, Y. Utin and X. Wang, "Progress of ITER vacuum vessel," *Fusion Engineering and Design*, vol. 88, pp. 590-596, 10 2013.
- [22] F. A. Garner, M. B. Toloczko and B. H. Sencer, "Comparison of swelling and irradiation creep behavior of fcc-austenitic and bcc-ferritic/martensitic alloys at high neutron exposure," *Journal of Nuclear Materials*, vol. 276, pp. 123-142, 1 2000.
- [23] S. J. Zinkle and G. S. Was, "Materials challenges in nuclear energy," *Acta Materialia*, vol. 61, pp. 735-758, 2 2013.

- [24] B. Raj and M. Vijayalakshmi, "Ferritic Steels and Advanced Ferritic–Martensitic Steels," in *Comprehensive Nuclear Materials*, Elsevier, 2012, pp. 97-121.
- [25] B. Raj and T. Jayakumar, "Development of Reduced Activation Ferritic–Martensitic Steels and fabrication technologies for Indian test blanket module," *Journal of Nuclear Materials*, vol. 417, pp. 72-76, 10 2011.
- [26] R. A. Forrest and J. Kopecky, "The activation system EASY-2007," *Journal of Nuclear Materials*, Vols. 386-388, pp. 878-881, 4 2009.
- [27] R. Lindau, A. Möslang and M. Schirra, "Thermal and mechanical behaviour of the reduced-activation-ferritic-martensitic steel EUROFER," *Fusion Engineering and Design*, Vols. 61-62, pp. 659-664, 11 2002.
- [28] S. J. Zinkle and B. N. Singh, "Analysis of displacement damage and defect production under cascade damage conditions," *Journal of Nuclear Materials*, vol. 199, pp. 173-191, 2 1993.
- [29] G. R. Odette and D. R. Doiron, "Neutron-Energy-Dependent Defect Production Cross Sections for Fission and Fusion Applications," *Nuclear Technology*, vol. 29, pp. 346-368, 6 1976.
- [30] R. E. Stoller, "Primary Radiation Damage Formation," in *Comprehensive Nuclear Materials*, Elsevier, 2012, pp. 293-332.
- [31] G. H. Kinchin and R. S. Pease, "The Displacement of Atoms in Solids by Radiation," *Reports on Progress in Physics*, vol. 18, pp. 1-51, 1 1955.
- [32] M. R. Gilbert, J. Marian and J.-C. Sublet, "Energy spectra of primary knock-on atoms under neutron irradiation," *Journal of Nuclear Materials*, vol. 467, pp. 121-134, 12 2015.
- [33] L. R. Greenwood, "Gas Production in Reactor Materials," in *STP1490-EB Reactor Dosimetry: 12th International Symposium.*, 2007.
- [34] Y. Dai, G. R. Odette and T. Yamamoto, "The Effects of Helium in Irradiated Structural Alloys," in *Comprehensive Nuclear Materials*, Elsevier, 2012, pp. 141-193.
- [35] H. Ullmaier and H. Trinkaus, "Helium in Metals: Effect on Mechanical Properties," *Materials Science Forum*, Vols. 97-99, pp. 451-472, 1992.
- [36] P. Jung, C. Liu and J. Chen, "Retention of implanted hydrogen and helium in martensitic stainless steels and their effects on mechanical properties," *Journal of Nuclear Materials*, vol. 296, pp. 165-173, 7 2001.
- [37] C. Liu, H. Klein and P. Jung, "Embrittlement of RAFM EUROFER97 by implanted hydrogen," *Journal of Nuclear Materials*, vol. 335, pp. 77-82, 10 2004.
- [38] Y. Dai, Y. Foucher, M. R. James and B. M. Oliver, "Neutronics calculation, dosimetry analysis and gas measurements of the first SINQ target irradiation experiment, STIP-I," *Journal of Nuclear Materials*,

vol. 318, pp. 167-175, 5 2003.

- [39] F. A. Garner and L. R. Greenwood, "Neutron irradiation effects in fusion or spallation structural materials: Some recent insights related to neutron spectra," *Radiation Effects and Defects in Solids*, vol. 144, pp. 251-286, 6 1998.
- [40] R. L. Klueh and D. R. Harries, High-Chromium Ferritic and Martensitic Steels for Nuclear Applications (Monograph (American Society for Testing and Materials), 3.), ASTM International, 2001.
- [41] E. Materna-Morris, A. Möslang and H.-C. Schneider, "Tensile and low cycle fatigue properties of EUROFER97-steel after 16.3dpa neutron irradiation at 523, 623 and 723K," *Journal of Nuclear Materials*, vol. 442, pp. S62--S66, 11 2013.
- [42] O. Anderoglu, T. S. Byun, M. Toloczko and S. A. Maloy, "Mechanical Performance of Ferritic Martensitic Steels for High Dose Applications in Advanced Nuclear Reactors," *Metallurgical and Materials Transactions A*, vol. 44, pp. 70-83, 12 2012.
- [43] Fundamentals of Radiation Materials Science, Springer Berlin Heidelberg, 2007.
- [44] J. Henry, X. Averty and A. Alamo, "Tensile and impact properties of 9Cr tempered martensitic steels and ODS-FeCr alloys irradiated in a fast reactor at 325 °C up to 78dpa," *Journal of Nuclear Materials*, vol. 417, pp. 99-103, 10 2011.
- [45] R. L. Klueh, "Reduced-activation bainitic and martensitic steels for nuclear fusion applications," *Current Opinion in Solid State and Materials Science*, vol. 8, pp. 239-250, 6 2004.
- [46] R. J. Kurtz, A. Alamo, E. Lucon, Q. Huang, S. Jitsukawa, A. Kimura, R. L. Klueh, G. R. Odette, C. Petersen, M. A. Sokolov, P. Spätig and J.-W. Rensman, "Recent progress toward development of reduced activation ferritic/martensitic steels for fusion structural applications," *Journal of Nuclear Materials*, Vols. 386-388, pp. 411-417, 4 2009.
- [47] E. Lucon, P. Benoit, P. Jacquet, E. Diegele, R. Lässer, A. Alamo, R. Coppola, F. Gillemot, P. Jung, A. Lind, S. Messoloras, P. Novosad, R. Lindau, D. Preininger, M. Klimiankou, C. Petersen, M. Rieth, E. Materna-Morris, H.-C. Schneider, J.-W. Rensman, B. Schaaf, B. K. Singh and P. Spaetig, "The European effort towards the development of a demo structural material: Irradiation behaviour of the European reference RAFM steel EUROFER," *Fusion Engineering and Design*, vol. 81, pp. 917-923, 2 2006.
- [48] E. Gaganidze, C. Petersen, E. Materna-Morris, C. Dethloff, O. J. Weiss, J. Aktaa, A. Povstyanko, A. Fedoseev, O. Makarov and V. Prokhorov, "Mechanical properties and TEM examination of RAFM steels irradiated up to 70dpa in BOR-60," *Journal of Nuclear Materials*, vol. 417, pp. 93-98, 10 2011.
- [49] C. Petersen, A. Povstyanko, V. Prokhorov, A. Fedoseev, O. Makarov and M. Walter, "Tensile and low cycle fatigue properties of different ferritic/martensitic steels after the fast reactor irradiation 'ARBOR 1'," *Journal of Nuclear Materials*, Vols. 386-388, pp. 299-302, 4 2009.
- [50] G. S. Was, "Irradiation Creep and Growth," in *Fundamentals of Radiation Materials Science*, Springer

New York, 2016, pp. 735-791.

- [51] A.-A. F. Tavassoli, "Present limits and improvements of structural materials for fusion reactors – a review," *Journal of Nuclear Materials*, vol. 302, pp. 73-88, 4 2002.
- [52] A. Alamo, J. L. Bertin, V. K. Shamardin and P. Wident, "Mechanical properties of 9Cr martensitic steels and ODS-FeCr alloys after neutron irradiation at 325 °C up to 42dpa," *Journal of Nuclear Materials*, Vols. 367-370, pp. 54-59, 8 2007.
- [53] K. Wallin, "Irradiation damage effects on the fracture toughness transition curve shape for reactor pressure vessel steels," *International Journal of Pressure Vessels and Piping*, vol. 55, pp. 61-79, 1 1993.
- [54] G. R. Odette, K. Edsinger, G. E. Lucas and E. Donahue, "Developing Fracture Assessment Methods for Fusion Reactor Materials with Small Specimens," in *Small Specimen Test Techniques*, ASTM International, pp. 298--298--30.
- [55] E. G. Donahue, G. R. Odette and G. E. Lucas, "On the mechanisms and mechanics of fracture toughness of a V-4Cr-4Ti alloy," *Journal of Nuclear Materials*, Vols. 283-287, pp. 518-522, 12 2000.
- [56] *ASTM E1921-17a Standard Test Method for Determination of Reference Temperature, T_o , for Ferritic Steels in the Transition Range*, 2017.
- [57] E. Lucon, "A closer look at the fracture toughness of ferritic/martensitic steels," *Journal of Nuclear Materials*, Vols. 367-370, pp. 575-580, 8 2007.
- [58] G. R. Odette, T. Yamamoto, H. Kishimoto, M. Sokolov, P. Spätig, W. J. Yang, J.-W. Rensman and G. E. Lucas, "A master curve analysis of F82H using statistical and constraint loss size adjustments of small specimen data," *Journal of Nuclear Materials*, Vols. 329-333, pp. 1243-1247, 8 2004.
- [59] P. Mueller, P. Spätig, R. Bonadé, G. R. Odette and D. Gragg, "Fracture toughness master-curve analysis of the tempered martensitic steel Eurofer97," *Journal of Nuclear Materials*, vol. 386, no. Supplement C, pp. 323-327, 30 4 2009.
- [60] S. Jitsukawa, A. Kimura, A. Kohyama, R. L. Klueh, A. A. Tavassoli, B. Schaaf, G. R. Odette, J. W. Rensman, M. Victoria and C. Petersen, "Recent results of the reduced activation ferritic/martensitic steel development," *Journal of Nuclear Materials*, Vols. 329-333, pp. 39-46, 8 2004.
- [61] R. L. Klueh, "Elevated temperature ferritic and martensitic steels and their application to future nuclear reactors," *International Materials Reviews*, vol. 50, pp. 287-310, 10 2005.
- [62] R. L. Klueh, K. Ehrlich and F. Abe, "Ferritic/martensitic steels: promises and problems," *Journal of Nuclear Materials*, Vols. 191-194, pp. 116-124, 9 1992.
- [63] H. Fan-Hsiung and M. L. Hamilton, "The fracture toughness database of ferritic alloys irradiated to very high neutron exposures," *Journal of Nuclear Materials*, vol. 187, pp. 278-293, 5 1992.

- [64] X. Jia and Y. Dai, "The change of fracture toughness of martensitic steels after irradiation in SINQ target-3," *Journal of Nuclear Materials*, vol. 356, pp. 50-55, 9 2006.
- [65] H.-C. Schneider, J. Aktaa and R. Rolli, "Small fracture toughness specimen for post-irradiation experiments," *Journal of Nuclear Materials*, Vols. 367-370, pp. 599-602, 8 2007.
- [66] R. Chaouadi, G. Coen, E. Lucon and V. Massaut, "Crack resistance behavior of ODS and standard 9% Cr-containing steels at high temperature," *Journal of Nuclear Materials*, vol. 403, pp. 15-18, 8 2010.
- [67] N. Ilchuk, P. Spätig and G. R. Odette, "Fracture toughness characterization in the lower transition of neutron irradiated Eurofer97 steel," *Journal of Nuclear Materials*, vol. 442, pp. S58--S61, 11 2013.
- [68] P. Dubuisson, D. Gilbon and J. L. Sèran, "Microstructural evolution of ferritic-martensitic steels irradiated in the fast breeder reactor Phénix," *Journal of Nuclear Materials*, vol. 205, pp. 178-189, 10 1993.
- [69] S. J. Zinkle and N. M. Ghoniem, "Prospects for accelerated development of high performance structural materials," *Journal of Nuclear Materials*, vol. 417, pp. 2-8, 10 2011.
- [70] J.-L. Boutard, A. Alamo, R. Lindau and M. Rieth, "Fissile core and Tritium-Breeding Blanket: structural materials and their requirements," *Comptes Rendus Physique*, vol. 9, pp. 287-302, 4 2008.
- [71] R. E. Stoller, A. S. Kumar and D. S. Gelles, Eds., *Effects of Radiation on Materials: 15th International Symposium*, ASTM International, 1992.
- [72] G. R. Odette, T. Yamamoto, H. J. Rathbun, M. Y. He, M. L. Hribernik and J. W. Rensman, "Cleavage fracture and irradiation embrittlement of fusion reactor alloys: mechanisms, multiscale models, toughness measurements and implications to structural integrity assessment," *Journal of Nuclear Materials*, vol. 323, pp. 313-340, 12 2003.
- [73] L. K. Mansur, "Kinetics of Nonhomogeneous Processes: A Practical Introduction for Chemists, Biologists, Physicists, and Materials Scientists," G. R. Freeman, Ed., Wiley, 1987, p. 377–463.
- [74] G. L. Kulcinski, D. G. Doran and M. A. Abdou, "Comparison of Displacement and Gas Production Rates in Current Fission and Future Fusion Reactors," in *Effects of Radiation on Structural Materials*, ASTM International, pp. 329--329--23.
- [75] S. M. Qaim, "14 MeV Neutron Activation Cross Sections," *Handbook of Spectroscopy*, vol. 3, p. 141, 1981.
- [76] P. J. Maziasz, R. L. Klueh and J. M. Vitek, "Helium effects on void formation in 9Cr-1MoVNb and 12Cr-1MoVW irradiated in HFIR," *Journal of Nuclear Materials*, Vols. 141-143, pp. 929-937, 11 1986.
- [77] M. Klimenkov, A. Möslang and E. Materna-Morris, "Helium influence on the microstructure and swelling of 9% Cr ferritic steel after neutron irradiation to 16.3 dpa," *Journal of Nuclear Materials*, vol. 453, pp. 54-59, 10 2014.

- [78] E. Wakai, N. Hashimoto, Y. Miwa, J. P. Robertson, R. L. Klueh, K. Shiba and S. Jitsukawa, "Effect of helium production on swelling of F82H irradiated in HFIR," *Journal of Nuclear Materials*, Vols. 283-287, pp. 799-805, 12 2000.
- [79] T. Yamamoto, Y. Wu, G. R. Odette, K. Yabuuchi, S. Kondo and A. Kimura, "A dual ion irradiation study of helium-dpa interactions on cavity evolution in tempered martensitic steels and nanostructured ferritic alloys," *Journal of Nuclear Materials*, vol. 449, pp. 190-199, 6 2014.
- [80] S. J. Zinkle and A. Möslang, "Evaluation of irradiation facility options for fusion materials research and development," *Fusion Engineering and Design*, vol. 88, pp. 472-482, 10 2013.
- [81] Z. Tong and Y. Dai, "The microstructure and tensile properties of ferritic/martensitic steels T91, Eurofer-97 and F82H irradiated up to 20dpa in STIP-III," *Journal of Nuclear Materials*, vol. 398, pp. 43-48, 3 2010.
- [82] Z. Tong and Y. Dai, "Tensile properties of the ferritic martensitic steel F82H after irradiation in a spallation target," *Journal of Nuclear Materials*, vol. 385, pp. 258-261, 3 2009.
- [83] D. S. Gelles, "Effects of irradiation on ferritic alloys and implications for fusion reactor applications," *Journal of Nuclear Materials*, vol. 149, pp. 192-199, 7 1987.
- [84] E. Wakai, S. Jitsukawa, H. Tomita, K. Furuya, M. Sato, K. Oka, T. Tanaka, F. Takada, T. Yamamoto, Y. Kato, Y. Tayama, K. Shiba and S. Ohnuki, "Radiation hardening and -embrittlement due to He production in F82H steel irradiated at 250 °C in JMTR," *Journal of Nuclear Materials*, vol. 343, pp. 285-296, 8 2005.
- [85] R. L. Klueh and D. J. Alexander, "Embrittlement of 9Cr-1MoVNb and 12Cr-1MoVW steels irradiated in HFIR," *Journal of Nuclear Materials*, vol. 187, pp. 60-69, 3 1992.
- [86] G. R. Odette, M. J. Alinger and B. D. Wirth, "Recent Developments in Irradiation-Resistant Steels," *Annual Review of Materials Research*, vol. 38, pp. 471-503, 8 2008.
- [87] A. Kimura, R. Kasada, R. Sugano, A. Hasegawa and H. Matsui, "Annealing behavior of irradiation hardening and microstructure in helium-implanted reduced activation martensitic steel," *Journal of Nuclear Materials*, Vols. 283-287, pp. 827-831, 12 2000.
- [88] A. Kimura, R. Kasada, K. Morishita, R. Sugano, A. Hasegawa, K. Abe, T. Yamamoto, H. Matsui, N. Yoshida, B. D. Wirth and T. D. Rubia, "High resistance to helium embrittlement in reduced activation martensitic steels," *Journal of Nuclear Materials*, Vols. 307-311, pp. 521-526, 12 2002.
- [89] Y. Dai and P. Marmy, "Charpy impact tests on martensitic/ferritic steels after irradiation in SINQ target-3," *Journal of Nuclear Materials*, vol. 343, pp. 247-252, 8 2005.
- [90] P. Jung, J. Henry, J. Chen and J.-C. Brachet, "Effect of implanted helium on tensile properties and hardness of 9% Cr martensitic stainless steels," *Journal of Nuclear Materials*, vol. 318, pp. 241-248, 5 2003.

- [91] J. D. Hunn, E. H. Lee, T. S. Byun and L. K. Mansur, "Helium and hydrogen induced hardening in 316LN stainless steel," *Journal of Nuclear Materials*, vol. 282, pp. 131-136, 12 2000.
- [92] J. D. Hunn, E. H. Lee, T. S. Byun and L. K. Mansur, "Ion-irradiation-induced hardening in Inconel 718," *Journal of Nuclear Materials*, vol. 296, pp. 203-209, 7 2001.
- [93] K. Farrell and T. S. Byun, "Tensile properties of ferritic/martensitic steels irradiated in HFIR, and comparison with spallation irradiation data," *Journal of Nuclear Materials*, vol. 318, pp. 274-282, 5 2003.
- [94] R. Lindau, A. Möslang, D. Preininger, M. Rieth and H. D. Röhrig, "Influence of helium on impact properties of reduced-activation ferritic/martensitic Cr-steels," *Journal of Nuclear Materials*, Vols. 271-272, pp. 450-454, 5 1999.
- [95] Y. Dai, X. J. Jia and K. Farrell, "Mechanical properties of modified 9Cr-1Mo (T91) irradiated at ≤ 300 °C in SINQ Target-3," *Journal of Nuclear Materials*, vol. 318, pp. 192-199, 5 2003.
- [96] S. M. G. Vicente, J.-L. Boutard, S. J. Zinkle and H. Tanigawa, "Materials testing facilities and programmes for fission and ion implantation damage," *Nuclear Fusion*, vol. 57, p. 092011, 6 2017.
- [97] H. Ullmaier, "The influence of helium on the bulk properties of fusion reactor structural materials," *Nuclear Fusion*, vol. 24, p. 1039, 1984.
- [98] D. J. Mazey, "Fundamental aspects of high-energy ion-beam simulation techniques and their relevance to fusion materials studies," *Journal of Nuclear Materials*, vol. 174, pp. 196-209, 11 1990.
- [99] P. Trocellier, Y. Serruys, S. Miro, E. Bordas, S. Pellegrino, S. Vaubaillon, M. O. Ruault, S. Henry and O. Kaïtasov, "Application of multi-irradiation facilities," *Nuclear Instruments and Methods in Physics Research Section B: Beam Interactions with Materials and Atoms*, vol. 266, pp. 3178-3181, 6 2008.
- [100] J. A. Hinks, "A review of transmission electron microscopes with in situ ion irradiation," *Nuclear Instruments and Methods in Physics Research Section B: Beam Interactions with Materials and Atoms*, vol. 267, pp. 3652-3662, 12 2009.
- [101] G. E. Lucas, G. R. Odette, M. Sokolov, P. Spätig, T. Yamamoto and P. Jung, "Recent progress in small specimen test technology," *Journal of Nuclear Materials*, Vols. 307-311, pp. 1600-1608, 12 2002.
- [102] M. R. Gilbert, S. L. Dudarev, D. Nguyen-Manh, S. Zheng, L. W. Packer and J.-C. Sublet, "Neutron-induced dpa, transmutations, gas production, and helium embrittlement of fusion materials," *Journal of Nuclear Materials*, vol. 442, pp. 755-760, 11 2013.
- [103] L. K. Mansur, A. F. Rowcliffe, M. L. Grossbeck and R. E. Stoller, "Isotopic alloying to tailor helium production rates in mixed-spectrum reactors," *Journal of Nuclear Materials*, vol. 139, pp. 228-236, 7 1986.
- [104] G. R. Odette, "New approaches to simulating fusion damage in fission reactors," *Journal of Nuclear*

Materials, Vols. 141-143, pp. 1011-1017, 11 1986.

- [105] R. L. Klueh, N. Hashimoto, M. A. Sokolov, K. Shiba and S. Jitsukawa, "Mechanical properties of neutron-irradiated nickel-containing martensitic steels: I. Experimental study," *Journal of Nuclear Materials*, vol. 357, pp. 156-168, 10 2006.
- [106] E. Gaganidze, C. Petersen and J. Aktaa, "Study of helium embrittlement in boron doped EUROFER97 steels," *Journal of Nuclear Materials*, Vols. 386-388, pp. 349-352, 4 2009.
- [107] N. Hashimoto, R. L. Klueh and K. Shiba, "Pros and cons of nickel- and boron-doping to study helium effects in ferritic/martensitic steels," *Journal of Nuclear Materials*, Vols. 307-311, pp. 222-228, 12 2002.
- [108] L. K. Mansur, E. H. Lee, P. J. Maziasz and A. P. Rowcliffe, "Control of helium effects in irradiated materials based on theory and experiment," *Journal of Nuclear Materials*, Vols. 141-143, pp. 633-646, 11 1986.
- [109] K. Farrell, "Experimental effects of helium on cavity formation during irradiation—a review," *Radiation Effects*, vol. 53, pp. 175-194, 1 1980.
- [110] X. Jia and Y. Dai, "Microstructure and mechanical properties of F82H weld metal irradiated in SINQ target-3," *Journal of Nuclear Materials*, Vols. 329-333, pp. 309-313, 8 2004.
- [111] B. M. Oliver and Y. Dai, "Helium and hydrogen measurements on pure materials irradiated in SINQ Target 4," *Journal of Nuclear Materials*, Vols. 386-388, pp. 383-386, 4 2009.
- [112] Y. Dai, X. Jia, R. Thermer, D. Hamaguchi, K. Geissmann, E. Lehmann, H. P. Linder, M. James, F. Gröschel, W. Wagner and G. S. Bauer, "The second SINQ target irradiation program, STIP-II," *Journal of Nuclear Materials*, vol. 343, pp. 33-44, 8 2005.
- [113] L. K. Mansur and E. H. Lee, "Theoretical basis for unified analysis of experimental data and design of swelling-resistant alloys," *Journal of Nuclear Materials*, Vols. 179-181, pp. 105-110, 3 1991.
- [114] P. Vladimirov and A. Möslang, "Comparison of material irradiation conditions for fusion, spallation, stripping and fission neutron sources," *Journal of Nuclear Materials*, Vols. 329-333, pp. 233-237, 8 2004.
- [115] W. Wagner, J. Mesot, P. Allenspach, G. Kuehne and H. M. Ronnow, "The Swiss spallation neutron source SINQ-developments and upgrades for optimized user service," *Physica B: Condensed Matter*, vol. 385, pp. 968-971, 15 11 2006.
- [116] G. S. Bauer, "Operation and development of the new spallation neutron source SINQ at the Paul Scherrer Institut," *Nuclear Instruments and Methods in Physics Research Section B: Beam Interactions with Materials and Atoms*, vol. 139, pp. 65-71, 4 1998.
- [117] W. E. Fischer, "SINQ - The spallation neutron source, a new research facility at PSI," *Physica B:*

Condensed Matter, vol. 234, pp. 1202-1208, 2 6 1997.

- [118] G. S. Bauer, "Target options for SINQ," in *Proceedings of the 2nd International Workshop on Spallation Materials Technology*, 1997.
- [119] J. Knaster, S. Chel, U. Fischer, F. Groeschel, R. Heidinger, A. Ibarra, G. Micciche, A. Möslang, M. Sugimoto and E. Wakai, "IFMIF, a fusion relevant neutron source for material irradiation current status," *Journal of Nuclear Materials*, vol. 453, pp. 115-119, 10 2014.
- [120] J. Knaster, F. Arbeiter, P. Cara, S. Chel, A. Facco, R. Heidinger, A. Ibarra, A. Kasugai, H. Kondo, G. Micciche, K. Ochiai, S. O'hira, Y. Okumura, K. Sakamoto and E. Wakai, "IFMIF, the European–Japanese efforts under the Broader Approach agreement towards a Li(d,xn) neutron source: Current status and future options," *Nuclear Materials and Energy*, vol. 9, pp. 46-54, 12 2016.
- [121] J. Knaster, A. Moeslang and T. Muroga, "Materials research for fusion," *Nature Physics*, pp. 424-434, 5 2016.
- [122] J. A. Joyce and R. L. Tregoning, "Determination of constraint limits for cleavage initiated toughness data," *Engineering Fracture Mechanics*, vol. 72, pp. 1559-1579, 7 2005.
- [123] A. Pineau, "Development of the Local Approach to Fracture over the Past 25 years: Theory and Applications," *International Journal of Fracture*, vol. 138, pp. 139-166, 3 2006.
- [124] C. J. McMahon and M. Cohen, "Initiation of cleavage in polycrystalline iron," *Acta Metallurgica*, vol. 13, pp. 591-604, 6 1965.
- [125] G. T. Hahn, "The Influence of Microstructure on Brittle Fracture Toughness," *Metallurgical and Materials Transactions A*, vol. 15, pp. 947-959, 6 1984.
- [126] S. Lee, S. Kim, B. Hwang, B. S. Lee and C. G. Lee, "Effect of carbide distribution on the fracture toughness in the transition temperature region of an SA 508 steel," *Acta Materialia*, vol. 50, pp. 4755-4762, 11 2002.
- [127] M. Kroon and J. Faleskog, "Micromechanics of cleavage fracture initiation in ferritic steels by carbide cracking," *Journal of the Mechanics and Physics of Solids*, vol. 53, pp. 171-196, 1 2005.
- [128] Y. Qiao and A. S. Argon, "Cleavage crack-growth-resistance of grain boundaries in polycrystalline Fe–2% Si alloy: experiments and modeling," *Mechanics of Materials*, vol. 35, pp. 129-154, 1 2003.
- [129] Y. Qiao and A. S. Argon, "Cleavage cracking resistance of high angle grain boundaries in Fe–3% Si alloy," *Mechanics of Materials*, vol. 35, pp. 313-331, 3 2003.
- [130] A. Lambert-Perlade, A. F. Gourgues, J. Besson, T. Sturel and A. Pineau, "Mechanisms and modeling of cleavage fracture in simulated heat-affected zone microstructures of a high-strength low alloy steel," *Metallurgical and Materials Transactions A*, vol. 35, pp. 1039-1053, 3 2004.

- [131] T. Lin, A. G. Evans and R. O. Ritchie, "Stochastic modeling of the independent roles of particle size and grain size in transgranular cleavage fracture," *Metallurgical and Materials Transactions A*, vol. 18, pp. 641-651, 4 1987.
- [132] A. A. Griffith, "The Phenomena of Rupture and Flow in Solids," *Philosophical Transactions of the Royal Society A: Mathematical, Physical and Engineering Sciences*, vol. 221, pp. 163-198, 1 1921.
- [133] R. O. Ritchie, J. F. Knott and J. R. Rice, "On the relationship between critical tensile stress and fracture toughness in mild steel," *Journal of the Mechanics and Physics of Solids*, vol. 21, pp. 395-410, 11 1973.
- [134] G. R. Odette and M. Y. He, "A cleavage toughness master curve model," *Journal of Nuclear Materials*, Vols. 283-287, pp. 120-127, 12 2000.
- [135] G. R. Odette and M. Y. He, "Micromechanical modeling of master curve temperature shifts due to constraint loss," *Journal of Nuclear Materials*, Vols. 307-311, pp. 1624-1628, 12 2002.
- [136] G. R. Odette, H. J. Rathbun, J. W. Rensman and F. P. Broek, "On the transition toughness of two RA martensitic steels in the irradiation hardening regime: a mechanism-based evaluation," *Journal of Nuclear Materials*, Vols. 307-311, pp. 1011-1015, 12 2002.
- [137] P. Spätig, G. R. Odette, E. Donahue and G. E. Lucas, "Constitutive behavior and fracture toughness properties of the F82H ferritic/martensitic steel," *Journal of Nuclear Materials*, Vols. 283-287, pp. 721-726, 12 2000.
- [138] G. R. O. H. J. Rathbun and M. Y. He, "On the Size Scaling of Cleavage Toughness in the Transition: A Single Variable Experiment and Model Based Analysis," in *International Congress on Fracture 10*, 2001.
- [139] H. J. Rathbun, G. R. Odette, T. Yamamoto, M. Y. He and G. E. Lucas, "Statistical and Constraint Loss Size Effects on Cleavage Fracture: Implications to Measuring Toughness in the Transition," in *Application of Fracture Mechanics in Failure Assessment*, 2003.
- [140] G. R. Odette, "On the ductile to brittle transition in martensitic stainless steels - Mechanisms, models and structural implications," *Journal of Nuclear Materials*, vol. 212, no. Part 1, pp. 45-51, 1 9 1994.
- [141] M. Nevalainen and R. H. Dodds, "Numerical investigation of 3-D constraint effects on brittle fracture in SE(B) and C(T) specimens," *International Journal of Fracture*, vol. 74, pp. 131-161, 5 1996.
- [142] M. Enmark, K. Edsinger, G. Lucas and G. R. Odette, "Fracture behavior of surface cracked panels of HT-9 at low temperatures," *Journal of Nuclear Materials*, Vols. 233-237, pp. 347-350, 10 1996.
- [143] K. Edsinger, G. R. Odette, G. E. Lucas and J. W. Sheckherd, "The effect of size, crack depth and strain rate on fracture toughness—temperature curves of a low activation martensitic stainless steel," *Journal of Nuclear Materials*, Vols. 233-237, pp. 342-346, 10 1996.
- [144] G. E. Lucas, G. R. Odette, K. Edsinger, B. Wirth and J. W. Sheckherd, "On the Role of Strain Rate, Size and Notch Acuity on Toughness: A Comparison of Two Martensitic Stainless Steels," in *Effects of*

Radiation on Materials: 17th International Symposium, ASTM International, pp. 790--790--25.

- [145] S. G. Roberts, S. J. Noronha, A. J. Wilkinson and P. B. Hirsch, "Modelling the initiation of cleavage fracture of ferritic steels," *Acta Materialia*, vol. 50, pp. 1229-1244, 3 2002.
- [146] P. Bowen, S. G. Druce and J. F. Knott, "Effects of microstructure on cleavage fracture in pressure vessel steel," *Acta Metallurgica*, vol. 34, pp. 1121-1131, 6 1986.
- [147] T. Saario, K. Wallin and K. Törrönen, "On the Microstructural Basis of Cleavage Fracture Initiation in Ferritic and Bainitic Steels," *Journal of Engineering Materials and Technology*, vol. 106, p. 173, 1984.
- [148] M. Sokolov and R. Nanstad, "Comparison of Irradiation-Induced Shifts of K_{IC} and Charpy Impact Toughness for Reactor Pressure Vessel Steels," in *Effects of Radiation on Materials: 18th International Symposium*, ASTM International, pp. 167-190.
- [149] F. M. Beremin, A. Pineau, F. Mudry, J.-C. Devaux, Y. D'Escatha and P. Ledermann, "A local criterion for cleavage fracture of a nuclear pressure vessel steel," *Metallurgical Transactions A*, vol. 14, pp. 2277-2287, 11 1983.
- [150] K. Wallin, "The scatter in K_{IC} -results," *Engineering Fracture Mechanics*, vol. 19, pp. 1085-1093, 1 1984.
- [151] K. Wallin, "The size effect in K_{IC} Results," *Engineering Fracture Mechanics*, vol. 22, pp. 149-163, 1 1985.
- [152] X. Gao, C. Ruggieri and R. H. D. Jr, "Calibration of Weibull stress parameters using fracture toughness data," *International Journal of Fracture*, vol. 92, pp. 175-200, 1998.
- [153] R. A. Bonadé, "Constitutive behavior and fracture properties of tempered martensitic steels for nuclear applications," 2006.
- [154] P. F. Mueller, "Finite element modeling and experimental study of brittle fracture in tempered martensitic steels for thermonuclear fusion applications," 2009.
- [155] H. J. Rathbun, G. R. Odette, M. Y. He and T. Yamamoto, "Influence of statistical and constraint loss size effects on cleavage fracture toughness in the transition - A model based analysis," *Engineering Fracture Mechanics*, vol. 73, pp. 2723-2747, 1 12 2006.
- [156] W. S. Farren and G. I. Taylor, "The Heat Developed during Plastic Extension of Metals," *Proceedings of the Royal Society of London A: Mathematical, Physical and Engineering Sciences*, vol. 107, pp. 422-451, 2 3 1925.
- [157] S.-H. Song and W. C. Choi, "FEM investigation on thermal effects on force in high-speed blanking of mild steel," *International Journal of Precision Engineering and Manufacturing*, vol. 17, pp. 631-635, 01 5 2016.
- [158] S. Yadav, E. A. Repetto, G. Ravichandran and M. Ortiz, "A computational study of the influence of thermal softening on ballistic penetration in metals," *International Journal of Impact Engineering*, vol.

25, pp. 787-803, 19 2001.

- [159] G. W. Cullen and Y. P. Korkolis, "Ductility of 304 stainless steel under pulsed uniaxial loading," *International Journal of Solids and Structures*, vol. 50, pp. 1621-1633, 15 5 2013.
- [160] K. Mergia and N. Boukos, "Structural, thermal, electrical and magnetic properties of Eurofer 97 steel," *Journal of Nuclear Materials*, vol. 373, pp. 1-8, 2 2008.
- [161] T. Hirose, T. Nozawa, R. E. Stoller, D. Hamaguchi, H. Sakasegawa, H. Tanigawa, H. Tanigawa, M. Enoeda, Y. Katoh and L. L. Snead, "Physical properties of F82H for fusion blanket design," *Fusion Engineering and Design*, vol. 89, pp. 1595-1599, 10 2014.
- [162] P. Knysh and Y. P. Korkolis, "Determination of the fraction of plastic work converted into heat in metals," *Mechanics of Materials*, vol. 86, pp. 71-80, 7 2015.
- [163] G. R. Odette, M. Y. He, E. G. Donahue and G. E. Lucas, "On the relation between engineering load-displacement curves and true stress strain behavior in tests of flat tensile specimens," 2002.
- [164] A. Husain, D. K. Sehgal and R. K. Pandey, "An inverse finite element procedure for the determination of constitutive tensile behavior of materials using miniature specimen," *Computational Materials Science*, vol. 31, pp. 84-92, 9 2004.
- [165] H. Liu, Y. Shen, S. Yang, P. Zheng and L. Zhang, "A comprehensive solution to miniaturized tensile testing: Specimen geometry optimization and extraction of constitutive behaviors using inverse FEM procedure," *Fusion Engineering and Design*, vol. 121, pp. 188-197, 10 2017.
- [166] M. Joun, J. G. Eom and M. C. Lee, "A new method for acquiring true stress-strain curves over a large range of strains using a tensile test and finite element method," *Mechanics of Materials*, vol. 40, pp. 586-593, 7 2008.
- [167] P. Spätig, R. Bonadé, G. R. Odette, J. W. Rensman, E. N. Campitelli and P. Mueller, "Plastic flow properties and fracture toughness characterization of unirradiated and irradiated tempered martensitic steels," *Journal of Nuclear Materials*, Vols. 367-370, pp. 527-538, 8 2007.
- [168] S. Knitel, P. Spätig and H. P. Seifert, "An inverse method based on finite element model to derive the plastic flow properties from non-standard tensile specimens of Eurofer97 steel," *Nuclear Materials and Energy*, vol. 9, pp. 311-316, 1 12 2016.
- [169] S. Knitel, Spätig, T. Yamamoto, H. P. Seifert, Y. Dai and G. R. Odette, "Evolution of the tensile properties of the tempered martensitic steel Eurofer97 after spallation irradiation at SINQ," *Submitted to Nuclear Materials and Energy*.
- [170] A.-A. F. Tavassoli, A. Alamo, L. Bedel, L. Forest, J.-M. Gentzbittel, J.-W. Rensman, E. Diegele, R. Lindau, M. Schirra, R. Schmitt, H. C. Schneider, C. Petersen, A.-M. Lancha, P. Fernandez, G. Filacchioni, M. F. Maday, K. Mergia, N. Boukos, Baluc, P. Spätig, E. Alves and E. Lucon, "Materials design data for reduced activation martensitic steel type EUROFER," *Journal of Nuclear Materials*, Vols. 329-333, pp.

257-262, 8 2004.

- [171] J. R. D. Associates, "Tensile Testing.," *ASTM International*, vol. 2nd ed., p. 25, 2004.
- [172] X. Gao and R. H. Dodds Jr, "An engineering approach to assess constraint effects on cleavage fracture toughness," *Engineering Fracture Mechanics*, vol. 68, pp. 263-283, 2 2001.
- [173] A. H. Sherry, C. C. France and M. R. Goldthorpe, "Compendium of T-Stress Solutions for Two and Three Dimensional Cracked Geometries," *Fatigue & Fracture of Engineering Materials & Structures*, vol. 18, pp. 141-155, 1 1995.
- [174] S. G. Larsson and A. J. Carlsson, "Influence of non-singular stress terms and specimen geometry on small-scale yielding at crack tips in elastic-plastic materials," *Journal of the Mechanics and Physics of Solids*, vol. 21, pp. 263-277, 7 1973.
- [175] H. K. D. H. Bhadeshia and S. R. Honeycombe, "5 - Formation of Martensite," in *Steels (Third Edition)*, Oxford, : Butterworth-Heinemann, 2006, pp. 95-128.
- [176] P. Fernández, A. M. Lancha, J. Lapeña and M. Hernández-Mayoral, "Metallurgical characterization of the reduced activation ferritic/martensitic steel Eurofer97 on as-received condition," *Fusion Engineering and Design*, Vols. 58-59, pp. 787-792, 11 2001.
- [177] H. Tanigawa, R. L. Klueh, N. Hashimoto and M. A. Sokolov, "Hardening mechanisms of reduced activation ferritic/martensitic steels irradiated at 300 °C," *Journal of Nuclear Materials*, vol. 386, no. Supplement C, pp. 231-235, 30 4 2009.
- [178] W. Yan, W. Wang, Y.-Y. Shan and K. Yang, "Microstructural stability of 9-12 % Cr ferrite/martensite heat-resistant steels," *Frontiers of Materials Science*, vol. 7, pp. 1-27, 1 3 2013.
- [179] M. Klimenkov, R. Lindau, E. Materna-Morris and A. Möslang, "TEM characterization of precipitates in EUROFER 97," *Progress in Nuclear Energy*, vol. 57, pp. 8-13, 1 5 2012.
- [180] C. Dethloff, E. Gaganidze and J. Aktaa, "Quantitative TEM analysis of precipitation and grain boundary segregation in neutron irradiated EUROFER97," *Journal of Nuclear Materials*, vol. 454, pp. 323-331, 1 11 2014.
- [181] R. Bonadé, P. Spätig and N. Baluc, "Fracture toughness properties in the transition region of the Eurofer97 tempered martensitic steel," *Journal of Nuclear Materials*, vol. 367, no. Part A, pp. 581-586, 1 8 2007.
- [182] R. Bonadé, P. Mueller and P. Spätig, "Fracture toughness behavior in the ductile-brittle transition region of the tempered martensitic Eurofer97 steel: Experiments and modeling," *Engineering Fracture Mechanics*, vol. 75, pp. 3985-4000, 9 2008.
- [183] M. L. Williams, "On the Stress Distribution at the Base of a Stationary Crack," *Journal of Applied Mechanics*, vol. 24, pp. 109-114, 3 1956.

- [184] G. H. Paulino and J.-H. Kim, "A new approach to compute T-stress in functionally graded materials by means of the interaction integral method," *Engineering Fracture Mechanics*, vol. 71, pp. 1907-1950, 19 2004.
- [185] P. S. Leevers and J. C. Radon, "Inherent stress biaxiality in various fracture specimen geometries," *International Journal of Fracture*, vol. 19, pp. 311-325, 18 1982.
- [186] P. Spätig, G. R. Odette and G. E. Lucas, "Low temperature yield properties of two 7-9Cr ferritic/martensitic steels," *Journal of Nuclear Materials*, vol. 275, pp. 324-331, 11 1999.
- [187] J. W. Rensman, "NRG Irradiation Testing: Report on 300 °C and 60 °C Irradiated RAFM Steels. 2.5 and 10 dpa neutron irradiated Eurofer97 Plate, HIPed Powder, HIP diffusion welds, TIG welds, EB welds, F82H and NRG 9Cr lab heats.," 2005.
- [188] E. Dorn J. and S. Rajnak, "Nucleation of Kink Pairs and the Peierls Mechanism of Plastic Deformation," *Trans. AIME*, vol. 230, pp. 1052--1064 , 1964.
- [189] P. Spätig, N. Baluc and M. Victoria, "On the constitutive behavior of the F82H ferritic/martensitic steel," *Materials Science and Engineering: A*, Vols. 309-310, pp. 425-429, 7 2001.
- [190] Y. Cao, J. Ahlström and B. Karlsson, "Mechanical Behavior of a Rephosphorized Steel for Car Body Applications: Effects of Temperature, Strain Rate, and Pretreatment," *Journal of Engineering Materials and Technology*, vol. 133, p. 021019, 2011.
- [191] U. F. Kocks, "Laws for Work-Hardening and Low-Temperature Creep," *Journal of Engineering Materials and Technology*, vol. 98, p. 76, 1976.
- [192] U. F. Kocks and H. Mecking, "Physics and phenomenology of strain hardening: the FCC case," *Progress in Materials Science*, vol. 48, pp. 171-273, 1 2003.
- [193] X. F. Fang and W. Dahl, "Strain hardening of steels at large strain deformation. Part I: Relationship between strain hardening and microstructures of b.c.c. steels," *Materials Science and Engineering: A*, vol. 203, pp. 14-25, 11 1995.
- [194] K. Wallin, "Macroscopic nature of brittle fracture," *Le Journal de Physique {IV}*, vol. 03, pp. C7--575--C7--584, 11 1993.
- [195] D. I. A. Stienstra, "Stochastic micromechanical modeling of cleavage fracture in the ductile-brittle transition region.," *PhD Thesis, A&M University Texas*, 1990.
- [196] R. H. Dodds, F. Shih C. and T. L. Anderson, "Continuum and micromechanics treatment of constraint in fracture," *International Journal of Fracture*, vol. 64, pp. 101-133, 1993.
- [197] K. K. Yoon, W. A. V. D. Sluys and K. Hour, "Effect of Loading Rate on Fracture Toughness of Pressure Vessel Steels," *Journal of Pressure Vessel Technology*, vol. 122, p. 125, 2000.

- [198] J. A. Joyce, "On the Utilization of High Rate Pre-Cracked Charpy Test Results and the Master Curve to Obtain Accurate Lower Bound Toughness Predictions in the Ductile-to-Brittle Transition," in *Small Specimen Test Techniques*, ASTM International, pp. 253--253--21.
- [199] J. Kohout, V. Jurásek, M. Holzmann and I. Dlouhý, "Evaluation of Strain Rate Effects on Transition Behaviour Applying the Master Curve Methodology," in *Transferability of Fracture Mechanical Characteristics*, Springer Netherlands, 2002, pp. 255-270.
- [200] T. Yamamoto, G. R. Odette and M. A. Sokolov, "On the fracture toughness of irradiated F82H: Effects of loss of constraint and strain hardening capacity," *Journal of Nuclear Materials*, vol. 417, pp. 115-119, 10 2011.
- [201] K. Wang, Y. Dai and P. Spätig, "Microstructure and fracture behavior of F82H steel under different irradiation and tensile test conditions," *Journal of Nuclear Materials*, vol. 468, pp. 246-254, 1 2016.

Curriculum Vitae

Serafin Knitel



Bruggerstrasse 9c
5103 Wildegg
+41 76 8166 844
+43 676 50 75 455
knitel.s@gmx.net

EDUCATION

2014-2018	Doctoral Program Physics	École Polytechnique Fédérale de Lausanne
	PhD Thesis	
Title	Investigations and numerical modeling of mechanical properties of tempered martensitic steel Eurofer97 at various loading rates, temperatures and after spallation irradiation	
2009-2013	Master Degree Program in Technical Physics	University of Technology, Graz
	Master Thesis	
Title	Defect analysis of abrasive wear of cutting inserts	
2011	Semester Abroad, Postech - University of Science and Technology, Pohang/South Korea	
2005-2009	Bachelor Degree Program in Technical Physics	University of Technology, Graz
	Bachelor Thesis	
Title	Plasma diagnostics by Thomson scattering	

EXPERIENCE

2014-2018	PhD Student	Paul Scherrer Institut, Villigen/Aargau, Switzerland
	<ul style="list-style-type: none"> - Microstructural investigation using SEM - Nonlinear finite element simulations of tensile and fracture specimen - Elaboration of radiation protection plans to conduct active experiments - Development of tensile and fracture test techniques for non-standard specimen 	
2013-2014	Medical Physicist	University Hospital Graz (KAGes), Graz/Styria
	<ul style="list-style-type: none"> - Supervision of the medical linear accelerator - Planning and ensuring safe and accurate radiotherapy - Quality control and quality assurance 	

2013-2014 **Master Student** University of Technology Graz, Graz/Styria

- Microstructural investigation using XRD, SEM and TEM
- EDX and energy filtered TEM analysis

PUBLICATIONS

2018 **Evolution of the tensile properties of the tempered martensitic steel Eurofer97 after spallation irradiation at SINQ**

S. Knitel, P. Spätig, T. Yamamoto, H.P. Seifert, Y. Dai, G.R. Odette
Nuclear Materials and Energy, submitted

2016 **An Inverse Method based on Finite Element Model to derive the Plastic Flow Properties from non-standard Tensile Specimens of Eurofer97 Steel**

S. Knitel, P. Spätig, H.P. Seifert
Nuclear Materials and Energy, Volume 9, Pages 311-316

2016 **Temperature and Loading-Rate Dependence on a Local Criterion for Cleavage Fracture in the Transition Region of the Tempered Martensitic Steel Eurofer97**

S. Knitel, P. Spätig, H.P. Seifert
Procedia Structural Integrity, Volume 2, Pages 1684-1691

PRESENTATIONS

- 18th International Conference on Fusion Reactor Materials, 2017, Aomori, Japan, Poster presentation
- Nuclear Materials Workshop, 2017, Oberschan, Switzerland, Oral presentation
- 21th European Conference on Fracture, 2016, Catania, Italy, Oral presentation
- 17th International Conference on Fusion Reactor Materials, 2015, Aachen, Germany, Poster presentation
- Nuclear Materials Workshop, 2015, Meiringen, Switzerland, Oral presentation
- Nuclear Energy and Safety PhD Day, 2015, 2016 & 2017, Villigen-PSI, Switzerland, Poster and oral presentation